

# Thèse de l'Université de Lyon

## délivrée par l'Ecole Centrale de Lyon

Spécialité : Electronique, micro et nano-électronique, optique et laser.

soutenue publiquement le 12 février 2016.

par

**Hélène Duprez**

préparée à l'Institut des Nanotechnologies de Lyon (INL)  
en partenariat avec le Commissariat à l'Energie Atomique et aux Energies Alternatives (CEA)

## From design to characterization of hybrid III-V on silicon lasers for photonic integrated circuits

Ecole doctorale : Electronique, Electrotechnique, Automatique

---

### Composition du jury:

Ariel LEVENSON	Directeur de recherche CNRS - LPN	Rapporteur
Leif Katsuo OXENLØWE	Professeur - DTU	Rapporteur
Bahaa E. A. SALEH	Professeur - CREOL	Examineur
Di LIANG	Ingénieur de recherche - HPE	Examineur
Olivier GAUTHIER-LAFAYE	Chargé de recherche - LAAS	Examineur
Christian SEASSAL	Directeur de recherche CNRS - INL	Directeur de thèse
Badhise BEN BAKIR	Ingénieur chercheur - CEA/Leti	Encadrant de thèse



---

# Remerciements

---

Même s'il n'y a que mon nom qui apparaît sur la page de garde de ce manuscrit, je n'aurai jamais pu arriver à ce travail seule et les doigts de la main ne suffisent pas à dénombrer ceux grâce à qui cette thèse a pu aboutir.

Evidemment, je tiens tout d'abord à remercier mon encadrant au CEA, Badhise Ben Bakir, qui a su me mettre sur les rails et me former à tous les aspects de la recherche : la conception, la fabrication et la caractérisation. Grâce à lui j'ai acquis non seulement des compétences dans ces trois domaines mais aussi plus d'assurance vis-à-vis de mon travail et de mes résultats. Même si nous nous sommes moins vus de par l'éloignement géographique, je suis aussi très reconnaissante envers mon directeur de thèse, Christian Seassal, qui m'a toujours aidée lorsque j'en avais besoin et qui a été notamment très présent à la fin de ma thèse. J'ai apprécié d'avoir avec lui un point de vue un peu plus extérieur, moins évident à avoir lorsque l'on a la tête dans le guidon.

J'ai eu la chance d'arriver à la fin de la thèse d'Antoine Descos et de prendre la suite de ses travaux. Notre entente et son aide avant qu'il ne parte m'ont été précieuses et m'ont permis de rentrer plus vite dans le vif du sujet. De plus, les discussions que j'ai pu avoir avec Corrado Sciancalepore et Karim Hassan, arrivés au laboratoire dans le courant de ma thèse, m'ont beaucoup apportée grâce à leur expérience mais aussi leur curiosité.

Comme vous pourrez le voir dans la suite du manuscrit, la fabrication d'un laser est complexe notamment pour tout ce qui concerne le III-V et je remercie chaleureusement l'équipe 'photonique' du LPFE : Christophe Jany, Tiphaine Card, Romain Thibond et Romain Guiavarch. Je les ai assaillis d'un grand nombre de plaques à traiter et malgré cela, tout a pu être terminé avant la fin de ma thèse ce qui a été pour moi un grand soulagement. Un grand merci aussi à Julie Harduin qui a suivi mes lots à ma place pendant mon congé maternité et m'a tenue informée de toutes les avancées. Sans elle, ils auraient pris beaucoup de retard.

Enfin, si j'ai pu mener à bien toutes les caractérisations des lasers présentés dans ce qui suit, c'est bien sûr grâce à l'équipe caractérisation du LCPC : André Myko qui m'a appris à être rigoureuse en mesure, Karen Ribaud qui se rend toujours disponible pour aider et qui défend bec et ongles les créneaux caractérisation des thésards, Olivier Lemonnier plus rapide que l'éclair sur Labview et bien sûr Philippe Grosse que j'ai notamment embêté avec les mesures RF. C'est aussi avec eux que j'ai partagé la plupart des pauses à midi et au café et ces moments-là vont me manquer.

Je n'oublie évidemment pas mes co-bureaux : d'abord Ségolène Olivier, puis Antoine Descos et Simon Plantier, et bien sûr Gilles Grand, présent durant les 3 années. Ils ont d'abord supporté une doctorante enceinte, puis une doctorante enceinte et en rédaction de thèse ! Merci pour les bons moments passés ensembles.

Je souhaite terminer par les personnes extérieures qui m'ont soutenue durant ces trois ans. D'abord, merci aux thésards du LCNA, qui ne sont pas seulement des geeks comme la rumeur le laisse entendre : Justin Rouxel, Julien Favreau et Cédric Durantin. Merci aussi à ma famille et surtout à mes parents qui ont toujours cru en moi et grâce à qui j'en suis là maintenant. Enfin, merci à mon mari, Anthony, qui m'a beaucoup aidée et sans qui le stress de la fin de thèse aurait été autrement plus difficile à gérer. Mes derniers remerciements vont à ma fille Alexia, qui sans le savoir m'a aidée à relativiser sur le travail de thèse et, quoique ça puisse paraître paradoxal, à être plus efficace.





---

# Table of content

---

Remerciements.....	3
Table of content.....	5
Introduction .....	7
Chapter 1. Description, state of the art and goal of III-V on silicon lasers .....	9
1.1. Laser Diode overview.....	10
1.1.1. The laser amplification .....	10
1.1.2. The cavity.....	13
1.1.3. Laser Characteristics.....	16
1.2. From classic III-V semiconductor lasers to hybrid III-V/Si lasers .....	19
1.2.1. III-V lasers developments .....	20
1.2.2. III-V on silicon lasers.....	21
1.3. Specifications for this study .....	25
1.3.1. Main requirements .....	25
1.3.2. Different optimization approaches.....	25
Chapter 2. Devices architecture and process .....	27
2.1. Overall view of the device .....	28
2.2. III-V to silicon coupling.....	29
2.2.1. Supermode theory .....	29
2.2.2. Taper shape calculations.....	33
2.2.3. Taper characteristics .....	35
2.3. Hybrid laser integration .....	37
2.3.1. Silicon structuration.....	38
2.3.2. III-V epitaxy.....	40
2.3.3. III-V to silicon wafer bonding.....	41
2.3.4. III-V structuration and contact deposition .....	42
2.4. Characterization procedure.....	48
2.5. Conclusion to chapter 2.....	50
Chapter 3. Hybrid III-V on Si single-mode lasers .....	51
3.1. Distributed Bragg reflector lasers .....	52
3.1.1. Theory of distributed Bragg reflectors .....	53
3.1.2. Mirrors design.....	55
3.1.3. Results .....	59
3.2. Distributed Feedback lasers.....	62

3.2.1.	DFB theory.....	62
3.2.2.	Cavity design .....	64
3.2.3.	Results: vertically coupled DFB lasers.....	67
3.2.4.	Results: laterally coupled DFB lasers .....	72
3.3.	Conclusion to chapter 3.....	77
Chapter 4.	Tunable III-V on Si lasers.....	79
4.1.	Tuning material.....	80
4.1.1.	Thermo-optic effect.....	80
4.1.2.	Heater fabrication .....	81
4.1.3.	Heater measurements .....	81
4.1.4.	Hybrid tunable lasers state of the art.....	83
4.2.	Tunability efficiency of DBR lasers.....	83
4.3.	Sampled-grating DBR laser as a high precision tunable device .....	85
4.3.1.	SGDBR theory and state of the art .....	85
4.3.2.	SGDBR mirrors design.....	89
4.3.3.	SGDBR lasers characterization .....	94
4.4.	Conclusion to chapter 4.....	98
	Conclusion and prospects .....	99
Appendix A.	Transfer matrix theory for gratings .....	105
Appendix B.	Author list of publications .....	107
Appendix C.	French summary .....	109
	Introduction et objectifs.....	109
1.	Architecture du laser et couplage adiabatique.....	112
1.1.	Vue d'ensemble d'un laser .....	112
1.2.	Couplage entre guide III-V et guide silicium.....	113
2.	Lasers DBR.....	125
3.	Lasers SGDBR .....	130
	Conclusion et perspectives.....	137
	Bibliography.....	139

---

# Introduction

---

Speed. Efficiency. Two words one cannot do without when it comes to technology. Globalization has made it a necessity to be able to reach easily any piece of information anytime, anywhere, and as fast as possible. Who has never complained about his or her computer, phone or any such device, for being too slow? Whether these devices should be faster, or whether we should rather take our time is a philosophical question beyond the reach of a scientific thesis. Nonetheless, this trend is concerning and technology should find solutions to adapt to it. Perhaps more importantly than to simply meeting consumer demand, if information traffic keeps growing at its current rate, at some point it will no longer be possible to provide the required energy.

In the domain of telecommunications, copper-based interconnects increasingly fail to meet bandwidth and distance requirements. Moreover, further shrinking within integrated electronic circuits induces overheating as well as the apparition of unwanted quantum effects. To solve this issue, science has thus turned to optics. Not only optical links are lighter and less cumbersome than their copper-based counterparts, but they are also insensitive to electro-magnetic noise and can in principle provide higher bandwidth. Since the 90's, fiber-optic solutions have been developed for long haul telecommunications. Now, demand is growing for shorter distance interconnects with chip to chip and even intra-chip communications using optical switches.

The attractiveness of optical solutions will however depend on their cost. For now, many optical components remain low-volume products based on III-V materials and are thus very expensive. They could only compete with micro-electronics components if processed and assembled in a mass production chain. *Silicon Photonics* could save the day! This technology consists in building optical functions (waveguides, gratings, interferometers...) within silicon. Silicon photonics is attractive for a number of reasons. Firstly, silicon (Si) is transparent at telecom wavelengths (1.31  $\mu\text{m}$  and 1.55  $\mu\text{m}$ ). Secondly, the index difference between silicon and silica, its native oxide, is very high which makes possible highly compact optical devices compared to their III-V counterparts. Last but not least, Si-related processes are very well known thanks to micro-electronics and the development of complementary metal oxide semiconductor (CMOS) technology. However, the main drawback of silicon photonics is that silicon is a poor light emitter, due to its indirect bandgap. The leading issue in silicon photonics thus lies in integrating an efficient light source to a silicon optical circuit while staying CMOS compatible. Once such a source exists, *Silicon Photonics* may enter the data race...

One of the solutions implemented to obtain a laser source in silicon photonics is to use a stack of direct bandgap III-V materials as a gain enabler and to bond it directly onto a Si waveguide. Except for the light amplification function of the laser which is implemented within the III-V, all the other functions are carried out within the silicon: waveguide, mirrors, couplers... The resulting device is called a hybrid III-V/Si laser. CEA/Leti has been working on the development of such lasers since 2005, in collaboration with INL. In particular, A. Descos, the PhD student who worked here before me, demonstrated different hybrid III-V/Si lasers at 1.55  $\mu\text{m}$ . Based on this knowledge, the work presented in this thesis concerns the design, processing and characterization of a new set of state-of-the-art hybrid III-V/Si lasers at 1.31  $\mu\text{m}$ . I focused on lasers with their cavity formed by gratings and designed so as to obtain single-mode, and tunable emission. The development of the III-V to silicon coupling had to be implemented as well. I dealt with all those design aspects. As for the fabrication, the whole SOI structuration took place at the CEA/Leti platform where I was in charge of following the progress. Once the III-V epitaxies (bought either to III-V Lab or to Landmark), were bonded, C. Jany was in charge of the whole back-end process except for some

steps for which I helped. Eventually, I conducted the lasers measurements with the help of the characterization team in my lab.

In the first chapter, all the material required to understand how a laser diode works is detailed from its gain region to its cavity, with an emphasis on laser standard characteristics. Then, the state-of-the-art of silicon lasers is given with a specific focus on hybrid III-V on silicon lasers with the different kinds of cavities that have been demonstrated already. The main requirements of the lasers made during this work follow as well as the approach chosen to comply with them in term of designs.

The second chapter gives details on the common features of the lasers made during the thesis. It starts with the theory of III-V to silicon coupling and an explanation of the couplers design. Their robustness faced with process variations (wider or thinner waveguides, different oxide layer thickness, shift between the different layers...) is computed. Then, the full fabrication process flow is detailed, from silicon structuration to III-V waveguide definition including the III-V to silicon bonding. Eventually, the static and dynamic characterization procedures of the devices are described.

The third chapter deals with the designs and results of single-mode lasers. The first section is dedicated to Distributed Bragg Reflector (DBR) lasers, namely lasers with a grating at each output of the laser gain region. The second section tackles Distributed Feedback (DFB) lasers, namely lasers with a grating directly underneath the gain region. Two such lasers are discussed with a grating etched either on top or on the sides of the silicon waveguide. In each case, the effect of the different grating parameters on the mirror response is analyzed: etching depth, waveguide width, grating length and so on.

The fourth and final chapter is dedicated to laser tunability: it starts with explanations on the thermo-optic effect and presents the heaters used to tune the devices: their fabrication process as well as measurements of their effect over the temperature changes are given. Results of the tuning of the DBR lasers only are then given since the DFB lasers made during this work cannot be tuned without reducing their performances. In spite of what can be reached with DBR, we will see that to obtain precise tuning over a wide wavelength range, a less common device had to be designed: a Sampled-Grating DBR (SGDBR) laser. Most of this chapter focuses on this device with its design (again studying the effect of the different parameters on the mirror response) and the results obtained.

---

# Chapter 1. Description, state of the art and goal of III-V on silicon lasers

---

1.1.	Laser Diode overview .....	10
1.1.1.	The laser amplification .....	10
1.1.2.	The cavity .....	13
1.1.3.	Laser Characteristics.....	16
1.2.	From classic III-V semiconductor lasers to hybrid III-V/Si lasers .....	19
1.2.1.	III-V lasers developments .....	20
1.2.2.	III-V on silicon lasers.....	21
1.3.	Specifications for this study .....	25
1.3.1.	Main requirements .....	25
1.3.2.	Different optimization approaches.....	25

This first chapter is an introduction to III-V on silicon lasers. First, laser diodes' operation is explained with the bases compulsory to the good understanding of this work. Since these lasers main application is telecommunication, a brief overview of optics for communication is presented. Then, a focus on the history of semiconductor lasers is made, showing how the research in this field led to an interest in silicon photonics, and more particularly in hybrid III-V on silicon lasers. A state of the art of such lasers follows and to finish with this chapter, the expectations from this work are specified with the different optimization approaches.

## 1.1. Laser Diode overview

Devices which deliver coherent light are commonly called Lasers for 'Light Amplification by Stimulated Emission of Radiation' and such components can be separated into three different parts. Thus, a laser consists of a gain material in which light is amplified making round trips thanks to an optical cavity.

As illustrated on Figure 1-1, a laser can be described as an optical oscillator. First, photons need to be created into a coherent amplification region which uses the stimulated emission phenomenon, explained later. A feedback loop, the optical cavity, gets outgoing light to enter the amplifier again for amplification and so on until the output signal saturates. The system reaches then a steady state for which the output signal frequency corresponds to the amplified one. Moreover, amplification is only possible by bringing energy to the active material which is said to be 'pumped'.

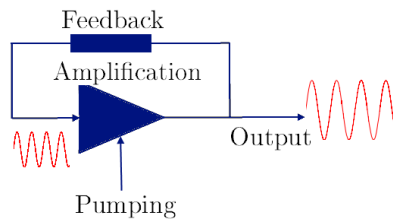


Figure 1-1: Oscillator schematic view

This paragraph addresses the principles associated to laser diodes [1], [2], namely lasers for which the active material consists of a semi-conductor.

### 1.1.1. The laser amplification

#### *Stimulated Emission*

As it can be deduced from the acronym, lasers are ruled by light-matter interaction laws and more precisely by the stimulated emission phenomenon described by Albert Einstein in 1917. Figure 1-2 represents an atom with two possible levels of energy  $E_1$  and  $E_2$ . If the atom is in the lower energy level, it can absorb a photon to reach the higher energy level. If an energy supply allows the atom to be in the excited state  $E_2$ , it can spontaneously transit from  $E_2$  to  $E_1$ , consequently releasing a photon. In the stimulated emission case, a photon interacting with the excited atom leads to the transition of the atom from  $E_2$  to  $E_1$  and the creation of a second photon identical to the first one. In all these configurations, the photon energy  $h\nu$  (with  $h$  the Planck constant and  $\nu$  the frequency) is equal to  $E_2 - E_1$ . Stimulated emission thus allows coherent light amplification at a frequency depending on the material energy levels.

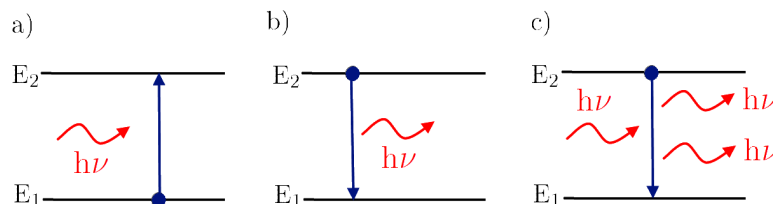
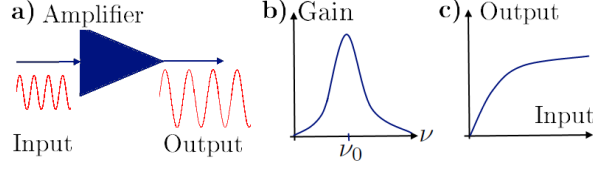


Figure 1-2 : Schematic views of a 2-level-system describing a) absorption, b) spontaneous emission, c) stimulated emission of a photon

### The amplifier

As represented in Figure 1-3 (a), an amplifier increases the power of an input signal without changing its incoming frequency. The output signal depending respectively on the frequency and on the input power is illustrated on Figure 1-3 (b) and (c). Beyond a certain value of the input signal, the output signal saturates.



**Figure 1-3 : Amplifier schematic view (a), gain versus frequency (b) and output power depending on the input power (c).**

The study of a photon flow  $\Phi$  going through a material with two different energy levels  $E_1$  and  $E_2$  shows that this flow changes as:

$$\phi(z) = \phi(0)e^{\gamma(\nu)z} \quad [1.1]$$

$$\gamma(\nu) = (N_2 - N_1)\sigma(\nu) \quad [1.2]$$

Where  $\phi(0)$  is the flux at the input of the material and  $N_1$  and  $N_2$  the number of atoms in the lower and higher energy levels respectively. The transition cross section  $\sigma(\nu)$  stands for the interaction between light and atoms and is a function of the optical modes density, the lifetime of an atom in an excited state, and a lineshape function centered on  $\nu_0 = (E_2 - E_1) / h$ .  $\gamma(\nu)$  is called the gain coefficient. If  $L_g$  is the active region length, the amplifier gain is then defined as:

$$G(\nu) = \frac{\phi(L_g)}{\phi(0)} = e^{\gamma(\nu)L_g} \quad [1.3]$$

Eq. [1.3] shows that amplification is only possible in the case where  $\gamma(\nu) > 0$  which means that more atoms have to be in the higher energy level than in the lower one:  $N_2 > N_1$ . This phenomenon is called population inversion and is only possible by bringing energy to the material, that is to say pumping it.

### The active region

Laser classification relies mostly on their active region which can either be under gaseous state as in the case of Helium-Neon laser [3], or made of solid material such as ruby-laser, the first material in which laser effect was observed in 1960. This work deals with laser which active material is a semiconductor. The two energy levels mentioned above correspond to the conduction and valence bands and the emission of a photon requires the recombination of an electron and a hole.

To allow for efficient recombination, the semiconductor bandgap needs to be direct because when it is not, the recombination is only possible with an energy supply, such as a phonon for instance as shown by Figure 1-4 (right). This is not the case for direct bandgap semiconductors like InP (Figure 1-4 (left)).

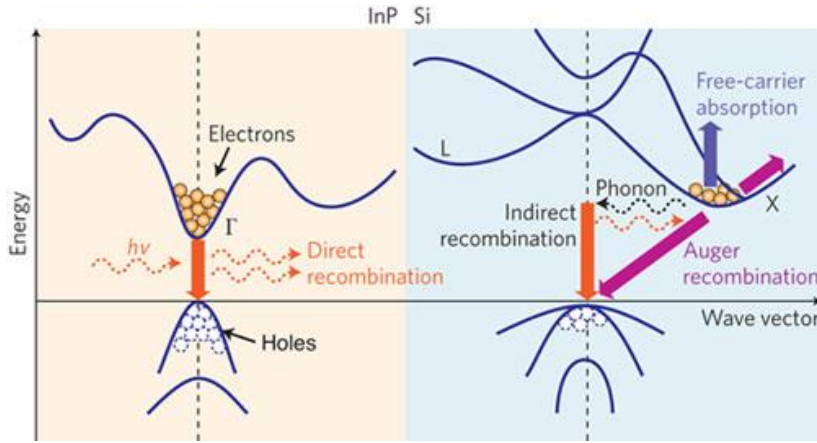


Figure 1-4 : Silicon (right) and InP (left) band diagrams[4].

To enhance the radiative recombination probability in the gain region, carriers have to be confined into it. To do so, the active material needs to be surrounded by materials with higher bandgaps thus creating a barrier for the carriers. The band diagram of such a stack is called a double hetero-structure and is represented on Figure 1-5. When the confinement is made along a very short distance, the structure becomes a quantum well (QW) and higher confinement is reached. However, heterojunctions are, by definition, thicker than QW and thus enable more carriers to recombine. To increase the gain meanwhile keeping a high confinement, a solution often chosen is to build a stack with a succession of barriers and quantum wells hence the name multiple quantum wells (MQWs).

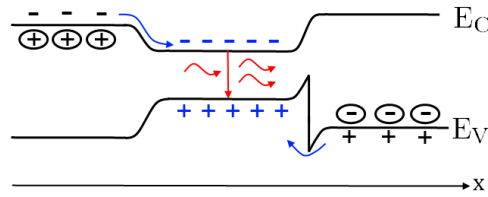


Figure 1-5: Band diagram of a double hetero-structure.

### Pumping

Optical and electrical pumping are two ways to reach population inversion. In the first situation, a light beam is sent through the material with enough energy to have the photons absorbed until reaching transparency ( $N_2 = N_1$ ). Electrical pumping consists in bringing electrons and holes in the material so that they recombine. This is usually made surrounding the active region by a  $p$ -doped and an  $n$ -doped material to create a PIN junction where the intrinsic region, namely the undoped region, is the active one, as represented on Figure 1-6. The carriers' motion is depicted on the Figure 1-6: a forward bias ( $V_{app}$ ) is applied which is opposite to the junction voltage ( $V_j$ ) thus lowering the barrier for the carriers. The majority electrons from the  $n$ -region (majority holes from the  $p$ -region) then overcome a transfer toward the  $p$ -region ( $n$ -region) passing through the active region. During this transfer, they get trapped into the quantum wells. The population inversion will be reached depending on the applied voltage.



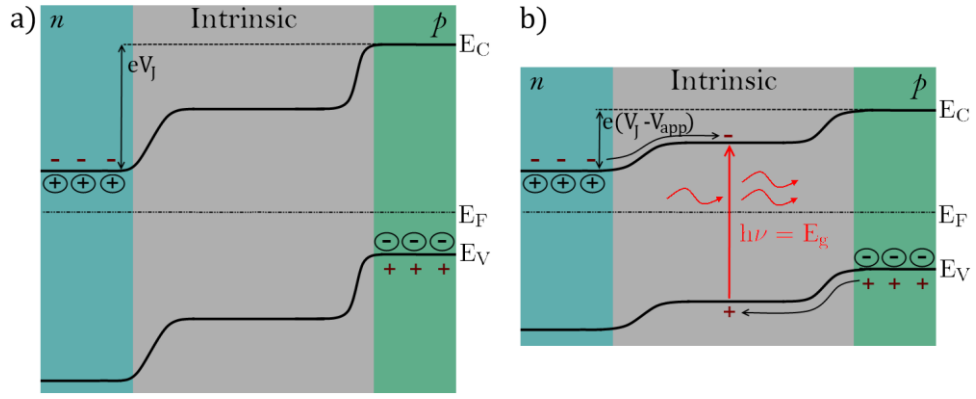


Figure 1-6: Schematic representation of a PIN junction a) at equilibrium, b) forward-polarized.

### 1.1.2. The cavity

In a resonant cavity, the light wave produces constructive interferences with itself for some specific wavelengths: the resonant frequencies. These frequencies are thus amplified while making round-trip in the cavity. Depending on the device geometry, the wave either turns around in circular cavities or goes back and forth in Fabry-Pérot-like cavities or stands by as in a distributed feedback scheme. We focused mainly on the two last types but a quick description of the others will be made in this paragraph. As represented in Figure 1-7, a Fabry-Pérot cavity can be defined by two mirrors surrounding an active region and an optional area in the cavity with no amplification called propagation region. The mirrors are defined by their reflectivity  $r_i = R_i e^{j\phi_i}$  ( $i = 1, 2$ ), the active and propagation regions are characterized by their internal losses  $\alpha_{i,a}$  and  $\alpha_{i,p}$  and the modal gain  $g$  in the first case.

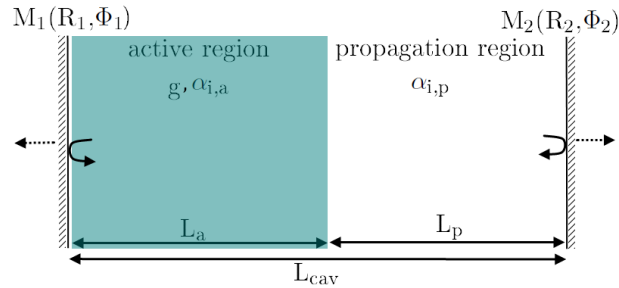


Figure 1-7: Schematic view of a Fabry-Pérot-like cavity

### Laser threshold

Regarding one particular mode in the cavity, this mode's threshold is defined as the moment when the losses are compensated by the gain. The ratio between the electric field ( $E$ ) after and before one round-trip is:

$$G_{\text{round-trip}} = \frac{E_{\text{round-trip}}}{E_0} = r_1 r_2 e^{-2j\tilde{\beta}_a L_a} e^{-2j\tilde{\beta}_p L_p} \quad [1.4]$$

where  $L_a$ ,  $L_p$  are respectively the lengths of the active and propagation regions.  $\tilde{\beta}_a$  and  $\tilde{\beta}_p$  are the complex propagation constants in these areas. Defining  $n_{\text{eff},i}$  the effective index of the mode,  $\Gamma_{xy,i}$  its transverse confinement factor and  $\lambda$  the wavelength, the propagation constant is (with  $i = a, p$ ):

$$\tilde{\beta}_i = \frac{2\pi n_{\text{eff},i}}{\lambda} + \frac{j}{2}(\Gamma_{xy,i} g_i - \alpha_{ii}) \quad [1.5]$$

For the magnitude, and assuming real mirror reflectivities, eq. [1.4] gives then:

$$|G_{\text{round-trip}}|^2 = R_1 R_2 e^{(\Gamma_{xy,a} g - \alpha_{ia}) L_a} e^{-\alpha_{ip} L_p} \quad [1.6]$$

At threshold, the wave electric field exactly replicates itself after one round-trip:  $G_{\text{round-trip}} = 1$  and we get:

$$\Gamma g_{\text{th}} = \langle \alpha_i \rangle + \alpha_m \quad [1.7]$$

With  $\langle \alpha_i \rangle = (\alpha_{ia} L_a + \alpha_{ip} L_p) / L_{\text{cav}}$  the average internal losses,  $\alpha_m = \ln(1/(R_1 R_2)) / L_{\text{cav}}$  the mirror losses and  $\Gamma = \Gamma_{xy,a} L_a / L_{\text{cav}}$  the confinement factor.

### Resonance condition

The imaginary part of eq. [1.4] provides the condition for the optical wave to build constructive interferences with itself after one round-trip, assuming threshold:

$$\frac{2\pi}{\lambda_l} 2(n_{\text{eff},a} L_a + n_{\text{eff},p} L_p) + \phi_1 + \phi_2 = l 2\pi \quad [1.8]$$

where  $l$  is an integer which defines the order of the interference. In the case of perfect mirrors, their phase shift is equal to  $-\pi$ . Thus, taking the cavity average effective index  $n_{\text{eff}}$  and the frequency  $\nu = c/\lambda$ , eq. [1.8] leads to the free spectral range of the cavity  $\Delta\nu$  which is the spacing between two interference orders:

$$\Delta\nu = \frac{c}{2n_{\text{eff}} L_{\text{cav}}} \quad [1.9]$$

The intensity transmitted by an optical wave at the output of a cavity with no amplification is represented on Figure 1-8 (a). Each peak stands for a resonant order but only those amplified contribute to the laser output power. To predict which mode will be selected, this curve and the gain curve  $\gamma(\nu)$  of the active region need to be superimposed as on Figure 1-8 (b). It can be noticed from eq. [1.9] that the longer the cavity, the smaller  $\Delta\nu$ , the more modes will be selected to lase thus leading to mode competition.

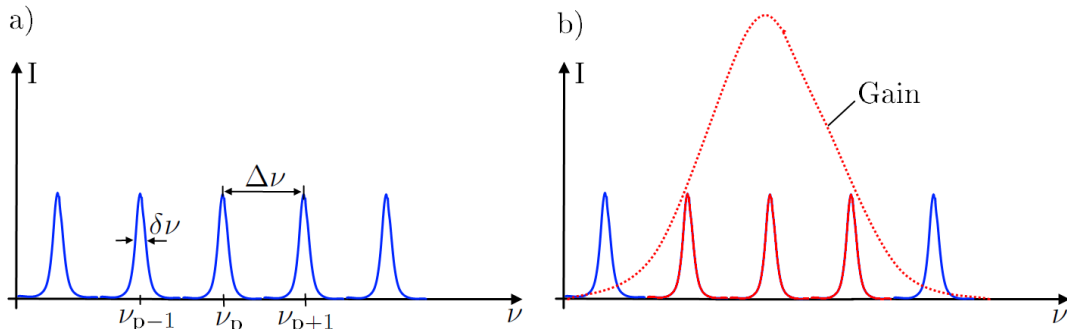


Figure 1-8: (a) Resonant frequencies in a cavity with no amplification. (b) Authorized modes in the laser.

An important characteristic of a cavity is its quality factor; it represents the confinement of the wave in the cavity and it is proportional to the ratio of the stored energy in the cavity and the energy loss per cycle. It is calculated as follows:

$$Q = \frac{\nu_p}{\delta\nu_p} = 2\pi\nu_p \tau_{ph} \quad [1.10]$$

$\nu_p$  is the resonant frequency at the order  $p$  and  $\delta\nu_p$  the full width at half maximum (FWHM) of the corresponding peak. The second way to define  $Q$  enables us to obtain  $\tau_{ph}$ , the photon lifetime in the cavity.

It is important to note that although a high  $Q$  value is necessary to have enough stimulated emission, it must not be too high to allow some photons to go out of the cavity. As it can be interpreted from Figure 1-7, the output of the laser comes from what is lost by the cavity. High- $Q$ -lasers thus have low thresholds since photons are well trapped and create a lot of stimulated emission but tend to have low output power as well because leakage from the cavity is too small.

### Circular cavities

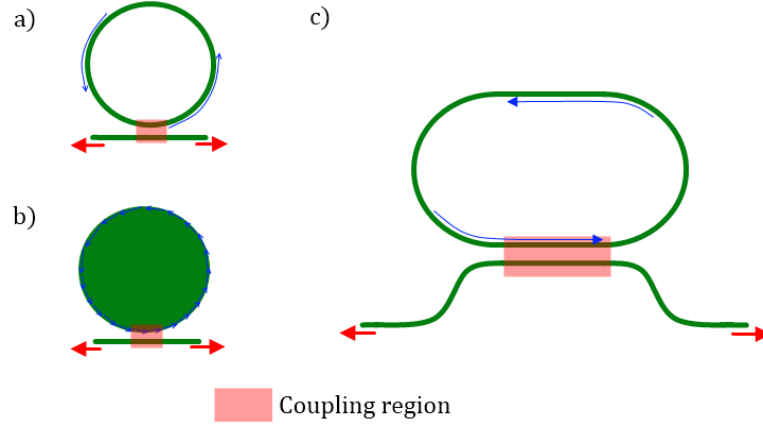


**Figure 1-9: (a) Ring resonator (b) Disk resonator (c) Racetrack cavity. In the three configuration, only one way is represented for the resonance.**

Many designs are possible when conceiving circular cavities: the cavity can either be a disk or a ring, namely filled or unfilled circles respectively, as represented in Figure 1-9 (a) and (b). Light is amplified and then coupled evanescently to an output waveguide only if the resonance condition is verified that is to say if its phase shift after one round trip is  $2\pi$ . The resonant modes are called whispering gallery modes (WGM). These cavities are advantageous in the sense that they have a small footprint (their diameter ranges from a few micrometers to a few tens of micrometers) and a high quality factor. The drawback of such a resonator is its high dependence on the fabrication process due to the need for the surface to be very smooth since it is where light propagates. Additionally, controlling accurately the coupling coefficient efficiency may be difficult.

Within racetrack resonator as well, the wavelength verifying the resonance condition is coupled to an output waveguide with two possible outputs. Contrary to the disk or the ring resonator, this architecture has a large footprint (its length can reach 700- $\mu\text{m}$ -long) and shows an erratic behavior due to light propagation in both ways in a device much longer than a disk.

### Grating-based cavities

In grating-based cavities, the mirrors consist of materials structured in a way to obtain periodic index changes as represented in Figure 1-10 (a). Such a mirror is called Distributed Bragg Reflector (DBR). At each layer interface, part of the optical wave is reflected and these different reflections give constructive interference only for wavelengths  $\lambda_{\text{Bragg},l}$  verifying the Bragg relation (see 3.1.1):

$$\lambda_{\text{Bragg},l} = 2an_{\text{eff}} \quad [1.11]$$

With  $a$  the periodicity,  $n_{\text{eff}}$  the effective index of the mode and  $l$  a natural integer representing the order of the grating.

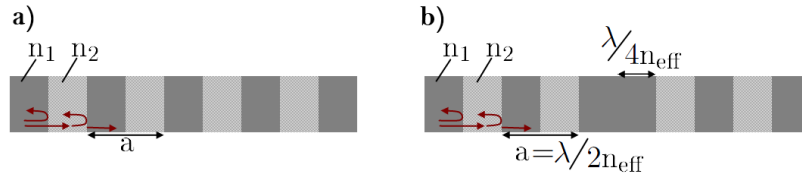


Figure 1-10: (a) 1D - periodic grating (b) grating with quarter wavelength shifter in the middle

Among the grating-based cavities, the most common are those using DBR and Distributed Feedback (DFB) mirrors, for which schematic views are available in Figure 1-11 (a) and (b) respectively. A DBR cavity is a Fabry-Pérot-like cavity in which the mirrors are DBR mirrors. This allows to better select the wavelength since resonances will only be possible for wavelengths verifying the Bragg condition. For a DFB laser, the grating lies within the active region thus generating a standing wave, and at the same time amplifying it. As it will be explained in 3.3.2, a quarter-wavelength layer needs to be added in the middle of the periodical structure (see Figure 1-10 (b)) to have one mode selected instead of the two modes existing with no phase shifter.

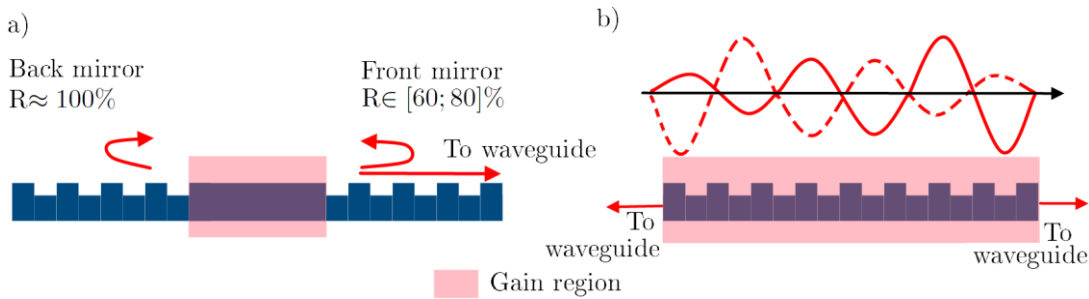


Figure 1-11: (a) DBR and (b) DFB laser cavities.

All the cavities quoted above are so-called 'in-plane' lasers: light is coupled in the plane of the device. Nonetheless, DBR lasers can also be made to get emission perpendicular from the surface as represented on Figure 1-12. These vertical cavity surface emitting lasers (VCSEL) are widespread in optic fiber communication since it avoids any output coupling issue.

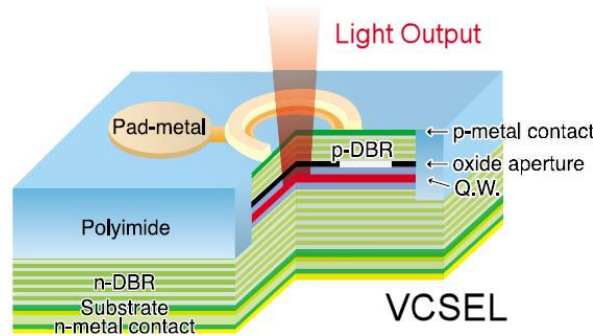


Figure 1-12: Schematic view of a VCSEL. Taken from 'Lasers pointer forum'

### 1.1.3. Laser Characteristics

In the following paragraph, different experimental characteristics are given as well as the influence of the different parameters on these characteristics. Some of the equations are given without any demonstration but the reader can refer to Coldren and Corzine as well as Saleh and Teich books [1], [2] to go deeper into theory.

### Static characteristics

Several typical plots have to be taken into account when evaluating any laser performance. The first thing to determine for an electrically pumped laser is whether the supply current is pulsed or continuous. Pulsed regime is often used to obtain laser operation without overheating of the device but the main goal is to reach laser operation in continuous wave regime. Then, to get most of the important static characteristic of a laser, two plots need to be observed: the power ( $P$ ) depending on the current ( $I$ ) and on the wavelength ( $\lambda$ ). Both are represented schematically on Figure 1-13. The first one is a good witness of the laser efficiency: it gives the maximum output power ( $P_{\max}$ ) and the laser threshold ( $I_{\text{th}}$ ), which is the current from which the losses are overcome by the gain allowing a laser beam at the output of the device. Above threshold, the power is a linear function of the current:

$$P(I) = \eta_{\text{diff}} \frac{h\nu}{q} (I - I_{\text{th}}) \quad [1.12]$$

Where  $q$  is the elementary charge and  $\eta_{\text{diff}}$  is the differential quantum efficiency of the laser and is experimentally deduced measuring the slope of the  $P$  versus  $I$  plot. In theory, it is defined as:

$$\eta_{\text{diff}} \equiv \eta_i \frac{\alpha_m}{\langle \alpha_i \rangle + \alpha_m} \quad [1.13]$$

$\eta_i$  being the injection efficiency: it represents the ‘fraction of terminal current that generate carriers in the active region’ [2]. We will see in 2.1 how it can be increased by modifying the device’s structure. It has to be noted that experimentally, the power stops increasing at some point as current increases due to an overheating of the device. This is commonly called the roll-off of the laser. Equations [1.12] and [1.13] show that to maximize the output power, not only the injection efficiency needs to be maximized, but also the threshold current as well as the internal losses have to be as low as possible. As for the latter, different parameters enter into account such as the type of material, its quality, the doping concentration...

Regarding the threshold current, a more complete analysis may be done using an analytic formula:

$$I_{\text{th}} \cong \frac{1}{\eta_i} q V B N_{\text{tr}}^2 e^{2(\langle \alpha_i \rangle + \alpha_m) / (\Gamma g_{0N})} \quad [1.14]$$

With  $V$  the active region volume occupied by electrons,  $B$  the bimolecular recombination coefficient depending on the material ( $B \sim 10^{-10} \text{ cm}^3/\text{s}$  for most III-V materials), and  $g_{0N}$  the gain coefficient. Equation [1.14] does not include non-radiative recombinations such as Auger effect but in regard to the parameters’ evolution, to decrease  $I_{\text{th}}$ , the trends stay the same. Firstly, the same deductions can be drawn for  $\eta_i$  and  $\langle \alpha_i \rangle$ . Moreover,  $V$  should be as low as possible and the product  $\Gamma g_{0N}$  as high as possible hence an interest in QWs which show good properties in this sense. The last, but not least parameter to minimize is the carrier concentration at transparency:  $N_{\text{tr}}$ . It depends on many things including the material and its geometry. It is for instance interesting to use strained QWs to influence the band curve and decrease  $N_{\text{tr}}$ .

Plotting the power versus the wavelength for a given injected current (as in Figure 1-13 (b)) is a way to check on the laser modes. In our case, the laser needs to be single mode, which means that the difference between the highest peak and the second highest one has to be as high as possible. This difference is called the side mode suppression ratio (SMSR) and is measured in decibel (dB). Another characteristic of each peak is their full width at half maximum (FWHM), often given in GHz. To adjust both of these characteristics, one has to modify the filtering function of the cavity as it will be tackled in Chapter 3.

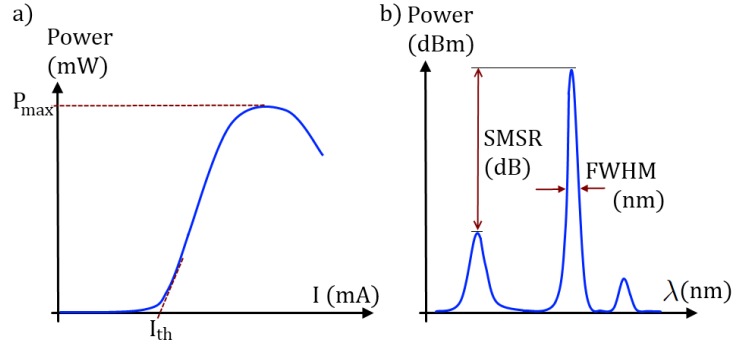


Figure 1-13 : Laser characteristics: output power as a function of a) the injected current b) the wavelength

The laser characteristic temperature  $T_0$  is also an important feature since it gives a glimpse on how robust the device is with increasing temperatures. More precisely, it is a measure of the threshold current variations as temperature increases and it should be as high as possible:

$$I_{th}(T) = I_0 e^{T/T_0} \quad [1.15]$$

Contrary to what was said before,  $T_0$  measurements have to be implemented in pulsed regime to take only the chuck temperature variations into account and not the temperature induced by the device self-heating. Another essential feature of the laser related to temperature is its maximum temperature operation  $T_{op,max}$ .

### High speed performances

In some cases, the laser needs to be modulated, and the device frequency response enables to evaluate the laser performances at high speed. Figure 1-14 (a) represents the modulation scheme for a laser diode: a DC current  $I_0$ , well above threshold, is applied to the device superimposed with an AC current  $I_1$  thus passing from a minimum ( $P_{AC,min}$ ) to a maximum ( $P_{AC,max}$ ) AC-power at the frequency  $f = \omega/2\pi$ . It has to be noticed that the modulation is made on the linear part of the  $P$  versus  $I$  curve. The calculation of the ideal frequency response of a laser diode is very well explained by Coldren [2] and starts with describing the current applied to the device as in eq. [1.16]:

$$I = I_0 + I_1 e^{j\omega t} \quad [1.16]$$

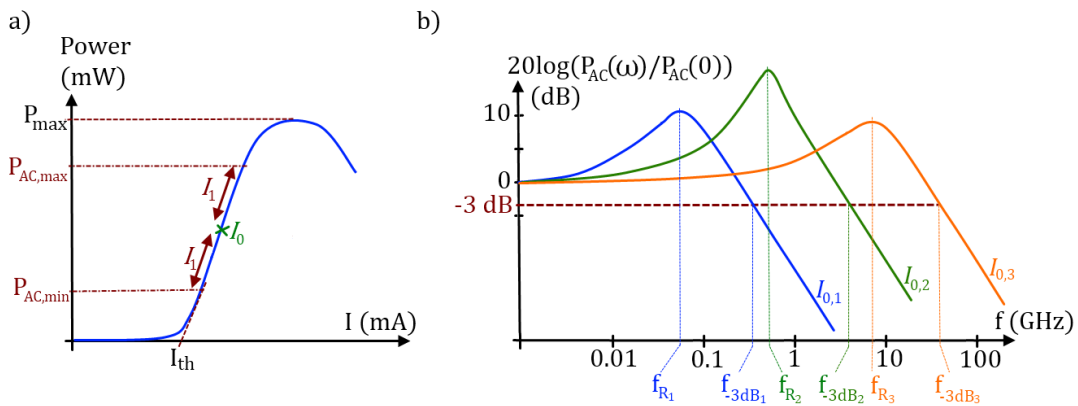


Figure 1-14: a) Modulation scheme b) Frequency response of an idealized laser diode for different DC currents ( $I_{0,1}$ ,  $I_{0,2}$  and  $I_{0,3}$ ).

Further calculations lead to the laser diode transfer function:

$$\frac{P_{AC}(\omega)}{I_1(\omega)} = \eta_{diff} \frac{h\nu}{q} \frac{1}{1 - (\omega/\omega_R)^2 + j(\omega/\omega_R)(\omega_R\tau_p + \frac{1}{\omega_R\tau})} \quad [1.17]$$

Where  $P_{AC}$  is the AC-power,  $\tau$  the carriers' lifetime, and  $\tau_p$  the photons lifetime. Eq. [1.17] shows that the system presents a resonance at  $\omega_R$  which can be observed with the frequency response of the laser diode represented on Figure 1-14 (b) for different DC-powers. This curve enables to determine the 3 dB-bandwidth ( $f_{-3dB}$ ) of the device which is the frequency for which the DC-signal received by the laser is divided by two. The higher value it reaches, the faster the device.

Another way to evaluate the high speed characteristic of the laser is to supply it with an electrical bit stream of '0' and '1' and to check on the reliability of the laser output thanks to an 'eye diagram'. One is displayed on Figure 1-15: the highest power level stands for the '1' and the lowest for the '0' but instead of plotting the response of the laser versus time, all the possible transitions in a 3 bit sequence ('000', '010', '100'...) are displayed. Such a representation provides a good view of the overall quality of the signal and what is aimed at is to have an open eye diagram even as the bit flow increases, which means the laser power is able to follow the power supply.

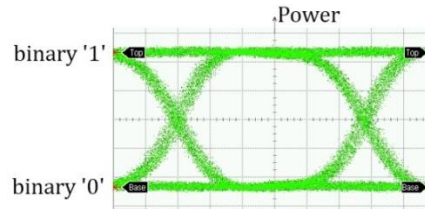


Figure 1-15: Eye diagram representation

## 1.2. From classic III-V semiconductor lasers to hybrid III-V/Si lasers

Lasers made with semiconductor materials appeared in the 1970's and at this time, research on the subject were mainly motivated by the use of optics in communication. Wires capacities were then sufficient to convey the performances needed and it is only ten years later that optics for digital computing was searched into. Today, diode lasers investigations are as much leaded by optical interconnects developments, with optical switchers, as datacommunication and telecommunication improvements which correspond respectively to short distance (~ few meters) and long distance (~ few kilometers) propagations of information. Figure 1-16 gives an overview of the basic components in an optical emitter-transmitter system for communication: light is first generated by lasers at different wavelengths and modulators allow encoding data on their output power. The different waveguides are then merged thanks to a multiplexer, an approach referred to as wavelength division multiplexing (WDM), and then light is transmitted through either a glass fiber or a waveguide. The receiver works the other way round: a demultiplexer separates the different wavelengths which are sent to photodetectors allowing the conversion of light into an electrical signal transferred through copper wires to an electronic chip. As this representation shows, the laser beam is a key point in this chain: it needs to be powerful enough to be detected after the propagation and since the different laser beams must not interfere with each other when in the same waveguide, the precision on the wavelength and the control of the spectral width are crucial.

This paragraph deals with semi-conductor laser developments during the last 40 years and with how the research has led to III-V on silicon lasers.

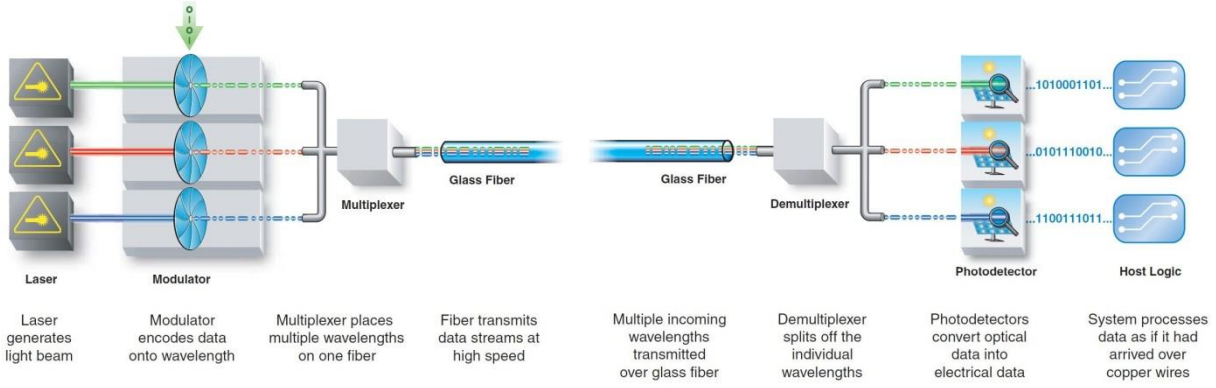


Figure 1-16: Basic components of an emitter (left) a receiver (right) system

### 1.2.1. III-V lasers developments

As explained in 1.1.1, III-V materials (In, Ga, As, Al, P, Sb) have a direct bandgap and consequently exhibit a high radiative efficiency. This is the reason why III-V lasers have been the starting point for semi-conductor lasers research well before the rise in interest in silicon photonics. Table 1-1 gives an overview of the advances in the field of bulk III-V lasers with different laser characteristics: the maximum temperature operation  $T_{op,max}$ , the current threshold  $I_{th}$  and the maximum output power.

Table 1-1: Bulk III-V lasers insight

Laser category	Dimensions	Characteristics	Ref.
Double Hetero-structure n-InP / n-GaInAsP / p-InP Fabry-Pérot cavity	$L_{cavity} \in [380; 400] \mu m$	$T_{op,max} = 34^\circ C$ $I_{th} \in [275; 450] mA$ $P_{max} \in [2; 4] mW$	[5]
Burried Hetero-structure p-InP / GaInAsP DFB cavity	$L_{cavity} \approx 200 \mu m$	$T_{op,max} = 37^\circ C$ $I_{th} = 55 mA @ 27^\circ C$ $P_{max} = 2 mW$	[23]
Single GaInNAs QW VCSEL and lateral emission DBR cavity	$L_{cavity} = 400 \mu m$ $\phi_{VCSEL} = 45 \mu m$	$T_{op,max} = 95^\circ C$ $I_{th,VCSEL} = 61 mA$ $P_{max,VCSEL} = 5 mW$	[6], [24]
Multiple QWs (x4) InGaAs/InGaAsP DBR cavity	$L_{cavity} = 400 \mu m$	$I_{th} = 19 mA @ 23^\circ C$ $P_{max} = 10 mW$	[25]
Multiple QW (x4) InGaAsP/InP $\mu$ -disk cavity	$\phi_{disk} = 3 \mu m$	$I_{th} = 150 \mu A @ 25^\circ C$ $P_{max} = arbitrary\ unity$	[20]
Multiple QW (x6) InGaAsP/InP Photonic crystal	$\phi_{laser} = 10 \mu m$	$I_{th} = 260 \mu A @ 23^\circ C$ $P_{max} = 5 nW$	[14]

The active region went from a double hetero-structure [5] to a single quantum well [6] quickly replaced by multiple quantum wells [7]. Lasers cavities evolved as well: in the first lasers, the Fabry-Pérot cavity was simply made by cleaving the facets of the gain area to enable reflection. Then DFB cavity appeared [8], [9] followed by DBR cavities which are harder to implement in III-V materials due to the low index difference between the Bragg mirror layers. DBR laser type S led to vertical cavity surface emitting lasers [10] (VCSEL) for which emission is perpendicular to the wafer surface. More recently, higher order



laterally coupled DFB [11], easier to make, were demonstrated. Other type of lasers, called micro-lasers were delved into as well to get devices with low threshold and low power consumption. Some of these lasers use photonic crystal cavities [12]–[19], for the other, the laser cavity consists of a micro-disk [20]–[22] and the amplified modes are whispering gallery modes. Since both these kind of devices show very low power output, they do not aim at the same applications as the formers which are intended for chip to chip propagation : they are more fit for intra-chip optics e.g. optical interconnects.

### 1.2.2. III-V on silicon lasers

With the improvements made in optical switching and the complexification of microelectronic nodes as they shrink, came the idea to develop optical interconnects on a very large scale integration (VLSI) as Goodman [26] explained in the mid 80's. However, III-V materials being rather rare on earth and complicated to process on a large scale, silicon started to be seen as an interesting material for optics. Not only silicon is transparent at the 1.31  $\mu\text{m}$  and 1.55  $\mu\text{m}$  data and telecommunication wavelengths but also the high index difference between silicon and silica, its native oxide, allows for a high confinement within these waveguides. Moreover, silicon wafers show a very low defect density compared with what can be made in other semi-conductors. Therefore, silicon photonics [27] appeared as a way to improve the bandwidth and the speed that can be reached with electrical interconnects and leverage at the same time the know-how acquired in processing silicon thanks to complementary metal oxide semiconductor (CMOS) foundries. Other than lasers, the development of some components compulsory into optical telecommunication circuits (see Figure 1-16) was necessary and many building blocks were demonstrated on the high index contrast silicon on insulator (SOI) circuitry: optical resonators and filters [28], input/output (I/O) couplers [29], [30], high-speed modulators [31], [32], Si-Ge photodiodes [33], and wavelength (de)multiplexers [34]. However, as aforementioned, silicon's indirect bandgap prevents its use as a gain enabler and bringing light to a silicon chip remains a challenge.

A continuous wave silicon laser based on Raman scattering [35] was demonstrated in 2005, which is very promising, but the laser was optically pumped and further developments need to be implemented to reach electrical pumping. The demonstration of an electrically pumped laser, using strained heavily doped Ge as a gain-enabler material [36], incites to keep looking in this direction as well, although the threshold current density is now way too high to regard this device as energetically viable. Some research also showed that an Er-doped SiN thin film deposited on silicon allows the formation of Si nanoclusters and induces a photoluminescence emission of the material around 1.55  $\mu\text{m}$  [37], [38]. This encourages inquiring further into an all CMOS-compatible laser source but a lot of work is still needed to get power-efficient devices.

So far, III-V hybridization with silicon seems to be the best compromise in term of flexibility in design, feasibility and functionality. It is a way to bring light directly on the chip where other optical functions, such as the laser feedback cavity or the components quoted above, are implemented within the SOI waveguides. Many solutions are possible when building III-V on silicon lasers not only regarding the type of laser but also the process chosen. The following paragraphs focuses on both these aspects.

#### *III-V on silicon integration*

When it comes to III-V on Si integration, the first issue arises from the high lattice parameter mismatch between both materials which prevents the direct epitaxy of the III-V on the silicon (there is for instance 8% lattice parameter mismatch between InP and Si). Although the use of a buffer layer such as SiGe [39] or GaSb [40] before growing the III-V enabled the demonstration of GaAs laser diodes grown on Si, the silicon is only used as a substrate in this case, with no integrated optical functions. To elude this problem,

many solutions are investigated as represented on Figure 1-17. The first one consists in making the whole photonic chip apart and then report it onto the silicon circuit. This is called flip-chip bonding [41]–[43], but although it is a very mature technology, it is expensive due to its low integration density and the time consuming alignment requirements and it gives less flexibility in the laser design. Another solution is to edge couple the laser source to the SOI wafer [44]–[46] as in figure 1-17 c). Again, the design is not so flexible due to coupling requirements between the laser source and the silicon wafer. Up to now, the most promising solution to integrate III-V together with silicon seems to be the wafer bonding [47], [48] which involves bonding a III-V stack to a processed SOI wafer. The III-V substrate is then removed before the etching of the III-V waveguides and the contacts deposition. This method enables to relax the alignment constraints, offers more possibilities in the devices design and gives the opportunity to bond the III-V material only where it is needed on the SOI wafer which is referred to as die-to-wafer bonding.

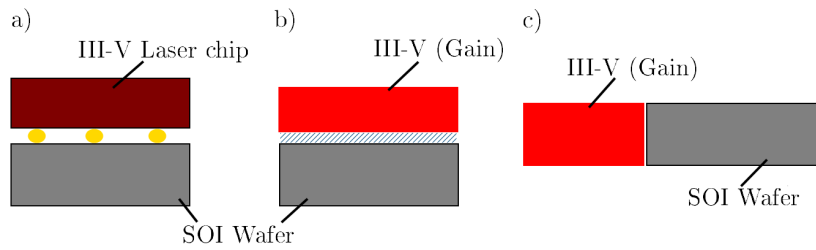


**Figure 1-17: Different III-V on Silicon integration schemes: a) flip-chip bonding, b) wafer bonding, c) edge coupling.**

Three ways to bond III-V onto silicon can be found in literature: metal bonding [18], [49], adhesive bonding [50] and direct bonding [51], [52]. In the first case, wafers are soldered together thanks to a metallic layer which high conductivity is an advantage for the laser's heat dissipation but which optical absorption is dangerously high. In the case of adhesive bonding, a polymer layer, the divinylsiloxane benzocyclobutene (DVS-BCB), is used to bond the wafers together [17]. Its interest relies on the low cost process associated since it is not too sensitive to the surface roughness and do not demand a high bonding temperature. On the other hand, the low thermal conductivity of DVS-BCB (0.3W/mK) may impinge on the device thermal properties. With direct bonding, the wafers surfaces are oxidized over a few nanometers and dangling bonds are freed using plasma: when in contact, the bonding is enabled by Van der Waals forces. Such a technique requires an ultra-clean and smooth surface. To relax this constraint on the surface, the oxide allowing the bonding can be thickened to values of a few tens of nanometers to better absorb the bonding defects: this is called molecular bonding.

### ***Different lasers architectures***

The extra issue in hybrid III-V on silicon lasers is the coupling between both materials. When conceiving the laser, there are two possibilities as regard with the optical mode in the active region: it can either be confined in the silicon waveguide [50], [53]–[56] or in the III-V medium [52], [57], [58]. In the first case, the mode stays mainly confined within the underlying silicon waveguide (see Figure 1-18 a)) and interacts with the III-V quantum wells only with its evanescent tail which limits the modal gain. Though such a configuration is subject to less complexity regarding coupling, the amplification is restricted and the bonding layer thickness is critical. In the second case which is represented in Figure 1-18 b) a better amplification is ensured but the transfer from the III-V to the silicon is critical. It is based on supermode theory (see 2.2.1) and it is usually implemented thanks to tapers in the III-V or in the silicon at the outputs of the active region.

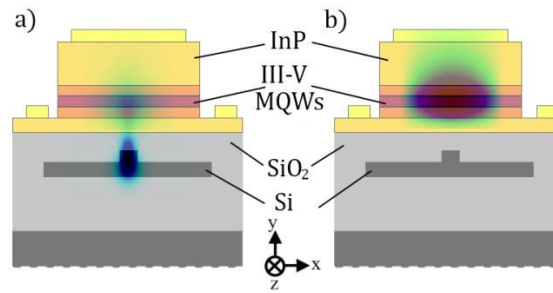


**Figure 1-18: Cross section views of the active region with a) evanescent coupling b) III-V confinement**

Table 1-2 gives an overview of III-V on silicon lasers state of the art. The first electrically-driven hybrid III-V on silicon laser was presented in 2006 by UCSB/Intel and consisted of a Fabry-Perot cavity [59] with cleaved and polished facets at each side of the active region. Then, other labs such as IMEC and CEA-Leti also demonstrated III-V on Si Fabry-Pérot lasers to prove their feasibility but the scientific community quickly moved on to more complex cavities with racetrack [60], [61], DBR [46], [53], [62], [63] and DFB [50], [54], [58] lasers.

Racetrack lasers have the advantage to be easily processed for there is no facet to cleave or grating to etch, only a waveguide to define. However the racetrack drawback, balanced by the high power that can be reached, is its large footprint which induces a high threshold current (see Table 1-2) and consequently high power consumption. The need for accurate wavelength addressing with low power consumption has thus raised a greater interest in DBR and DFB cavities lasers. As it can be seen in Table 1-2, these lasers have a much higher SMSR (at least 30 dB) which proves that they are single-mode. The current thresholds for these lasers often lies in the few tens of mA with maximum output powers within the 1-40 mW range. Although there has been DFB lasers made with the Bragg grating in the III-V [64], in most cases, the gratings dedicated to the cavity are etched in the silicon waveguide.

The concern in tuning the wavelength has also grown during the last few years. DBR lasers offer such a possibility although on a restricted wavelength range (15 to 20 nm maximum) and not very precisely: an index change is imposed on the Bragg mirrors leading to a jump from one mode to another mode in the cavity. Therefore, novel types of lasers showed up such as the laser proposed by III-V Lab and IMEC which uses a ring resonator superimposed with a DBR [65] to provide a precise filtering by changing the ring resonance thanks to a metallic heater, thus enabling tuning over 45 nm range pseudo-continuously. More details about laser tunability will be given in 3.3.3.

As for bulk III-V lasers, lower power than the milliwatt may be needed, and the so-called 'laser micro-sources' may be sufficient to reach the power then required. Many developments were implemented in this sense with micro-disk lasers at INL, IMEC and LETI [66], [67] in which small footprint is also an advantage. Demonstrated at the same time as the first 'large' lasers, the device consists of a III-V micro-disk evanescently coupled to a silicon waveguide. Research led for these lasers helped develop many technological processes now used in the lasers quoted above such as the molecular bonding, the III-V epitaxy structure and so on. HP Lab keeps working on this field with micro-ring lasers [56] with higher diameter than the disks (15 to 20  $\mu\text{m}$  instead of 7.5  $\mu\text{m}$ ) but higher output power and SMSR.

Lasers designed at CEA-LETI will be described in more details in the next chapter.

Table 1-2 : III-V on silicon hybrid lasers state of the art

III-V to Si Coupling	Bonding scheme	$\lambda$ ( $\mu\text{m}$ )	Cavity type	Characteristics			Year	Ref.
				$I_{\text{th}}$ (mA)	$P_{\text{max}}$ (mW)	SMSR (dB)		
Evanescent (confinement in Si waveguide)	Direct	1.55	Fabry-Pérot	50	12	$\sim 10$	2009	UCSB/ INTEL [53], [54], [60], [68], [69]
		1.31	Pérot	35	4	unknown	2007	
		1.55	Racetrack	200	23	$\sim 7$	2007	
		1.55	DBR	65	8	50	2008	
		1.55	DFB	25	3.5	50	2008	
Evanescent (confinement in III-V)	Molecular	1.55	$\mu$ -disk	0.5	0.01	$> 25$	2007	IMEC/ INL / LETI[67]
Evanescent (confinement in Si)	Direct	1.55	$\mu$ -ring	12	0.2	40	2009	HP Labs[56]
Evanescent (confinement in Si)	Adhesive	1.31	Fabry-Pérot	65	3.1	$\sim 15$	2011	IMEC [50], [70]
		1.31	DFB	25	2	45	2012	
Supermode : Tapers in III-V and in Si	Molecular	1.55	DBR + Ring resonator	35	4	50	2013	III-V Lab/IMEC[57]
'Edge-coupling' (III-V embedded in SOI)	Metal	1.55	DBR	41	8	$> 40$	2013	Skorpios[63]
Edge-coupling	No bonding	1.55	DBR	15	10	45	2012	Kotura [46]
Supermode: Taper in Si	Molecular	1.55	Fabry-Pérot	55	13	12	2011	CEA- LETI[52], [58]
		1.55	Racetrack	30	2.8	9		
		1.55	DBR	19	15	52		
		1.55	DFB	65	40	$> 30$		

### 1.3. Specifications for this study

#### 1.3.1. Main requirements

Although other applications can be contemplated for the lasers designed during this thesis, those mostly aim at matching telecommunication requirements for the km-long optical links 'Long Reach 4' (100GbaseLR4[71] or 40GbaseLR4). This standard purpose is to provide information through four wavelengths around 1310 nm (1295 nm, 1300 nm, 1305 nm, 1310 nm) over 10 km using wavelength division multiplexing. The '100GBASE' or '40GBASE' refers to the lasers speed: it consists of four lasers either modulated at 25 Gbit/s or 10 Gbit/s. To ensure propagation along the suitable distance, not only a sufficient power of a few milliwatts is necessary but also a side mode suppression ratio (SMSR) over 30 dB needs to be reached for the propagating mode to guarantee the differentiation of the modes at the output of the system. In addition, temperature operation of the device has to fit into the 10-80 °C range to stay compatible with the heat flow inside a circuit. Since optics for communication aims at reducing the energy consumption, it is also mandatory to obtain as low threshold as possible (<50 mA) and as high efficiency as possible (>10 %).

As aforementioned, WDM is required from these lasers hence the importance to get lasers with different wavelengths using a single process, all of them having a thin enough FWHM (<1 nm) so that they do not interfere when in the same waveguide. The ability to control the wavelength directly on the processed chip may be an advantage as well.

Furthermore, modulation of the signal is necessary for telecommunication applications. It can either be a modulation of the optical signal at the output of the laser thanks to optical modulators or a direct modulation that is to say a modulation of the electrical signal sent at the input of the signal. The integration of an optical modulator at the output of the laser was the subject of another PhD work in the lab during this thesis. However, the possibility to directly modulate the lasers designed in this work was explored. To fit into the LR4 necessities, the lasers modulation ought to reach 10 or 25 Gbit/s which implies to have more than 6.5 GHz and 16.5 GHz 3 dB-bandwidth respectively.

#### 1.3.2. Different optimization approaches

To reach an adequate power and high enough efficiency, different parts of the laser need to be analyzed. Firstly, the III-V gain region has to be optimized as described in the following chapter. The second thing to enhance is the coupling between the III-V and the silicon waveguides which, as mentioned earlier, is made using adiabatic tapers. These tapers need to be as robust as possible to get low losses and their design is also detailed in 2.2. At last, the cavity needs to be designed so that its Q-factor enable at the same time a good confinement but also enough 'leaks' which correspond to the output power. The frame of this work focused mostly on laser cavities and more precisely on gratings based cavities. The main difficulty lies in the fact that at this wavelength, the period of the gratings is much smaller than at 1.55  $\mu\text{m}$  which render their fabrication harder.

To achieve single mode lasers with the different wavelengths required for WDM, with one same process, DFB and DBR cavities were first designed and built as explained in Chapter 3. However, although DFB cavities have very thin peak (or FWHM), they are hard to tune in hybrid lasers configuration contrary to DBR gratings. This is why a last laser structure gathering both the peak thinness and the tunability was analyzed through sampled grating DBR lasers as detailed in Chapter 4.



---

## Chapter 2. Devices architecture and process

---

2.1.	Overall view of the device .....	28
2.2.	III-V to silicon coupling.....	29
2.2.1.	Supermode theory .....	29
2.2.2.	Taper shape calculations.....	33
2.2.3.	Taper characteristics .....	35
2.3.	Hybrid laser integration.....	37
2.3.1.	Silicon structuration.....	38
2.3.2.	III-V epitaxy.....	40
2.3.3.	III-V to silicon wafer bonding.....	41
2.3.4.	III-V structuration and contact deposition .....	42
2.4.	Characterization procedure.....	48
2.5.	Conclusion to chapter 2.....	50

This chapter focuses on the common aspects of the lasers designed during this work. First, a complete description of the devices is given with the different materials, geometries and other specific features. Then, the coupling between III-V and silicon is explained, starting with the basis of supermode theory from which the adiabatic couplers calculations ensue. The robustness of the taper regarding process variation is finally given. Since the different lasers share the same process flow their whole fabrication process is detailed here with the silicon structuration, the III-V to silicon bonding and the process of the hybrid structure which starts with the III-V definition and finishes with the contacts deposition. Eventually, the characterization procedure of the lasers is described from static to dynamic measurements.

## 2.1. Overall view of the device

Schematic longitudinal and transversal cross-section views of the devices designed during this work are represented on Figure 2-1 in the case of a distributed feedback laser. The III-V and the silicon waveguide are separated by a  $\text{SiO}_2$  gap of about 100 nm. The active region is either 500, 600 or 700- $\mu\text{m}$ -long ( $L_{\text{gain}}$ ) and consists of InGaAsP MQWs exhibiting maximum gain centered (ideally) on 1310 nm, surrounded by  $p$ - and  $n$ -doped InP layers thus forming the PIN junction. In this case, the DFB grating is etched along the 500-nm-thick silicon waveguide underneath the III-V active layers. In the case of a distributed Bragg reflector laser, the gratings are built at each side of the gain region (see 3.3.1), in the silicon as well. The silicon waveguide consists of a 200-nm-thick rib on a 300-nm-thick slab as it can be seen on the transversal cross-section of the laser (cf. Figure 2-1 (b)). Depending on where light is to be confined, the silicon rib of the waveguide ( $W_{\text{Si}}$ ) is widened or thinned down. As it was said in the first chapter, we made the choice to confine light mostly in the III-V QWs when in the active region hence the need for the silicon waveguide underneath to be narrow enough. At both terminations of the gain region, the latter is widened adiabatically, enabling light to be coupled into the silicon with more than 90% efficiency. These 100- $\mu\text{m}$ -long mode transformers are a key point in the design of the device and the next section delve deeper into their design. Laser light emission is collected with a fiber positioned on the top of a waveguide-to-fiber surface grating coupler.

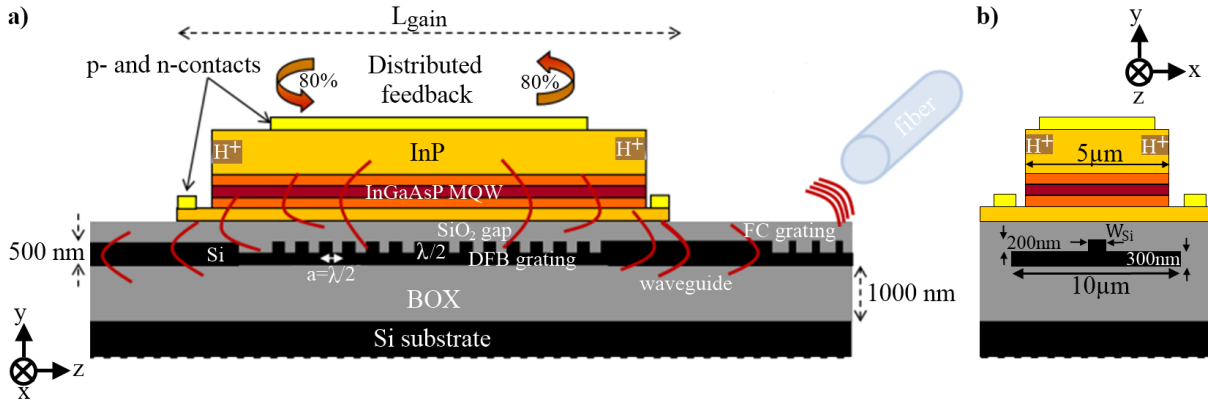


Figure 2-1: Longitudinal (a) and transversal (b) schematics views of the laser.

### Implantation and injection efficiency

As it can be seen on Figure 2-1, the sides of the 5- $\mu\text{m}$ -wide InP ridge are implanted with  $\text{H}^+$  ions thus inducing a region with a higher resistivity [72] which is represented by an electrical schematic of the implanted active region on Figure 2-2 (a). This enables to concentrate carrier injection in the center of the III-V waveguide as shown by the current lines on Figure 2-2 (b). This technique is a way to increase injection efficiency by decreasing the current leakage due to defect recombinations at the edges of the ridge and reducing the parasitic capacitance. This method was already implemented through semi-insulating InP layers in III-V bulk lasers [73]–[76]. Moreover, it allows an increase of the mode overlap ( $\Gamma$ ) with the carriers (cf. Figure 2-2 (b)) thus reducing the laser threshold and increasing the practical power operation as eq. [1.7] demonstrates.



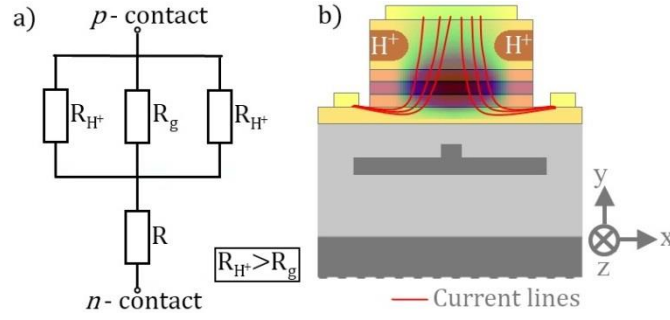


Figure 2-2: (a) Electrical schematic of the implanted active region. (b) Transversal view of the laser with the representation of the optical mode and the current lines.

## 2.2. III-V to silicon coupling

As it was said earlier (cf. 1.2.2), the device is designed in a way that light is confined in the III-V in the active region and then transferred into the silicon waveguide. The coupling between III-V and silicon is an essential part in the design of the laser. Two schemes can be implemented when coupling light from a waveguide to another. The first one is resonant or directional coupling and it consists in building waveguides with the appropriate size and spacing so that at the wavelength of interest, light oscillates from a waveguide to another meanwhile it propagates as represented in Figure 2-3 (a). It is advantageous in the sense that it allows very short coupling lengths, however, it is very hard to determine the exact maximum coupling length.

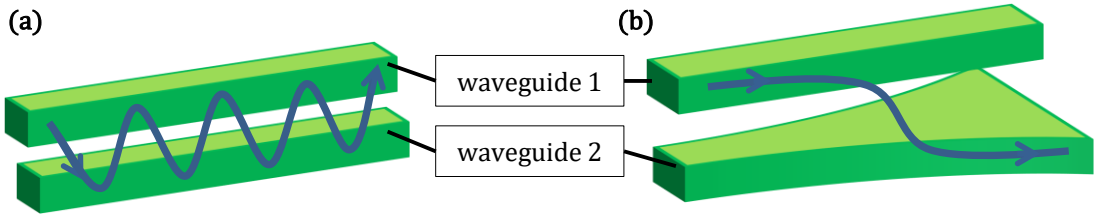


Figure 2-3: Schematic view of a two waveguides coupling scheme using (a) resonant coupling (b) coupling thanks to a mode transformer.

In our case, light coupling is enabled thanks to a mode transformer, called a taper, embedded in the silicon waveguide as it can be seen in Figure 2-3 (b). Although it can lead to coupling lengths several times longer than in the resonant case, this method is much more reliable and robust regarding process variations. The following sections describe how supermode theory enables to reach the shape of the tapers, and how different parameters, such as their input and output widths are chosen.

### 2.2.1. Supermode theory

#### *Supermodes*

The modes in presence in a coupled waveguides structure are called supermodes and are nothing more than the eigenmodes of the coupled structure [77]. In the hypothesis of weak coupling, the coupled mode theory leads to describe them as a linear combination of the modes from each separated waveguides: for one mode in an isolated waveguide, there are two supermodes in the coupled structure called even and odd modes ( $E_e$  and  $E_o$  respectively). As it is shown by Yariv and Sun in [78]–[80], these fundamental modes are expressed using column vector with their components being the amplitudes of the two individual waveguide modes ( $u_i(x, y)$ ,  $i \in [1, 2]$ ) :

$$\begin{cases} E_e(x, y, z) = \frac{1}{\sqrt{2}} \begin{pmatrix} \sqrt{1 - \delta/S} \\ \sqrt{1 + \delta/S} \end{pmatrix} e^{-j\beta_e z} = \vec{e}_e e^{-j\beta_e z} \\ E_o(x, y, z) = \frac{1}{\sqrt{2}} \begin{pmatrix} -\sqrt{1 + \delta/S} \\ \sqrt{1 - \delta/S} \end{pmatrix} e^{-j\beta_o z} = \vec{e}_o e^{-j\beta_o z} \end{cases} \quad [2.1]$$

With

$$\begin{cases} \delta = (\beta_2 - \beta_1)/2 \\ S = \sqrt{\delta^2 + \kappa^2} = (\beta_e - \beta_o)/2 \end{cases} \quad [2.2]$$

In equation [2.1] and [2.2],  $\beta_e$ ,  $\beta_o$ ,  $\beta_1$  and  $\beta_2$  are the propagation constants of the even and the odd modes of the coupled structure and of the fundamental mode in the isolated waveguide 1 and 2 respectively ( $\beta_i = \frac{2\pi}{\lambda} n_{\text{eff},i}$ ).  $\kappa$  is the coupling strength and it is defined as the overlap integral of the modes' transverse dependency functions for the isolated waveguides.

Three limit cases can be deduced from equation [2.1] and they are detailed on Figure 2-4. The mode distribution calculated using finite element method (FEM) is represented for the even and odd modes for all these cases in the coupled structure of interest namely a III-V waveguide on top of a silicon waveguide. Firstly, if the effective index of the isolated waveguide 1 (2) is much higher than that of waveguide 2 (1), e.g.  $\beta_2 < \beta_1$ ,  $|\delta| \gg |\kappa|$  ( $\beta_1 < \beta_2$ ,  $|\delta| \gg |\kappa|$ ), calculations shows that the even mode is mostly confined into the top (bottom) waveguide while the odd mode is in the bottom (top) waveguide. If both waveguides have the same propagation constant ( $\beta_2 = \beta_1$ ), the mode intensity for each mode is equally spread; this is called phase matching.

Using this phenomenon, it is clearly possible to transfer a mode from one waveguide to the other by changing the effective index in one or both waveguides. This change can be made widening or narrowing the waveguide slowly enough to minimize the losses induced by the effective index alterations. When the mode transformation happens with no losses, the transfer is said to be adiabatic. The easiest way to make an adiabatic taper is to widen (or narrow) the waveguide linearly on a very long distance. However, it was seen in 1.1.2 that the longer the laser cavity, the more numerous were the lasing modes, hence an interest in reducing the taper length. The next paragraph deals with a way to reach quasi adiabatic taper shape while reducing the length compared to a linear taper.

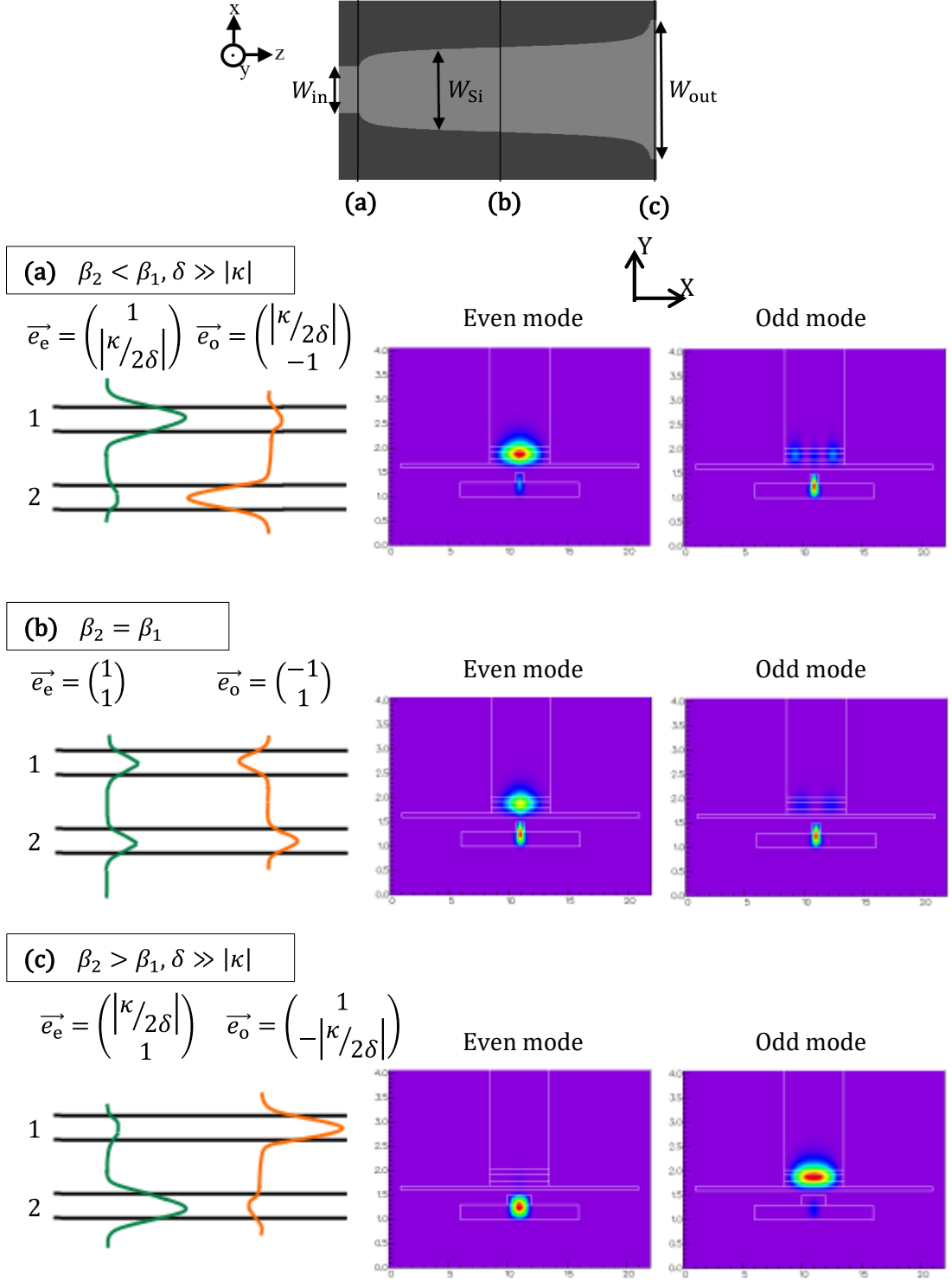


**Figure 2-4: Even and Odd mode representation and their transverse intensity for different configurations of the coupled structure with  $W_{III-V}=5\mu\text{m}$ ,  $\text{SiO}_2$  gap=100 nm, and (a)  $W_{Si} = 0.62 \mu\text{m}$ , (b)  $W_{Si} = 0.70 \mu\text{m}$ , (c)  $W_{Si} = 2.00 \mu\text{m}$ . The intensity repartition was calculated with a FEM mode solver. The top figure stands for a top view of the Si waveguide.**

To illustrate this coupling effect with our case, the mode overlap with the MQWs (including their barriers) as well as with the silicon waveguide as a function of the silicon waveguide's width is plotted on Figure 2-5. It shows that before phase matching, the confinement factor is at a steady value of 0.35 in the MQWs and the barriers. It corroborates as well the fact that for widths higher than  $1.50 \mu\text{m}$ , the mode is entirely in the silicon.

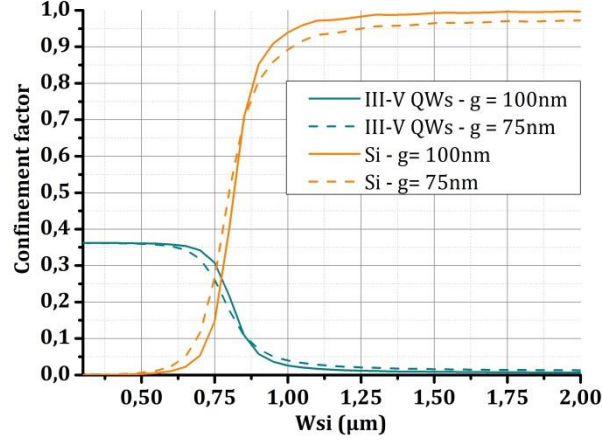


**Figure 2-5: Confinement factor in the III-V QWs (including their barriers) and in the silicon depending on the silicon waveguide's width in the case of 2 different thicknesses ( $g = 75$  nm or  $g = 100$  nm) between the III-V and the Si. The calculations were implemented using a FEM mode solver.**

### Adiabaticity criterion

The choice made here is to build the mode transformer in the silicon waveguide, widening it, because it is easier to process silicon with more precision than III-V materials. The method to obtain a short adiabatic taper is explained by Sun et al in [79] and it is summed up in what follows, starting from the overall electric field in the coupled structure which is a linear combination of the supermodes:

$$\vec{E}(z) = a_e(z)\vec{e}_e(z)\exp\left(-j\int_0^z\beta_e(z')dz'\right) + a_o(z)\vec{e}_o(z)\exp\left(-j\int_0^z\beta_o(z')dz'\right) \quad [2.3]$$

The electric field follows Fresnel equation:

$$j\frac{d\vec{E}}{dz} = \hat{B}\vec{E} \quad [2.4]$$

where it is assumed that  $\hat{B}\vec{e}_i = \beta_i\vec{e}_i$  ( $i \in [1,2]$ ). The aim of the taper is to keep as much power as possible into the even mode which means that  $a_o \approx 0$ . This hypothesis together with equations [2.3] and [2.4] lead, after a few calculations, to:

$$a_o = -\left(\frac{1}{2\kappa(1+\gamma^2)^{\frac{3}{2}}}\frac{d\gamma}{dz}\right)e^{-j\bar{S}z}\sin(\bar{S}z) \quad [2.5]$$

Where  $\bar{S} = \int_0^z S(z')dz'$  and  $S = (\beta_e + \beta_o)/2$ .  $\gamma(z) \equiv \delta(z)/\kappa(z)$  is the normalized mismatch propagation constant. Equation [2.5] displays an upper bound for the fraction of light in the odd mode:

$$|a_o| \leq \frac{1}{2\kappa(1+\gamma^2)^{\frac{3}{2}}}\frac{d\gamma}{dz} \quad [2.6]$$

Consequently, the fraction of power radiated in the unwanted mode can be limited to a certain value  $\varepsilon$  e.g.  $|a_o| \leq \sqrt{\varepsilon}$ . This leads to the adiabaticity criterion:

$$\frac{1}{2\kappa(1+\gamma^2)^{\frac{3}{2}}}\frac{d\gamma}{dz} = \sqrt{\varepsilon} \quad [2.7]$$

Eventually, making the hypothesis of a constant  $\kappa$  value, equation [2.7] can be solved as follows:

$$\begin{cases} \gamma(z) = \frac{u}{\sqrt{1+u^2}} = \tan(\arcsin(u)) \\ u \equiv 2\kappa\sqrt{\varepsilon}(z - z_0) \end{cases} \quad [2.8]$$

$z_0$  is the position where phase matching happens, namely when light is equally spread in both waveguides. This adiabaticity criterion gives the distribution of  $\gamma$  along the taper region and the next section shows how to get the shape of the taper from this. The validity domain for  $u$  proves that  $(z - z_0)$  varies from  $-1/(2\kappa\sqrt{\varepsilon})$  to  $+1/(2\kappa\sqrt{\varepsilon})$  hence a total taper's length  $L = 1/(\kappa\sqrt{\varepsilon}) = 2z_0$  showing that the lower the power penalty ( $\varepsilon$ ), the higher  $L$ .

### 2.2.2. Taper shape calculations

To find the taper shape, the silicon waveguide's width as a function of the  $z$ -position is needed:  $W_{\text{Si}} = f(z)$ . The distribution  $\gamma$  required to have an adiabatic mode transformation is known (see 2.2.1). Moreover,  $\gamma$  depending on the silicon waveguide width,  $\gamma(W_{\text{Si}})$  can be calculated using a mode solver. The reciprocal function can be taken from  $\gamma(W_{\text{Si}})$ , and using the right  $\gamma$  distribution, the taper contour can be reached:

$$W_{\text{Si}} = g(\gamma(z)) = f(z) \quad [2.9]$$

Following this reasoning, it is clear that the first data to calculate are the local modes' effective indices for the isolated waveguides versus the width of the silicon waveguide to deduce  $\delta(W_{\text{Si}})$ . Figure 2-6 shows these calculations in the case of a  $\text{SiO}_2$  thickness ( $g$ ) of either 100 nm or 75 nm between the two waveguides. Both these configurations were analyzed because this oxide thickness is very hard to control during process and to ensure the demonstration of efficient lasers, we chose to have tapers designed for both cases on the same run. The even and odd supermodes are also represented on the figure showing that the even supermode does not exactly fit the silicon fundamental mode after phase matching, especially when the separation between the waveguide is smaller. This demonstrates that the coupling is in fact quite strong and the hypothesis of weak coupling, made to obtain the supermodes, reaches its limit. The following computations show that the mode transformers built using coupled mode theory are still adiabatic.

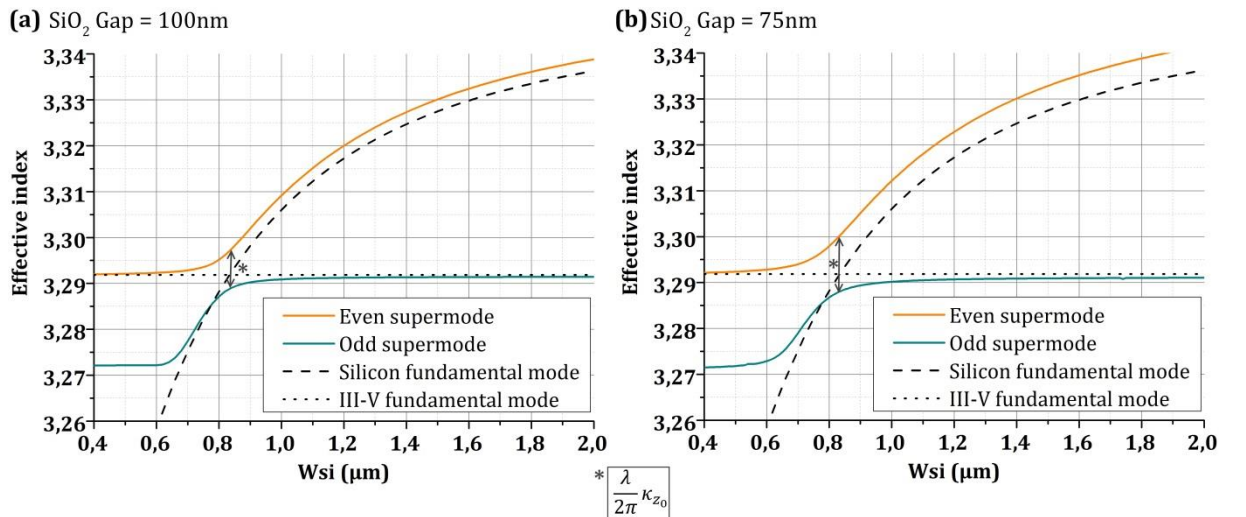


Figure 2-6: Supermodes evolution with  $W_{\text{Si}}$  for two different oxide thicknesses between III-V and Si: (a)  $g=100$  nm, (b)  $g=75$  nm. Calculations were made using a FEM mode solver.

Far from the phase matching, the overlap between the modes is very weak and can be neglected. Consequently, to calculate  $\gamma$ , the coupling constant  $\kappa$  is supposed not vary with  $W_{\text{Si}}$  and to be equal to its

value at phase matching ( $\kappa_{z_0}$ ). However, the taper calculated with this approximation did not allow the full transfer of the mode into the silicon which may be explained by the fact that the coupling between the waveguides is strong. To compensate for the error caused by the weak coupling approximation, we had to take higher value for  $\kappa$ , hence  $\kappa = 2\kappa_{z_0} = (\beta_{e,z_0} - \beta_{o,z_0})$ . The normalized mismatch propagation constant become thus:  $\gamma(W_{Si}) \equiv \delta(W_{Si})/(\beta_{e,z_0} - \beta_{o,z_0})$ . In the case of weak coupling, the phase matching ( $\delta = 0$ ) should coincide with the moment when the mismatch between the even and odd propagation constants is minimum e.g.  $W_{Si,\phi\text{matching}} = W_{Si,\min(\beta_e - \beta_o)}$ . This is the case when  $g=100$  nm but not when  $g=75$  nm:  $W_{Si,\delta=0}(g=75 \text{ nm})=0.84 \text{ }\mu\text{m}$  while  $W_{Si,\min(\beta_e - \beta_o)}(g=75 \text{ nm})=0.79 \text{ }\mu\text{m}$ . We chose to regard phase matching as the moment when  $(\beta_e - \beta_o)$  is at its minimum value for it is the supermode calculation which shows what really happens in the coupled system. The values found for  $W_{Si,\phi\text{matching}}$  and  $\kappa$  are displayed in Table 2-1 for both oxide thicknesses' values confirming that the coupling is much stronger for a gap of 75 nm.

**Table 2-1: Different coupling characteristics for 2 bonding oxide thicknesses**

g (nm)	$W_{Si,\phi\text{matching}}$ ( $\mu\text{m}$ )	$\kappa$ ( $\text{cm}^{-1}$ )	$W_{Si} = f(\gamma)$	$\epsilon$ (%)	$z_0$ ( $\mu\text{m}$ )
75	0.79	534	$W_{Si}(\gamma) = y_0 + A_1 e^{\gamma/t_1} + A_2 e^{\gamma/t_2} + A_3 e^{\gamma/t_3}$	2	65
100	0.84	384	$W_{Si}(\gamma) = y_0 + A_1 e^{(\gamma-x_0)/t_1} + A_2 e^{(\gamma-x_0)/t_2}$	4	65
Coefficients for g=75 nm:			Coefficients for g=100 nm:		
$y_0 = -0.37032 \text{ }\mu\text{m}$		$A_2 = 9.53\text{E-}2 \text{ }\mu\text{m}$	$y_0 = 0.22041 \text{ }\mu\text{m}$	$A_1 = 0.00445 \text{ }\mu\text{m}$	
$A_1 = 1.10872 \text{ }\mu\text{m}$		$t_2 = 1.90388$	$x_0 = -0.72385 \text{ }\mu\text{m}$	$t_1 = 1.28766$	
$t_1 = 19.62169$		$A_3 = 1.32\text{E-}4 \text{ }\mu\text{m}$		$A_2 = 0.56132 \text{ }\mu\text{m}$	
		$t_3 = 0.53297$		$t_2 = 8.69502$	

The dependence of  $\gamma$  on  $W_{Si}$  is represented on Figure 2-7 (a). Plotting then  $W_{Si}$  versus  $\gamma$ ,  $W_{Si} = f(\gamma)$  was deduced by fitting the curves and the results are reported in Table 2-1. Eventually, the taper shape was found using the adiabaticity criterion for  $\gamma$ . 2% and 4% losses were selected respectively for the thinnest and thickest gap between the waveguides.  $\epsilon$  is arbitrarily chosen different in each case to obtain the same taper length in both configurations (cf.  $z_0$  in Table 2-1). The normalized amplitudes  $f(z)$  of the tapers are represented on Figure 2-7 (b) (e.g. the shape of the side of the taper). The choice was made to work with 100- $\mu\text{m}$ -long tapers. To get the width's variations, the following equation needs to be used, with  $W_{in}$  and  $W_{out}$  the input and output widths respectively:

$$W_{Si}(z) = W_{in} + (W_{out} - W_{in})f(z) \quad [2.10]$$

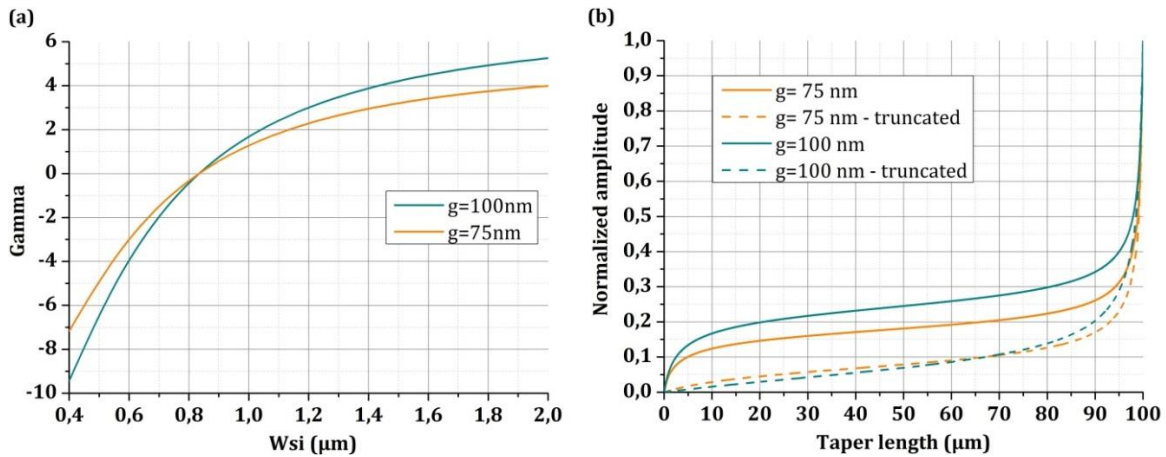


**Figure 2-7: (a)  $\gamma$  values versus the silicon waveguide width. (b) Normalized amplitude for different taper shapes**



On Figure 2-7 (b), the curves for truncated tapers are added. It corresponds to taper for which the input width is wider than 600 nm. The actual shape of the taper was calculated using mode computations from  $W_{\text{Si}}=0.4 \mu\text{m}$ . It will be seen below that for input widths wider than 600 nm, the taper shape is not suited any longer. However, for some mirror reflectivity reasons addressed in 3.2.2, wider input widths were needed. The appropriate shape can then be easily found by using the same function after a truncation from the proper width. In our case, the truncation was made for input widths centered on  $0.7 \mu\text{m}$ .

### 2.2.3. Taper characteristics

#### Robustness

Once the shape of the tapers is reached, computations need to be implemented to optimize the input and output widths. A beam propagation method (BPM) mode solver was used to calculate the coupling efficiency of the taper while both parameters were swept on a few tens of nm range. The resulting 2D-maps are displayed on Figure 2-8 for the four different cases tackled above. It is clear that there is a lot more flexibility on the output width than on the input width. This can be explained by the fact that for high widths values, the supermode variations are slowed down as the dimension increases. The idea is then to select a  $(W_{\text{in}}; W_{\text{out}})$  couple so as to maximize the coupling efficiency, staying robust regarding process variations. During process, the patterns' size varies typically of  $\pm 30 \text{ nm}$  for the dimensions tackled which is represented by dashed squares around the couples chosen. Here, the  $(W_{\text{in}}; W_{\text{out}})$  pairs are such that the process window contains mostly efficiencies higher than 90% or 85% on the very edges of the frame.

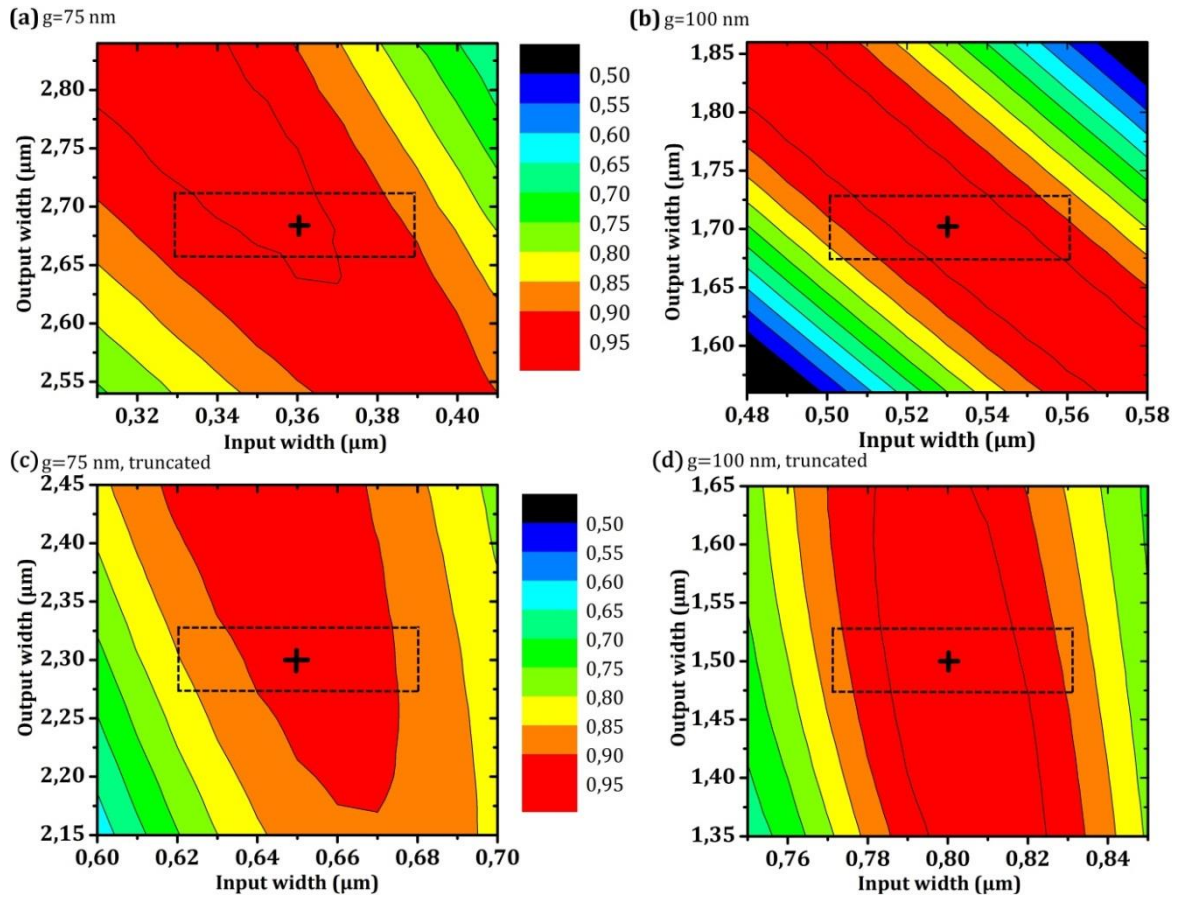


Figure 2-8: 2D-map of the 100- $\mu\text{m}$ -long taper's coupling efficiency depending on the input and output widths. The four cases seen above are represented: (a)  $g=75 \text{ nm}$ , (b)  $g=100 \text{ nm}$ , (c) truncated version of  $g=75 \text{ nm}$ , (d) truncated version of  $g=100 \text{ nm}$ . The efficiency was calculated using a BPM mode solver. The cross stands for the highest coupling value and the dashed square for the process window ( $\pm 30 \text{ nm}$ ).

Other uncertainties on the process are the SiO<sub>2</sub> oxide thickness ( $g$ ) and the alignment between the two waveguides ( $dX$ ). The tapers' coupling efficiency depending on these parameters are plotted on Figure 2-9, where each curve stands for one of the tapers selected from the ( $W_{in}$ ;  $W_{out}$ ) map. Until 0.5  $\mu\text{m}$ , the misalignment does not impact too much on the coupling which stays above 90%. As for the gap thickness, the influence on the taper's performances is much stronger and its control is critical. The plot shows that to have all the tapers efficient enough (e.g. >90%),  $g$  should be centered on 90 nm.

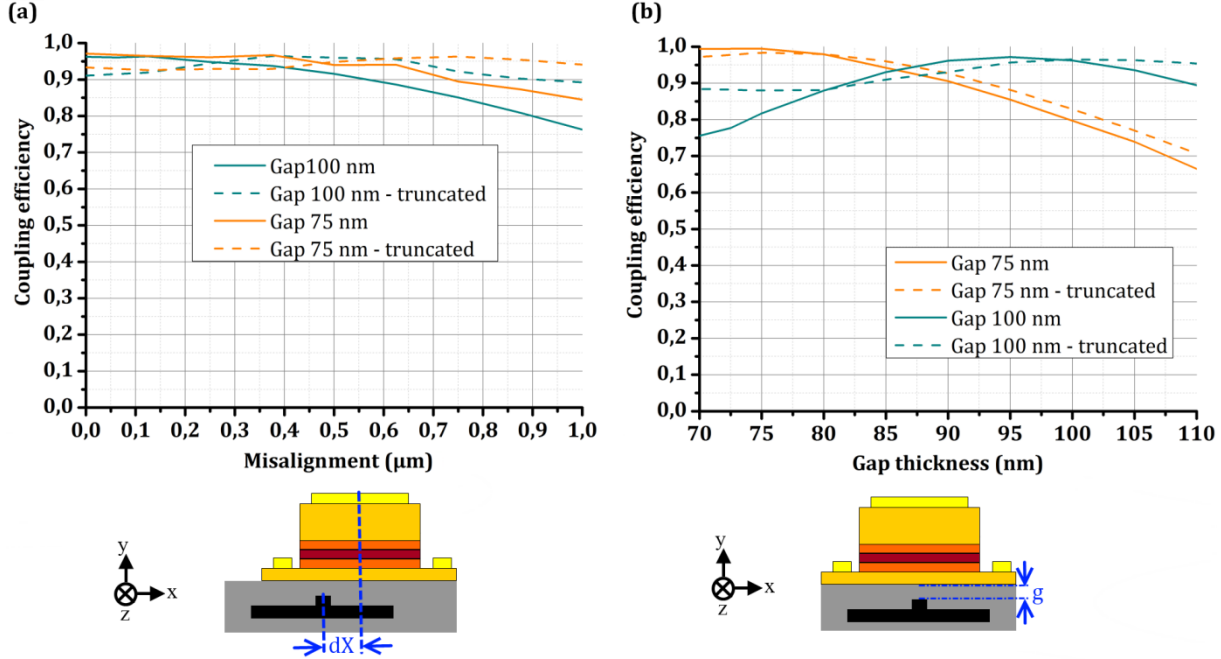


Figure 2-9: Tapers' coupling efficiency dependence on the process variations : (a) misalignment between the III-V and the silicon, (b) silicon gap thickness between the waveguides.

### Adiabaticity

Another computation compulsory to the design of the mode transformers is the study of the coupling efficiency evolution with the taper length as plotted of Figure 2-10. This plot allows validating that the taper is adiabatic: if it is, the coupling efficiency should not change with the length once the maximum is reached. If the tapers were not adiabatic, strong oscillations would be observed due to resonant coupling (as it is illustrated on Figure 2-3). Here, the adiabaticity is corroborated since from 100  $\mu\text{m}$ , the coupling efficiency does not go below 0.90 for the four tapers (0.89 for the taper designed for a gap of 100 nm). However, small oscillations are seen as the taper's length increases although their amplitude is small enough to validate the hypotheses made above. In fact, these are due to the coupling to the odd mode which is inherent to the adiabaticity criterion used: the latter includes a fraction of the power  $\varepsilon$  which is coupled to the second supermode (see 2.2.1). This phenomenon is represented for one of the truncated tapers on Figure 2-10 (b) where two lines separated by a value  $\varepsilon$  are drawn. One can notice that the oscillations stay almost confined between these lines. The mode transformers can thus be said to be quasi-adiabatic which demonstrates that the hypothesis of weak coupling is still applicable here although the  $\kappa$  value needs to be adjusted. To complete the taper study, the power repartition along propagation was represented on Figure 2-10 (c) for the truncated taper with a gap of 75 nm showing that the power does oscillate between the even and odd mode during propagation.



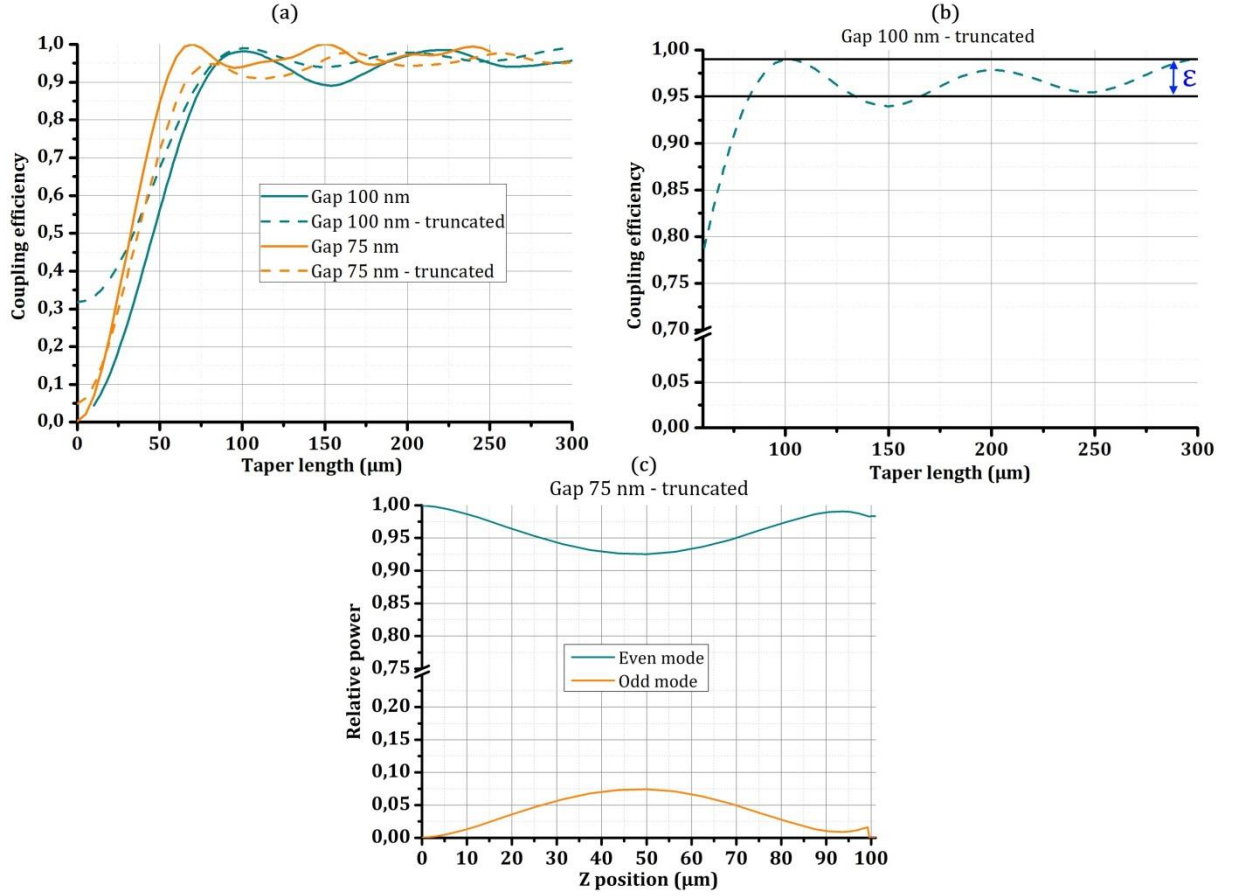


Figure 2-10: (a) Coupling efficiency of the mode transformers as a function of their length. (b) Focus on the truncated taper with a 100 nm oxide thickness where the losses toward the odd mode are schematized. (c) Relative power in the even and odd modes along the taper.

## 2.3. Hybrid laser integration

Now that the whole structure of the lasers was given as well as the designs common to all the devices, the next paragraph deals with their whole process fabrication (see Figure 2-11). First, the silicon waveguide is etched on a 200-mm-platform meanwhile 2 inches or 3 inches III-V wafers are grown. Then, bonding is implemented between the III-V and the silicon wafers, and the resulting wafer is downsized to 3 or 4 inches depending on the size of the III-V wafer. Eventually the III-V material is processed until contact deposition.

The advantage of such a sequence is that the III-V is processed after the bonding which means that no specific alignment is required during this step. Moreover, although it was not the subject of this work, it is possible to bond small dies (of a few  $\text{mm}^2$ ) only where the III-V is needed instead of 3 inches wafers, which would save some of this material, not as abundant as silicon.

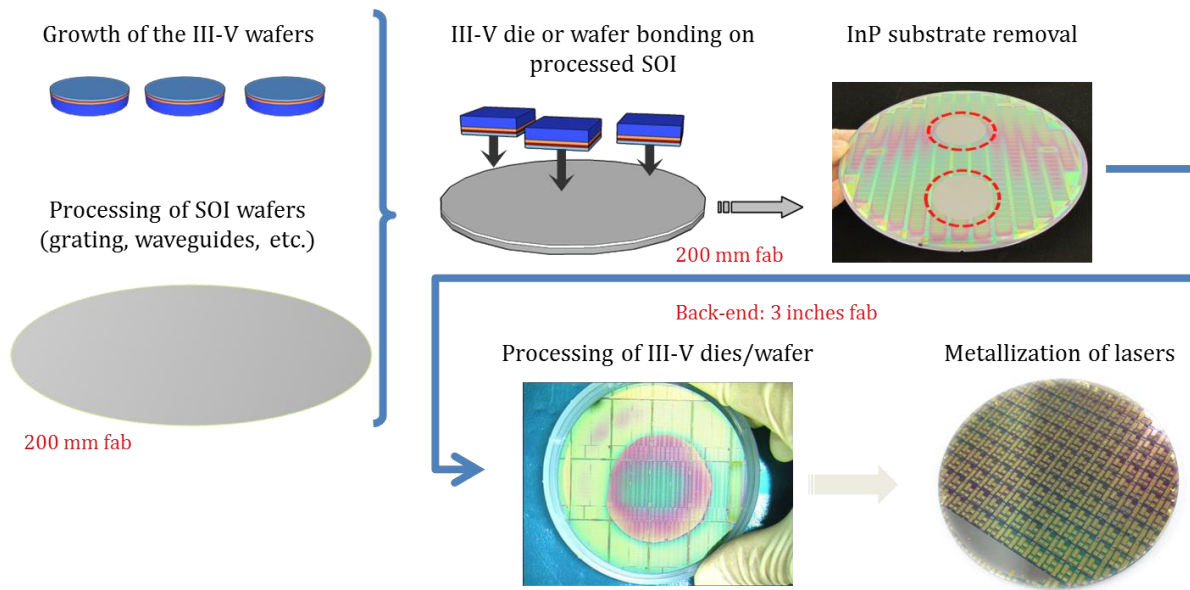


Figure 2-11: Overview of the hybrid III-V to silicon integration.

### 2.3.1. Silicon structuration

#### Four etching levels

The whole process starts with a silicon on insulator (SOI) wafer, namely a 500-nm-thick silicon layer on either a 1000-nm or a 700-nm-thick silica layer deposited on a 725- $\mu\text{m}$ -thick silicon wafer. The 200-mm SOI wafer is processed with four successive 193-nm-deep UV (DUV) photolithography and reactive ion etching (RIE) steps. Figure 2-12 illustrates the first three steps, giving a schematic cross section view of each level after etching and a top view obtained with a scanning electron microscope (SEM). First the grating is etched (from 10 to 80 nm depending on whether the laser is a DFB or a DBR), then the rib etching ensues with a depth of 200 nm. The third level which is 150-nm-deep corresponds to the definition of the fiber coupler grating. A last phase consists in separating all the lasers on the wafer, etching all the silicon left around the devices (150 nm). The 2<sup>nd</sup> and 3<sup>rd</sup> levels are defined using respectively 160-nm-thick and 100-nm-thick  $\text{SiO}_2$  hard masks while photoresist is sufficient for the two other levels. All the steps defining one etching level are described below.

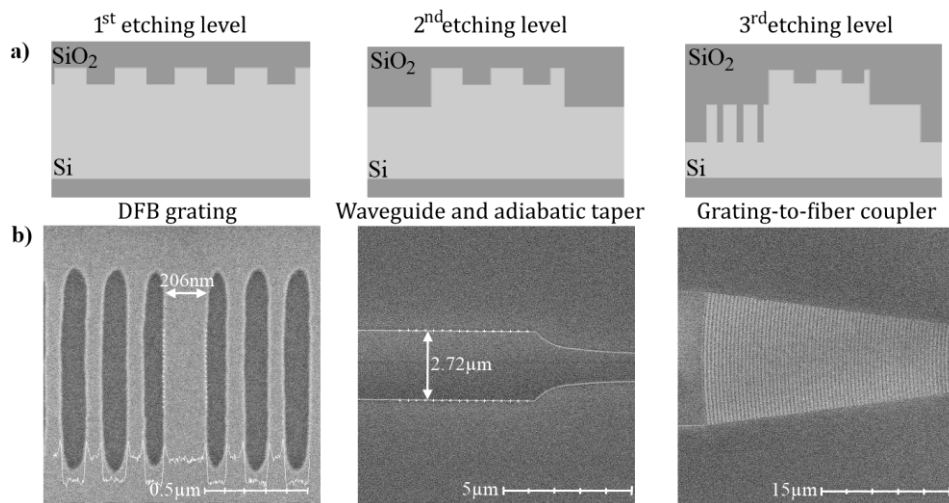
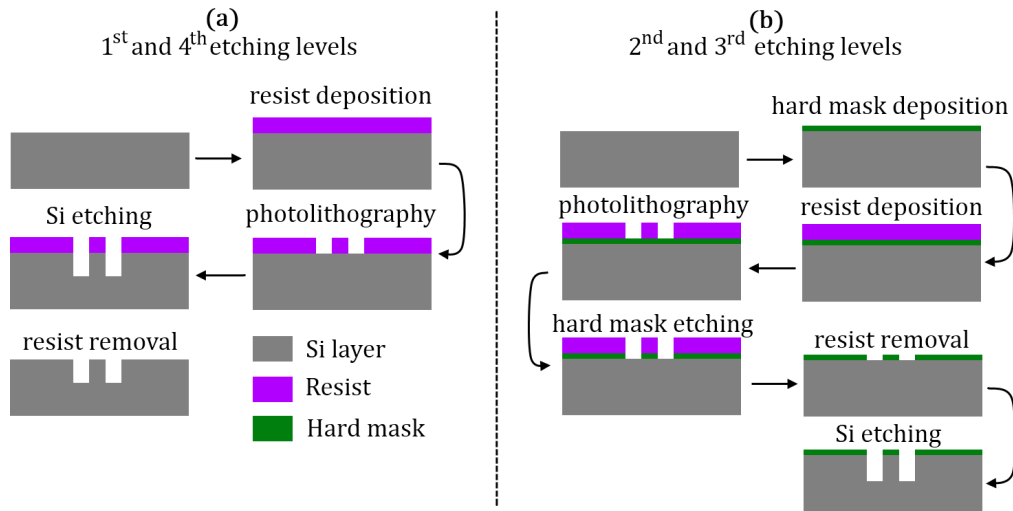


Figure 2-12 : (a) Schematic side views of the Si waveguide for the first three etching levels: the DFB grating, the rib waveguide with the adiabatic taper and the grating-to-fiber coupler (b) Corresponding top SEM view after each etching.

### ***From photolithography to pattern definition***

The process flow needed to obtain one etching level is represented on Figure 2-13 where the cases with or without the use of a hard mask are tackled. In the latter case, resist is deposited directly on the silicon. Then, a photolithography step enables drawing the pattern wanted on the resist which is reported to the silicon using RIE technique. Finally, the resist is removed and the surface is cleaned and oxidized with SiO<sub>2</sub> on 5 nm. It can be necessary to use a hard mask for the etching when some patterns size is critical, or when the etching depth is high, which may induce a slope on the edges of the pattern instead of steep sidewalls. The hard mask has the advantage to fluctuate less than the resist hence a better protection of the surface. The process sequence changes as follows: a SiO<sub>2</sub> hard mask is deposited before resist deposition. As before, a photolithography is made on the resist, but this time, only the hard mask is etched (with RIE) and the resist removal ensues. Eventually, the patterns are replicated into the silicon by using RIE thanks to the hard mask which replaces the resist. In our case, the silica hard mask was not removed since it is the same material as the one used for the final encapsulation. Moreover, it allows protecting the gratings made on the levels before (level 1 and 2 here) by filling the holes with oxide.



**Figure 2-13: Steps sequence for one silicon level etching without (a) and with (b) hard mask deposition.**

### ***A planar surface ready for bonding***

Once all the etching levels in silicon are over, the waveguides are encapsulated with silica and a chemical mechanical planarisation (CMP) enables to reach the oxide thickness wanted on top of the waveguide, namely 90 nm (see 2.2.2). These steps are schematically represented on Figure 2-14. Before encapsulation there is around 150 nm of hard mask on top of the waveguide (from the 260 nm deposited in total ~50 nm was attacked at each etching) and the step to fill with silica is thus ~650 nm. To make sure the step is filled, 900 nm of SiO<sub>2</sub> is deposited and a CMP is implemented to obtain a planar surface with 90 nm  $\pm$  15 nm of silica left on top of the silicon waveguide. The reader should be aware that this planarisation is very hard to control accurately and the variations around the value aimed at are  $\pm$ 15 nm only on the center of the 200 mm-wafer (e.g. on a diameter of 100 mm centered on the wafer's center) which is where the III-V wafer will be bonded. On a 200 mm level, these variations rather become  $\pm$ 25 nm.

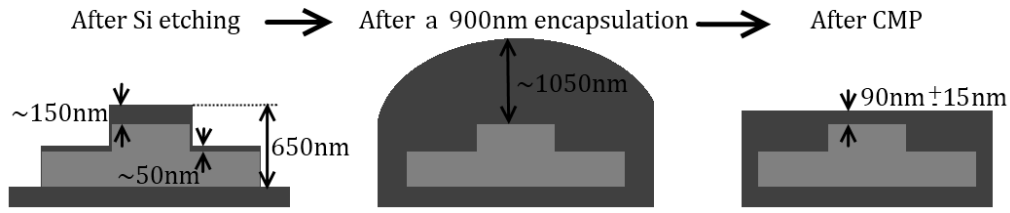


Figure 2-14: Schematic view of the different steps after the silicon's etching levels: the waveguides are encapsulated with silica and a CMP ensures the control of the SiO<sub>2</sub> thickness on top of the waveguide.

### 2.3.2. III-V epitaxy

The III-V epitaxial structure to bond is depicted on Table 2-2 where the 4 top lines stand for the InP substrate and other layers necessary for the process (see 2.3.3). Gain is provided by eight 8-nm-thick InGaAsP QWs separated by 10-nm-thick barriers. To better trap the carriers into the MQWs, those are separated from the *n*- and *p*-layers by 100-nm-thick InGaAsP separated confinement hetero-structure (SCH). A cladding layer is used between the SCH and the *p*-contact layer to progressively dope the material (from  $5 \times 10^{18}$  to  $1 \times 10^{19} \text{ cm}^{-3}$ ). This cladding layer thickness (1800 nm) ensures the optical mode to be far enough from the metallization thus minimizing its absorption. Superlattice layers are added within the *n*-contact to prevent the defect propagation from the bonded interface to the QWs [81].

Table 2-2: III-V epitaxial growth layer structure

Layer	Material	Bandgap (eV)	Doping (cm <sup>-3</sup> )	Thickness (nm)
Substrate	InP			350 μm
Transition	InP			50
Stop-etch	InGaAs			300
Sacrificial layer	InP			300
<i>p</i> - contact layer	InGaAs	0.77	$3 \times 10^{19}$	200
Transition	InGaAsP	1.13	$1 \times 10^{19}$	50
<i>p</i> - cladding layer	InP	1.34	$5 \times 10^{18} \rightarrow 1 \times 10^{19}$	1800
SCH	InGaAsP	1.13	undoped	100
MQW barriers (x7)	InGaAsP	1.13	undoped	10
MQWs (x8)	InGaAsP	0.95	undoped	8
SCH	InGaAsP	1.13	undoped	100
<i>n</i> - contact layer	InP	1.34	$3 \times 10^{18}$	110
Super-lattice (x2)	InGaAsP	1.13	$3 \times 10^{18}$	7.5
Super-lattice (x2)	InP	1.34	$3 \times 10^{18}$	7.5
Bonding interface	InP	1.34	undoped	10

These epitaxies were made using molecular beam epitaxy. They were ordered to two external companies (III-V Lab for some of the wafers and Landmark for the others) and the technique used will not be developed here since it is not the object of this work.

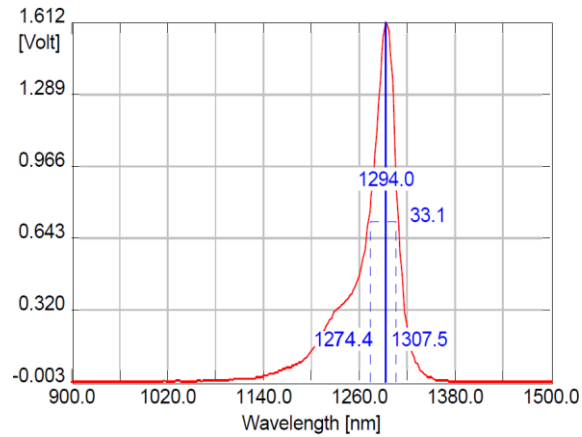


**Figure 2-15: Photoluminescence response of the III-V MQWs.**

The photoluminescence response of one of the III-V wafers is represented on Figure 2-15. It is centered at 1294 nm to anticipate a 10-nm-redshift which occurs after bonding. For this epitaxy the FWHM of the gain is 33.1 nm. Among the different III-V wafers used, this value varied between 33 nm and 60 nm.

### 2.3.3. III-V to silicon wafer bonding

Once the silicon wafer's CMP is over and the III-V epitaxy is obtained, a few steps are necessary to get both wafers ready for molecular bonding as explained in [82]. First, a 10 nm SiO<sub>2</sub> layer is deposited onto the InP bonding interface by using plasma-enhanced chemical vapor deposition (PECVD). To make the bonding possible, interfaces' roughness for both the III-V and SOI wafers need to be less than 0.5 nm root-mean-square (RMS). This is ensured for the first wafer by controlling the PECVD speed and temperature and for the latter by finishing the Si process with a CMP step. The two surfaces are then cleaned and a 30 s oxygen (O<sub>2</sub>) plasma ensues to activate them by creating a high density of hydroxyl groups (-OH)[83] which will allow the formation of covalent SiO<sub>2</sub>-SiO<sub>2</sub> bonds. The bonding is then achieved by putting the wafers in contact at room temperature. To strengthen it, they are then annealed at 200 °C for 3 hours or 300 °C for 2 hours which enables to release the gasses produced and trapped during the bonding reaction. A picture of the wafers after bonding is represented on Figure 2-16 (a) in the case of a 2 inches III-V epitaxy. In our case, since the overall oxide thickness is quite high (around 100 nm) the formations of interface voids [84] is limited compared to what can be seen with very thin bonding layers.

During this work, it was tried to planarise the SOI wafer using CMP but then, instead of carrying on with CMP until reaching the targeted oxide thickness, this was done using RIE to limit the thickness dispersion within the wafer. However, the bonding in this case happened to be very bad or even impossible probably because the surface did not have the appropriate roughness then. Consequently, it was decided to always finish the SOI processes with CMP, even a very short one for wafers first thinned with RIE.

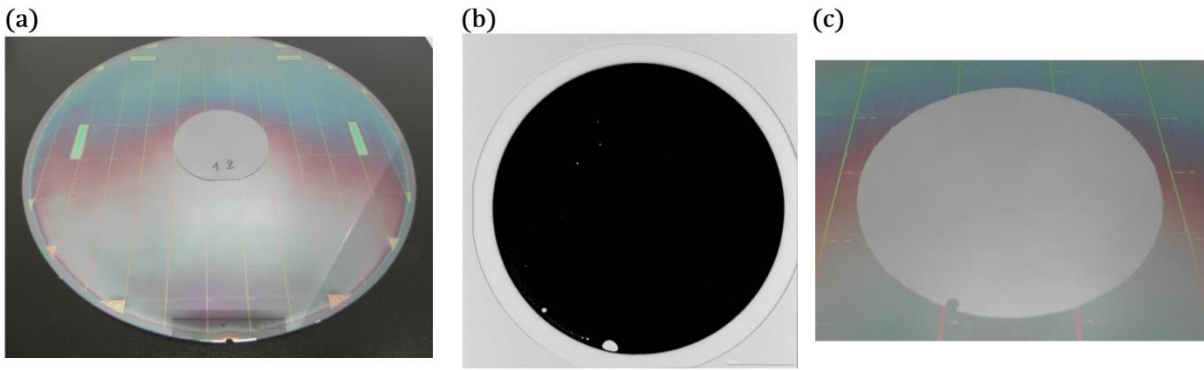


**Figure 2-16: (a) 200 mm SOI wafer with the III-V epitaxy bonded. (b) Acoustic picture showing the strength of the bonding (the white marks are area where the bonding is weak). (c) Picture of the III-V bonded wafer after the InP substrate removal.**

After the bonding, an acoustic analysis is made to determine whether the bonding worked or not. Figure 2-16 (b) displays the acoustic image of the bonded wafer beside. The parts in white correspond to places where the bonding energy is not strong enough. To keep on with the fabrication, the InP substrate must be removed. To do so, the wafer is wet etched using a  $\text{HCl}:\text{H}_2\text{O}$  (3:1) solution. During this step, the parts which were shown as weakly bonded by the acoustic analysis often peel away or make bubbles as it can be seen on Figure 2-16 (c) which is a picture of the wafer after the substrate removal. The solution's selectivity being a lot higher on InGaAs, wet etching of the substrate stops at this 'stop-etched' layer (see Table 2-2). This layer is also removed with a  $\text{H}_2\text{SO}_4:\text{H}_2\text{O}_2:\text{H}_2\text{O}$  (1:1:10) solution and the etching stops this time on the InP sacrificial layer. This layer will be removed later but it is used to protect the  $p$ -contact layer from the  $\text{H}^+$  implantation to come. Once the III-V wafer is bonded with its substrate removed, the wafer is ready for the back-end of line (BEOL) process which consists in the definition of the III-V patterns and the contact deposition.

#### 2.3.4. III-V structuration and contact deposition

Once the III-V and silicon wafers are bonded, the process is far from being over. First, the  $\text{H}^+$  implantation is implemented before etching the III-V waveguide. Then, the mesa level is defined which corresponds to the separation of the different lasers on the wafer. The contacts deposition follows, ensued by the devices encapsulation and the pads deposition. The following subsections detail each part of the process.

##### ***$\text{H}^+$ implantation***

The implantation sequence, represented on Figure 2-17, starts with the deposition of a 500-nm-thick SiN hard mask and a 4- $\mu\text{m}$ -thick photoresist. The photolithography and hard mask etching follow but the resist is not removed because the hard mask alone is not sufficient to protect the non-implanted regions hence the high thickness of the resist deposited. Three successive  $\text{H}^+$  implantations are then fulfilled with a  $1 \times 10^{14}$  atoms/ $\text{cm}^2$  dose. The current and energy used for each implantation session are respectively:  $I_1 = 60 \mu\text{A}$  and  $E_1 = 200 \text{ keV}$ ,  $I_2 = 250 \mu\text{A}$  and  $E_2 = 220 \text{ keV}$ ,  $I_3 = 130 \mu\text{A}$  and  $E_3 = 240 \text{ keV}$ . The resist is then stripped and the hard mask removed with RIE. The InP sacrificial layer can finally be removed by wet etching with the same  $\text{HCl}:\text{H}_2\text{O}$  (3:1) solution as before.

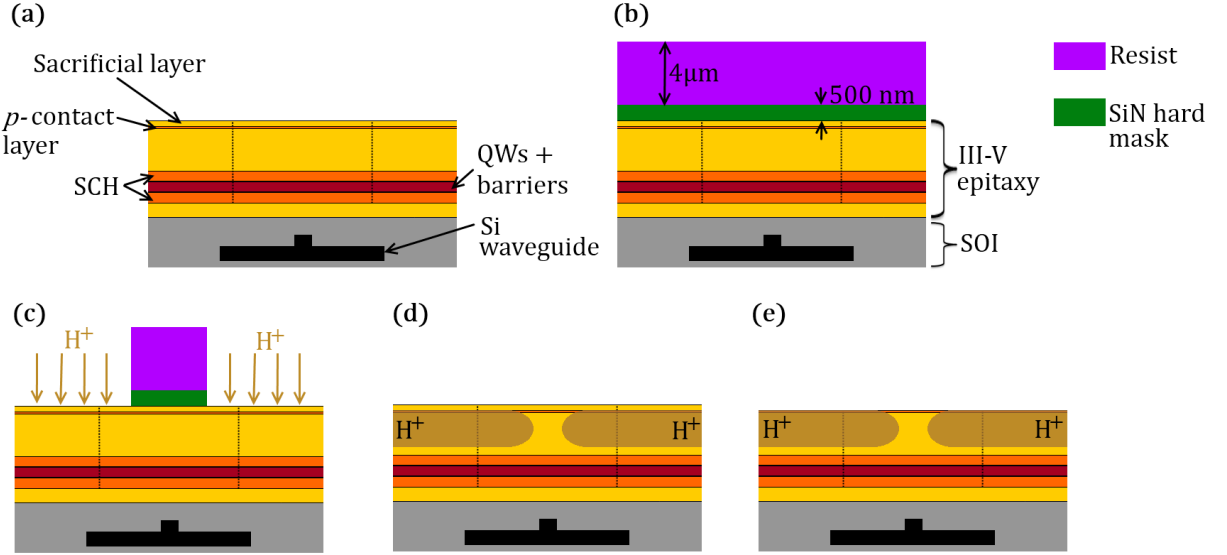


Figure 2-17: Process flow describing the  $H^+$  implantation sequence with the bonded wafer (a) after substrate removal, (b) after the SiN hard mask and resist deposition. In (c), the III-V is being implanted with  $H^+$  ions after photolithography and hard mask etching. (d) and (e) show the stack after resist and hard mask removal and after the sacrificial layer removal respectively.

### III-V waveguide definition

To begin with the III-V waveguide definition, a 500-nm-thick SiN hard mask is deposited and another photolithography, hard mask etching, and resist stripping follows (as summed up on Figure 2-18 (a)). Two possible solutions were chosen for the waveguide etching depending on when the wafer was downsized (and the equipment available accordingly). In the first case (see Figure 2-18 (b)), the wafer is downsized right after the hard mask etching and then the InGaAsP  $p$ -contact layer is etched using RIE in a  $CH_4$ - $H_2$ -Ar plasma [85], [86]. The 1.8- $\mu$ m-thick InP layer is then wet etched in a  $H_3PO_4$ :HCl (3:1) solution in which the edges of the waveguide are inevitably attacked thus inducing a slight slope on the shape of the waveguide. Another RIE with the same  $CH_4$ - $H_2$ -Ar plasma enables to etch the QWs and the SCH layers.

In the second case (see Figure 2-18 (c)), only one step of dry etching is used for all the layers thanks to a  $Cl_2$ - $CH_4$ - $H_2$  inductively coupled plasma [87] (ICP). To control the etching in situ, the different materials in presence are detected by spectrometry and the results are shown by the plot on Figure 2-19 (a). The curve showing the indium presence is a good witness of the etching progress: first it increases as the InGaAsP layer is removed, then it stays constant for a while and decreases as the thick InP layer disappears. When this curve goes up again, this means that the QWs and SCH layers are etched and that the plasma is starting to etch the InP  $n$ -contact layer. The plot is precise enough to distinguish when the QWs are being etched. Although this method is the quickest, it is not uniform on the whole wafer: the etching speed is higher on the edges than on the center of the wafer. Great care was paid to stop the etching as soon as the InP increased again to make sure not to remove all the  $n$ -contact layer of some devices. The drawback of this method is that for some of the devices, a thin part of the SCH may be left on the InP  $n$ -contact. It would be incompatible with an ohmic contact if the metal was to be deposited on it and this InGaAsP layer needs to be removed, as it will be seen further down. It is only after this RIE step that the wafer is downsized. A SEM picture of the III-V waveguide and a cut into the waveguide are displayed on Figure 2-19 (b) and (c) respectively. In both cases, the SiN hard mask is then removed.



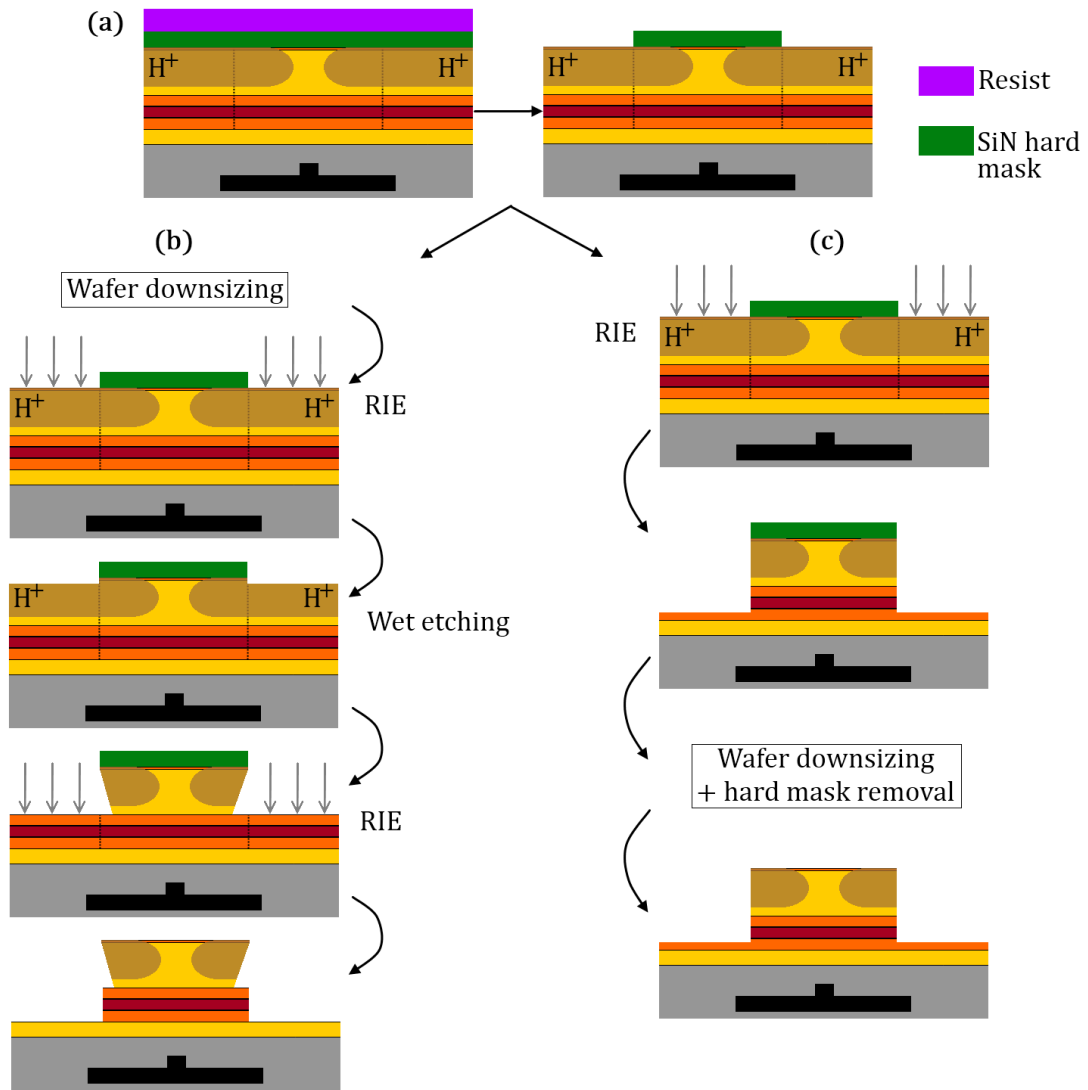


Figure 2-18: Process flow used to define the III-V waveguide. (a) Displays the photolithography's steps. (b) and (c) show the two possible sequences for the waveguide etching.

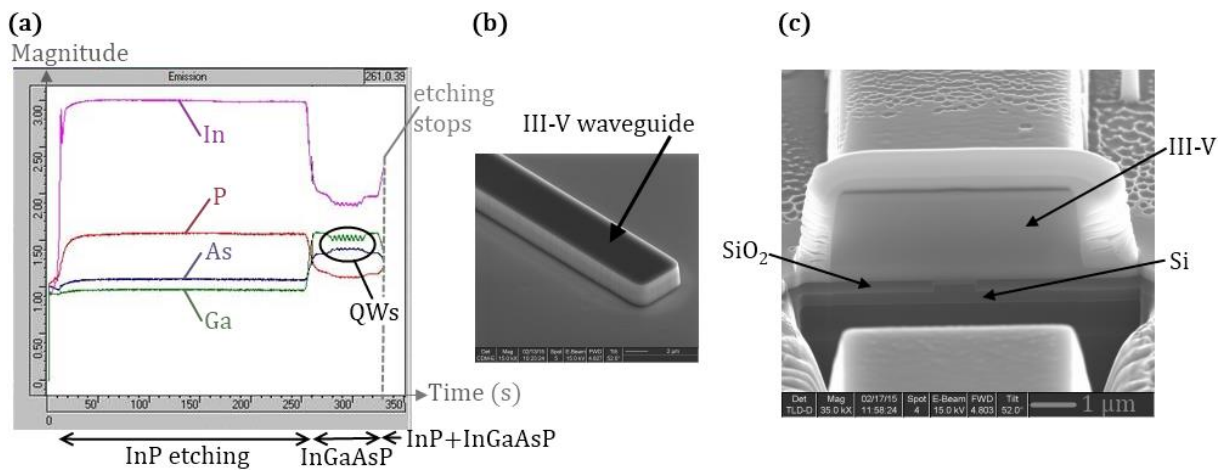
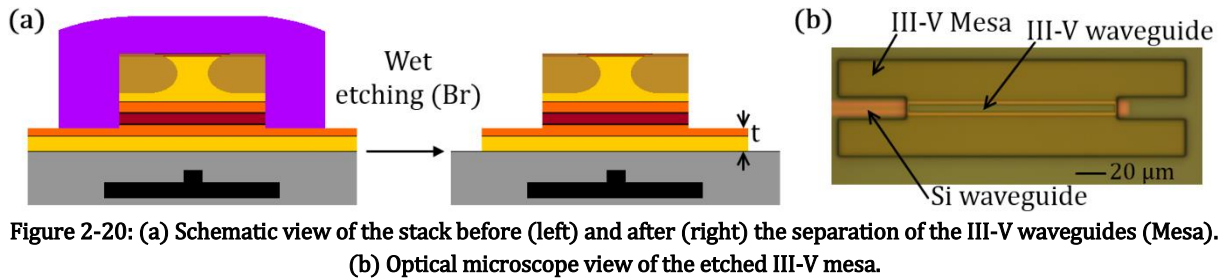


Figure 2-19: (a) 'In situ' control of the materials present during the III-V waveguide RIE. SEM view of the III-V waveguide (b) and focus ion beam (FIB) analysis (c) after the etching.



Once the III-V gain is defined, the lasers can be separated from one another thanks to a photolithography and wet etching (in a  $\text{Br}_2:\text{HBr}:\text{H}_2\text{O}$  (1:17:140) solution) sequence as represented on Figure 2-20 (a). This part of the process is also useful for thickness controls: by measuring the step between the  $\text{SiO}_2$  layer and the III-V, it is possible to deduce the thickness ( $t$ ) of the InGaAsP left on the InP layer (assuming the InP layer thickness is known). An optical microscope view of a device after this step is displayed on Figure 2-20 (b).



### Contact deposition

The following sequences lies in the metal deposition for the  $p$ -contact. For all metallic depositions, a lift-off process was used here, as described in Figure 2-21. First, a photolithography step is fulfilled but instead of using only a usual photoresist, another specific resist called LOR (for lift-off resist) is deposited underneath and open as well. The metal is then deposited using evaporation and it was either a classic Pd (10nm) Ti (30nm) Pt (80nm) Au (200nm) contact or a simple Pt(150 nm) contact [88], [89], depending on the equipment available. In both cases, a quick etching preceded the deposition to remove the native oxide on the surface. The resist and LOR are then lifted-off in an acetone solution for a few hours and ultrasounds can be added in order to speed up the lift-off. The sequence is over when all the resist went away and the only regions with metal stand where the resist had been open (see inset on Figure 2-21).

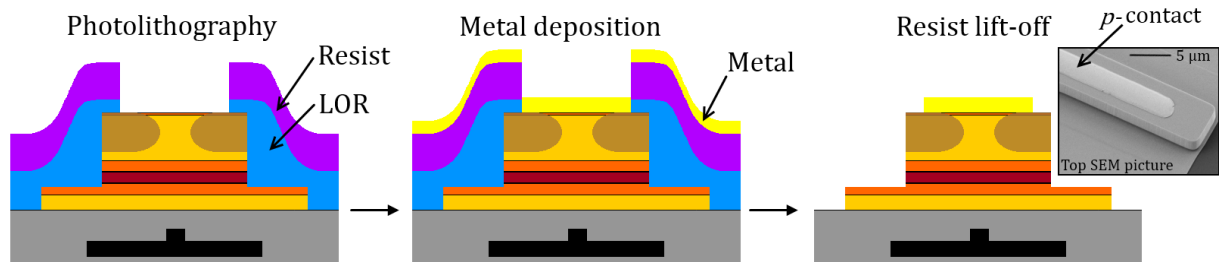


Figure 2-21: Process flow for the  $p$ -contact metal deposition. On the right is an inset with a top SEM picture at the end.

Before the  $n$ -contact metal deposition (CTN), another sequence may be needed in the case were some InGaAsP was left at the end of the III-V waveguide etching. To remove it a photolithography using the CTN mask has to be done using a SiN hard mask (see Figure 2-22) to better protect the  $p$ -metal than resist. A wet etching in a  $\text{H}_2\text{SO}_4:\text{H}_2\text{O}_2:\text{H}_2\text{O}$  (1:1:10) solution allows removing all the InGaAsP left.

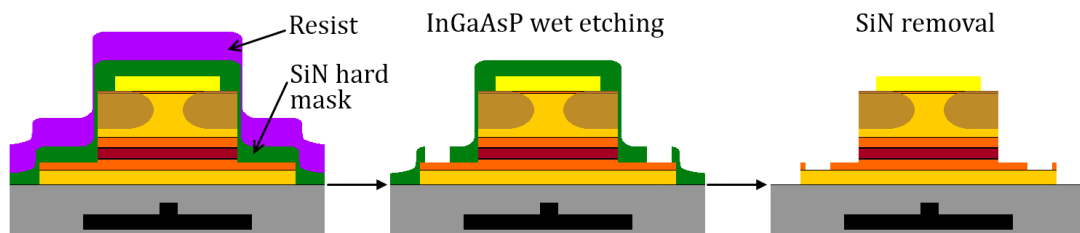


Figure 2-22: Process flow for the InGaAsP SCH removal (only when needed).

Using the same lift-off process as described for the  $p$ -contact metal, the  $n$ -metal is then deposited (see Figure 2-23). Again, the metal was either a Ni (5nm)Ge(10nm)Au(20nm) Ni(5nm)Au(150nm) stack or a Ti(50nm)Pt(75nm)Au(250nm) one [90]. A SEM picture of a device after this step is represented on Figure 2-24.

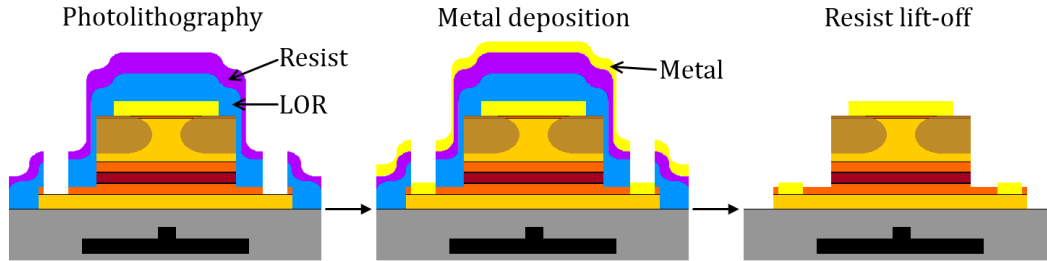


Figure 2-23: Process flow for the  $n$ -contact metal deposition.

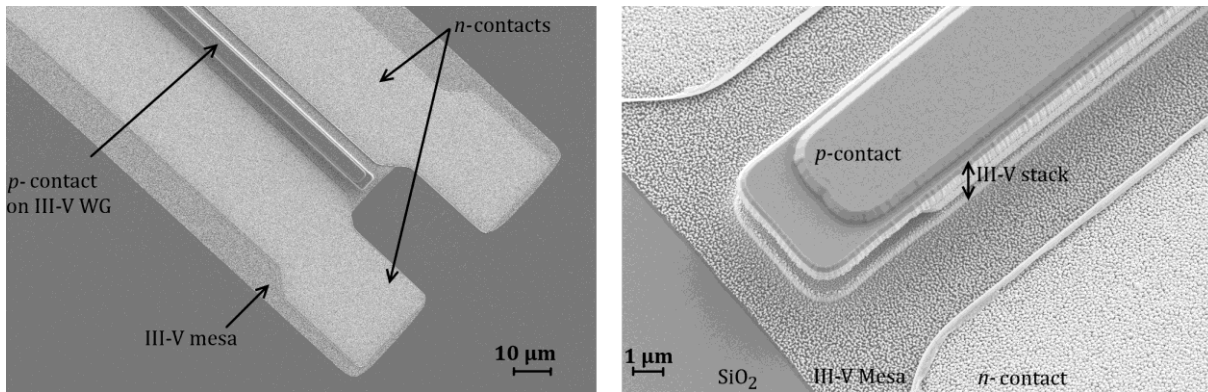
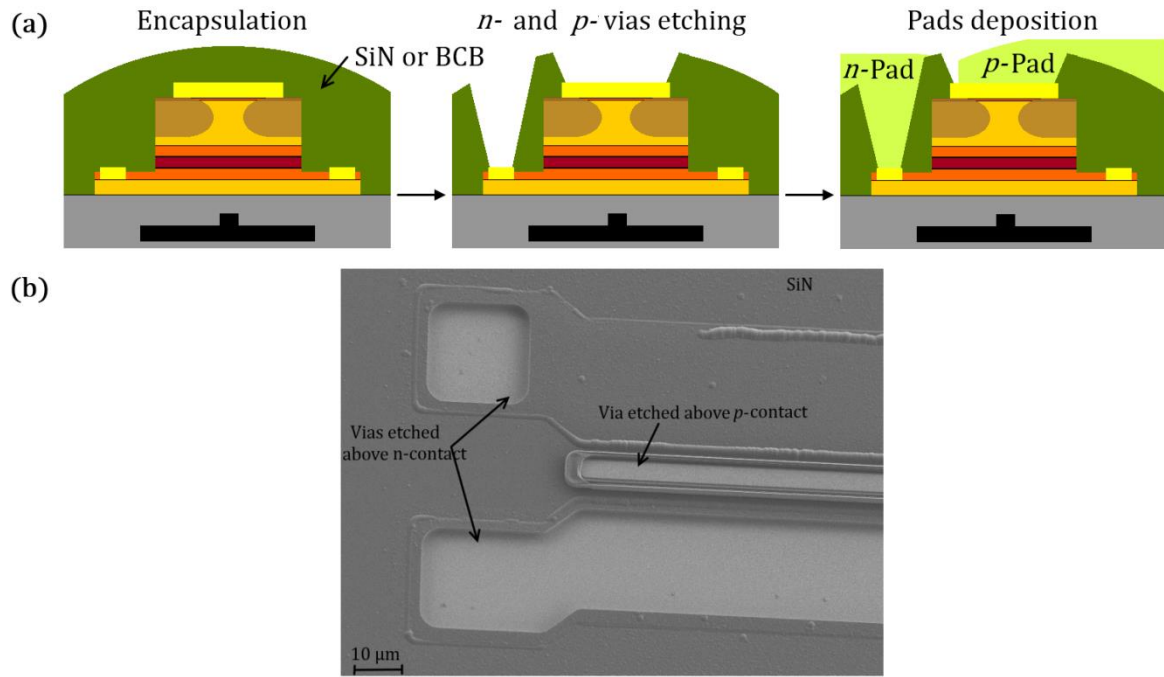


Figure 2-24: SEM pictures of one of the device after the  $n$ -contact deposition. The III-V stack includes the  $p$ -contact layer, the InP cladding layer and the MQWs layers.

### Encapsulation and Pads deposition

To finish with the laser fabrication, the devices are encapsulated with 1800 nm of either SiN or the benzocyclobutene polymer (BCB) [91]. The former has the advantage to better evacuate the temperature since its thermal conductivity has been measured between 1 and 10  $\text{WK}^{-1}\text{m}^{-1}$  depending on the thickness and method of deposition [92]–[94], while the thermal conductivity of BCB is within the  $[0.18;0.40]$   $\text{WK}^{-1}\text{m}^{-1}$  range [92], [95], [96]. However, the BCB encapsulation allows getting a more planar surface after the oxide deposition. This encapsulation layer is etched above the  $n$ - and  $p$ -contacts allowing the access to the metals. Eventually, a last lift-off step occurs to deposit the 1.5- $\mu\text{m}$ -Au-metal pad. The Figure 2-25 (a) sums up these last steps skipping the photolithography steps ( $n$ - and  $p$ -vias and the pads) and a SEM picture of a device after the vias etching is represented on Figure 2-25 (b).



**Figure 2-25:** (a) Final sequence for the back-end process including device encapsulation, vias etching and pads deposition. (b) SEM picture of a device after the vias etching.

An optical microscope view of a device at the end of the process is shown on Figure 2-26. To summarize the whole process, Table 2-3 gives an overview of all the etchants used to remove each layer of the III-V stack.



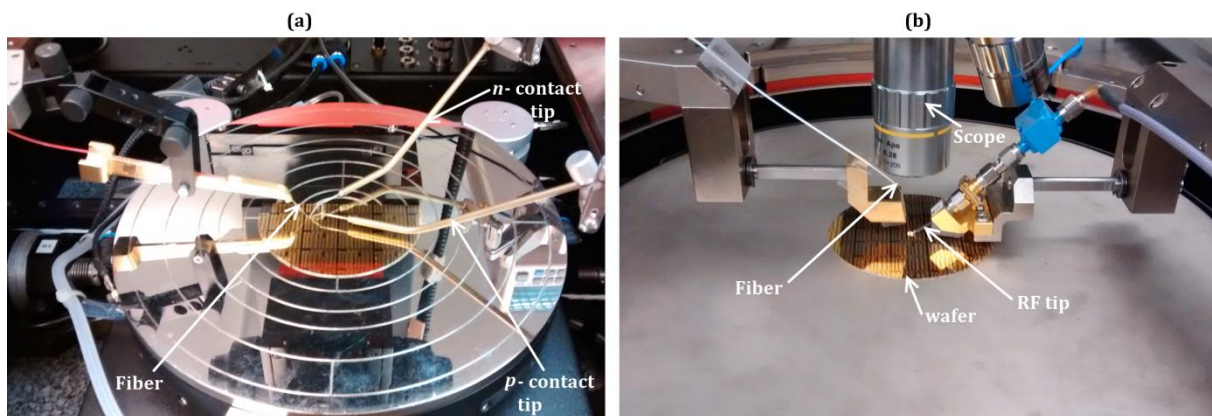
**Figure 2-26:** Optical microscope view of a DFB laser at the very end of the process.

**Table 2-3: Overview of the methods used to etch each layer (with  $t$  the layer thickness).**

Step	Layer	Material	$t$ (nm)	Etching		Etchant	
Substrate removal	Substrate	InP	350 $\mu$	Wet		HCl : H <sub>2</sub> O (3:1)	
	Transition	InP	50				
	Stop-etch	InGaAs	300	Wet		H <sub>2</sub> SO <sub>4</sub> :H <sub>2</sub> O <sub>2</sub> :H <sub>2</sub> O (1:1:10)	
Implant	Sacrificial layer	InP	300	Wet		HCl : H <sub>2</sub> O (3:1)	
III-V waveguide	$p$ - contact layer	InGaAs	200	Dry	Dry	CH <sub>4</sub> -H <sub>2</sub> -Ar	Cl <sub>2</sub> -CH <sub>4</sub> -H <sub>2</sub>
	Transition	InGaAsP	50			H <sub>3</sub> PO <sub>4</sub> : HCl (3:1)	
	$p$ - cladding layer	InP	1800	Wet		CH <sub>4</sub> -H <sub>2</sub> -Ar	
	SCH	InGaAsP	100	Dry			
	MQW barriers (x7)	InGaAsP	10				
	MQWs (x8)	InGaAsP	8			Wet	H <sub>2</sub> SO <sub>4</sub> :H <sub>2</sub> O <sub>2</sub> :H <sub>2</sub> O (1:1:10)
	SCH	InGaAsP	100				
III-V mesa	$n$ - contact layer	InP	110	Wet		Br <sub>2</sub> : HBr : H <sub>2</sub> O (1:17:140)	
	Super-lattice (x2)	InGaAsP	7.5				
	Super-lattice (x2)	InP	7.5				
	Bonding interface	InP	10				

## 2.4. Characterization procedure

This paragraph tackles the laser characterization methods which is the same for the three kinds of lasers tested during this work (DBR, DFB and SGDBR lasers). The wafer is settled on a chuck whose temperature can be controlled from 20°C to 80°C. Pictures of the static and RF characterization setups are displayed on Figure 2-27.

**Figure 2-27: Picture taken while implementing static measurements (a) and RF measurements (b).**

Static measurements of the lasers were made at room temperature but the laser temperature performances were also measured by varying the chuck temperature. To get lower temperatures than 20°C, a Peltier module was put between the laser and the chuck. Figure 2-28 (a) is a schematic representation of the installation implemented when measuring a laser static characteristic. The focus is made on each laser separately: two tips are put on the  $n$ - and  $p$ -contacts and connected to a current source which also measures the laser voltage. An optical fiber is set above the grating-to-fiber coupler with the appropriate angle to collect light and send it either to an optical spectrum analyzer (OSA) or a power meter. The OSA minimum resolution is 0.004 nm. To accelerate the measurement procedure, a beam splitter can be used to send 10% of the collected power to the OSA and the other 90% to the power meter. On the figure, the other side of the laser is connected to a photodetector: a photodiode was designed either for DFB lasers or for symmetrical DBR or SGDBR lasers to measure directly the optical power in the waveguide. The losses induced by the grating to fiber coupling are de-embedded thanks to the patterns represented on Figure 2-28 (b): two grating coupler facing each other are linked by a Si waveguide. Different lengths are chosen. Some similar test patterns include a mirror between the two grating couplers: this enable to check the mirror response itself.

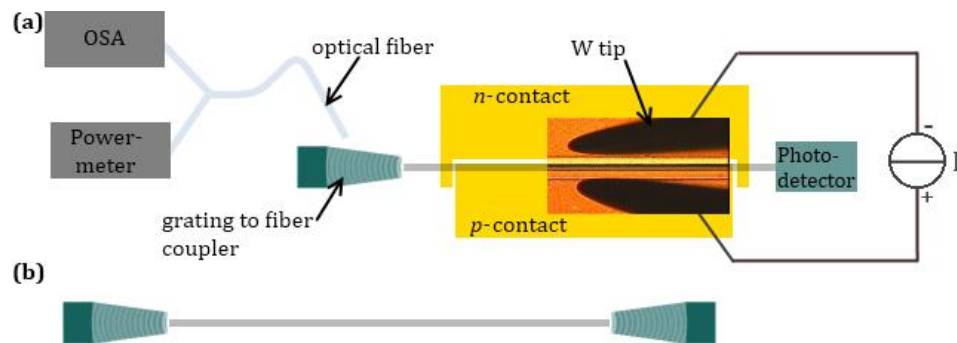
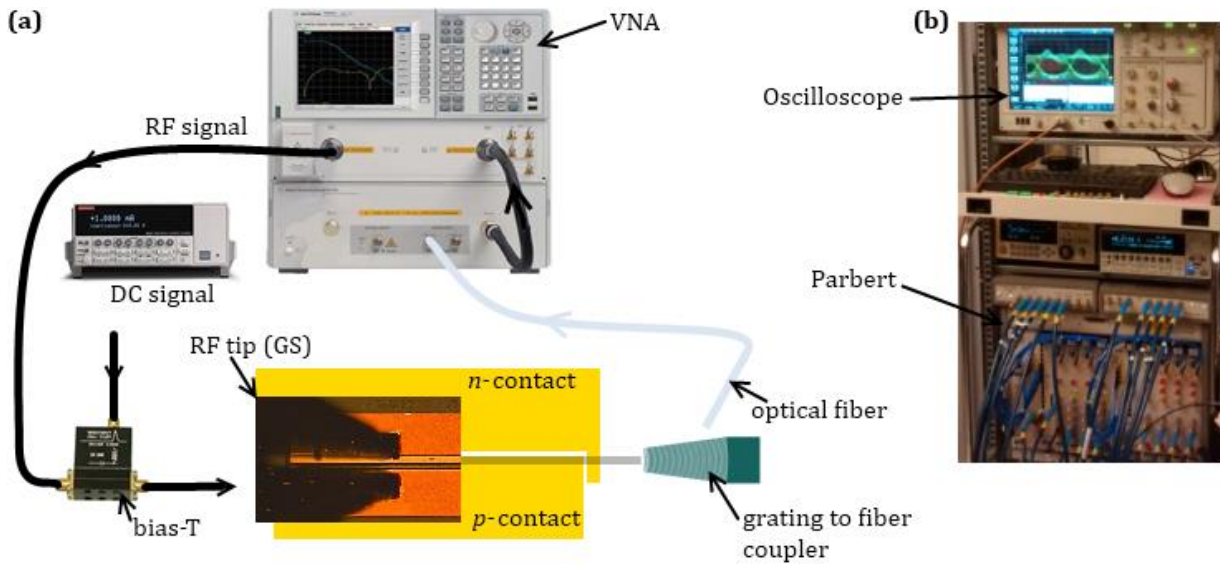


Figure 2-28: (a) Schematic representation of the static installation measurement. A picture of the two tungsten tips is superimposed to the laser. (b) Test pattern for the grating coupler or mirror de-embedding.

The radio-frequency (RF) performances of the best devices were evaluated using the tests explained on Figure 2-29. The first thing to estimate in an RF analyze is the -3dB-bandwidth of the laser as explained in Chapter 1. The AC signal is obtained thanks to a vectorial network analyzer (VNA) and is superimposed to the DC current by using a bias-T (see Figure 2-29 (a)). The overall signal is sent to the laser thanks to a ground-signal (GS) tip and the device output power is again collected with an optical fiber which is connected to a photodetector underneath the VNA. The corresponding electrical signal is then sent through a RF wire to the entry port of the VNA to analyze the laser response to high speed signals.

It was also explained in 1.1.3 that the RF analyze of a device can be completed by a bit error rate (BER) test. This was made replacing the VNA on Figure 2-29 (a) by a PARBERT (for 'parallel bit error rate test') and an oscilloscope which are represented on Figure 2-29 (b). The parbert used here consists of four parts, each of them delivering an electrical bit stream of '0' and '1' at the speed wanted. All of them are then multiplexed in the same wire allowing the signal obtained in the end to be four times faster. Again, this signal is superimposed to a DC signal (delivered by the parbert itself) using a bias-T, and the optical response of the laser is sent to an oscilloscope to evaluate the eye diagram's quality.





**Figure 2-29: (a) Schematic representation of the RF installation measurement with a VNA. A picture of the RF tip is superimposed to the laser. For other RF tests, the VNA can be replaced by a Parbert and an oscilloscope which are displayed on (b).**

## 2.5. Conclusion to chapter 2

In this chapter, the devices were first described giving details on the III-V structure, and the silicon rib. Then, the coupling theory between the III-V and the silicon waveguide was explained, showing how to get the adiabatic taper shape needed and checking the robustness of the taper regarding process variations. The calculations made to check on the adiabaticity of the transition validated the hypotheses (weak coupling,  $\kappa = 2\kappa_{z_0}$ ) made to get the taper shape. Computations showed that the different tapers designed are quite robust with the input and output variations. The most critical parameter is the oxide thickness between the III-V and the silicon. To relax the constraints on this parameter, tapers with different oxide thicknesses were designed. All the fabrication process followed, with the different options chosen from the process of the SOI to the III-V waveguide's structuring and contacts' deposition. At last, the measurement procedure, similar to all the devices, was explained for the static as well as the high-speed characterization. Strong from this knowledge, we will now dive more deeply into the laser theory and more particularly into the study of the different laser cavities which are DBR, DFB and SGDBR.

---

## Chapter 3. Hybrid III-V on Si single-mode lasers

---

3.1.	Distributed Bragg reflector lasers .....	52
3.1.1.	Theory of distributed Bragg reflectors .....	53
3.1.2.	Mirrors design.....	55
3.1.3.	Results.....	59
3.2.	Distributed Feedback lasers.....	62
3.2.1.	DFB theory.....	62
3.2.2.	Cavity design.....	64
3.2.3.	Results: vertically coupled DFB lasers .....	67
3.2.4.	Results: laterally coupled DFB lasers .....	72
3.3.	Conclusion to chapter 3.....	77

This chapter concerns the lasers designed during this work to reach single-mode devices. First, theory and designs of distributed Bragg reflector (DBR) lasers are explained and, in particular, the mirrors dimensioning: namely their length, period, waveguide width and so on. The provisional results obtained are presented and, although the lasers are not as powerful as wished (due to some process issues), they show all the properties of a DBR laser. The second part of the chapter is dedicated to distributed feedback (DFB) lasers and more precisely DFB lasers with their grating etched in the silicon waveguide underneath the III-V, either on its top or on its sides. Their principles are given as well as details on those designed. In both cases, the experimental results associated are very promising, as it is presented in the end of the chapter.

### 3.1. Distributed Bragg reflector lasers

As it was said earlier, the DBR lasers are lasers for which the cavity consists of one DBR at each side of the gain region. In our case, the DBRs are etched in the silicon waveguide at the output of the tapers as represented in Figure 3-1. It was chosen in this work to have an asymmetric cavity: at the Bragg frequency, all the light is reflected from the left DBR, called back-mirror (BM) while the reflectivity of the right mirror (called FM for front mirror) is lower so that the laser has only one output. This paragraph will first describe the theory of one DBR mirror and how they were designed studying the mirrors' dependence on each parameter.

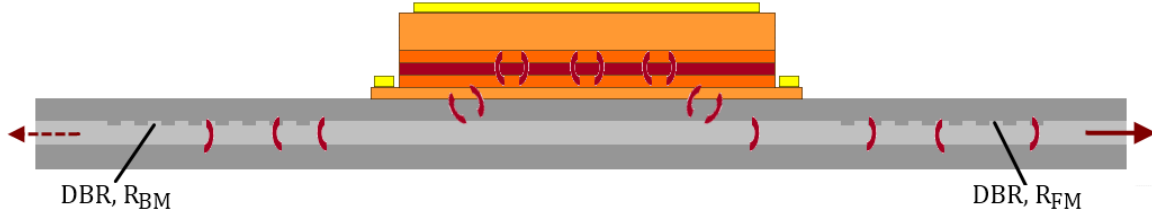


Figure 3-1: Schematic representation of a III-V on silicon DBR laser.

Before going deeper into DBR mirrors physics, it is necessary to focus briefly on a characteristic of the cavity tackled in 1.1.2 : the free spectral range (FSR). It was seen that in a Fabry-Perot-like cavity, there is a finite number of authorized modes separated by:

$$\text{FSR} = \Delta\lambda = \frac{\lambda^2}{2n_{\text{eff,avg}}L_{\text{cav}}} \quad [3.1]$$

Where  $L_{\text{cav}}$  is the total cavity length and  $n_{\text{eff,avg}}$  the average effective index. In the case when  $\lambda = 1310$  nm,  $n_{\text{eff,avg}} = 3.3109$  and  $L_{\text{cav}} = 941$   $\mu\text{m}$ , equation [3.1] gives  $\Delta\lambda = 0.28$  nm. These values correspond to the case of a DBR cavity with one 383- $\mu\text{m}$ -long mirror and another 185- $\mu\text{m}$ -long surrounding a 700- $\mu\text{m}$ -long active region. The calculation of the cavity length will be developed later.

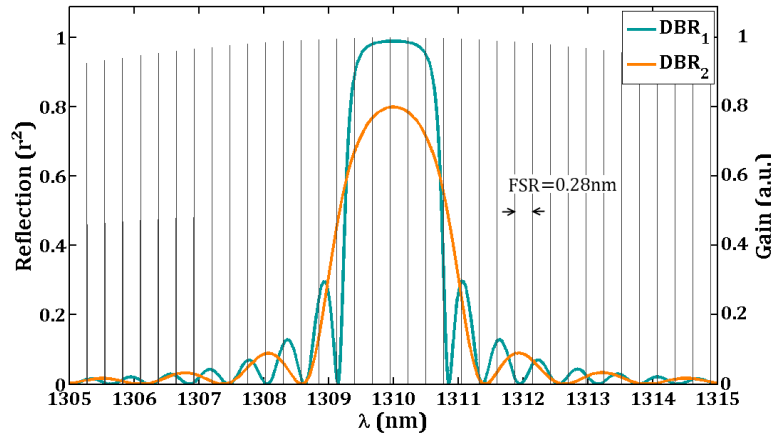


Figure 3-2: Variation of the reflection with  $\lambda$  for two different mirrors. The parameters used to obtain the curves were:  $W_{\text{Si}} = 3$   $\mu\text{m}$ ,  $e = 10$  nm,  $a = 196$  nm,  $L_{\text{DBR1}} = 383$   $\mu\text{m}$ ,  $L_{\text{DBR2}} = 185$   $\mu\text{m}$ . The comb associated with the cavity formed by the two DBRs surrounding a 700  $\mu\text{m}$ -long active region is represented underneath.

Figure 3-2 displays the comb obtained with such an FSR, assuming a Lorentzian shape for the gain with a 33 nm linewidth and no widening for the modes' response. The reflectivity of the mirrors at each side of the cavity is superimposed to this plot, in the case of an etching depth ( $e$ ) of 10 nm, a rib width  $W_{\text{Si}} = 3$   $\mu\text{m}$



and a grating period of 196 nm. The FWHM of each mirror is respectively 1.48 nm and 1.85 nm showing that at least 5 modes can be selected by this cavity. This shows that when conceiving a mirror, it is very important to minimize its FWHM to select the least lateral modes as possible. This does not mean that these potentially selected modes shall all be seen in the final laser spectrum: only one of them shall appear higher in the end, corresponding to the mode with higher gain. However the more existing modes, the lower the laser's stability with changes in the cavity. This leads for instance to mode hops as the drive current increases.

### 3.1.1. Theory of distributed Bragg reflectors

#### The Bragg relation

To begin the DBR mirror study, one has to focus on a medium constituted of  $N$  periodic layers on which a light beam is sent making an angle  $\theta$  with the axis normal to the layers plane, as represented on Figure 3-3 (a). At each layer interface, part of the light is reflected and the rest is transmitted. It is assumed that each reflection is weak enough so that the amplitudes ( $U_m$ ) of the reflected waves are approximately equal. The secondary reflections are neglected. Thus, successive waves only differ by a phase difference  $\Delta\varphi = U_m = \sqrt{I_0} \exp(j(m-1)\varphi)$  (where  $m \in \llbracket 1; N \rrbracket$ ). With these hypotheses, the total intensity of the  $N$  interfering waves is [1]:

$$I = \left| \sum_m U_m \right|^2 = I_0 |1 + e^{j\varphi} + e^{2j\varphi} + \dots + e^{(N-1)j\varphi}|^2 = I_0 \frac{\sin^2(\frac{N\varphi}{2})}{\sin^2(\frac{\varphi}{2})} \quad [3.2]$$

It can be shown that the phase difference between each reflected beam is:

$$\varphi = \frac{2\pi n_{\text{avg}}}{\lambda} (2a \cos(\theta)) \quad [3.3]$$

In equation [3.3],  $n_{\text{avg}}$  is the average index in the layered media,  $\lambda$  is the wavelength and  $a$  is the period. Equation [3.2] proves that the intensity of the reflected light reaches its maximum when  $\varphi = q2\pi$  where  $q$  is an integer. From this, equation [3.3] leads to the Bragg condition:

$$\cos(\theta_{\text{Bragg}}) = \frac{q\lambda_{\text{Bragg}}}{2an_{\text{avg}}} \quad [3.4]$$

The DBR mirrors designed in this work are included into the Si waveguide (see Figure 3-3 (c)) therefore the propagation direction is perpendicular to the interfaces, and  $\theta = 0$ . Hence, the Bragg relation:

$$\lambda_{\text{Bragg}} = \frac{2an_{\text{avg}}}{q} \quad [3.5]$$

Where  $q$  stands for the order of the mirror.

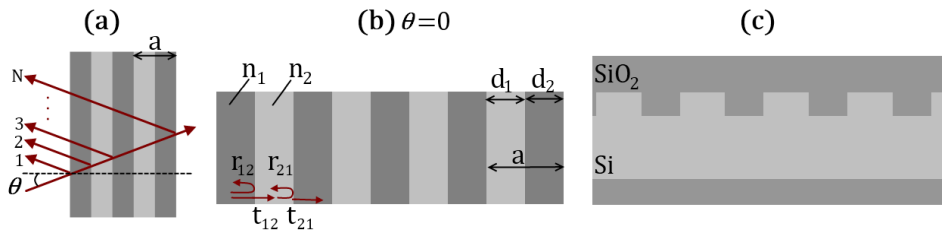


Figure 3-3: Different representation of Bragg mirror. (a) Periodic layer media with incident light at angle  $\theta$ . (b) Dielectric Bragg mirror at normal incidence. (c) Side view of the Bragg mirror etched in the Si waveguide.

### ***Reflectivity and grating coupling strength***

The previous section shows how to get an analytic formula for the Bragg wavelength but does not include multiple transmissions and reflections nor take into account the intensity losses while light propagates within the layers. To do so, a matrix approach called transfer matrix theory was used ; its bases were extracted from [2] and are described in Appendix A.

The mirror reflectivity ( $R_g$ ) can be deduced taking  $R_g = |r_g|^2$  where  $r_g$  is the reflection of the grating (calculated with [A.6]). From the matrix transfer calculation, it is possible to obtain an analytic formula for the reflection at the Bragg frequency. Again, the demonstration can be found in [2] and, assuming  $|r_{12}| = |r_{21}| = r$ , it leads to:

$$r_g = \tanh(N \cdot \ln\left(\frac{1+r}{1-r}\right)) \approx \tanh(2Nr) \quad [3.6]$$

The second part of equation [3.6] comes from a Taylor expansion of  $\ln((1+r)/(1-r))$  around zero. The amount ' $2Nr$ ' stands for the reflection for one period ( $2r$ ) multiplied by the number of periods  $N$ . However, another more historical way to describe this quantity is to multiply the reflection per unit length, called the grating coupling constant ( $\kappa_g$ ), with the length of the grating ( $L_g$ ). The grating's reflection can thus be written:

$$r_g \approx \tanh(\kappa_g L_g) \quad [3.7]$$

$\kappa_g$  is the coupling constant of the grating and it can be calculated using the definition  $\kappa_g L_g \equiv N \cdot 2r$ :

$$\kappa_g L_g \equiv N \cdot 2r = \frac{L_g}{a} \cdot 2 \frac{|n_{\text{eff}2} - n_{\text{eff}1}|}{(n_{\text{eff}2} + n_{\text{eff}1})} \quad [3.8]$$

Moreover, using the Bragg relation (equation [3.5]), and assuming a 50 % duty cycle and  $n_{\text{avg}} = (n_{\text{eff}2} + n_{\text{eff}1})/2$ :

$$a = \frac{\lambda_{\text{Bragg}}}{2n_{\text{avg}}} = \frac{\lambda_{\text{Bragg}}}{(n_{\text{eff}2} + n_{\text{eff}1})} \quad [3.9]$$

Which leads to:

$$\kappa_g = \frac{2|n_{\text{eff}2} - n_{\text{eff}1}|}{\lambda_{\text{Bragg}}} \quad [3.10]$$

### ***Cavity representation and mirror effective length***

To calculate the FSR of the cavity, it is convenient to represent the DBR as a discrete mirror placed at a distance  $L_{\text{eff}}$  from the real start of the grating as represented on Figure 3-4. Using the transfer matrix theory, it can be shown (see [2]) that the effective length is defined as:

$$L_{\text{eff}} \approx \frac{1}{2\kappa_g} \tanh(\kappa_g L_g) \quad [3.11]$$



Figure 3-4: Schematic representation of the effective length of a DBR mirror (Top views of a laser).

Equation [3.11] was mostly used here to take into account the dependence of the cavity FSR on the DBR parameters.

### 3.1.2. Mirrors design

Several parameters, represented on Figure 3-5, need to be chosen to obtain the DBRs, such as the width of the silicon waveguide ( $W_{Si}$ ), but also the etching depth ( $e$ ), the grating period ( $a$ ) and its filling factor or duty cycle (DC) and finally the total grating length. Equations [3.5], [3.7] and [3.10] were used during the mirrors' design to get a glimpse of what the period of the gratings or their lengths would be. However, to obtain the exact grating responses, computations were made using the transfer matrix theory described above. The effective indices needed to fulfill these computations were calculated using a FEM mode solver.

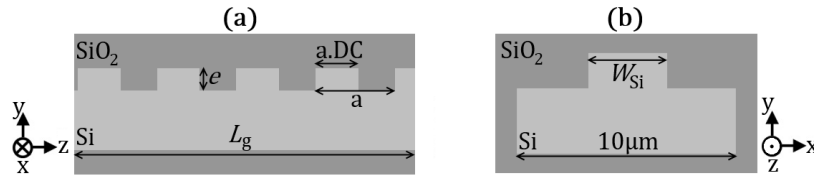


Figure 3-5: Schematic view of the DBR in the SiO<sub>2</sub>-Si matrix with the different parameters chosen.

#### *The rib width*

The first parameter to define is the rib width. The wider it is, the stronger will be the index change (and consequently the grating coupling constant) between an etched and un-etched region of the grating. It can thus be interesting to widen the rib to get shorter grating. However, this widening is length-consuming and not only increases the device footprint but also the cavity length which, as seen above, induces more allowed lateral modes. The grating coupling constant versus  $W_{Si}$  is plotted on Figure 3-6 (a) for different etching depths, showing that from a certain value of the silicon rib width, the index change is too low to have any influence on the reflectivity. To maximize the grating strength without the need for a too long transition from the taper output to the grating, the chosen value for the rib width was the beginning of the plateau, namely  $W_{Si} = 3 \mu m$ . Most of all, this choice has the advantage to limit that the process' variations on  $W_{Si}$  would affect the grating reflectivity. For narrower rib widths ( $W_{Si} < 2 \mu m$ ), the slope of the grating coupling is very steep, thus making a too high uncertainty on the expected mirror reflectivity.

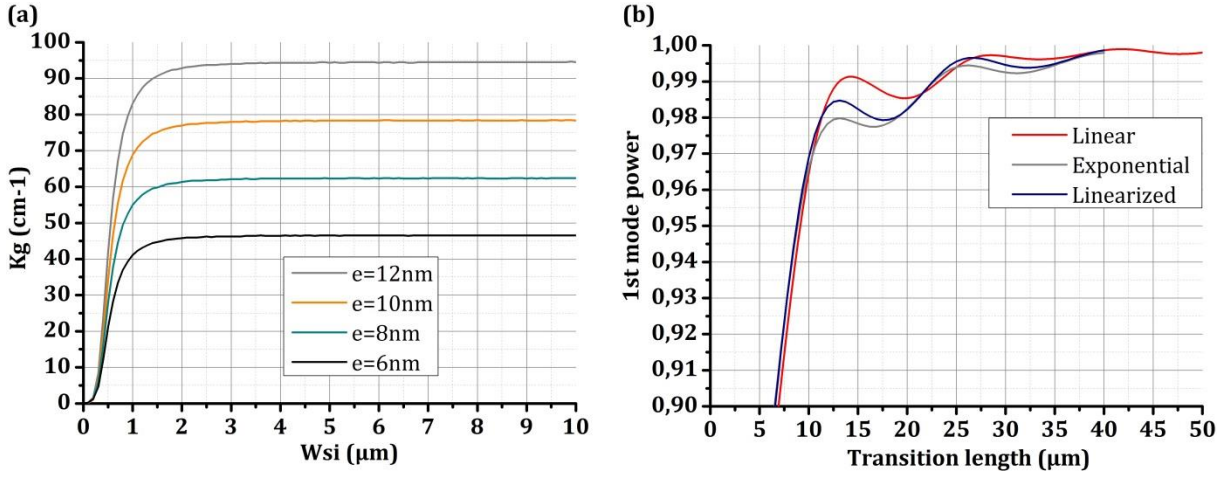


Figure 3-6: (a) Grating coupling constant as a function of the rib's width.  $\kappa_g$  was calculated using eq. [3.10] after computing the effective indexes value with an FEM mode solver. (b) Power transmitted in the 1st mode as  $W_{\text{Si}}$  goes from  $1.5 \mu\text{m}$  to  $3.0 \mu\text{m}$  as the transition length increases.

To get from the taper output ( $W_{\text{Output}} \in [1.5; 2.7] \mu\text{m}$ ) to the beginning of the grating, the rib width needs then to be increased. An analysis of the transition taking the worst case scenario (i.e.  $W_{\text{Output}} = 1.5 \mu\text{m}$ ) was implemented to optimize its shape but it was found that the linear widening was the most efficient one (see Figure 3-6 (b)). On the plot, the 'linearized' curve correspond to the shape of a transition that follows the index variations with  $W_{\text{Si}}$ . The transition length selected is:  $L_{\text{transition}} = 40 \mu\text{m}$  (the shorter length from which the oscillations become insignificant).

### The grating period and Bragg wavelength

The period of the first order grating needed to get the appropriate wavelength was calculated using equation [3.5] (with  $q=1$  and  $\lambda_{\text{Bragg}} = 1310 \text{ nm}$ ). The average effective index depends on the waveguide's width, which is already set to  $3 \mu\text{m}$ , the etching depth and the filling factor of the mirror. The period that should be targeted to reach  $1.31 \mu\text{m}$  is represented on Figure 3-7 (a) as a function of the etching depth for a duty cycle of 0.5. It shows that the period's variations with  $e$  are not so high and can be assumed linear with  $\Delta a / \Delta e \sim 0.017 \text{ nm/nm}$ . Reciprocally, the Bragg wavelength is also plotted for a  $196 \text{ nm}$  grating period and its variations with the etching depth is calculated to be:  $\Delta \lambda_{\text{Bragg}} / \Delta e \sim 0.11 \text{ nm/nm}$ . Changes in the duty cycle are taken into account on Figure 3-7 (b) and it shows that the duty cycle has even less effects on the Bragg wavelength than the etching depth especially for weak values of  $e$  ( $< 20 \text{ nm}$ ) which are our values of interest (as it will be seen below).

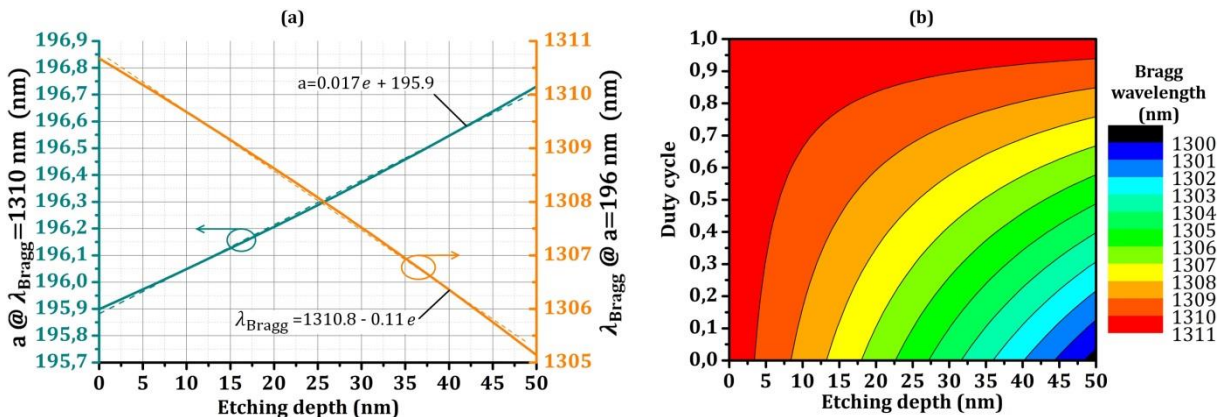


Figure 3-7: Grating's period at Bragg wavelength (1310 nm) and Bragg wavelength for  $a=196 \text{ nm}$  depending on the etching depth (a) for a 0.5 duty cycle, (b) with varying duty cycles.

Since the precision of the photolithography's masks used here does not go below 1 nm, the period was set to  $a=196$  nm. To anticipate process variations in the silicon that would change  $n_{\text{avg}}$ , as well as in the III-V epitaxy that induces a shift the Bragg wavelength, different grating periods were chosen for each laser's version:  $a \in [193; 195; 196; 197; 199]$  nm.

### *The etching depth and grating length*

Two other important parameters are the etching depth and the grating length. Figure 3-2 showed that the longer the mirror, the higher the reflectivity and the smaller the FWHM. This is displayed on Figure 3-8 (a) where the reflectivity at Bragg wavelength ( $R_{\text{Bragg}}$ ) as well as the FWHM are represented as a function of the grating length for different etching depths. Here, the grating responses were calculated using the transfer matrix theory. Figure 3-8 also proves that, as  $e$  increases, so do  $R_{\text{Bragg}}$  and the FWHM meaning that although it might be interesting to minimize the FWHM lowering  $e$ , it induces longer gratings for a specific reflectivity wanted. When using the effective mirror model, a longer grating means a longer cavity and the FSR might be impacted. To check on it, Figure 3-8 (b) represents the FWHM/FSR ratio (e.g. the mode's number) of a cavity formed by two DBRs surrounding a 700- $\mu\text{m}$ -long active region (with an additional 60  $\mu\text{m}$  separating each mirror from the III-V). One is almost totally reflecting at 1310nm:  $R_{\text{Back-mirror}} = 0.99$ , and the other one has its parameters ( $e, L_{\text{Front mirror}}$ ) varying to get the reflectivity obtained on the abscissa of the graph. This shows that the tendency stays the same: the number of modes in the cavity decreases for higher reflectivities and lower etching depths.

There is then a trade-off to make when choosing the etching depth so that mirrors get low FWHM without being too long. It was just proved that for a given mirror reflectivity, the number of modes in the cavity is not impacted by the increase in the grating's length due to the lower etching depth. However, increasing the front mirror length not only means an increase in the laser footprint but also a higher number of periods. This last point is dangerous in the sense that it increases the chance to have defects in the grating letting other modes appear in the mirror response. The etching depth chosen was then  $e = 10 \text{ nm} \pm 0.5 \text{ nm}$  where the ' $\pm 0.5 \text{ nm}$ ' comes from the process variations.

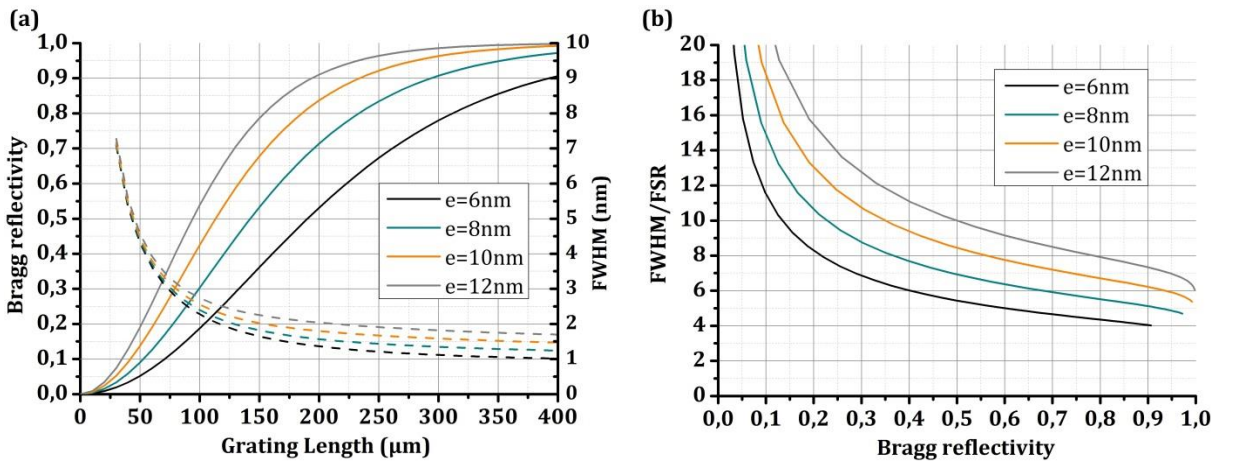


Figure 3-8: Grating response depending on its length: (a) Reflectivity at Bragg wavelength and FWHM, (b) FWHM/FSR ratio (nm/nm) calculated using  $L_{\text{cav}} = L_{\text{gain}} + 2L_{\text{transition}} + L_{\text{eff1}} + L_{\text{eff2}}$ .

To study cavities with different quality factors, it was chosen to select three different front-mirror's lengths:  $L_{\text{FM}} \in [75; 150; 200] \mu\text{m}$  while the back-mirror length would stay at  $L_{\text{BM}} = 700 \mu\text{m}$ . The calculated mirrors' characteristics as well as the associated cavities parameters are displayed on Table

3-1. Three different active region lengths were also chosen:  $L_{\text{gain}} \in [500; 600; 700] \mu\text{m}$ . Table 3-1 shows that the gain length has less influence on the FSR than the front-mirror's length. As expected by the decrease in FWHM, fewer modes are likely to be selected on the cavities constituted by longer front-mirrors.

**Table 3-1: Selected mirrors and their associated cavities characteristics.**

Back-mirror's characteristics	$R_{\text{FM}}$	$L_{\text{FM}}$ ( $\mu\text{m}$ )	$L_{\text{eff,FM}}$ ( $\mu\text{m}$ )	$\text{FWHM}_{\text{FM}}$ (nm)	$L_{\text{gain}}$ ( $\mu\text{m}$ )	$L_{\text{cav}}$ ( $\mu\text{m}$ )	FSR (nm)	FWHM/FSR (nm/nm)
$R_{\text{BM}} = 0.9999$ $L_{\text{BM}} = 700 \mu\text{m}$ $L_{\text{eff,BM}} = 64 \mu\text{m}$ $\text{FWHM}_{\text{BM}} = 1.31 \text{ nm}$	0.28	75	34	3.16	500	718	0.36	9
					600	818	0.32	10
					700	918	0.28	11
	0.68	150	53	2.02	500	737	0.35	6
					600	837	0.31	7
					700	937	0.28	7
	0.84	200	59	1.80	500	743	0.35	5
					600	843	0.31	6
					700	943	0.27	6

### Duty cycle study

A last important parameter which was already alluded to above is the filling factor of the grating. It was seen that its influence on the Bragg wavelength, is insignificant. It is relevant to observe how the reflectivity changes with the duty cycle. A software based on the coupled mode theory was used to compute the exact grating coupling constant as a function of the duty cycle:  $\kappa_g = f(DC)$ . In the case of a 10-nm-deep etched grating with  $W_{\text{Si}} = 3 \mu\text{m}$ , the results are displayed on Figure 3-9 (a) (dotted curves) for a 1<sup>st</sup>-order grating but also for a 3<sup>rd</sup> and 5<sup>th</sup> order grating i.e. when  $a = q \cdot a_{1\text{st-order}}$  where  $q$  is the order of the grating. A fit of the three curves was made (see Figure 3-9 (a)) to find an analytic formula for  $\kappa_g$  giving:

$$|\kappa_g| = \frac{2|n_{\text{eff}2} - n_{\text{eff}1}|}{\lambda_{\text{Bragg}} q} |\sin(\pi q DC)| \quad [3.12]$$

Equation [3.12] at 1<sup>st</sup> order is the same as equation [3.10] except that in the latter case, the duty cycle had been assumed to be 0.5 hence the appearance here of the  $|\sin(\pi q DC)|$  when taking the DC variations into account. This shows that the grating coupling coefficient is maximal for a 0.5 filling factor and that it decreases very quickly away from this value.

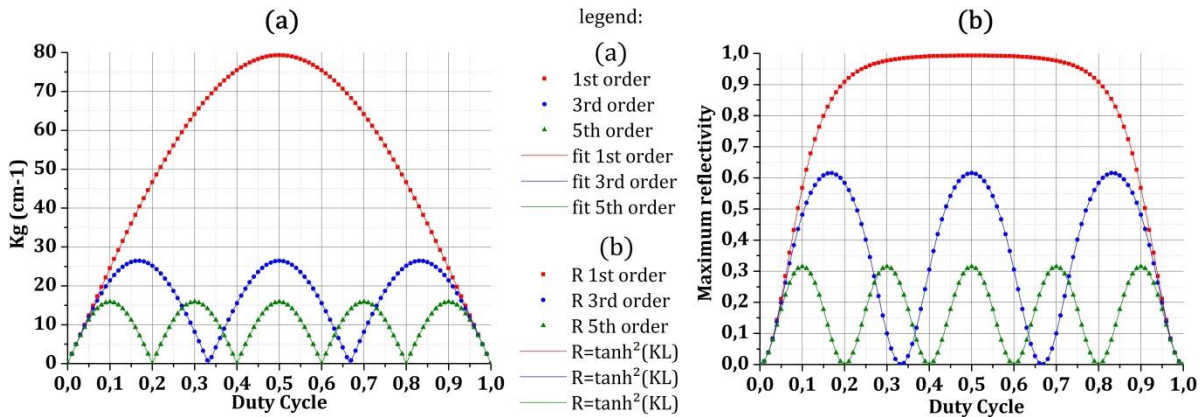


**Figure 3-9:  $\kappa_g$  (a) and  $R_{\text{max}}$  (b) evolution with the duty cycle in the case of a 400- $\mu\text{m}$ -long grating with a 10-nm-deep etching.**



The consequences on the maximum reflectivity are represented on Figure 3-9 (b) were the computed reflectivity of a 400- $\mu\text{m}$ -long grating (obtained with the transfer matrix theory) is superimposed with the reflectivity calculated with equation [3.7]. First of all, this plot shows that the approximations made to get the analytic formula [3.7] are validated for shallow etchings since both curves coincide quite well for the different grating order. Moreover, it shows that the influence of the grating duty cycle on the reflectivity is not as strong as on  $\kappa_g$ : the maximum reflectivity is reached as long as DC stands between 0.4 and 0.6. During the process fabrication, great care was taken to obtain gratings with filling factor within this range.

### 3.1.3. Results

#### *Mirrors characterization*

On the wafers, some test patterns allowed to measure the mirror response, as explained in 2.4. A tunable laser delivers a 1-mW-power to the input fiber coupler at different wavelengths and the transmitted power is collected from the fiber coupler located at the other side of the mirror. The coupling-to-fiber losses are de-embedded using the test pattern detailed on Figure 2-28 (b).

The experimental results are compared on Figure 3-10 with the computations implemented using transfer matrix theory for each mirror length. Both curves are very similar which means that the waveguides dimensions and grating etching depths comply with the designs and this is very encouraging for the rest of the measurements.

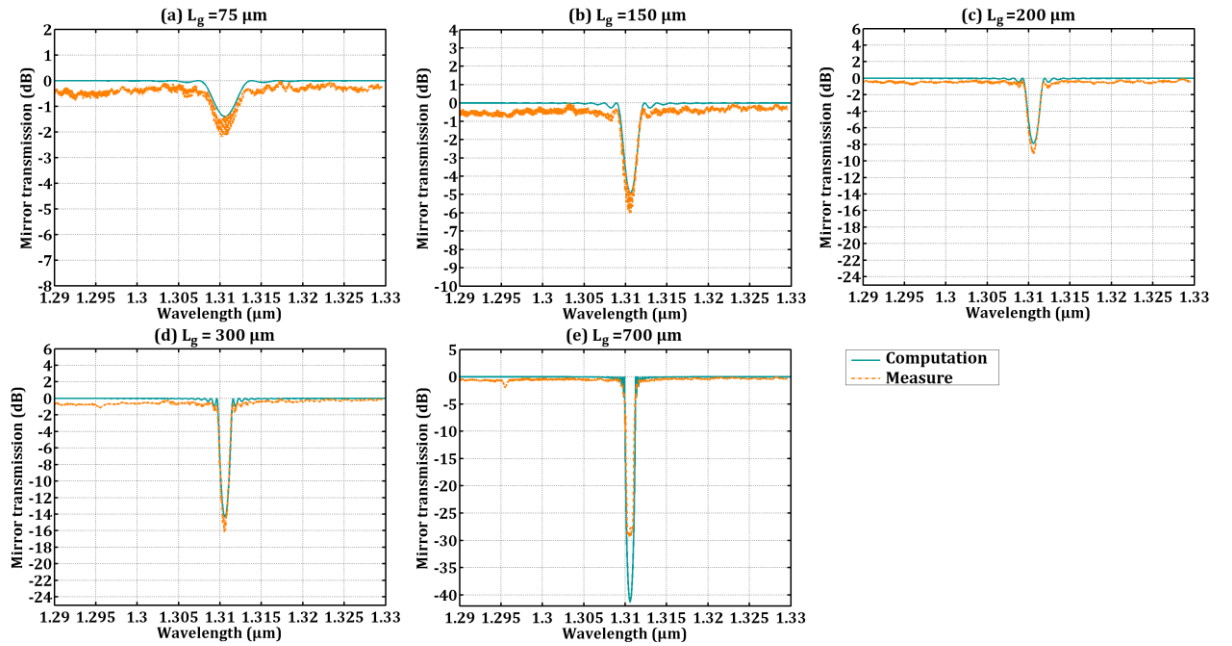


Figure 3-10: Comparison between computations and measures of the different DBR mirrors designed with  $a=196$  nm.

#### *Laser characterization*

Unfortunately, the process of the wafers with all the DBR lasers was not finished by the end of this work and all the different possibilities could not be analyzed experimentally. Luckily, another PhD student (T. Ferrotti) had some of the lasers designed above on his wafers because his thesis tackles optical transmitters as it will be explained in the prospects of my work. I thus had the chance to characterize some of the DBR lasers. All of them had a truncated taper designed for a 100 nm  $\text{SiO}_2$  gap, a gain length of 700  $\mu\text{m}$ , a grating period of either 195 nm or 197 nm and a front mirror length of either 150  $\mu\text{m}$  or

200  $\mu\text{m}$ . An optical microscope picture of a device with a 200  $\mu\text{m}$  long front mirror is represented on Figure 3-11.

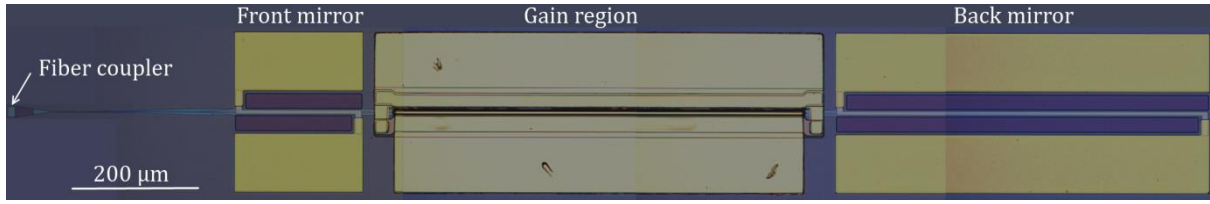


Figure 3-11: Optical microscope picture of one of the DBR lasers.

Due to some process issues, the  $\text{SiO}_2$  thickness between the Si and the III-V waveguides was only 60 nm, which is way below the 90 nm expected. According to the taper study presented in 2.2.3 the taper efficiency is in that case only 69 %. Since in a DBR laser the optical wave bounces forth and back a huge number of times from one mirror to another and it has to go through the tapers each time, the cavity losses are very much increased. The lasers performances, especially the threshold and power, are greatly affected by that. For this reason, only the lasers with a higher Q-factor, namely a longer front mirror (200  $\mu\text{m}$ ), were of any interest. Three of these lasers are presented below with their characteristics detailed in Table 3-2. One of them has a grating period of 197 nm and its lasing wavelength is 1315 nm and the two others have a grating period of 195 nm and a lasing wavelength of 1303 and 1304 nm respectively which is in good agreement with what was expected from the computations.

Table 3-2: Selected DBR laser properties

Laser	Taper	a (nm)	$\lambda_{\text{peak}}$ (nm)	Real $\text{SiO}_2$ gap	$L_{\text{FM}}$ ( $\mu\text{m}$ )	$R_{\text{FM}}$	WG to fiber coupler losses
DBR 1	Gap 100 nm truncated	197	1315	~60 nm	200	0.85	> 6 dB
DBR 2	Gap 100 nm truncated	195	1304				
DBR 3	Gap 100 nm truncated	195	1303				

The lasers voltage and power are represented as a function of the laser injection current on Figure 3-12 (a) and (b) respectively. The lasers characteristics extracted from these graphs (and the following ones) are gathered in Table 3-3. DBR 1 contact resistance is as high as 14.1  $\Omega$  while it is 6.2 and 6.7  $\Omega$  for DBR 2 and 3 respectively which can be explained by the fact that DBR 1 and DBR 2 and 3 are diametrically opposed on the wafer and the QWs etching is not uniform on the wafer. The power values were reached by removing the WG to fiber coupler losses (measured to be at least 6 dB) to the fiber coupled output power. Surprisingly, the laser output power is much higher for the former laser than for the latter: 1.6 mW in the waveguide compared to 0.42 and 0.83 mW. This is due to the fact that the peak wavelength is situated where the QWs maximum gain lies while it is slightly shifted for DBR 2 and 3. This also explains that the current threshold is lower: 48 mA for DBR 1 while it is 73 and 52 mA for DBR 2 and 3.



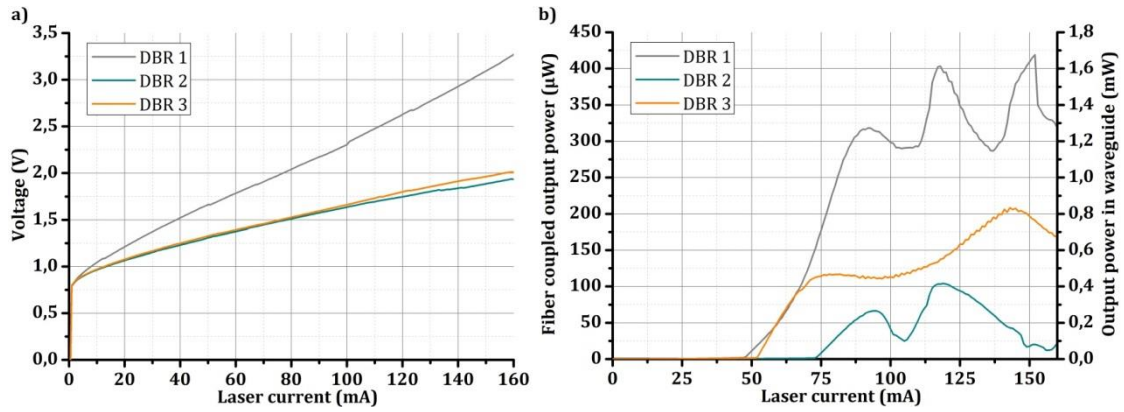


Figure 3-12: Voltage (a) and output power (b) depending of the laser current for the three DBR lasers selected.

The laser spectra as well as their SMSR as a function of the injection current are displayed on Figure 3-13. The Fabry-Pérot peaks, inherent to DBR lasers (which consist of a Fabry-Pérot-like cavity), are clearly visible and mode hopping as current increases demonstrates the DBR lasing effect. For all three lasers, the SMSR is higher than 35 dB on the whole current range except when a mode-hopping occurs, which proves that the grating is well defined.

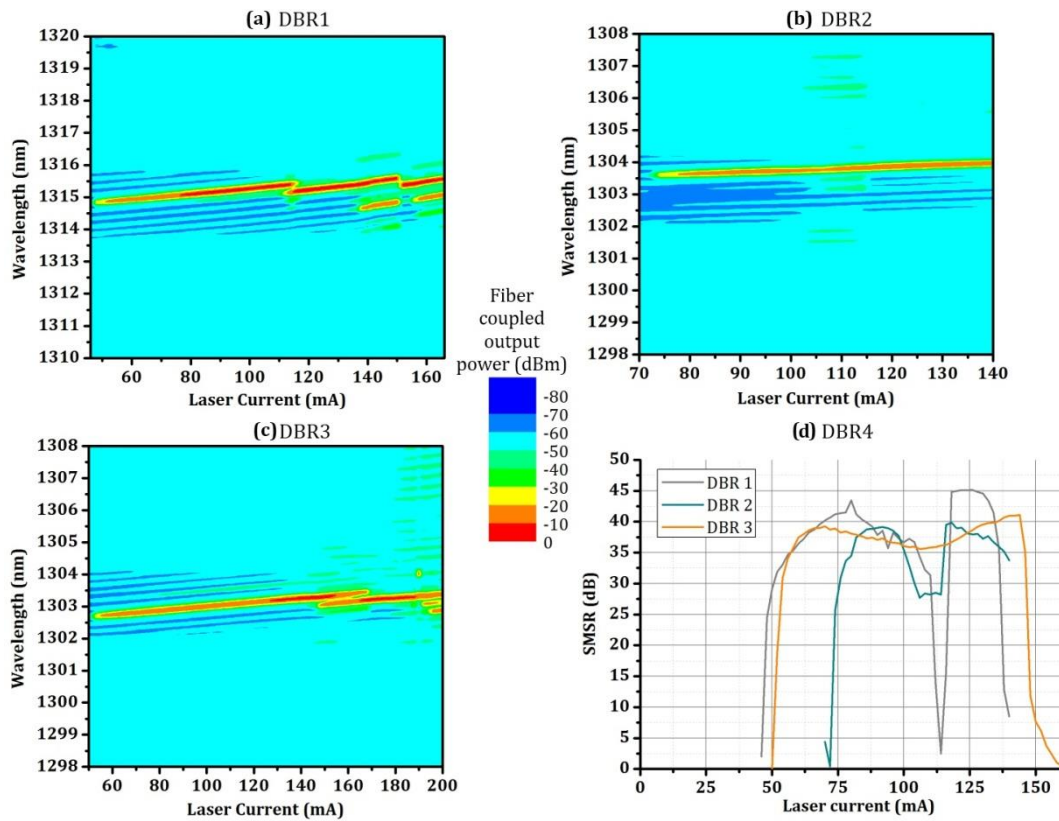


Figure 3-13: Spectra as a function of the laser current for DBR 1 (a), 2 (b) and 3 (c). The SMSR of the three lasers are displayed on (d).

Although those preliminary results are not as good as hoped, especially in regard of the laser output power and threshold, they are promising in the sense that for a wafer with the appropriate SiO<sub>2</sub> thickness, the performances shall be a lot better. The mirrors designs are validated by the measured SMSR values

and more proves shall be given when testing the wafers with all the different designs and with a proper gap thickness between III-V and Si. The tunability of the lasers is tackled in the next chapter.

**Table 3-3: DBR lasers measured properties.**

DBR laser	R ( $\Omega$ )	$\lambda_{\text{peak}}$ (nm)	$R_{\text{FM,calc}}$	$I_{\text{th}}$ (mA)	$J_{\text{th}}$ (kA/cm <sup>2</sup> )	$P_{\text{max}}$ (mW)	$\eta_{\text{diff}}$ (%)	$\text{SMSR}_{\text{max}}$ (dB)
1	14.1	1315	0.85	48	1.37	1.61	3.6	45.1
2	6.2	1304		73	2.09	0.42	1.6	39.8
3	6.7	1303		52	1.49	0.83	2.4	41.1

## 3.2. Distributed Feedback lasers

In a distributed feedback laser, there is only one grating embedded in the silicon right underneath the III-V as represented on Figure 3-14. As in the case of DBR lasers, the theory of DFB lasers will be explained first. Then, the cavity design is detailed for the two types of DFB lasers regarded and the characterization results reached in each case are given.

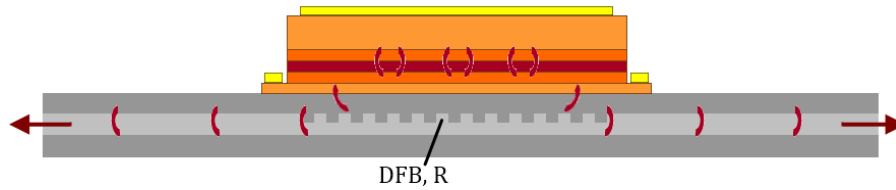


**Figure 3-14: Schematic representation of a hybrid III-V on Si DFB laser.**

### 3.2.1. DFB theory

#### *A quarter wavelength shifter*

To better understand the spectral response of a DFB, it is convenient to focus on the photonic crystal theory. A photonic crystal is a periodic material where light propagates, which means that a DBR grating is nothing more than a one-dimension photonic crystal. This paragraph gives only a glimpse of this approach and more information can be found in [97].

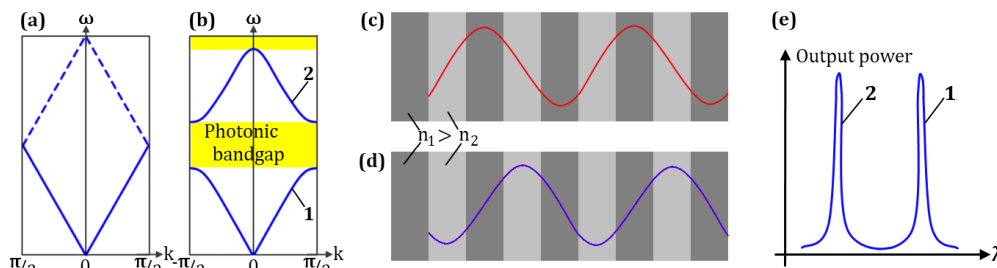


**Figure 3-15: Optical band diagram of (a) a bulk media, (b) a layered media. Band 1 and 2 are respectively the dielectric and air bands. (c) and (d) represent the local electric field distribution for the top of band 1 and bottom of band 2 respectively. (e) gives the spectral response of a DFB laser with a simple layered media for the feedback.**

As with semiconductor material, a photonic crystal can be described by its band diagram where the angular frequency  $\omega = 2\pi c/\lambda$  is represented as a function of the wave vector  $\vec{k}$ . The band diagram of a bulk material can be represented taking an imaginary period 'a': in this case, the following dispersion relation can be applied for the angular frequency:

$$\omega = \frac{c\|\vec{k}\|}{n} \quad [3.13]$$

This is represented on Figure 3-15 (a) with the solid lines. The dashed ones represent the same relation for higher  $\|\vec{k}\|$  values. Being outside the Brillouin zone (which correspond to  $\|\vec{k}\| \in [-\pi/a; \pi/a]$ ), they fold back into it when reaching its edges (i.e. when  $\|\vec{k}\| = \pm\pi/a$ ). In a periodic layered media, as it is the case for electrons in semiconductor materials, the period induces a zone where no optical frequencies are allowed between the lower and the upper curves of the diagram (see Figure 3-15 (b)). This zone is called the photonic bandgap and the higher the index difference between the layers, the wider the bandgap. At the edges of the Brillouin zone, the dispersion relation's slope becomes equal to zero:  $v_g = d\omega/dk = 0$  at each side of the bandgap. This means that two stationary waves (or slow waves) are trapped in the grating. Two mode's configurations are possible: the stationary wave can either have its energy mostly concentrated in the layers with higher refractive index or those with lower refractive index. The electric field distributions are represented for both cases on Figure 3-15 (c) and (d) respectively. It can be shown (see [97]) that the low frequency modes have their energy concentrated in high index regions while the high frequency modes have theirs in lower index regions. Thus, the lower band (band '1' or dielectric band) corresponds to the case where the electric field is concentrated in the layers with index  $n_1$  (because  $n_1 > n_2$ ) and the higher band (band '2' or air band) to the case where it is in the layers with index  $n_2$ . A DFB laser constituted of such a grating shall have two peaks in its spectrum as it is displayed on Figure 3-15 (e). Since it is linked to the index difference between both layers, the spacing between both modes can be related to the coupling strength of the grating by:

$$\Delta\omega = \frac{2\kappa_g c}{n_G} \quad [3.14]$$

Where  $n_G$  is the group index of the unperturbed layer.

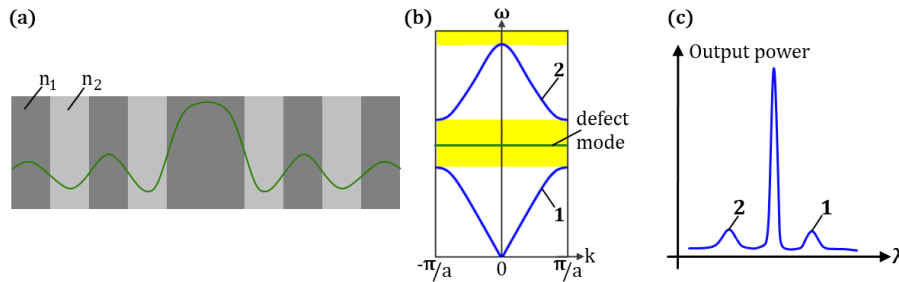


**Figure 3-16: (a) Representation of the local electric field distribution in a grating with a  $\lambda/4$  defect in the middle. (b) Optical band diagram of such a grating with the defect mode in the photonic bandgap. (c) Spectral response of a DFB laser with such a mode shifter.**

It is possible to introduce a defect in the perfectly symmetric grating for example by widening one of the layers as represented on Figure 3-16. Alike the doping effect in semiconductor materials, this induces the existence of a discrete frequency inside the bandgap (see Figure 3-16 (b)). Each grating surrounding the defect reflects light which is consequently trapped by the localized defect as shown by the field distribution on Figure 3-16 (a). To have the defect mode in the middle of the photonic bandgap, the widening of the layer needs to be a quarter of a wavelength namely  $\lambda_{\text{Bragg}}/(4n_{\text{avg}})$ . This defect mode having a higher Q-factor than the modes still existing at the edges of the bandgap, it will be the only one

selected in a DFB laser thus insuring a real single-mode effect. The spectral response of a DFB laser with a quarter wavelength shifter is represented on Figure 3-16 (c) showing the single peak selected by the defect surrounded by the two minor peaks corresponding to the edges' modes. It is shown in [2] that the  $\lambda/4$  shifter (QWsh for quarter wavelength shifter) should be in the middle of the grating to get a good modal purity. Such a laser is then symmetric with the same light power outgoing from both sides of the grating.

### The DFB reflectivity

Since the mirror in a DFB laser is also a DBR, the matrix theory can be applied and the grating coupling constant calculated the same way (eq. [3.10]). Since the shifter is in the middle of the grating, light is reflected with the same proportions at each side of the grating and the reflection is calculated modifying slightly equation [3.7]:

$$r_{g,DFB} \approx \tanh(\kappa_g L_g / 2) \quad [3.15]$$

The reflectivity at each side of the cavity is plotted on Figure 3-17 using  $R_{g,DFB} = \tanh(\kappa_g L_g / 2)^2$ . To cover the whole reflectivity range,  $\kappa_g L_g / 2$  should fit in  $[0.1; 3]$ . The DFB lasers made during this work had either a 500- $\mu\text{m}$ -long grating or a 1000- $\mu\text{m}$ -long one. Table 3-4 shows the  $\kappa_g$  limit values for these lengths: for  $L_g = 500 \mu\text{m}$ , the grating coupling constant belongs to the  $[4; 120] \text{ cm}^{-1}$  range while for  $L_g = 1000 \mu\text{m}$  it is rather in the  $[2; 60] \text{ cm}^{-1}$  range.

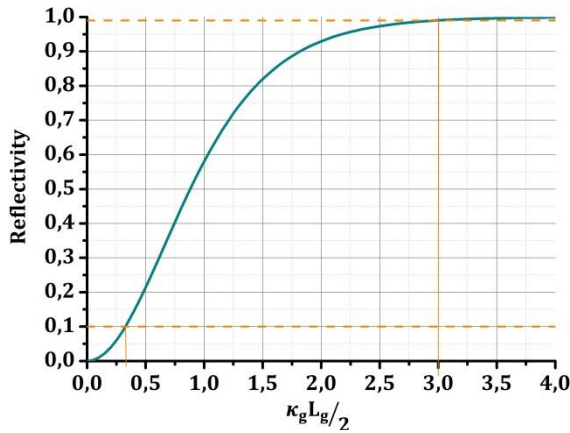


Figure 3-17: DFB reflectivity at one side as a function of  $\kappa_g L_g$

Table 3-4: Grating coupling constant values for different grating and reflectivity lengths.

$L_g$ ( $\mu\text{m}$ )	$R_g$	$\frac{\kappa_g L_g}{2}$	$\kappa_g$ ( $\text{cm}^{-1}$ )
500	0.10	0.10	4
	0.99	3.00	120
1000	0.10	0.10	2
	0.99	3.00	60

### 3.2.2. Cavity design

During this work, two types of DFB lasers were studied: the first one is a classic vertical DFB with the layers built by etching the top of the silicon waveguide. The DFB tackled in the III-V/Si lasers state of the art (see 1.2.2) consists of vertical gratings. The second DFB laser type is a little bit more unusual since it is the edges of the silicon waveguide which are etched to form the grating. To our knowledge, although more common in pure III-V lasers, only one such device has been demonstrated in the literature up to now (in 2015) using a III-V/Si technology. It showed low output power ( $<100 \mu\text{W}$ ) and a SMSR of  $\sim 20 \text{ dB}$  at  $1550 \text{ nm}$ [98]. The designs of both gratings are described below.

### Vertically coupled DFB laser

In the case where the grating is etched on top of the Si waveguide, referred to as ‘vertically coupled DFB laser’, the waveguide’s width does not vary and it is the same as the input width of the tapers. A schematic view of the gain region of the DFB is represented on Figure 3-18. The side view shows the mode distribution in the case of the un-etched or etched waveguide. The effective index is higher for the former case than for the latter hence a stronger part of the mode in the Si for the un-etched region. Figure 3-18 (a) also shows the quarter wavelength shifter in the middle of the grating. As for the DBR laser, the parameters to find are the etching depth  $e$ , the grating length ( $L_{g,DFB}$ ), the period ( $a$ ) and the silicon waveguide’s width ( $W_{Si}$ ).

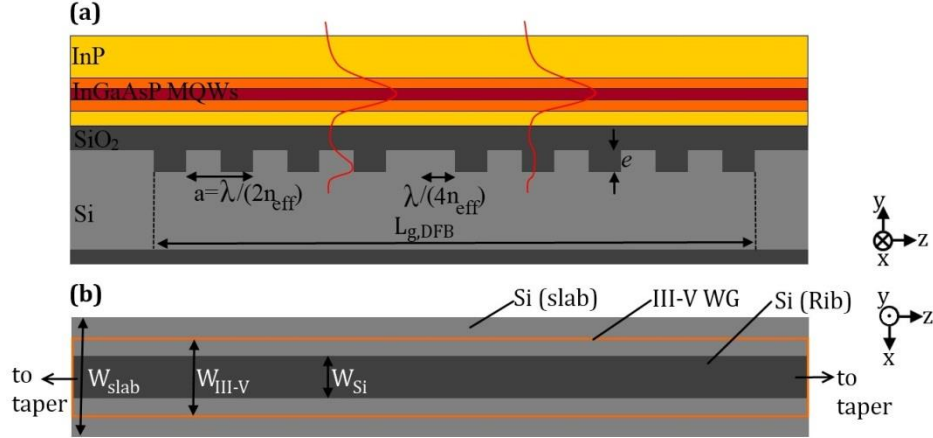


Figure 3-18: Side (a) and top (b) schematic views of the DFB laser with a grating etched on the top of the Si waveguide. The Si slab width is  $W_{slab}=10\text{ }\mu\text{m}$  and the III-V WG width is  $W_{III-V}=5\text{ }\mu\text{m}$ .  $W_{Si}$  needs to be defined.

In a DFB laser, the grating length is closely linked to the gain length:  $L_{gain} = L_{g,DFB} + 2L_{taper} = L_{g,DFB} + 200\text{ }\mu\text{m}$  since  $L_{taper} = 100\text{ }\mu\text{m}$ . Using results from earlier work (see [99]), two different gain lengths were chosen:  $L_{gain} = 700\text{ }\mu\text{m}$  or  $L_{gain} = 1200\text{ }\mu\text{m}$  meaning the grating length is either 500- $\mu\text{m}$ -long or 1000- $\mu\text{m}$ -long. This is also true for laterally coupled DFB lasers. As for the period calculation, equation [3.5] was used and again, to compensate for the III-V epitaxy uncertainties and the process variations (both for the III-V and the silicon), a wide panel of periods was selected around the central one ( $a=198\text{ nm}$ ):  $a \in [194; 196; 198; 199; 200; 202]\text{ nm}$ .

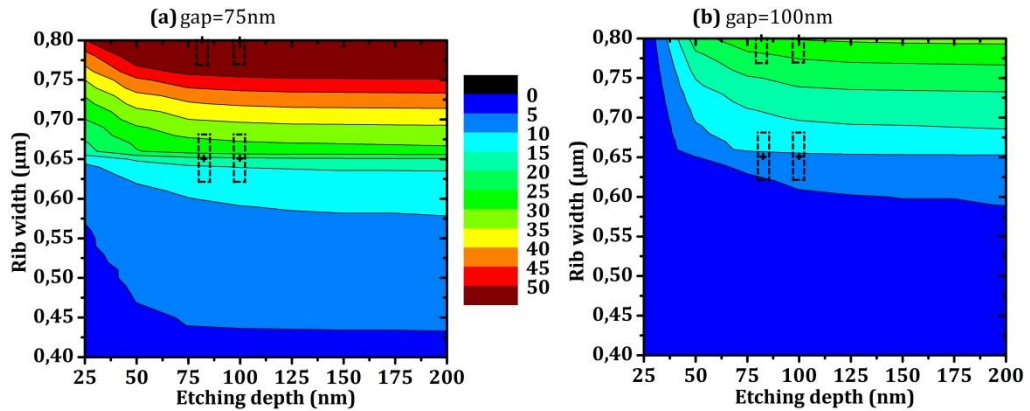


Figure 3-19: Grating coupling constant for the vertically coupled DFB laser with an  $\text{SiO}_2$  thickness of 75 nm (a) and 100 nm (b). The crosses stand for the coupling constant selected and the dashed squares for the process window ( $W_{Si} = \pm 30\text{ nm}$ ,  $e = \pm 3\text{ nm}$ )

The rib width and the etching depth were defined after a study of the coupling strength of the grating ( $\kappa_g$ ) which is a witness of how the supermode, which is mostly confined in the III-V, 'sees' the grating underneath. Figure 3-19 shows 2D-maps of  $\kappa_g$  values depending on the rib width and the etching depth in the cases of a  $\text{SiO}_2$  gap of 75 nm or 100 nm. It is clear that the rib width has a much higher influence on the grating strength than the etching depth. The larger the rib width, the less the even supermode stays confined in the III-V (see 2.2.1) and the higher  $\kappa_g$ . The tendency is the same for  $e$  although the effects are less strong: the deeper the etching, the larger the effective index difference and the higher  $\kappa_g$ . One last obvious remark is that the coupling strength is higher in the case of a lower thickness between the III-V and the silicon. For  $W_{\text{Si}} < 0.45 \mu\text{m}$ , Figure 3-19 shows that  $\kappa_g < 5 \text{ cm}^{-1}$  which is quite low and to get at least a reflectivity of 0.20 at each side of the grating, it is necessary to have  $W_{\text{Si}} \geq 0.60 \mu\text{m}$ . This is the reason why truncated tapers had to be designed (see 2.2.2): otherwise, the vertically coupled DFB lasers would have a too low quality factor. Thus, among the tapers designed, two of them have the satisfactory input width for a grating etched from the top, meaning that  $W_{\text{Si}} \in [0.65; 0.80] \mu\text{m}$ . Although the etching depth does not have much effect on the reflectivity, different values were chosen for they lead to different grating qualities. The best wafers remain those with a 80-nm-deep or a 100-nm-deep etching. The selected  $(W_{\text{Si}}; e)$  couples are represented by a cross on Figure 3-19 and the process window by a dashed square. The coupling constants' exact values and the reflectivities associated are gathered in Table 3-5 showing that for a given wafer, i.e. a given (gap;  $e$ ) couple, a wide panel of cavities is available (with both the 500- $\mu\text{m}$  and 1000- $\mu\text{m}$ -long gratings).

### Laterally coupled DFB laser

The DFB laser with the grating etched on the sides of the Si waveguide is a 'laterally coupled' DFB laser and a side and top schematic views are represented on Figure 3-20. The period and length of the grating are the same as for the former DFB type presented. The parameters to define specifically for this kind of DFB grating are the wider and thinner silicon width ( $W_{\text{Large}}$  and  $W_{\text{Narrow}}$ ) as shown on the top view of the grating.

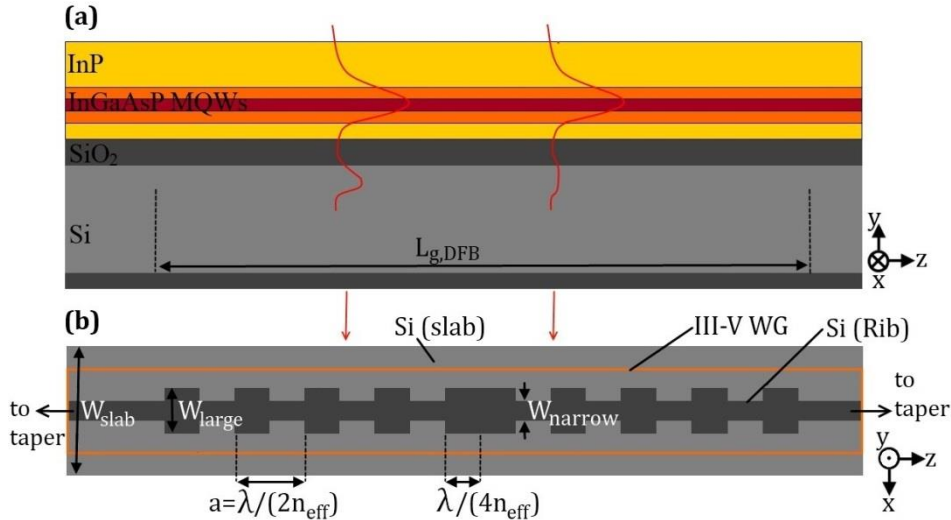


Figure 3-20: Side (a) and top (b) schematic views of the DFB laser with a grating etched on the edges of the Si WG. The Si slab width is  $W_{\text{slab}}=10 \mu\text{m}$  and the III-V WG width is  $W_{\text{III-V}}=5 \mu\text{m}$ .  $W_{\text{Large}}$  and  $W_{\text{Narrow}}$  need to be defined.

Again, to select the appropriate  $(W_{\text{Large}}; W_{\text{Narrow}})$  couples, 2D-maps of the grating coupling constant depending on these parameters are displayed on Figure 3-21 for the two different silica thicknesses. The smaller width is set by the input width of the taper: one of the advantages of this grating is that smaller



taper's input widths are possible compared to the vertically coupled grating case. Another advantage is that no specific photolithography step is required for the grating definition since it is defined at the same time as the rib is etched. The two tapers that were not truncated (see 2.2.3) were selected for the laterally coupled DFB lasers which thus set the narrow width of the grating to either 0.36  $\mu\text{m}$  or 0.53  $\mu\text{m}$ . For each  $W_{\text{Narrow}}$ , two different  $W_{\text{Large}}$  were chosen: this enable to get several lasers with different reflectivities in the [0.7;0.99] and [0.36; 0.99] ranges for a  $\text{SiO}_2$  gap thickness of 75 nm or 100 nm respectively. Moreover, the fact that lasers with four different grating coupling constants are on the same wafer ensures to get in each case at least one or two appropriate devices out of the four available ones in spite of the process variations. All the possibilities are displayed in Table 3-5.

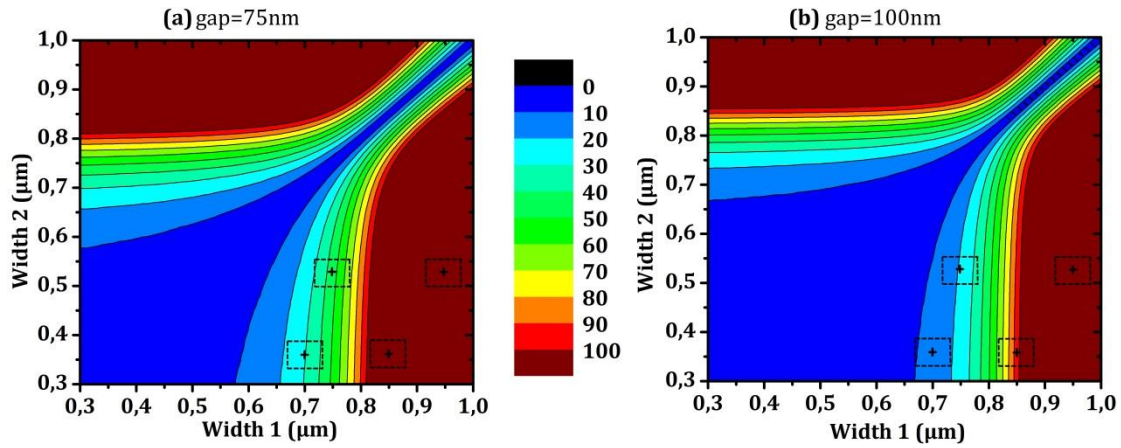


Figure 3-21: Grating coupling constant for the laterally coupled DFB laser with an  $\text{SiO}_2$  thickness of 75 nm (a) and 100 nm (b) The crosses stand for the coupling constant selected and the dashed squares for the process window ( $W_{\text{Si}} = \pm 30$  nm). They are represented taking Width 1 for  $W_{\text{Large}}$  and Width 2 for  $W_{\text{Narrow}}$ .

Table 3-5: Coupling constants and reflectivities (for one side) expected for each kind of DFB for the different parameters selected.

SiO <sub>2</sub> gap (nm)	Vertically coupled grating					SiO <sub>2</sub> gap (nm)	Horizontally coupled grating				
	$W_{\text{Si}}$ ( $\mu\text{m}$ )	$e$ (nm)	$\kappa_g$ ( $\text{cm}^{-1}$ )	$R_{g,\text{DFB}}$ [ $L_g = 500\mu\text{m}$ ]	$R_{g,\text{DFB}}$ [ $L_g = 1000\mu\text{m}$ ]		$W_{\text{Narrow}}$ ( $\mu\text{m}$ )	$W_{\text{Large}}$ ( $\mu\text{m}$ )	$\kappa_g$ ( $\text{cm}^{-1}$ )	$R_{g,\text{DFB}}$ [ $L_g = 500\mu\text{m}$ ]	$R_{g,\text{DFB}}$ [ $L_g = 1000\mu\text{m}$ ]
75	0.80	80	65	0.86	0.99	75	0.53	0.75	38	0.74	0.96
		100	66	0.87	0.99			0.95	248	0.9998	1
	0.65	80	31	0.42	0.83		0.36	0.70	34	0.70	0.94
		100	32	0.44	0.85			0.85	107	0.99	1
100	0.80	80	31	0.41	0.82	100	0.53	0.75	17	0.40	0.69
		100	31	0.42	0.84			0.95	199	0.9997	1
	0.65	80	14	0.11	0.35		0.36	0.70	15	0.36	0.64
		100	14	0.11	0.37			0.85	59	0.90	0.99

### 3.2.3. Results: vertically coupled DFB lasers

This paragraph details the results obtained for vertically coupled DFB lasers. Three 2-inches-wafers were obtained for the laser characterization. On each of them, there is respectively 9%, 22% and 2% of these DFB that are out of order (mostly due to short circuits). The average yield on the three wafers is thus 89%. Because of process variations, not all the devices exhibit the same quality: the two first wafers have a  $\text{SiO}_2$  bonding gap of approximately 100 nm and 70 nm respectively which means that some of the devices have better performances on one wafer than on the other as it will be seen below. As for the last wafer, most of the lasers, present a mode competition: although single-mode, it is not always the same mode which is

selected. This is probably due to the grating that is not properly defined and presents some other defects than the quarter wavelength shifter. All the following results focus only on the two first wafers. For the same reason, the DFB designed with a 1000- $\mu\text{m}$ -long grating often present a mode competition with increasing injected currents. This is either due to the presence of a defect along the grating or to the fact that with such a long grating, the dielectric or the air-mode can be pumped as well, as it will be seen below. Again, only the 500- $\mu\text{m}$ -long vertical DFB lasers are tackled here.

Not to overwhelm the reader with data, it was chosen to focus only on 3 lasers: the two first ones are lasers for which the tapers were designed for the appropriate gap thickness. The first (second) laser is issued from the wafer with a 70 nm (100 nm)  $\text{SiO}_2$  thickness between the Si and the III-V and its taper are the truncated one designed for a 75 nm (100 nm) gap. The third one was designed for a 75 nm gap and comes from the wafer with a 100 nm gap. Unfortunately, there is no operational laser with a taper designed at 100 nm on the wafer with a 70 nm gap but watching Table 3-5, this can be explained by the fact that in this case, the grating coupling constant is way too high to have power outgoing from the cavity. The features of the three lasers are given in Table 3-6. For each laser with a given taper, the best ones are those with the highest periods (i.e. 199 nm, 200 nm or 202 nm). This is due to the fact that the epitaxies are not as thick as expected which leads to an effective index difference between what was calculated with the FEM mode solver and what was deduced from the lasing wavelength ( $\Delta n_{\text{eff,calc-real}}$ ) of -0.07 for the first wafer and -0.06 for the second one. The static properties of the lasers are studied below.

**Table 3-6: Selected vertically coupled DFB lasers characteristics.**

Laser	Taper	Real SiO <sub>2</sub> gap	a (nm)	$\lambda_{\text{peak}}$ (nm)	$\Delta n_{\text{eff,calc-real}}$	WG to fiber coupler losses
1	Gap 75 nm truncated	~70 nm	202	1305	-0.07	6 dB
2	Gap 100 nm truncated	~100 nm	202	1305	-0.06	
3	Gap 75 nm truncated	~100 nm	200	1292		

### Static measurements

The static measurements of the lasers at room temperature (RT) were implemented using the method explained in 2.4. First, the losses induced by the coupling to the fiber were measured using the appropriate patterns (see Figure 2-28 (b)). For both wafers, there were at least 6 dB per coupler, which is quite high, but which may be explained by some roughness induced by one of the hard mask deposition steps. The lasers voltage depending on the injected current is represented on Figure 3-22 (a). It shows clearly that laser 1 is not from the same wafer: the resistance is higher than for the two others. A linear fit of the curves enables to reach the device resistance  $R$  (since  $U=RI$ ) which is 7.0  $\Omega$ , 5.4  $\Omega$  and 5.6  $\Omega$  respectively for lasers 1, 2 and 3. These values include the resistance induced by the tips contact which could not be de-embedded. They are gathered in Table 3-7 as well as all the others static properties of the lasers. The lasers output power is displayed on Figure 3-22 (b) as a function of the injected current showing a threshold of 36 mA, 50 mA and 60 mA and a maximum output power in the waveguide of 22.3 mW, 11.4 mW and 8.5 mW respectively for laser 1, 2 and 3. The power in the waveguide was obtained removing the coupling losses from the power in the fiber and taking into account the fact that the same power is available from both outputs of the laser. From the slope of the P-I curve, the lasers differential efficiency was calculated to be 25%, 12% and 10%.



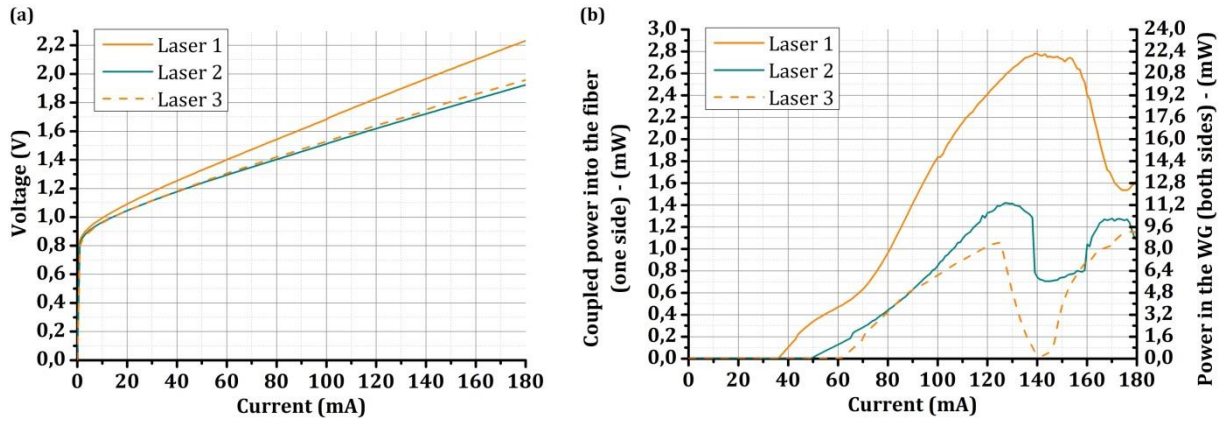


Figure 3-22: Lasers' voltage (a) and output power (b) as a function of the injected current for vertically coupled DFB lasers 1, 2 and 3.

The lasers spectra are represented on Figure 3-23 (a), (b) and (c) for increasing injected currents. Laser 1 displays a very high spectral purity along the [60; 160] mA range. The two other lasers seem worse and a mode competition appears for laser 2 at currents higher than 140 mA. Figure 3-23 (d) shows the spectrum for each laser at the current corresponding to their highest SMSR values which are respectively 56.6 dB, 52.3 dB and 39.9 dB. The FWHM of the peaks in the spectra from Figure 3-23 (d) was measured taking the FWHM of the Lorentzian fit for each peak. However, these values showed FWHM of the order of the GHz which correspond in fact to the OSA precision limit. To compare precisely one value from the other, a real linewidth measurement should be implemented [100], [101].

The SMSR depending on the laser injected current is also represented on Figure 3-24 (a) showing that for laser 1, it is higher than 50 dB on the [60; 164] mA range. Laser 2 is also quite good regarding spectral purity since its SMSR is higher than 45 dB on the [60; 140] mA range while laser 3 is only higher than 20 dB on the same range. The SMSR fall of lasers 2 and 3 at high currents are both due to a different reason as it is shown by the lasers spectra at 170 mA current injection on Figure 3-24 (b) and (c). At high currents, two modes grow around the defect mode of laser 2 and they clearly correspond to the air and dielectric modes introduced in the DFB theory (see 3.2.1). These modes appear as well for lasers 1 and 3 but very lightly and not enough to damage their SMSR. As for laser 2, Figure 3-24 (c) displays several modes arising at higher wavelengths than the selected one. These modes are induced by a Fabry-Pérot cavity. The average spacing between the Fabry-Pérot peaks is 0.33 nm which leads to a cavity length of 770  $\mu\text{m}$ . From this, it seems fair to suppose that the Fabry-Pérot cavity is created by the facets of the III-V (which are 700  $\mu\text{m}$  apart). The Fabry-Pérot modes appear on this laser and not the others, not only because its grating coupling constant is lower (as it is detailed below), but also because the selected wavelength is decentered compared to the gain maximum. Thus, at high current injections, the pumping of the Fabry-Pérot modes is as efficient as the one of the defect mode. This mode hopping explains the output power decrease of laser 2 and 3 from  $I=125$  mA and 140 mA respectively.

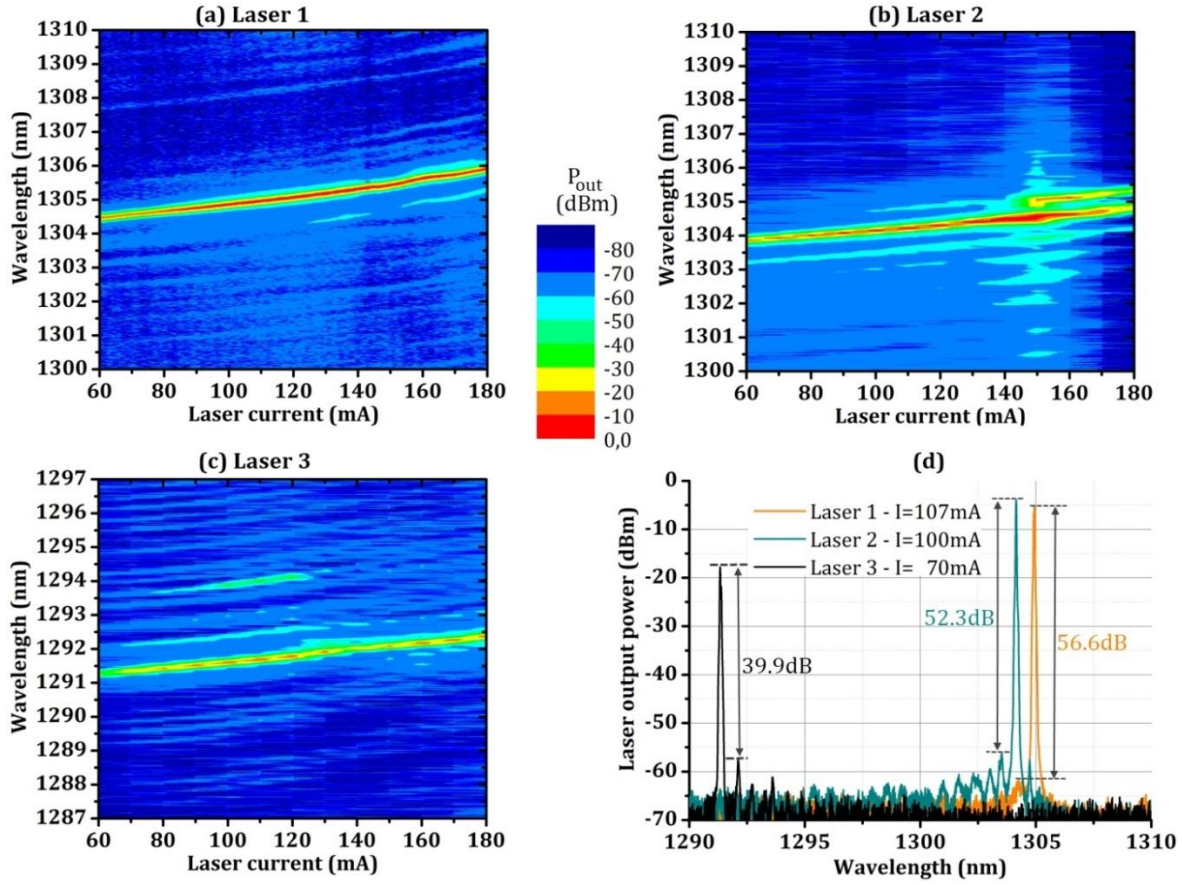


Figure 3-23: Lasers spectra with varying injected current for lasers 1 (a), 2 (b) and 3 (c). (d) displays the spectrum of each laser at the current for which the best SMSR is obtained.

The differences in SMSR from one laser to the other can be very well explained by the coupling constant of the grating. Their calculated and measured values are displayed in Table 3-7. The calculated ones ( $\kappa_{g,calc}$ ) are a little bit different from what was given in Table 3-5 because they were recalculated here using the exact laser wavelength.  $\kappa_{g,meas}$  was reached by measuring the wavelength difference between the air and dielectric peaks (see Figure 3-24 (b)) and by using equation [3.14]. In this equation, the group index of the 1<sup>st</sup> supermode is needed and it was calculated by using a FEM mode solver, assuming that at first order, the index variations between what is calculated and what is real are the same for the group index as for the effective index (i.e. -0.07 for laser 1 and -0.06 for laser 2 and 3). For both  $\kappa_{g,calc}$  and  $\kappa_{g,meas}$ , the tendency is the same : the grating coupling constant is higher for laser 1 and lower for laser 3 and this follows the SMSR tendency: the higher the laser grating coupling constant, the higher its SMSR.

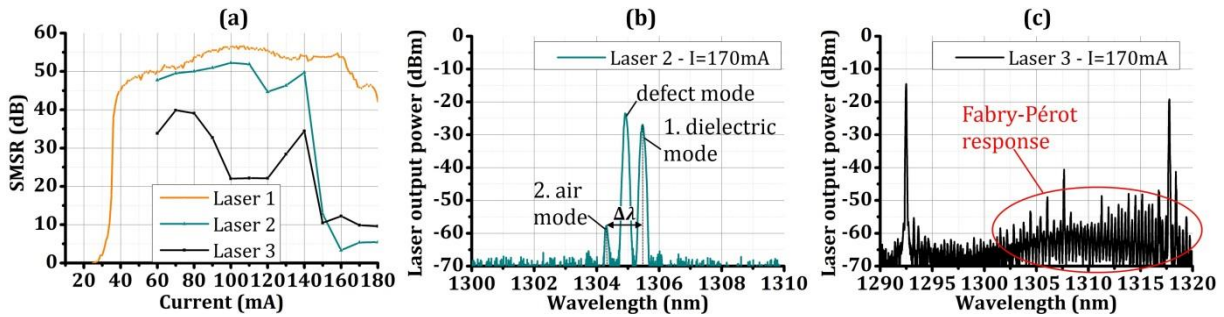


Figure 3-24: (a) Lasers SMSR as a function of the injected current. (b) and (c) show spectra of lasers 2 and 3 respectively when the SMSR is low.

These first measurements were in good agreement with the DFB theory and design presented above. It can be noticed that although the resistance was higher for laser 1, its performances are better than for the two others. As long as the resistance is not too high, it appears that this parameter has less influence on the laser characteristics than the grating coupling constant. Further measurements were implemented but only on the best laser (laser 1): they consisted in checking the laser evolution with temperature and its RF performances. Since the lasers have the same dimension and contacts size, it is most probable that both the RF and temperature characteristics stay roughly the same between the different lasers.

**Table 3-7: Vertically coupled DFB lasers measured properties.**

Laser	R ( $\Omega$ )	$\lambda_{\text{peak}}$ (nm)	$\kappa_{\text{g,calc}}$ ( $\text{cm}^{-1}$ )	$\kappa_{\text{g,meas}}$ ( $\text{cm}^{-1}$ )	$I_{\text{th}}$ (mA)	$J_{\text{th}}$ ( $\text{kA}/\text{cm}^2$ )	$P_{\text{max}}$ (mW)	$\eta_{\text{diff}}$ (%)	$\Delta\lambda/\Delta P_{\text{el}}$ (nm/W)	$\text{SMSR}_{\text{max}}$ (dB)
1	7.0	1305	38	43.0	36	1.03	22.3	25.3	3.7	56.6
2	5.4	1305	32	36.5	50	1.43	11.4	12.7	3.5	52.3
3	5.6	1292	9	15.4	61	1.74	8.5	10.5	4.2	39.9

### Temperature analysis

For a first qualitative estimate of the laser temperature performances, the output power as a function of the injected current is plotted for different chuck temperatures on Figure 3-25 (a). It shows lasing operation until 55°C. To go further into the thermal analysis, measurements were implemented in pulsed regime (0.1% duty cycle and 1 ms pulse repetition) to limit heating from self-induced power dissipation in the laser. Measurements of the threshold for each temperature from 15 °C to 75 °C led to a characteristic temperature  $T_0$  of 44 °C which is coherent with the fact that the laser effect stops for temperatures higher than 60 °C. A linear fit of the peak wavelength shift versus stage temperature in pulsed regime gives  $(\Delta\lambda/\Delta T)_{\text{DC}0.1\%,1\text{ms}} = 0.08 \text{ nm}/^\circ\text{C}$  as shown in Figure 3-25 (c). Since the peak wavelength shift versus dissipated power in CW regime is  $(\Delta\lambda/\Delta P)_{\text{CW}} = 3.72 \text{ nm}/\text{W}$  (Figure 3-25 (b)), the thermal impedance, defined as the ratio of both values, is  $Z_T = 44.1^\circ\text{C}/\text{W}$ .

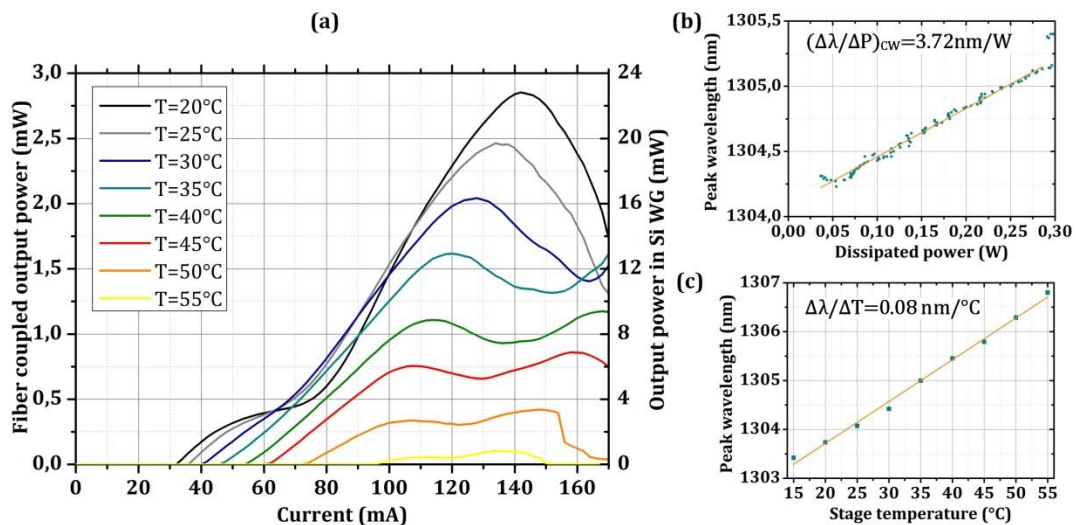


**Figure 3-25: (a) Laser 1's output power depending on the current with increasing temperatures. Laser peak wavelength as a function of the dissipated power (CW) (b) as well as of the stage temperature in pulsed regime (c).**

### High speed measurements

The high speed performances of the laser were measured by implementing the procedure detailed in 2.4. The laser electro-optic response is represented on Figure 3-26 (a) for different DC currents. The DC current that enables to reach the highest -3dB bandwidth is 85 mA and it gives:  $f_{-3dB} = 6.7$  GHz. The eye diagrams of the laser at 5 Gbit/s, 10 Gbit/s and 12 Gbit/s are displayed on Figure 3-26 (b) showing that the eye starts to close at 12 Gbit/s. These results may have been improved by using pads specifically designed for RF measurements which was not the case here.

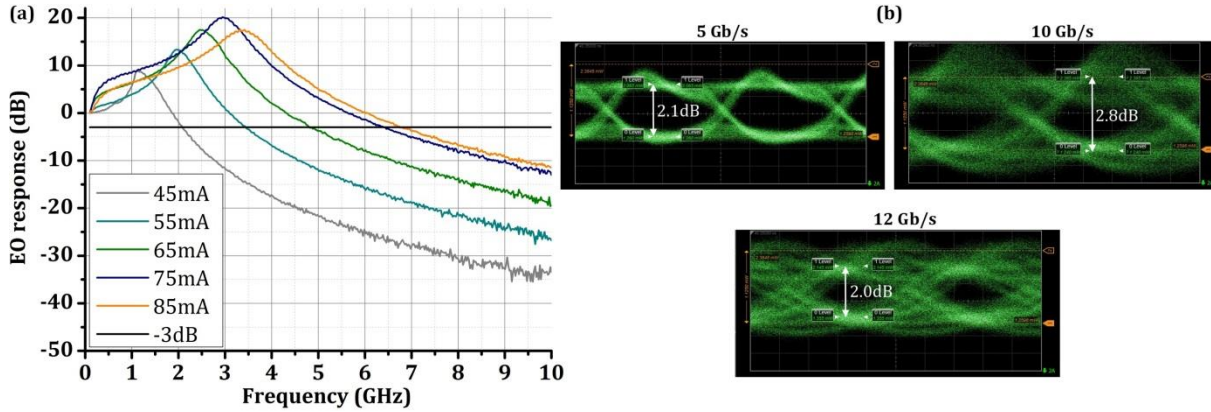


Figure 3-26: Laser 1's electro-optic response with frequency (a), eye diagrams at different speeds obtained using a random bit sequence of  $2^{15}-1$  (b).

### Conclusion to the vertically coupled DFB lasers characterization

To conclude with these measurements, a comparison between the results and the requirements set in 1.3.1 is made. Selecting the appropriate grating constant, we could realize lasers which exhibit static performance matching with what is necessary namely a few milliwatt of output power in the waveguide, a SMSR higher than 30dB and a FWHM lower than 1 nm although this last point needs to be validated by a specific linewidth measurement in Hz. With regard to the temperature performance, these are a little bit disappointing since the highest temperature showing lasing effect is 55 °C compared to the 80 °C targeted. This may be explained by the fact that the III-V wafers were not as thick as expected, thus inducing a higher influence of the temperature on the gain region. The RF behaviour of the laser match what is needed for the 40GbaseLR4 since we got a -3dB bandwidth of 6.7 GHz and an open eye diagram until 10 Gbit/s. However, on the wafers characterized, only 3 different wavelengths were available (1285 nm, 1290 nm and 1305 nm) instead of the 4 targeted. This was due to the III-V epitaxy which was not as thick as expected thus modifying the effective index expected. With an appropriate III-V wafer, it is most probable that the 4 wavelengths shall be reached.

Eventually, these results are quite good in term of static performances although some efforts need to be implemented on the temperature performance of the lasers as well as their RF performances (changing the pads design) to reach the 100GbaseLR4.

#### 3.2.4. Results: laterally coupled DFB lasers

The vertically couple DFB lasers talked above were processed using DUV photolithography for the four levels on Si (cf. 2.3.1). For the laterally coupled DFB lasers, the gratings, built during the 200-nm-deep rib level, were not properly defined as it can be seen on Figure 3-27 (a): instead of reaching well demarcated periods, the gratings looked like waves. This led to very low grating coupling constants, thus preventing any suitable single-mode devices: the spectra of lasers with such a grating are represented on Figure 3-27



and it is clear that either other modes than the defect modes enter into competition (b) or the Fabry-Pérot modes are stronger (c).

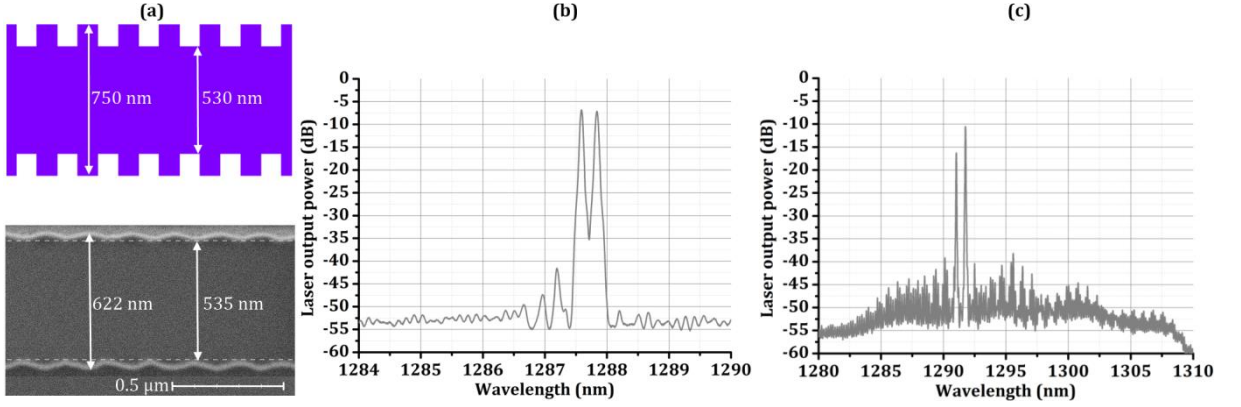


**Figure 3-27:** (a) Grating design (top) and SEM picture (bottom) after the DUV photolithography and the 200-nm-deep etching. (b) and (c) stands for spectra of lasers made with these steps recorded for  $I=140$  mA.

To ensure well-defined gratings, the rib level was implemented using e-beam photolithography. The result is represented on Figure 3-28 (a): the periods are very well demarcated and the dimensions correspond better to the designs than what was reached with DUV. The drawback of e-beam photolithography, which was not anticipated when choosing this solution, is that some defect may appear at some point in the grating due to some stitching issues which correspond to an imperfect control of the electron beam when moving from one point to another. This hardly ever happens but since the grating in the DFB is quite long (500-μm-long which leads to 2551 periods in the case of a 196-nm-long period), the chance to get such a defect in the grating is significant. For this reason, on the single wafer that was processed until the end with e-beam photolithography during this work, many lasers were not single-mode: a mode competition happens because of the presence of other defects than the quarter-wavelength shifter in the grating. This is illustrated by the spectra displayed on Figure 3-28 (b) where a second mode appears at higher wavelengths. Another problem encountered with this wafer was that the gain maximum occurred at higher wavelengths than what was wanted (around 1315 nm instead of 1295 nm) and the lasers with the best performances are consequently those for which the period 'a' is higher (i.e.  $a=199$  nm and more). For those with lower periods (from 194 nm to 198 nm), the Fabry-Pérot modes compete with the mode selected by the QWsh as displayed on Figure 3-28 (c).

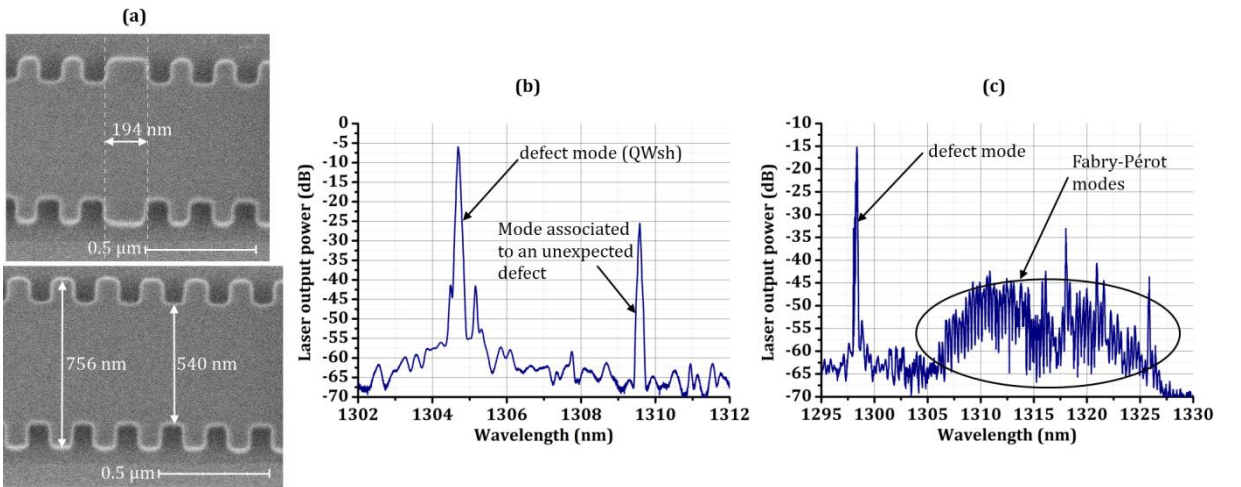


**Figure 3-28:** (a) SEM pictures a laterally coupled grating (with  $W_{\text{Narrow}} = 530$  nm and  $W_{\text{Large}} = 750$  nm) after the e-beam photolithography and the 200-nm-deep etching. The QWsh can be seen on the top picture. (b) and (c) stands for spectra of lasers made with these steps but for which some defect in the grating prevented to reach single mode devices.

The SOI wafer used for the bonding has a higher SiO<sub>2</sub> thickness than wanted: the average gap is around 120 nm. Thus, not only the grating coupling constant is lower than expected for most of the devices but also the tapers performances are much degraded by this. Less good devices were thus found than in the case of vertically coupled DFB lasers. However, those found are very promising and shows better performances than what can be found in the literature for III-V on Si laterally coupled DFB lasers up to now. Three of them are presented below with their characteristics in Table 3-8. The two first ones have the same properties save for their grating periods which are respectively 199 and 200 nm. The coupling losses from the Si waveguide to the fiber where measured between 5.5 and 6.5 dB depending on the laser output wavelength.

**Table 3-8: Selected horizontally coupled DFB lasers characteristics.**

Laser	Taper	$W_{\text{Large}}$ ( $\mu\text{m}$ )	$W_{\text{Narrow}}$ ( $\mu\text{m}$ )	Real SiO <sub>2</sub> gap	$a$ (nm)	$\lambda_{\text{peak}}$ (nm)	$\Delta n_{\text{eff,calc-real}}$	WG to fiber coupler losses
1	Gap 100 nm	0.950	0.600	~120 nm	199	1299	-0.03	-6 dB
2	Gap 100 nm	0.950	0.600		200	1305		-5.5 dB
3	Gap 75 nm truncated	0.850	0.370		200	1299		-6.5 dB

### Static measurements

The static measurements of the lasers are presented in what follows, beginning with the voltage as a function of the laser current (see Figure 3-29 (a)). A fit of the curve slope leads to a laser resistance between 4.1 and 5.0  $\Omega$  for the three lasers. All the static results are summed up in Table 3-9. The output power delivered by the lasers in the waveguide, assuming the same power into both sides of the laser, is represented as a function of the laser current on Figure 3-29 (b). Laser 1 and 2 show classical P-I laser signature and reached a maximum output power of 10.3 and 8.5 mW with a threshold current of 56 and 50 mA respectively. As for laser 3, the power is twice higher (20.2 mW) and  $I_{\text{th}}=48$  mA. However, a bump on the curve can be seen around 150 mA which cannot be explained by a mode hop as it will be seen below. The lasers differential efficiencies (deduced from the slopes on Figure 3-29 (b)) are respectively 7.7 %, 4.1 % and 12.7 % for lasers 1, 2 and 3. The fact that the power and efficiencies are not as high for these lasers as for the vertically coupled DFB lasers may be explained by their higher SiO<sub>2</sub> gap thickness leading to lower taper coupling efficiencies and lower grating coupling constants but also because  $W_{\text{Narrow}}$  is narrower for laser 3 which means that the mode is more confined in the III-V and consequently more amplified.

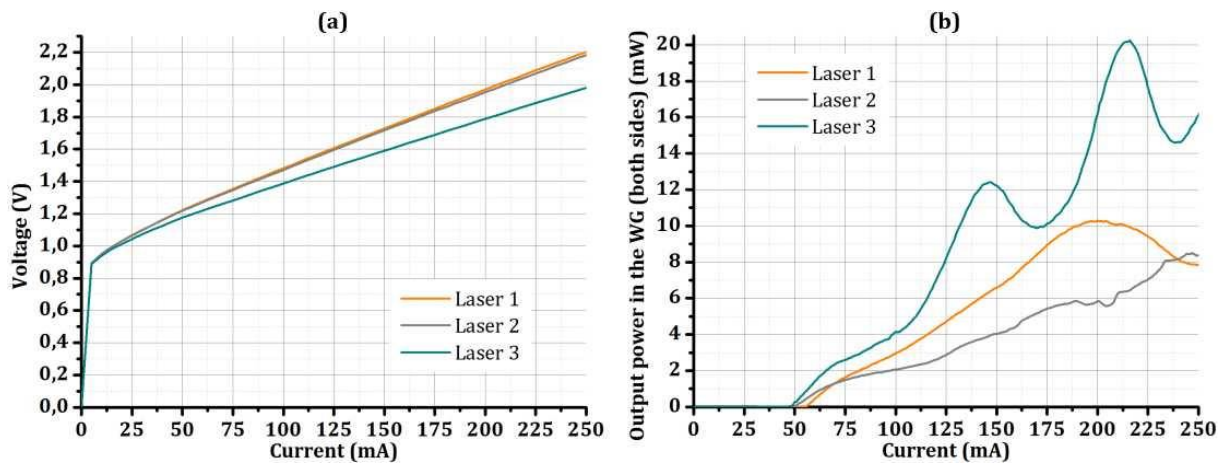


**Figure 3-29: Voltage (a) and power delivered by the laser in the WG (b) as a function of the laser current for the laterally coupled DFB lasers.**

Figure 3-30 and Figure 3-31 show the modal performances of the three lasers. The spectrum of laser 1 is very pure on the [56, 175] mA range with a SMSR higher than 40 dB and a maximum SMSR of 49.7 dB.

From 175 mA of current injection, the ‘air mode’ of the grating enters into competition (as it was explained on Figure 3-24 (c)) and the laser becomes then bi-mode.

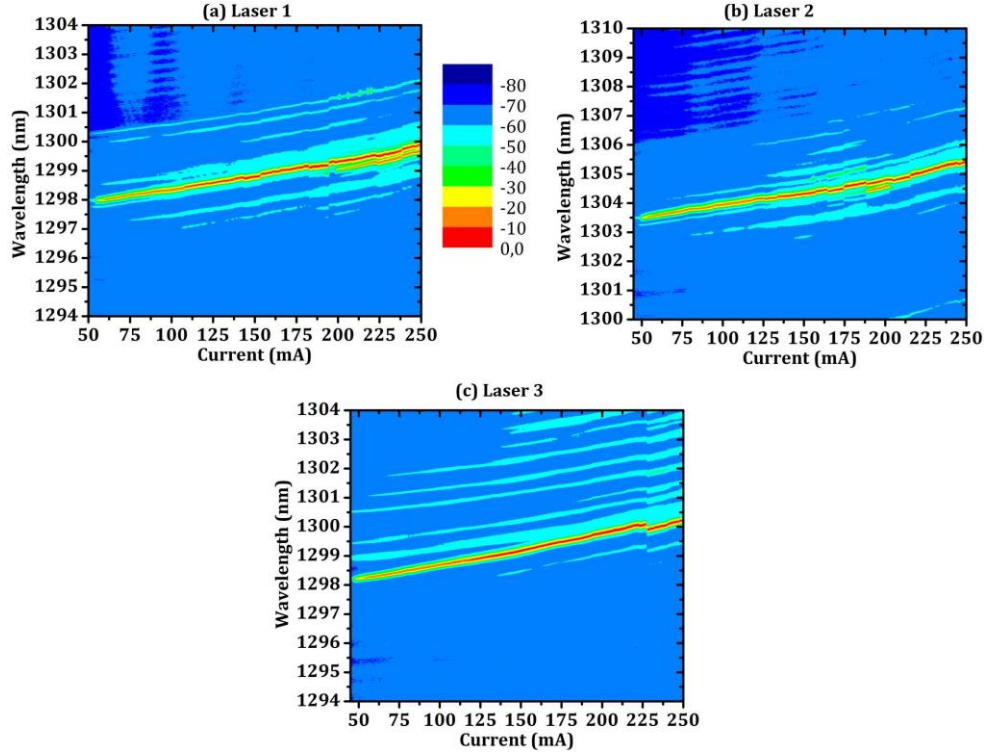


Figure 3-30: Lasers spectra with varying injected current for laterally coupled DFB lasers 1 (a), 2 (b) and 3 (c).

The second laser is single-mode on the whole current range with a SMSR higher than 42 dB except for laser currents between 155 and 205 mA where the air and dielectric modes both seem to compete with the grating defect mode. Until 155 mA, its highest SMSR is 48 dB. Eventually, laser 3 shows a high spectral purity on the whole [48; 225] current range with a SMSR higher than 40 dB and  $SMSR_{\max} = 49.0$  dB which is particularly high for this type of device. This result is quite surprising since regarding the P-I curve, one would expect some mode competition. In the end, this bump could not be explained: maybe a thermal effect (overheating due to a problem in the III-V waveguide?) appeared between 150 mA and 175 mA of injection current? Further inquiries shall be implemented to verify this hypothesis but since the analysis of the III-V waveguide implies damaging the device, it was not done yet.

Using equation [3.14], the real grating coupling constants of the lasers were deduced from the measured spectra. They were respectively of 21, 23 and 20  $\text{cm}^{-1}$  for laser 1, 2 and 3 which is a lot lower than expected especially for laser 1 and 2. The high  $\text{SiO}_2$  gap thickness does not solely explain this phenomenon and the device dimensions variations play a great part in the  $\kappa_g$  deviations. To get  $\kappa_g = 20 \text{ cm}^{-1}$  for laser 3 would mean that  $W_{\text{Large}} = 800 \text{ nm}$  instead of 850 nm (with a gap of 125 nm). As for laser 1 and 2, the measured values can only be reached with some computations assuming a  $\text{SiO}_2$  gap thickness above 140 nm and  $W_{\text{Large}}$  below 900 nm instead of the 950 nm expected. The fact that the gap is higher for laser 1 and 2 than for laser 3 is possible since they are far apart on the wafer. The high deviation in  $W_{\text{Large}}$  ( $\geq 50 \text{ nm}$ ) for all three cases may be explained by the contrast between  $W_{\text{Large}}$  and  $W_{\text{Narrow}}$  which is too high to be well marked at such low periods. Unfortunately, no measurements of these specific gratings were made before the bonding to confirm the real width values. The temperature performances of laser 2 are presented in the following paragraph.

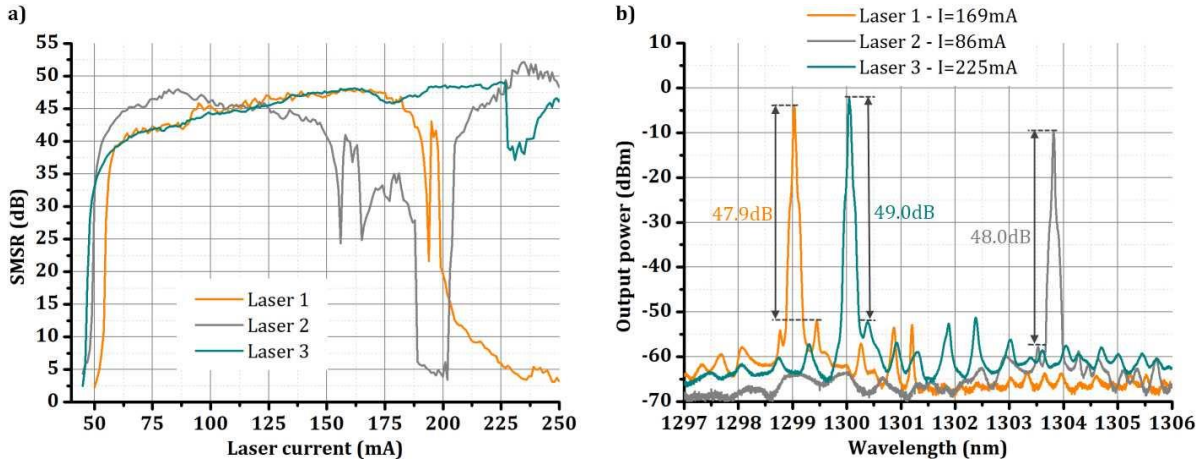


Figure 3-31: SMSR with increasing lasers currents (a) and best spectra (b) for laterally coupled DFB laser 1, 2 and 3.

Table 3-9: Horizontally coupled DFB lasers measured properties

Laser	R ( $\Omega$ )	$\lambda_{\text{peak}}$ (nm)	$\kappa_{\text{g,calc}}$ ( $\text{cm}^{-1}$ )	$\kappa_{\text{g,meas}}$ ( $\text{cm}^{-1}$ )	$I_{\text{th}}$ (mA)	$J_{\text{th}}$ ( $\text{kA}/\text{cm}^2$ )	$P_{\text{max}}$ (mW)	$\eta_{\text{diff}}$ (%)	$\Delta\lambda/\Delta P_{\text{el}}$ (nm/W)	$\text{SMSR}_{\text{max}}$ (dB)
1	5.0	1299	208	21	56	1.60	10.3	7.7	3.1	47.9
2	4.9	1305	198	23	50	1.43	8.5	4.1	3.1	48.0
3	4.1	1299	46	20	48	1.37	20.2	12.7	3.4	49.0

### Temperature analysis

As for the vertically coupled DFB laser, the output power as a function of the injected current is plotted for different chuck temperatures on Figure 3-32 (a). It shows lasing operation until 65°C, namely 10°C more than what was obtained with the vertically coupled DFB lasers. Measurements were also implemented in pulsed regime with the same pulsed conditions (0.1% duty cycle and 1 ms pulse repetition) to limit heating from self-induced power dissipation in the laser. Measurements of the threshold for each temperature from 20 °C to 65 °C led to a characteristic temperature  $T_0$  of 60 °C which is coherent with the fact that the CW laser effect is better for those laser than those with  $T_0=44$  °C (see 3.2.3). A linear fit of the peak wavelength shift versus stage temperature in pulsed regime gives  $(\Delta\lambda/\Delta T)_{\text{DC}0.1\%,1\text{ms}}=0.07$  nm/°C as shown in Figure 3-32 (c). Since the peak wavelength shift versus dissipated power in CW regime is  $(\Delta\lambda/\Delta P)_{\text{CW}}=3.10$  nm/W (Figure 2-29 (b)), the thermal impedance is  $Z_T=44.3$  °C/W.

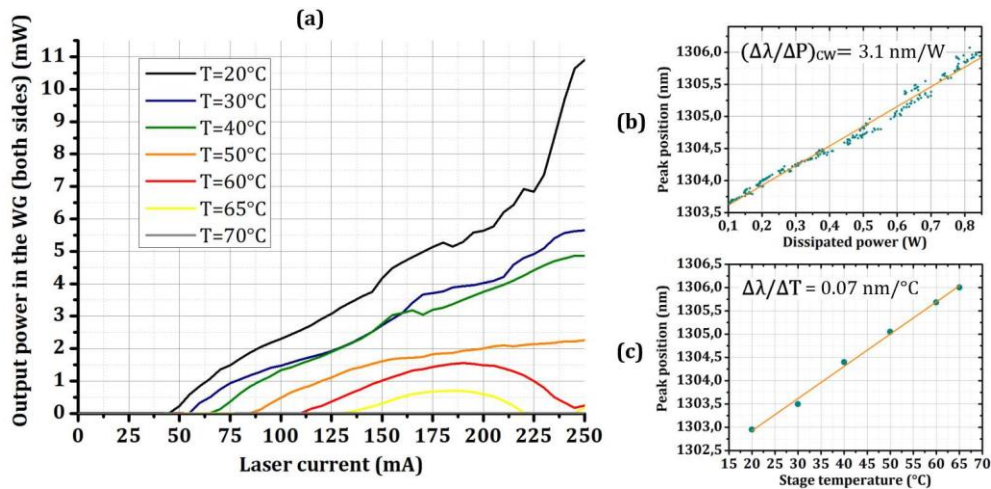


Figure 3-32: (a) Laser 2's output power depending on the current with increasing temperatures. Laser peak wavelength as a function of the dissipated power (CW) (b) as well as of the stage temperature in pulsed regime (c).



### ***Conclusion to the laterally coupled DFB lasers measurements***

Confronting these results with those required, the static measurements are very well suited: the power in the waveguide is higher than a few milliwatts, and the SMSR higher than 30 dB. The temperature performance is improved compared to the vertically coupled DFB lasers, although not reaching yet what is required (lasing effect until 80 °C). This is probably due to the better III-V epitaxy quality. The differences in output power from one laser to the other can be explained mostly by the grating design changes: the narrower the teeth of the device (which is the case for DFB laser 3 for instance), the better the confinement in the III-V and the higher the gain. A trade-off must be found between this and having an appropriate grating coupling constant.

No dynamic response was measured, but since no changes on the pads designs were implemented, the RF performance of the devices shall be equivalent. However, one can predict that the direct modulation of laser 3, although possible, may be a little bit trickier due to the bump on the P-I curve.

Again, only three different wavelengths out of the four required were reached. The fact that the maximum gain of the III-V is higher than expected can explain this but it may also be due to the fact that the gain FWHM (see 2.3.2) is too small to cover four peaks.

The results reached for such lasers are thus very promising since the lasers presented here show performance that were not reached yet for this type of DFB laser. Furthermore, it is very encouraging for it proves that in spite of the high dimension deviations on this wafer (higher SiO<sub>2</sub> gap than expected, lower contrast between the wide and narrow parts of the grating...), the devices still presented interesting characteristics meaning that the designs are quite robust. As alluded to at the beginning of the paragraph, although the e-beam photolithography enabled to obtain very well defined gratings, the chance to get another defect than the QWsh is higher. To improve the wafer yield, a solution may be to use optical proximity corrections (OPC) which takes into account the photolithography-induced distortions.

## **3.3. Conclusion to chapter 3**

In this chapter, the design and characterization of three types of single-mode laser were detailed: DBR laser, vertically coupled DFB lasers and laterally coupled DFB lasers. In each case, the mirrors designs were analyzed and different possibilities were chosen to validate the computations.

Due to process delays, only few DBR lasers could be measured and but their performance turned out to be lower than expected because of the SiO<sub>2</sub> thickness. This proves that in a III-V on silicon DBR laser, this parameter is essential to the proper operation of the device. However, the measured SMSR values (> 35 dB) validate the DBR mirrors designs and gives hopes that with a proper gap thickness, the lasers performances shall greatly increase.

As for vertically coupled DFB lasers, the results are very promising: lasers with more than 22 mW of output power and 55 dB of SMSR were demonstrated as well as the possibility to directly modulate the laser. The gap thickness was closer to the value needed. This parameter is not as important as in the case of DBR lasers since in a DFB, light only goes through the tapers once at each laser output: damaging the taper efficiency will not induce as much losses in a DFB cavity that in a DBR one. However, the grating coupling constant of the DBR laser is impacted by the gap thickness. The lasers characterizations proved that for too low grating coupling constants ( $<10 \text{ cm}^{-1}$ ), the power is impacted while for too high ones ( $>150 \text{ cm}^{-1}$ ), no power at all could be extracted from the 500- $\mu\text{m}$ -long cavity.

The horizontally coupled DFB lasers are very encouraging as well with equivalent power in the waveguide and SMSR higher than 45 dB. The fact that this kind of DFB laser only requires three photolithography steps instead of four is a real advantage compared to the DFB laser with the grating etched on top. However, the rib level had to be process with an e-beam photolithography and this is not only time consuming but also engendered in our case some unwanted defects within the gratings. This DFB laser design would be the best one if a solution could be found to process the rib level using a DUV photolithography.

The main point to improve with those lasers are the temperature behaviour: on the best wafers, laser effect up to 65 °C was shown but this is not enough compare to the 80 °C needed. On the next designs, more efforts should be made on improving this characteristic either by finding a way to drain away the heat or by using quantum dash or quantum dots instead of QWs.

In the next chapter, the possibility to tune the laser so as to choose precisely its wavelength is tackled. Another kind of single-mode, highly tunable laser is presented and characterized.

---

## Chapter 4. Tunable III-V on Si lasers

---

4.1.	Tuning material.....	80
4.1.1.	Thermo-optic effect.....	80
4.1.2.	Heater fabrication .....	81
4.1.3.	Heater measurements .....	81
4.1.4.	Hybrid tunable lasers state of the art.....	83
4.2.	Tunability efficiency of DBR lasers.....	83
4.3.	Sampled-grating DBR laser as a high precision tunable device .....	85
4.3.1.	SGDBR theory and state of the art .....	85
4.3.2.	SGDBR mirrors design.....	89
4.3.3.	SGDBR lasers characterization .....	94
4.4.	Conclusion to chapter 4.....	98

In the previous chapter, it was seen that it is very hard to predict the laser wavelength with accuracy. It is thus very convenient to be able to control the wavelength of the laser post-fabrication. This chapter deals with tunable devices based on gratings: a first paragraph gives details on the thermo-optic effect, which is the phenomenon used here to tune the lasers, and finishes with the heater process fabrication and measured characteristics. Then, the results reached when tuning the DBR lasers fabricated in this work are presented. Eventually, the design of an unusual, highly tunable device is detailed: the sampled grating DBR (SGDBR) laser. The principles of the mirrors constituting the laser are given as well as the dimensioning associated and the computations are in good agreement with the mirror characterization. The lasers obtained are very promising since a continuous tuning over a 27 nm range is reached at 1.31  $\mu\text{m}$ .

## 4.1. Tuning material

### 4.1.1. Thermo-optic effect

Laser tuning is well-known regarding semiconductor laser, and is implemented by changing the effective index of the optical mode in the mirror, thus shifting its modal response. Thanks to the Bragg relation, the index change is linked to the wavelength shift as follows:

$$\frac{\Delta\lambda_{\text{Bragg}}}{\lambda_{\text{Bragg}}} = \frac{\Delta n_{\text{eff,avg}}}{n_{\text{eff,avg}}} \quad [4.1]$$

At  $\lambda_{\text{Bragg}} = 1.31 \mu\text{m}$ , and to reach  $\Delta\lambda_{\text{Bragg}} = 10 \text{ nm}$ , the effective index change should be  $\Delta n_{\text{eff,avg}} = 0.0255$  for the mirrors designed here (DBR as well as SGDBR). Two main solutions exist to change the effective index: carriers' injection or depletion and temperature variations. The changes in carriers' concentration in III-V bulk lasers are enabled by a PIN junction formed on top of the mirrors, to which a forward or reversed bias is applied. In our case, the mirrors are built in the silicon and it is more convenient to use the thermo-optic effect: a temperature change in the material induces an index change. This solution also has the advantage to create fewer defects. However, this approach is not appropriate in III-V bulk lasers since it would heat the gain region as well, thus damaging the laser properties. In [102], it is shown that the effective index change with temperature at  $1.31 \mu\text{m}$  is :  $\partial n_{\text{eff,avg}}/\partial T \sim 0.0002 \text{ K}^{-1}$  for Si rib waveguides with  $W_{\text{rib}} > 1000 \text{ nm}$ , as it is the case here. Eventually, to reach  $\Delta\lambda_{\text{Bragg}} = 10 \text{ nm}$  from  $1.31 \mu\text{m}$ , a temperature difference of  $127.5 \text{ }^\circ\text{C}$  is needed.

In this work, the mirrors temperature is increased (which is easier and less energy consuming than decreasing it) thanks to a heater (HT) on top of them, which solely consists of a metallic strip as represented on Figure 4-1 (a). A current transiting through the metal induces temperature changes due to Joule effect:

$$P_{\text{dissipated}} = R_{\text{HT}} I_{\text{HT}}^2 = U_{\text{HT}}^2 / R_{\text{HT}} \quad [4.2]$$

Where  $P_{\text{dissipated}}$  is the power dissipated by the heater and  $R_{\text{HT}}$ ,  $I_{\text{HT}}$  and  $U_{\text{HT}}$  are the heater resistance, current and voltage respectively. Explanations will be given below on how to deduce experimentally the temperature difference induced by the heater.

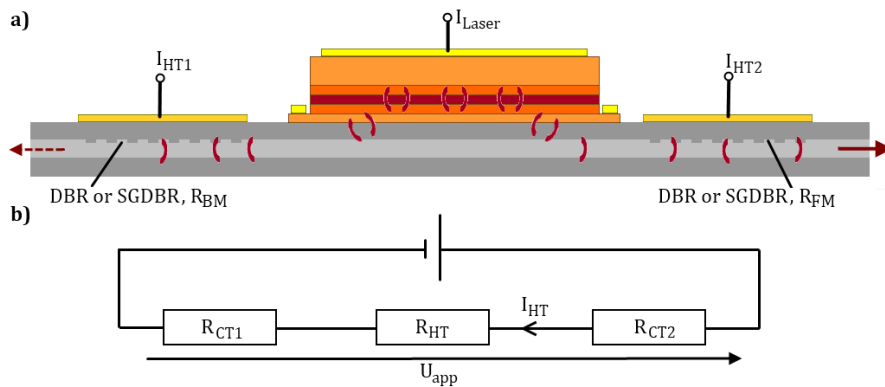


**Figure 4-1: a) Schematic view of a SGDBR or DBR laser with a heater on top of each mirror. b) Electrical representation of one heater:  $R_{\text{CT1}}$  and  $R_{\text{CT2}}$  stand for the resistances of each contact and  $U_{\text{app}}$  is the applied voltage.**

An electrical representation of the heater is displayed on Figure 4-1 (b) including the resistance of the contacts. This show that the heater needs to have an appropriate resistance: if smaller than the contact resistance, the power dissipation occurs within the contacts instead of the heater. It is thus convenient to

get  $R_{CT1}$  and  $R_{CT2} \ll R_{HT}$  so that  $U_{HT} \sim U_{app}$ . On the other hand, if  $R_{HT}$  is too high the current injected is too low and no power is dissipated at all. This trade-off necessitates a heater resistance within the  $[100; 400] \Omega$  range.

#### 4.1.2. Heater fabrication

After all the steps implemented to process the DBR or SGDBR lasers, those were tested to check their proper functioning. It is only afterward that the heaters were deposited, following the process flow detailed on Figure 4-2. The heater is deposited on the SiN encapsulation layer, directly above the mirrors. It consists of a 250 nm thick NiFe layer: less had been deposited in a first time (150 nm) but the resistance was almost  $500 \Omega$  which is too high to reach an efficient mirror heating. After building the heater, the pads are deposited using a lift-off method (see 2.3.4). A last optional step consists in etching air trenches on the sides of the silicon waveguide. Those serve to isolate the mirror region to concentrate the temperature increase on the mirror only thus ensuring a more efficient heating. The top microscope view of a heater built above a SGDBR mirror is illustrated on Figure 4-3 with part of its associated laser.

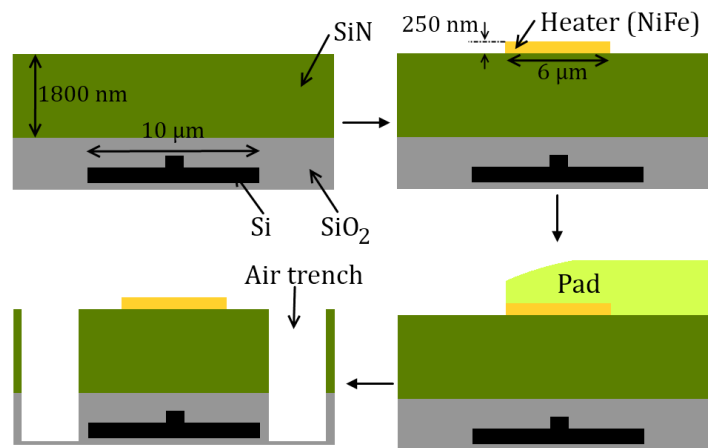


Figure 4-2: Process flow implemented for the heater.

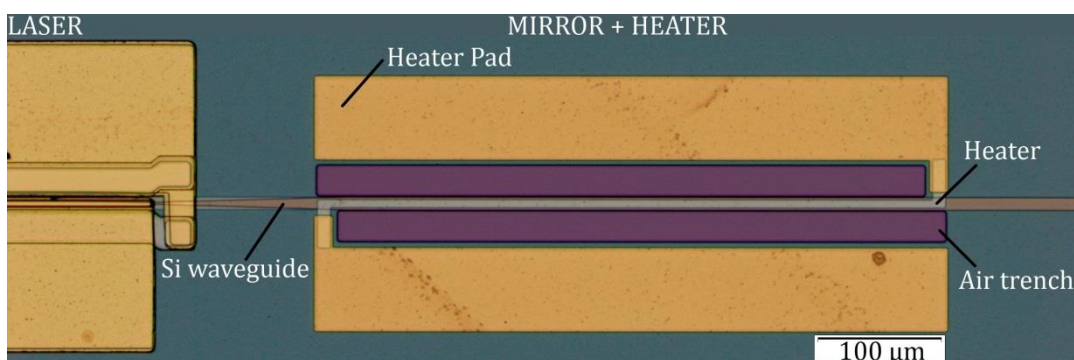


Figure 4-3: Heater picture of a SGDBR laser taken with an optical microscope.

#### 4.1.3. Heater measurements

The heaters processed were characterized to evaluate the tuning performances that the lasers could reach. Firstly, moving the tips at different positions on the heater pads did not induce any change on the measured resistance showing that the contact resistance is insignificant compared to the heater resistance

and that the heating happens mostly along the heater. Then, to be able to relate the heater resistance change to a temperature change, the temperature coefficient resistance (TCR) of the heater had to be determined. It is defined as the relative resistance change ( $dR_{HT}$ ) associated with the temperature change ( $dT$ ):

$$\frac{dR_{HT}}{R_{HT}} = \alpha dT \quad [4.3]$$

Where  $\alpha$  is the TCR. Assuming that  $\alpha$  does not change with the temperature change, equation [4.3] leads to:

$$R(T) = R(T_0)(1 + \alpha dT) \quad [4.4]$$

With  $T_0$  a temperature reference. The TCR of the heater was evaluated measuring the resistance of different heater at a low current (10 mA) while increasing the chuck temperature. The current is low enough to assume that the heater temperature is set to the chuck temperature and is not subject to self-heating. The results are presented on Figure 4-4 (a) for temperatures going up to 175 °C. The TCR deduced from those curves is  $\alpha_{HT} = 3 \text{ mK}^{-1}$ .

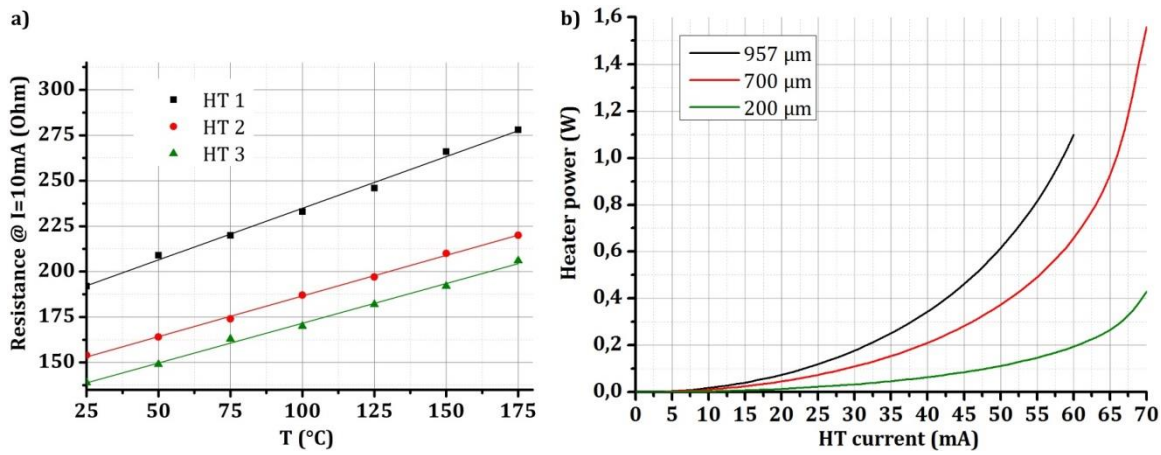


Figure 4-4: a) Heater resistance depending on the chuck temperature for three different devices. b) Heater power as a function of its injected current for three different heater lengths.

Three heaters with different lengths (200 μm, 700 μm and 957 μm) were then studied and the heaters resistance, temperature difference and power dissipated are represented as a function of the heater current on Figure 4-5 (a) and (b) and Figure 4-4 (b) respectively. The temperature change induced by the current going through the heater was deduced from Figure 4-5 (a) by using equation [4.3] with  $\alpha_{HT} = 3 \text{ mK}^{-1}$ . As it could be expected, the longer the heater, the higher the resistance and the higher the power needed to reach the same temperature change. To tune a mirror so that  $\Delta\lambda_{\text{Bragg}} = 10 \text{ nm}$  (as discussed in 4.1.1) the electrical power needed shall be 0.66 W, 0.44 W and 0.15 W for the 957, 700 and 200-μm-long heaters respectively.

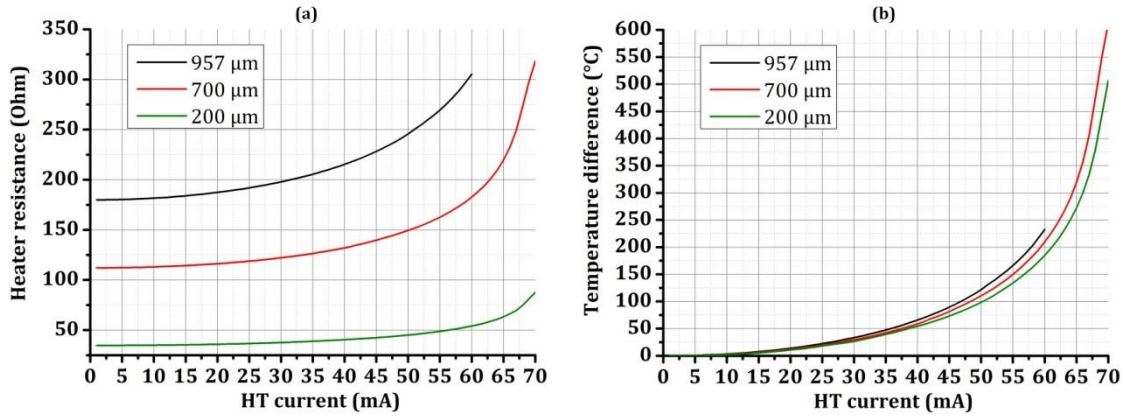


Figure 4-5: Heater resistance (a) and temperature difference (b) depending on its current for three different heater lengths (957  $\mu\text{m}$ , 700  $\mu\text{m}$  and 200  $\mu\text{m}$ ).

#### 4.1.4. Hybrid tunable lasers state of the art

The demand for tunable laser started in telecommunication with the need for lasers with precise wavelengths to enable multiplexing. For this reason, tunable lasers demonstrated up to now are mostly at 1.55  $\mu\text{m}$ . The demand for tunable laser for a use in datacommunication is only rising now and those demonstrated in this work are the first tunable lasers at 1.31  $\mu\text{m}$  to our knowledge. The state of the art of III-V on silicon tunable lasers is presented in Table 4-1. Although highly tunable, the SGDBR lasers are not included in the table since they will be detailed later (see 4.3.1). All the lasers presented in the table below are tuned thanks to a heater on the grating or the ring that enables the wavelength filtering. In a cavity consisting of a ring on each side of the gain region (referred to as 'double-ring cavity'), the Vernier effect allows a quasi-continuous tuning over a 40 nm range with high side mode suppression ratio. The drawback of such a cavity is that the rings are very much more sensitive to process variations than gratings.

In this work, the aim was to find a way to tune the lasers wavelength precisely and on a wide range using grating-based lasers. The results reached when tuning DBR lasers are presented below. Since it does not allow a precise wavelength filtering, the development of less common lasers, based on particular DBR called 'sample-grated DBR', and which uses the Vernier effect, was implemented.

Table 4-1: III-V on Si laser state on the art (except for SGDBR lasers).

$\lambda$ ( $\mu\text{m}$ )	Cavity type	Tunability range	Continuous?	SMSR (dB)	Year	Ref.
1.55	$\mu$ -disk	2 nm	quasi	?	2010	IMEC [103]
	DBR + ring filter	8 nm	no	> 40	2013	IMEC, III-V Lab [57]
	2 DBR + MMI	~20 nm	quasi	>40	2013	Skorpios [63]
	DBR	21 nm	no	>35	2012	CEA Leti [104]
	Double ring	40 nm	quasi	>35	2013	UCSB [105]
	Double ring	45 nm	quasi	>40	2012	III-V Lab [106]

## 4.2. Tunability efficiency of DBR lasers

Heaters were built above the mirrors of the DBR lasers presented in 3.1.3. The front heater is thus 200  $\mu\text{m}$  long and the back heater 700  $\mu\text{m}$  long. The effect induced by the heating is displayed on Figure 4-6. Around the selected peak, the front and back mirrors signatures can clearly be differentiated. For a given



front heater current, the back heater current is increased thus shifting the back mirror signature to higher wavelengths and selecting another peak. These spectra show that to tune the laser, both mirrors need to be heated for if the temperature difference between each mirror is too high, their responses would be too far apart to get any peak alignment.

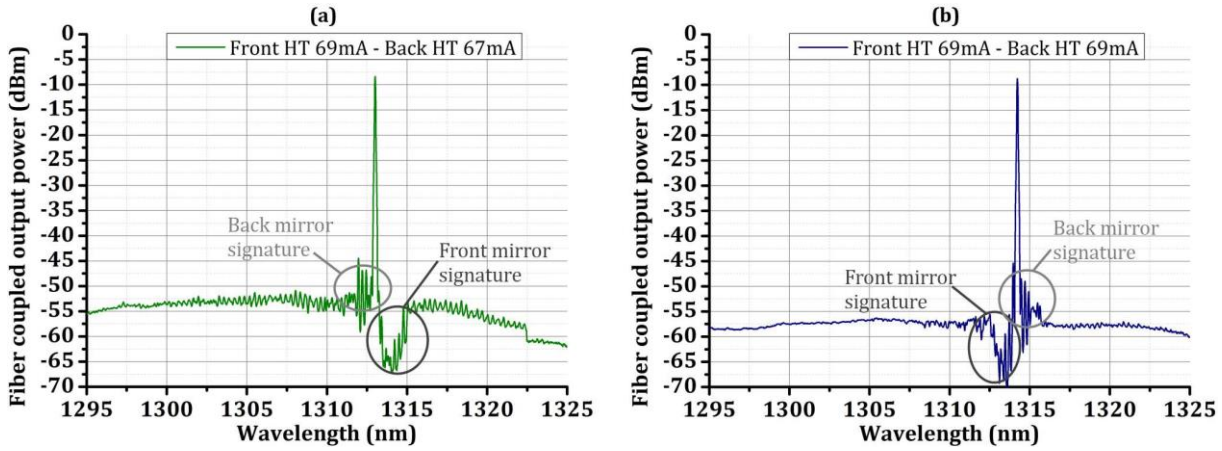


Figure 4-6: Spectra for two different injection current for the back mirror heater with a 69 mA current for the front mirror heater of DBR 3.

Consequently, DBR 3 from paragraph 3.1.3 was tuned by heating carefully both its mirrors. Spectra from Figure 4-7 shows that tunability on a 13.8 nm range was reached for a front and back mirror dissipated powers higher than 0.45 W and 1.60 W. This tunability range could be increased by thickening the heaters layer to decrease their resistance and thus be able to supply more current to the heater. This way, only the QWs gain range would limit the tuning. Due to delay related to technological issues, this experiment was conducted at the very end of this work and there was no time to implement it by increasing the current with more precise steps than the mA. Doing so would enable to get curves with the same shift between the peak wavelengths of each spectrum contrary to what is displayed here. However, the tuning here cannot be regarded as continuous: as the mirrors are heated, the peak 'jumps' to the next DBR mode. The separation between these modes is measured to be between 0.25 and 0.30 nm. Furthermore it is hard to control this jump with accuracy.

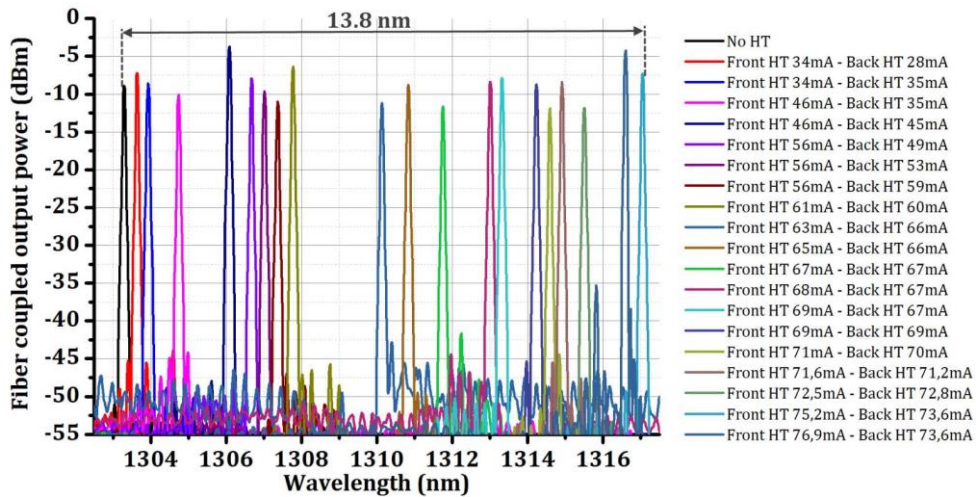


Figure 4-7: Example of the tunability range of one of the DBR lasers presented in 3.1.3 (DBR 3).

Eventually, using DBR lasers as tunable devices seems a good opportunity to reach accurate wavelengths. However, the facts that they are not continuously tunable and that the jumps from one mode to another are not so well controlled are major drawbacks. Moreover, the power needed to get this tunability range is



quite high. Because of all those reasons, a large part of this work was focused on the design of a highly and continuously tunable laser which is detailed in the following paragraph.

### 4.3. Sampled-grating DBR laser as a high precision tunable device

The first sampled-grating DBR (SGDBR) lasers were demonstrated by L. A. Coldren in 1989 with III-V materials. Figure 4-8 shows a schematic view of a hybrid III-V on silicon SGDBR laser: as for the DBR laser, the gain region is surrounded by two mirrors. The only difference is that, for each mirror, parts of the grating are periodically removed. This paragraph first explains the physics and use of such a device. Then, the design implemented during this thesis is detailed and eventually the results obtained are presented.

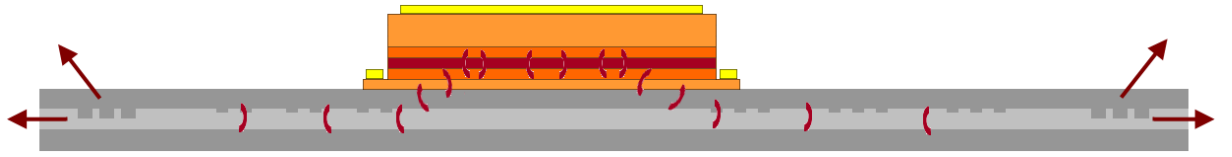


Figure 4-8: Schematic view of a III-V on Si SGDBR laser.

#### 4.3.1. SGDBR theory and state of the art

##### *Definition of a SGDBR mirror*

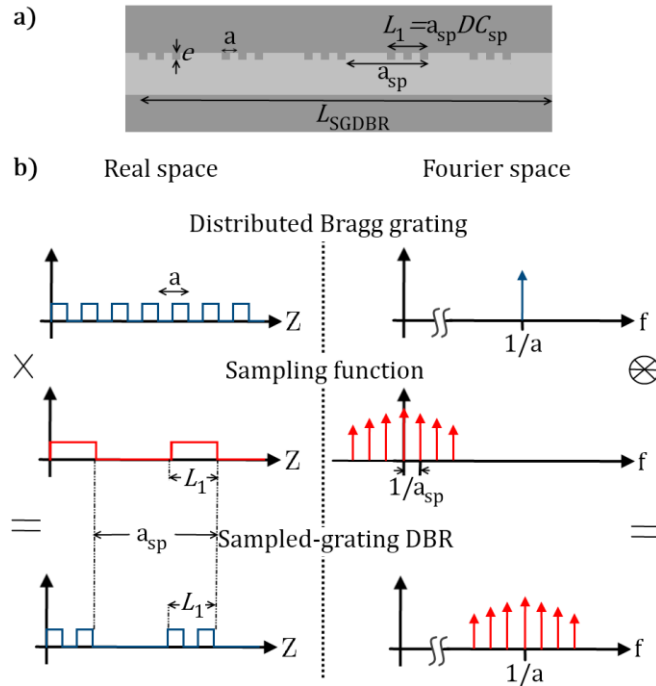


Figure 4-9: (a) Side schematic view of a SGDBR. (b) Real and Fourier space representations of such a grating.

A schematic view of the sampled-grating mirror is represented on Figure 4-9 with its real and Fourier space representation. Two periods coexist: the grating period ( $a$ ) imposes the central wavelength of the mirror reflectivity response. To this small period, a wider one is superimposed, called sampling period

( $a_{sp}$ ), and it is associated to a periodical removal of part of the grating. As represented on Figure 4-9 (b), the Fourier representation of such a system is a comb centered on  $1/a$  where the spacing between each peak is  $1/a_{sp}$ . The response of a SGDBR mirror is thus a comb-like curve centered on the Bragg wavelength with periodic maxima separated by a FSR  $\Delta\lambda_{SGDBR}$  [107]:

$$\Delta\lambda_{SGDBR} = \frac{\lambda^2}{2n_{g,avg}a_{sp}} \quad [4.5]$$

$n_{g,avg}$  is the average group index and  $\lambda$  the wavelength in the mirror. The example of a SGDBR mirror response is displayed on Figure 4-10 where the mirror maximum reflectivity ( $R_{max,SGDBR}$ ) is represented as well as the FWHM of one peak. The tuning range ( $\Delta\lambda_{tuning}$ ) is defined arbitrarily as the range on which the reflectivity of the peaks stays higher than 75% of the maximum reflectivity. The graph also shows the peak orders around the central wavelength which stands for the order 0.

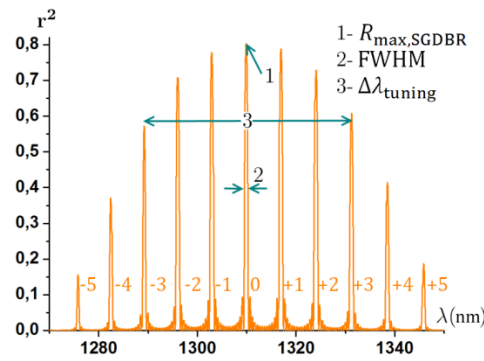


Figure 4-10: Example of the response of a SGDBR mirror.

As for the mirror maximum reflectivity and its effective length  $L_{eff,SGDBR}$ , an analogy with DBR mirrors gives:

$$R_{max,SGDBR} = \tanh(\kappa_0 L_{SGDBR}) \quad [4.6]$$

$$L_{eff,SGDBR,n} = \frac{1}{2|\kappa_n|} \tanh(|\kappa_n| L_{SGDBR}) \quad [4.7]$$

Where  $\kappa_n$  is the grating coupling constant which depends on the order of the reflection peak of the comb ( $n$ ), hence a dependency of the effective length on the peak order.  $\kappa_0$  is the grating coupling constant at order 0, namely for the middle peak.  $\kappa_n$  is defined by [107]:

$$\kappa_n = \kappa_g \frac{L_1}{a_{sp}} \frac{\sin(\pi n L_1 / a_{sp})}{\pi n L_1 / a_{sp}} e^{-i\pi n L_1 / a_{sp}} = \kappa_g DC_{sp} \frac{\sin(\pi n DC_{sp})}{\pi n DC_{sp}} e^{-i\pi n DC_{sp}} \quad [4.8]$$

$\kappa_g$  is the coupling constant of the unsampled grating, defined in 3.3.1.  $L_1/a_{sp}$  is nothing else but the filling factor of the sampled grating ( $DC_{sp}$ ) as displayed on Figure 4-9. It will be seen below that this parameter has a huge influence on the SGDBR design.

***SGDBR laser: the Vernier effect***

From what was explained above, it can be deduced that in a SGDBR laser, if both mirrors are built with a different sampling period, each of them will have a different spacing between the peaks of the spectral response. With a proper mirror design, a peak alignment between the two mirrors shall only happen for one specific wavelength. This phenomenon is called the Vernier effect and it is illustrated on Figure 4-11 where the responses of two SGDBR mirrors were computed using the transfer matrix method. Both of them are alike except for their sampling periods which are a little bit dissimilar to get a 1 nm FSR difference. On the figure, the product of the two responses proves that the peak coincidence only happens for one wavelength (1312 nm).

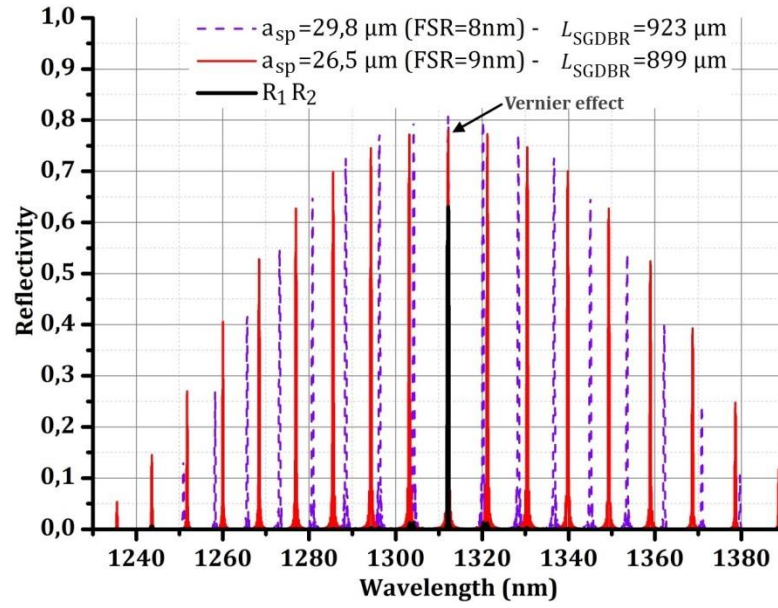


**Figure 4-11:** Spectral response of two SGDBR mirrors with different sampling periods. For both mirrors,  $a=196$  nm,  $e=20$  nm,  $DC_{sp} = 0.1$  and  $R_{max,SGDBR} = 0.8$ .

As with the DBR lasers, it is possible to tune the device changing the effective index of either one mirror only or both of them. In the latter case, a continuous tuning is possible. The former solution offers rather a mode-hop tuning on a wider wavelength range. Moreover, this choice allows a tuning toward either higher or lower wavelengths which is not possible with DBR lasers which only offer the possibility to tune toward higher wavelengths. Let us take the example of a laser with the cavity consisting of the two mirrors from Figure 4-11. Heating the 1<sup>st</sup> mirror (dashed purple line) shifts its response toward the higher wavelengths: the peak at 1321 nm is thus selected. On the other hand, when heating the 2<sup>nd</sup> mirror (solid red line) instead, its response is also red-shifted which induces a selection of the peak at 1304 nm. This possibility to tune toward both higher and lower wavelengths is one of the advantages of this device.

It is important to notice that the Vernier effect happens periodically and the separation between two wavelength matchings ( $\Delta\lambda_{align}$ ) is calculated as:

$$\Delta\lambda_{align} = \frac{\Delta\lambda_{SGDBR,1} \Delta\lambda_{SGDBR,2}}{|\Delta\lambda_{SGDBR,1} - \Delta\lambda_{SGDBR,2}|} \quad [4.9]$$

On Figure 4-11, those second order alignments can be seen at the edges of the spectra: one at 1243 nm and another one at 1388 nm. In this example, they are too weak to compete with the selected wavelength

because the FSR of each mirror is high enough so that the repetition occurs for low reflectivity wavelengths: here,  $\Delta\lambda_{\text{align}} = 72$  nm. For lower FSR values or higher difference between the FSR, the 2<sup>nd</sup> wavelength matching can be very important if the mirror reflectivity is high at this wavelength occurrence. Such a case is represented on Figure 4-12: the FSR of each mirror are respectively  $\Delta\lambda_{\text{SGDBR},1} = 6$  nm and  $\Delta\lambda_{\text{SGDBR},2} = 8$  nm which gives  $\Delta\lambda_{\text{align}} = 24$  nm. Three peaks are then in competition on the  $R_1 R_2$  curve: such a scheme is to be avoided to get single mode SGDBR lasers. The solution when dealing with mirrors with small FSR values is to build them to have their reflectivities very low for the 2<sup>nd</sup> wavelength coincidence. The drawback then is that the tuning range is limited.

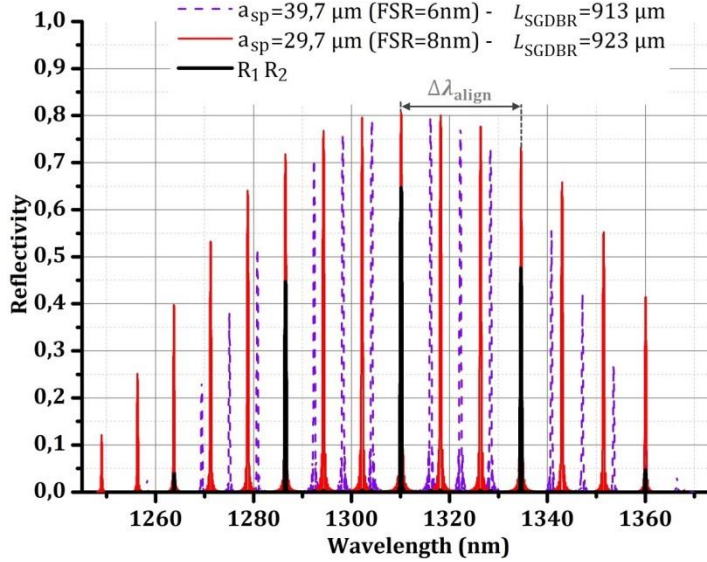


Figure 4-12: Spectral response of two SGDBR mirrors with different sampling periods. For both mirrors,  $a=196$  nm,  $e=20$  nm,  $DC_{\text{sp}} = 0.1$  and  $R_{\text{max,SGDBR}}=0.8$ .

### SGDBR lasers state of the art

As precised earlier, the first SGDBR laser was demonstrated by Larry A. Coldren and his team. This group also made further developments of those devices in III-V bulk first [108]–[110] and using hybrid III-V on Si technology later [111], [112]. Their characteristics are summed up on Table 4-2. Some of the lasers use quantum well intermixing (QWI) which is a technic that locally shifts the bandgap energy of the material [113]. It is used when the whole laser consist of III-V material to render its mirror and phase sections non absorbing while the gain region bandgap stays as grown. The hybrid III-V on Si SGDBR lasers presented here also have their mirror and phase regions in the III-V and light is only coupled to the Si waveguide at the output of the laser hence a need for QWI which would be unnecessary for lasers with their mirrors in the Si. The index change enabling the tuning for those five devices is made by carrier injection because heaters would also heat the gain region and damage its lasing properties. Since 2008, a proceeding was published with computations regarding a III-V on silicon SGDBR laser with mirrors in the silicon waveguide [114] but no experimental results followed. To our knowledge, no results were found for III-V on Si SGDBR lasers at 1310 nm.

**Table 4-2: State of the art of SGDBR lasers. SOA = semiconductor optical amplifier**

Laser specificities	Performances	Other characteristics	Year	Ref.
III-V bulk $\lambda = 1507$ nm	$\Delta\lambda_{\text{range}} = 35$ nm $\text{SMSR} \geq 30$ dB	$P_{\text{max}} = 4$ mW $I_{\text{th}} = 25$ mA	1993	[108]
III-V bulk Integrated with a SOA $\lambda = 1550$ nm	$\Delta\lambda_{\text{range}} = 54$ nm $\text{SMSR} \geq 35$ dB	$P_{\text{max}} = 2$ mW $I_{\text{th}} = 20$ mA	2000	[109]
III-V bulk QW intermixing (QWI) $\lambda = 1550$ nm	$\Delta\lambda_{\text{range}} = 40$ nm $\text{SMSR} \geq 35$ dB	$P_{\text{max}} = 10$ mW $I_{\text{th}} = 15$ mA	2002	[110]
III-V on Si QWI $\lambda = 1506.5$ nm	$\Delta\lambda_{\text{range}} = 13$ nm $\text{SMSR} \geq 35$ dB	$P_{\text{max}} = 1$ mW $I_{\text{th}} = 60$ mA	2008	[111]
III-V on Si QWI + Integrated with an EAM $\lambda = 1518$ nm	$\Delta\lambda_{\text{range}} = 42$ nm	$P_{\text{max}} = 0.5$ mW $I_{\text{th}} = 50$ mA	2008	[112]

#### 4.3.2. SGDBR mirrors design

As in the case of DBR lasers, the different parameters to choose when designing the SGDBR mirrors are the period ( $a$ ), the duty cycle (DC), the total length ( $L_{\text{SGDBR}}$ ) and the grating etching depth ( $e$ ). Two others are to be taken into account: the sampling period ( $a_{\text{sp}}$ ) and the filling factor of the sampling period ( $DC_{\text{sp}}$ ). Since the grating coupling constant ( $\kappa_g$ ) is still calculated the same way, the effect of the duty cycle on the mirror response should be the same and according to what was established in 3.1.2, DC was set to 0.5. This paragraph details how the other parameters were selected, with a first overall approach to understand their effects on the mirror response, and then a more precise study will be given for some of the mirrors designed in this work.

##### *Overall approach*

To begin with the SGDBR mirror study, its response was computed using transfer matrices. The influence of the etching depth, the sampling period duty cycle and the total mirror length were evaluated altogether. Figure 4-13 (a) and (b) shows the grating maximum reflectivity depending on  $e$  and  $DC_{\text{sp}}$  for different grating lengths' and  $R_{\text{max,SGDBR}}$  is plotted as a function of  $L_{\text{SGDBR}}$  for different ( $e$ ,  $DC_{\text{sp}}$ ) pairs. As it could be expected from the study of the DFB and DBR gratings, the higher  $e$ ,  $DC_{\text{sp}}$  or  $L_{\text{SGDBR}}$ , the higher  $R_{\text{max,SGDBR}}$ . It is also important to check on the FWHM of the peaks: if this FWHM is too high, there may be an overlap between two peaks from each mirror even though they are not aligned. The effects of the same parameters on the FWHM are displayed on Figure 4-14 (a) and (b). The deeper  $e$ , the higher  $DC_{\text{sp}}$ , of the lower  $L_{\text{SGDBR}}$ , the higher the FWHM of the peaks.

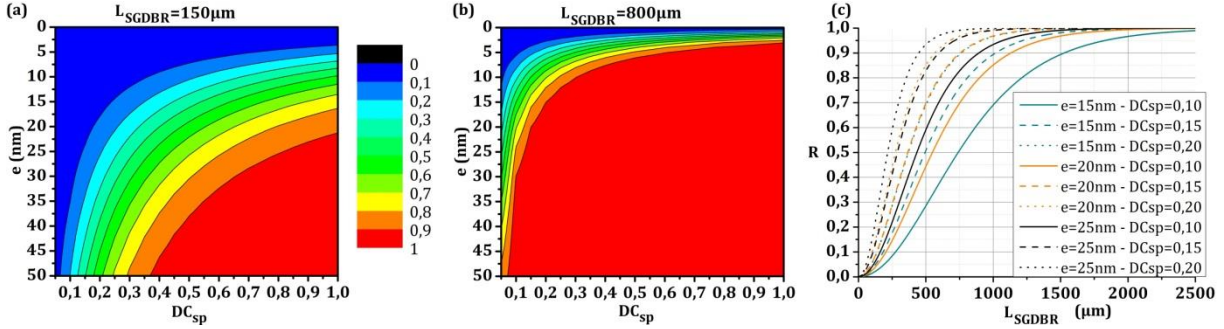


**Figure 4-13: Maximum reflectivity of a SGDBR mirror depending on  $DC_{sp}$  and  $e$  for  $L_{SGDBR}=150 \mu m$  (a) and  $L_{SGDBR}=800 \mu m$ . This reflectivity is plotted on (c) as a function of  $L_{SGDBR}$  for some specific  $(e; DC_{sp})$  couples. The period of the grating is  $a = 196$  nm and its sampling period  $a_{sp} = 39.7 \mu m$ .**

To ensure a FWHM lower than 1 nm allowing at the same time reasonable reflectivities ( $>0.4$ ), the etching depth was set in the [15; 25] nm range and the sampling period duty cycle was chosen between 0.10 and 0.20. The total mirror length needs to be adapted to each case depending on the reflectivity targeted for the mirrors.

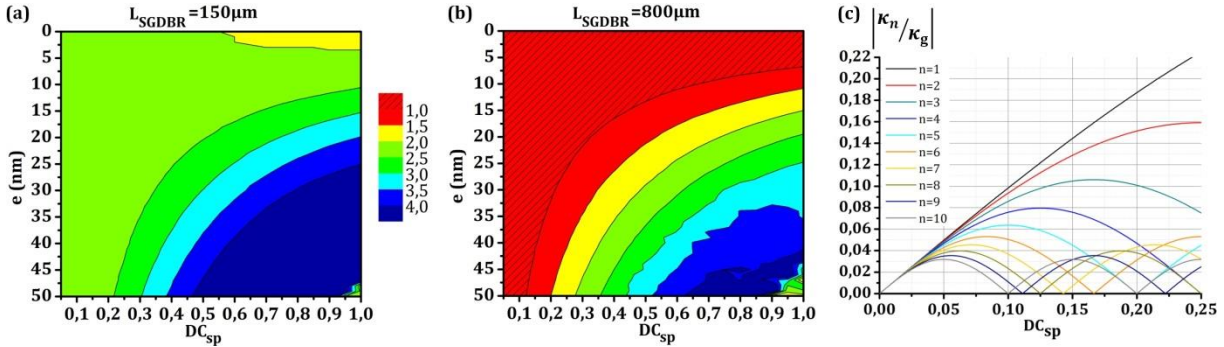


**Figure 4-14: FWHM of the peaks in the SGDBR comb-like response depending on  $DC_{sp}$  and  $e$  for  $L_{SGDBR}=150 \mu m$  (a) and  $L_{SGDBR}=800 \mu m$  (b) for a grating period  $a = 196$  nm and a sampling period  $a_{sp} = 39.7 \mu m$ . The ratio  $|\kappa_n/\kappa_g|$  is plotted on (c) as a function of  $DC_{sp}$ .**

Another major characteristic of the SGDBR mirror is the range over which it can be tuned ( $\Delta\lambda_{tuning}$ ). To be more interesting than a DBR mirror, it shall be higher than 20 nm. It was seen (see 4.3.1) that the tuning is necessarily limited by the periodicity of the alignment phenomenon between the combs:  $\Delta\lambda_{tuning} \leq \Delta\lambda_{align}$  otherwise the laser single-modicity is jeopardized. To maximize the tuning range, the first thing to do is to maximize  $\Delta\lambda_{align}$  which is possible choosing very low FSR differences ( $\Delta FSR$ ) between the two SGDBR mirrors. However, when too low, this FSR difference may induce an overlap of the non-coincident peaks. It was chosen here to work with  $\Delta FSR \in [0.5; 2]$  nm. The FSR themselves also need to be high enough (and thus the sampling periods low enough) and the sampling periods were always selected to reach an FSR above 4 nm. The following explanations will show that another parameters that has much impact on the tuning range is  $DC_{sp}$ .

To delve deeper into the influence of the etching depth and the duty cycle of the sampling period, two examples are considered below. First,  $DC_{sp}$  is set to 0.10 and the responses of two SGDBR mirrors with an FSR of 6 and 6.5 nm respectively are observed on Figure 4-15 for three different etching depths:  $e=15$  nm,  $e=20$  nm, and  $e=25$  nm. The computations are made using transfer matrix method and the mirror lengths are picked so that the maximum reflectivity reaches 0.8. The change in the etching depth does not have any influence on the tuning range since the reflectivity of the higher order peaks stay the same as  $e$



increases. However, the FWHM is a little bit damaged for higher etching depths: the first order peaks overlap more for  $e=25$  nm as it can be seen from the  $R_1 R_2$  curve. To work with reasonable FWHM while limiting the grating length, the etching depth was set to  $e = 20 \text{ nm} \pm 1 \text{ nm}$ , the  $\pm 1 \text{ nm}$  standing for the process variations.

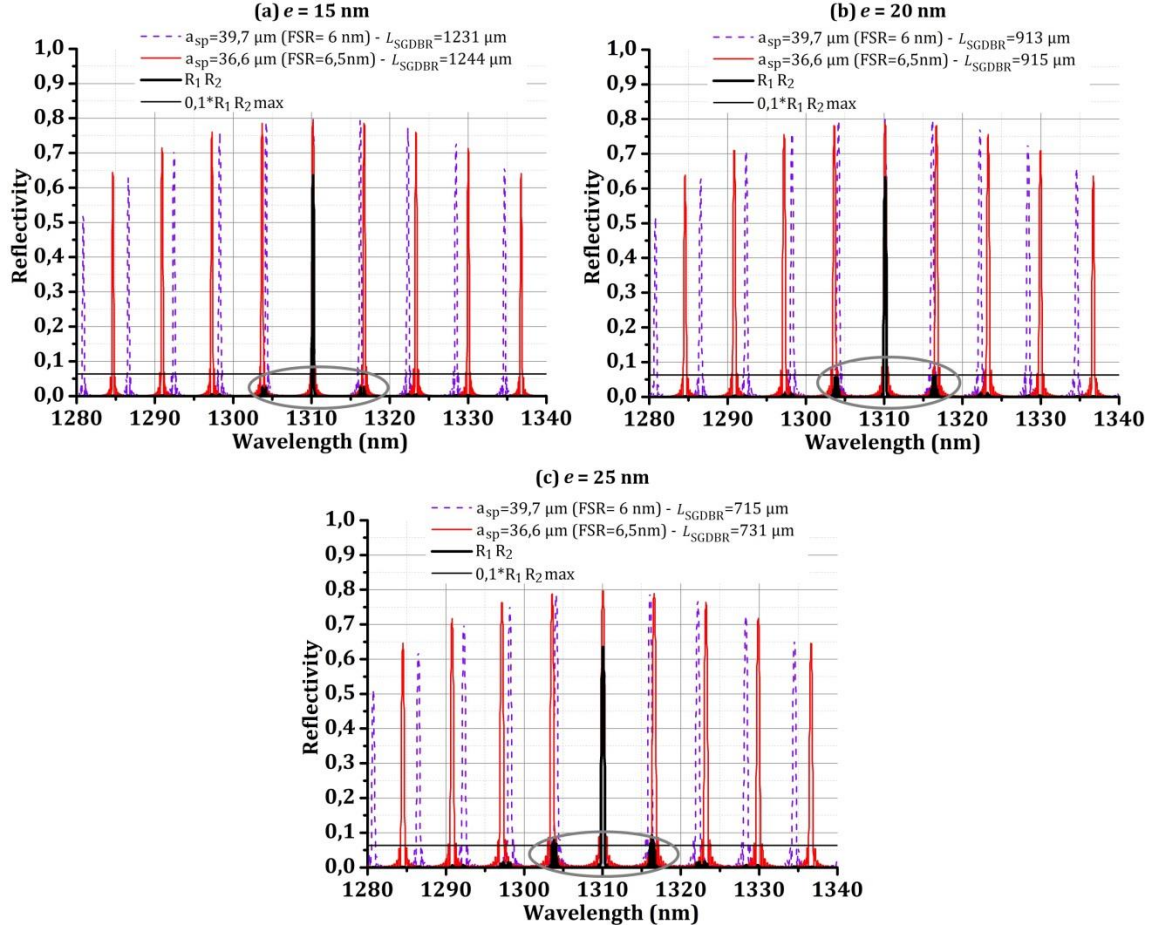


Figure 4-15: Responses of two SGDBR mirrors with different FSR,  $a=196$  nm,  $DC_{sp}=0.10$  and  $R_{max,SGDBR}=0.8$ . For each plot, the etching depth is different: (a)  $e=15$  nm, (b)  $e=20$  nm and (c)  $e=25$  nm.

In the second example, represented on Figure 4-16, the etching depth is set to 20 nm and  $DC_{sp}$  changes. Not only the FWHM is altered (proved by the overlap of the 1<sup>st</sup> order peaks), but also the tuning range is clearly damaged as  $DC_{sp}$  increases. This can be explained by Figure 4-14 (c) where the ratio  $|\kappa_n/\kappa_g|$  is calculated using equation [4.8] until the 10<sup>th</sup> order. Although the three first orders around the central wavelength still have high  $\kappa_n$  values for  $DC_{sp} = 0.20$ , the higher orders (4<sup>th</sup> and 5<sup>th</sup>) start decreasing from  $DC_{sp} = 0.10$  and are very low for  $DC_{sp} = 0.20$ . Thus, in the  $[0.10; 0.20]$  range, the lower  $DC_{sp}$ , the higher the reflectivity of the 5 first peaks around the central wavelength, and thus the higher  $\Delta\lambda_{tuning}$ . This is not true anymore for higher order modes (6 and more) but those are very weakly reflected and have thus less impact on the tuning range. Nevertheless, no ‘proper’  $DC_{sp}$  can be chosen as a value adapted for any design. In this case, 0.15 seem more suited because it offers the best trade-off between a wide tuning range while staying below  $\Delta\lambda_{align}$  (which is not the case for  $DC_{sp} = 0.10$  where the 2<sup>nd</sup> aligned peaks appear at 1269 nm and 1354 nm). But for other FSR or reflectivity values, it may very well be  $DC_{sp} = 0.10$  or  $DC_{sp} = 0.20$  that present the more advantages.

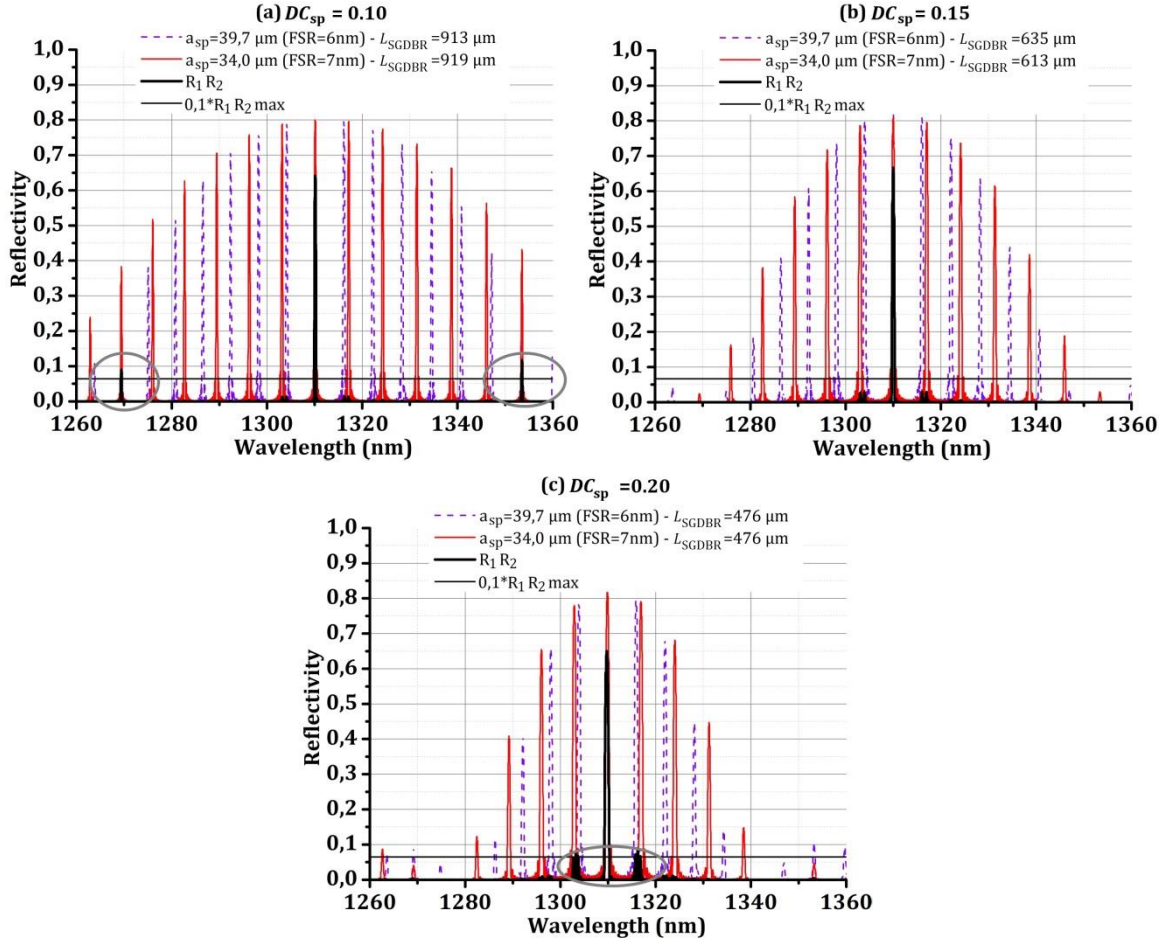


Figure 4-16: Responses of two SGDBR mirrors with different FSR,  $a=196$  nm and  $e=20$  nm and  $R_{\max,SGDBR}=0.8$ . For each plot, the sampling period duty cycle is different: (a)  $DC_{sp}=0.10$ , (b)  $DC_{sp}=0.15$  and (c)  $DC_{sp}=0.20$ .

All the computations above were implemented with a grating period  $a=196$  nm. Figure 4-17 displays the influence of the gratings period on the Vernier selected wavelength in the case of two SGDBR mirrors with respectively 6 and 7 nm of FSR. From this map, it is clear that it is very hard to predict the selected wavelength when the device is not tuned. For a period change of less than a nanometer, the peak position can vary of more than 20 nm. Since the period precision does not go below the nm, it was decided to set the period to  $a=196$  nm for all the mirrors and then change the selected wavelength by tuning the mirrors.

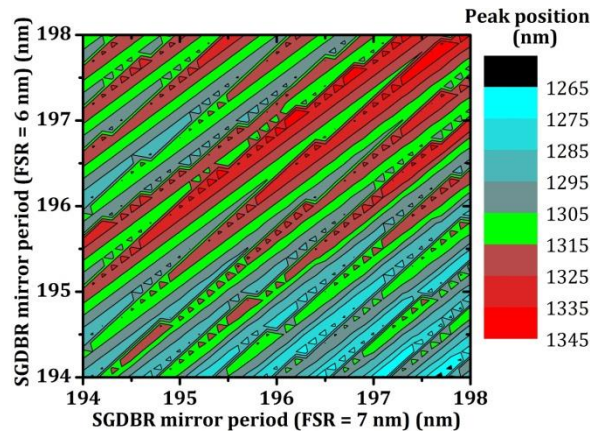


Figure 4-17: Peak selected by Vernier effect as a function of the periods (a) of each SGDBR mirrors. The computations were made using  $e=15$  nm,  $DC_{sp}=0.15$ ,  $a_{sp,1st\ mirror}=39.7 \mu m$ ,  $a_{sp,2nd\ mirror}=34.0 \mu m$ .



To sum up, when designing a SGDBR laser, the sampling period and the grating length have to be chosen depending respectively on the FSR and reflectivity wanted. The etching depth was set to 20 nm to minimize its impact on the FWHM while limiting the grating length. The sampling period duty cycle has to be adapted in each case as long as it stays in the  $[0.10; 0.20]$  range. Eventually, the grating period was set to 196 nm since there is no way to predict for sure which peak will be selected when no tuning of the laser occurs.

### *Mirror and cold cavity responses*

Again, some test patterns allowed comparing the mirrors responses computed with those measured (as in the case of DBR mirrors in 3.1.3). The results are displayed on Figure 4-18 and show very good agreement between what is expected and the experimental curves. However, the mirrors measured responses have an FSR slightly lower than what has been calculated with transfer matrix theory and this probably comes from a silicon waveguide a bit wider or thicker than expected.

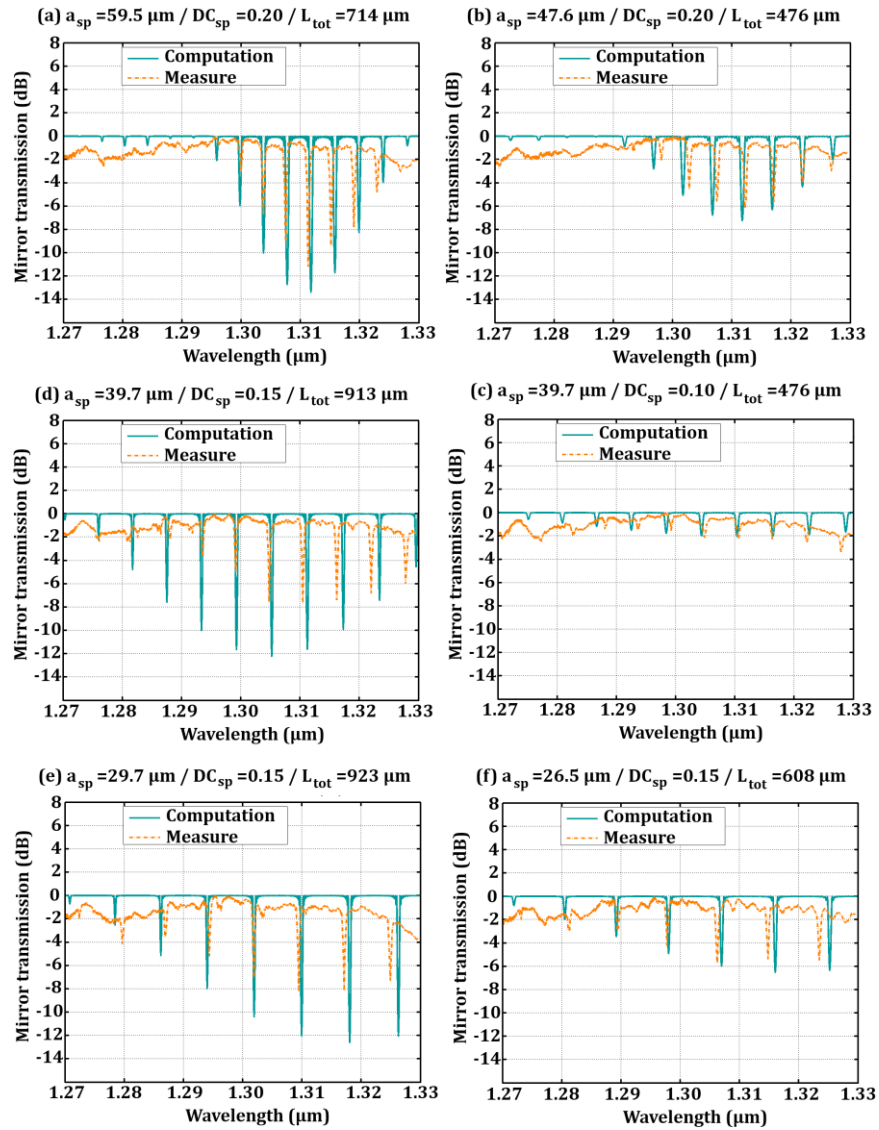


Figure 4-18: Comparison between computations and measure of some of the different SGDBR mirrors designed with  $a=196$  nm.

The transmission of the cold cavity, namely the cavity without the gain material on top, was measured for the symmetric cavities (since there is a fiber coupler at the input and the output of the cavity, which is not the case for the asymmetric ones where a fiber coupler is only present after the front mirror). Three of these cavities responses are presented on Figure 4-19, each of them built with SGDBR mirrors designed with a different FSR. The results are very similar to the theory although the likeness is not as strong for the cavity with smaller FSR for which the FSR difference between the designed and the processed wafers has a greater influence. This gives great hopes regarding the real cavity response.

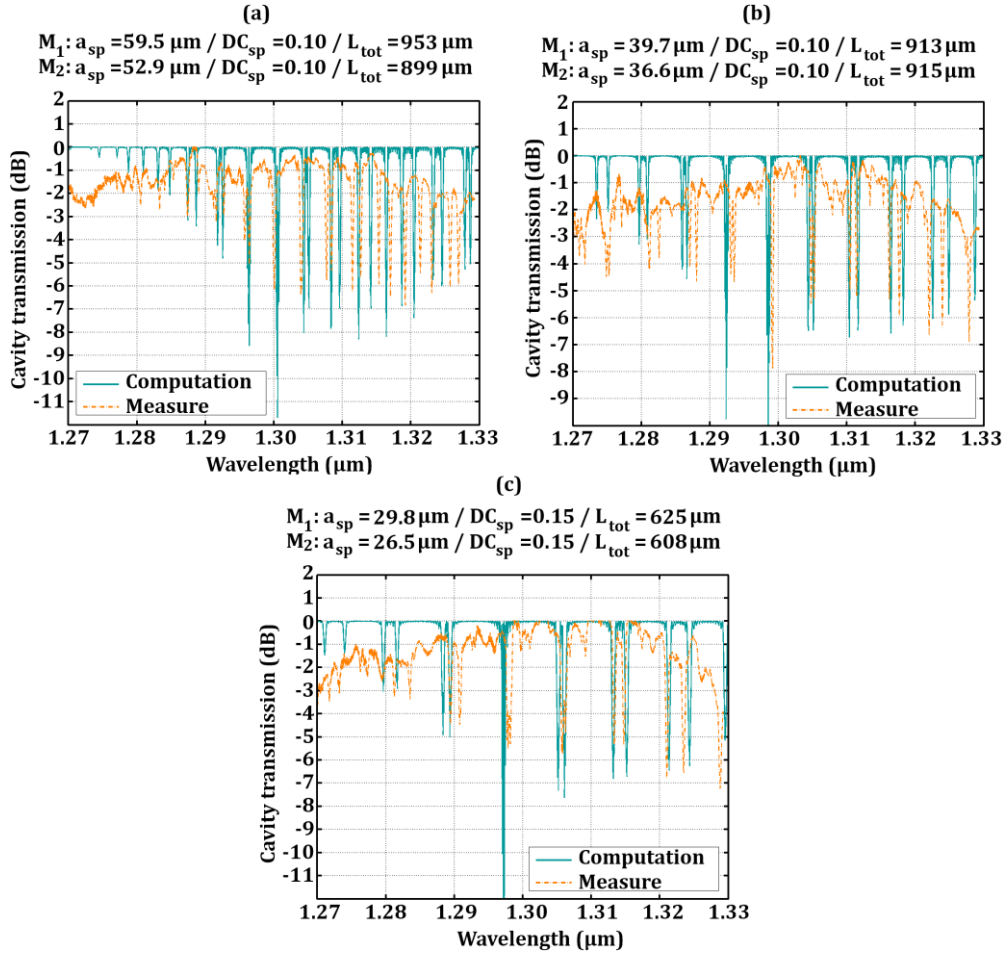


Figure 4-19: Cold cavity responses for SGDBR mirrors designed with an FSR of 4 and 4.5 nm (a), 6 and 6.5 nm (b), 8 and 9 nm. In the three cases, the grating period is  $a=196$  nm.

#### 4.3.3. SGDBR lasers characterization

Figure 4-20 represents an optical microscope picture of one of the SGDBR at the end of the process. It is very much alike the DBR laser and the only perceptible difference is the length of the mirrors which are longer here. Again, the gain region is  $700\text{ }\mu\text{m}$  long.

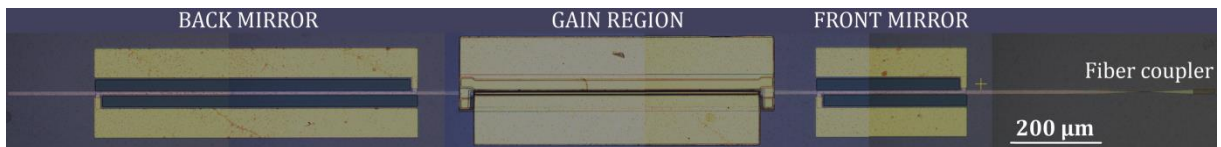


Figure 4-20: Optical microscope picture of one of the SGDBR lasers.

Two wafers were processed with the SGDBR lasers. However, the QWs were probably etched too deeply, meaning that the  $n$ -contact layer is not thick enough which increases the contact resistance. To reduce this problem, the wafers were heated at 450 °C for 2 minutes. This allows the doping particles to diffuse toward the InGaAsP layer and get a better ohmic  $n$ -contact. In spite of this, the resistance of the device remained high thus damaging the power performances. However, all the properties of the SGDBR lasers could be demonstrated as it will be shown below. Only the results of the symmetric SGDBR lasers will be given here for the asymmetric ones were localized on regions with too high resistance on the wafer. The coupler-to-fiber losses were again higher or equal to 6 dB. The lasers with a mirror reflectivity of 0.4 had a too low Q-factor to be of any interest: either no lasing effect occurred or the output power was too low. The results obtained for three different lasers with a mirror reflectivity of 0.8 are discussed below and their properties are detailed in Table 4-3.

Table 4-3: SGDBR lasers properties.

SGDBR laser	Taper	a (nm)	R	$DC_{sp}$	Real SiO <sub>2</sub> gap	Fiber coupler losses	
1	Gap	196	0.80	0.10	~85 nm	> 6 dB	
2	100 nm			0.15	~95 nm		
3	truncated			0.10	~95 nm		
SGDBR laser	$FSR_{M1}$ (nm)	$a_{sp,M1}$ (μm)	$L_{tot,M1}$ (μm)	$FSR_{M2}$ (nm)	$a_{sp,M1}$ (μm)	$L_{tot,M1}$ (μm)	$L_{HT}$ (μm)
1	6	39.7	913	6.5	36.6	915	957
2	6	39.7	635	7.5	31.6	602	668
3	4	59.5	953	5.5	43.3	909	957

The output power and voltage depending on the laser injection current is displayed for two such lasers on Figure 4-21. Their resistances are measured to be respectively 51 and 22 Ω. Despite those huge resistances values, the maximum output power within the waveguide (regarding both laser outputs) reaches 7.5 mW. As in the case of DBR lasers and DFB lasers, this proves once again that the laser resistance is not what impacts the laser performance more (as long as it does not reaches a too high limit value): the coupling from III-V to Si as well as the grating quality has a greater influence. As current increases, the output powers from both curves display big mode bumps. This is a classical response for a laser based on Vernier effect: meanwhile the current increases, the cavity is slightly modified and the next peak is selected. This is in agreement with what was explained earlier, on Figure 4-17: the peak position is very hard to predict because very little change in the cavity is enough to select another peak.

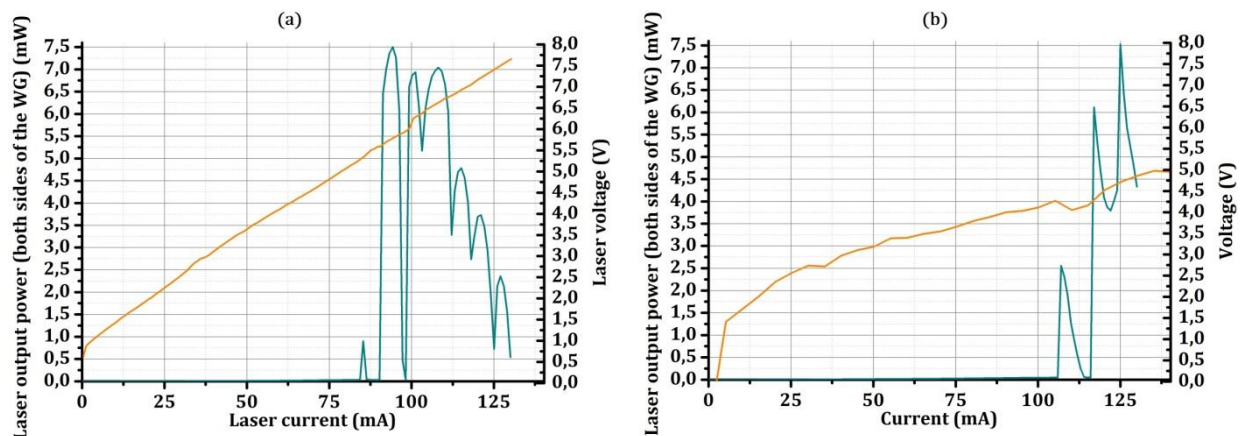


Figure 4-21: Laser output power (taking into account both laser outputs) and voltage as a function of the laser injection current for two different SGDBR lasers (laser 1 and 2 from Table 4-3).

Spectra of the SGDBR lasers 2 and 3 are displayed on Figure 4-22 for different heater currents. On each spectrum, the peaks related to each mirror are well distinguishable. After observing how the peaks shifted when heating only one mirror, it was possible to deduce that the 'positive' peaks are related to the left mirror while the 'negative' ones are related to the right mirror.

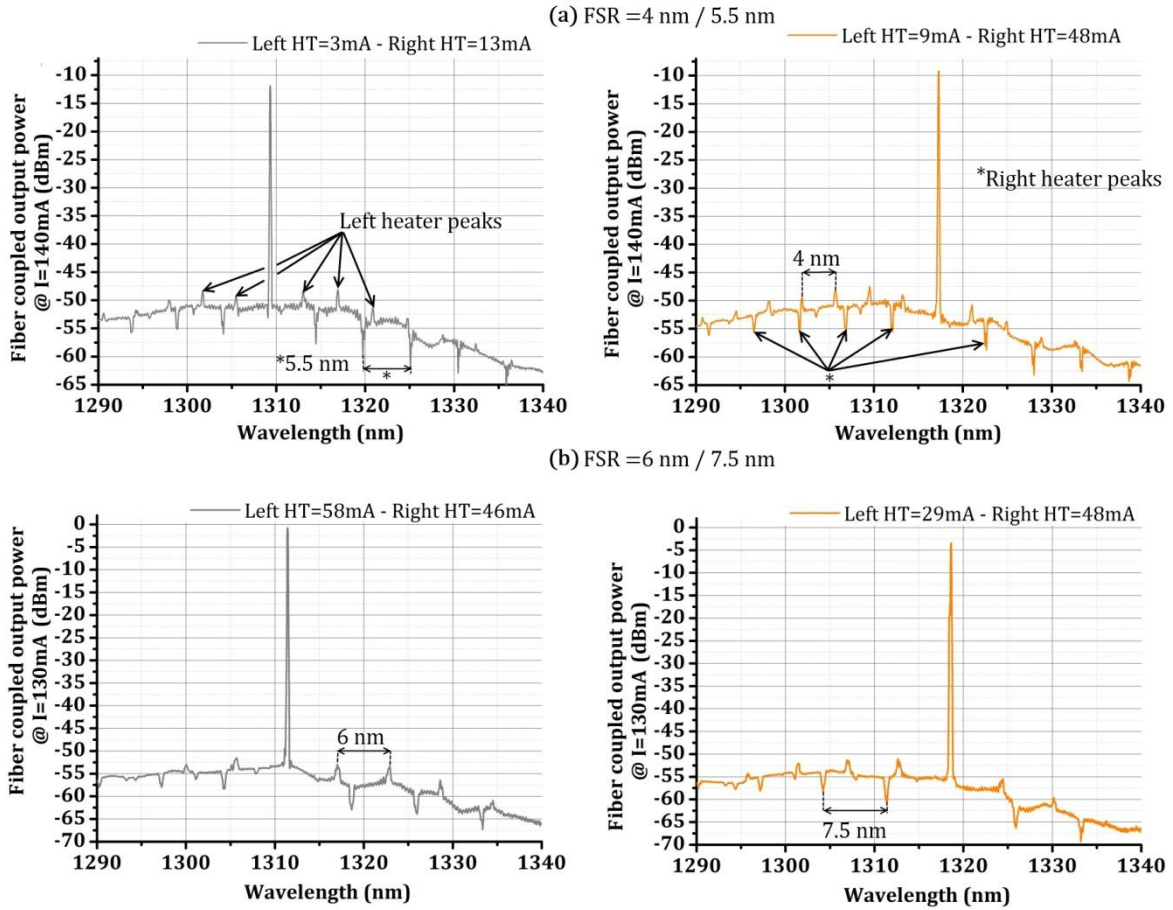


Figure 4-22: Spectra for two SGDBR lasers with their mirrors having different FSR: (a)  $\text{FSR}_{\text{left}}=4 \text{ nm} / \text{FSR}_{\text{right}}=5.5 \text{ nm}$ , (b)  $\text{FSR}_{\text{left}}=6 \text{ nm} / \text{FSR}_{\text{right}}=7.5 \text{ nm}$ .

Continuous tuning over a 27 nm range with an SMSR higher than 35 dB is demonstrated on Figure 4-23 (a) for laser SGDBR 2. To better understand how the tuning is implemented, Figure 4-23 (b) displays the peak wavelength depending on both the right and left heater currents. For a given left heater current, increasing the right heater current implies a wavelength decrease. On the opposite, for a given right heater current, heating the left mirror shifts the wavelength toward higher values. For this laser, only 4 peaks are selected (as shown by Figure 4-23 (a)). Unfortunately, no fifth peak could be reached either toward higher or lower wavelengths because the QWs gain at these wavelengths becomes too low. This can be seen on Figure 4-22 on which the power suddenly decreases from 1325 nm. On laser SGDBR 1, tunability over a 32 nm range was reached but not continuously because one of the heaters burnt out. Six peaks were reached for this laser because its highest FSR was of 6.5 nm only compared to the 7.5 nm of SGDBR 2. The fifth and sixth peaks remain in a wavelength region with enough gain.

It has to be notice that the heater reaches its limits here: to get continuous tuning from one peak to the other, the right heater current is set to 65 mA, which corresponds to a heater power of 0.9 W (according to Figure 4-4 (b)). To reduce this power, a thicker NiFe layer shall be deposited on the next wafers. It is due to both this reason and the fact that the QWs gain is too narrow that no result are presented here with



SGDBR lasers consisting of mirrors with a 8 nm FSR. Tunability from one peak to another was not reached continuously due to the too thin heater. Moreover, the gain was not wide enough to get more than 24 nm (e.g. 4 peaks separated by 8 nm).

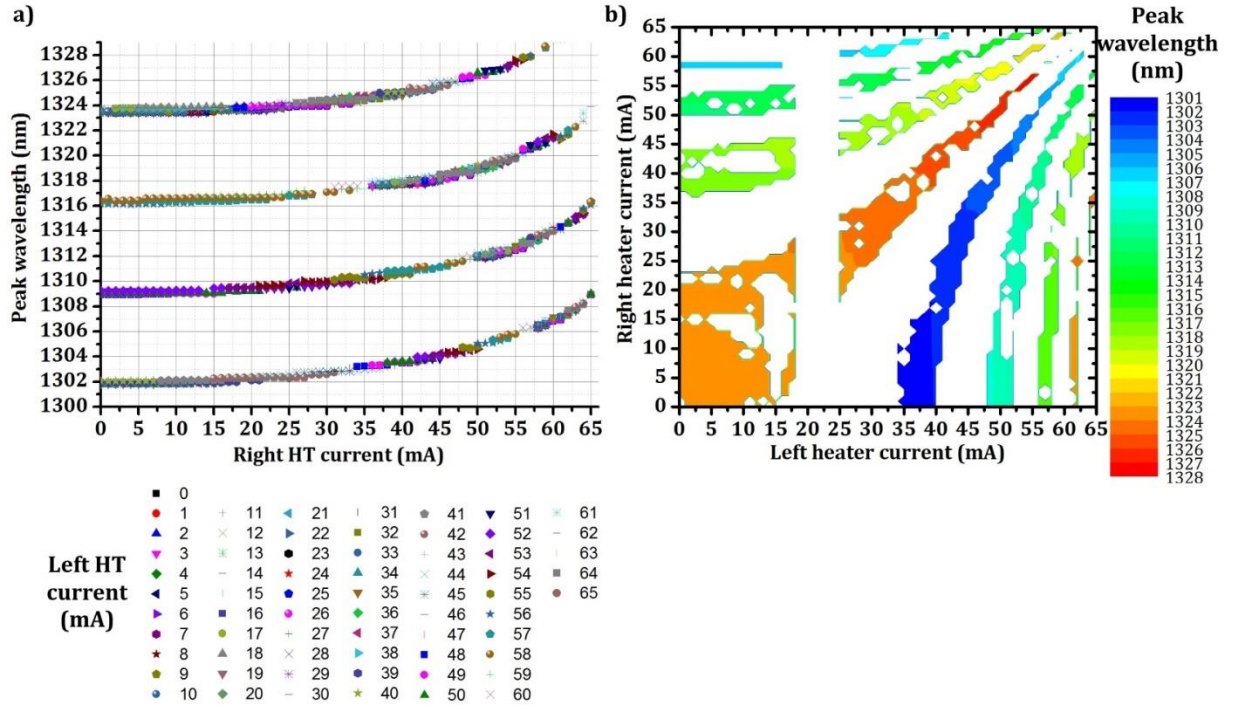


Figure 4-23: a) and b) display two different representations of the peak wavelength depending on both heaters injection currents for a fixed laser current of 130 mA applied to laser SGDBR 2. In (b), some data are missing in the [19; 23] range of the left heater current, hence the white column.

To allow for dense division multiplexing, telecommunication rules require as many laser sources as possible all separated by 0.8 nm. Since this need may arise in datacommunication applications soon, such a graph was built with laser SGDBR 2 (see Figure 4-24) where the SMSR of the selected peaks is higher than 35 dB. Here, only the two heaters currents were changed. This graph could be improved since the lasers power difference shall not be higher than 3 dB. To get such low variations between the peaks power, the current shall be modified as well.

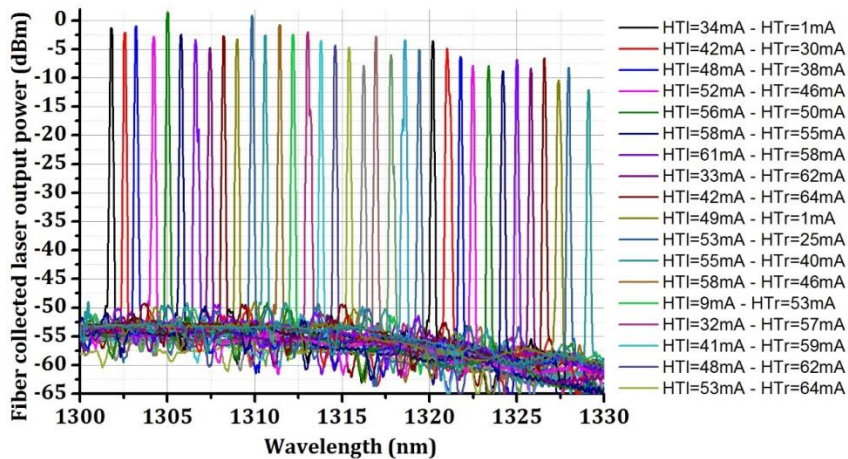


Figure 4-24: Laser spectra with a 0.8 nm spacing on a 27 nm range reached for a 130 mA laser injection current on laser SGDBR 2. HTl and HTr stand respectively for the left heater and the right heater.

#### **4.4. Conclusion to chapter 4**

This last chapter discussed the tunability of single-mode DBR and SGDBR lasers using thermo-optic effect. First, details on the heaters physics were given. The resistance measurements of different heaters showed that temperature changes as high as 600 °C could be reached with the heaters processed in this work. A brief state of the art of tunable lasers at 1.55  $\mu\text{m}$  was also presented but no comparison with tunable lasers at 1.31  $\mu\text{m}$  could be made since no such lasers have been demonstrated up to now.

Some experiments made on the DBR lasers presented in chapter 3 showed tunability over a 13 nm range but it is neither continuous nor precise. To get a continuous tunability on a wider wavelength range, an important part of this work consisted in developing hybrid III-V/Si sample-grated DBR lasers which are based on Vernier effect, as in double-ring cavities.

The principle of SGDBR lasers was thus explained in this chapter and the design of SGDBR mirrors followed. Those lasers were successfully processed and continuous tunability was reached on a 27 nm range with an SMSR higher than 35 dB and a laser output power in the waveguide higher than 7 mW. To increase this range, III-V epitaxies with a wider gain range shall be needed. Moreover, the mirror heating might be improved by thickening the heater layer, thus lowering its power consumption.

---

# Conclusion and prospects

---

## *Conclusion and feedbacks on the requirements*

As the data stream keeps increasing every day in the world, solutions need to be found to go faster without demanding more power supply. The use of optics to transmit information seems to be a good way to solve the problem. However, to obtain devices that can compete with the micro-electronics costs, optical devices have to be produced on a high scale, and silicon photonics could render that possible. Nonetheless, as long as no efficient laser source is demonstrated, silicon photonics won't break through. The goal of this three-year-thesis was thus to develop hybrid III-V on silicon laser sources at 1.31  $\mu\text{m}$  for datacommunication applications compatible with a silicon photonic optical circuit. I worked as much on the design as the fabrication process and the characterization of the devices.

While some of the laser integration schemes use so called flip-chip bonding or edge coupling, CEA/Leti made the choice to bond a III-V stack upon the silicon waveguide. Among the several possible bonding methods presented (adhesive, metallic, direct and molecular), molecular bonding seems the more attractive for us since it allows for more possible designs and also because the surfaces to bond do not need to be as clean and smooth as with direct bonding. To maximize light amplification, the laser is designed so as to have light confined within the III-V waveguide when in the active region and within the Si waveguide elsewhere. This is made possible thanks to an adiabatic coupler which transfers light from one waveguide to the other with as little loss as possible. The first part of this thesis focused on the design of those tapers. Their shape has been calculated using supermode theory and a study of their robustness regarding process variations was implemented showing that the coupling efficiency remains higher than 90 % with the assumed variations of the waveguides dimensions ( $\pm 30$  nm). The most critical parameter is rather the oxide thickness between the III-V and the silicon which shall be within the [70; 110] nm range.

After the optimization of the adiabatic tapers, the lasers cavities were designed and more specifically cavities based on gratings because those consisting of rings seem less robust regarding fabrication process. To reach single-mode devices, we chose to work on DBR and DFB lasers. In the former case, shallow etched (10 nm deep) Bragg gratings are formed upon the silicon waveguide at each output of the gain region. The fabricated devices were single-mode with an SMSR higher than 35 dB but the laser output power did not exceed 2 mW within the waveguide due to a too low ( $\sim 60$  nm) oxide thickness between III-V and Si thus inducing too much coupling losses within the tapers. More hopes are expected for the next DBR lasers which are to come very soon but those characterized already enabled to verify the designs.

As for the DFB lasers, a single grating, with a quarter wavelength shifter in its middle, was etched either on top or on the edges of the Si waveguide, right underneath the III-V stack. Both solutions proved to be very promising: more than 55 dB and 45 dB of SMSR as well as 22 mW and 20 mW of output power within the waveguides were reached for the vertically and laterally coupled DFB lasers respectively. The lasers fabricated with the best III-V epitaxies showed laser effect until 65  $^{\circ}\text{C}$ , which is very encouraging, although not reaching yet what is required (lasing effect until 80  $^{\circ}\text{C}$ ). To improve this value even more, further efforts should be made either by finding a way to drain away the heat or by using quantum dash or quantum dots instead of QWs. The vertically coupled DFB lasers were also directly modulated showing an open eye diagram until 10 Gbit/s thus matching the 40GbaseLR4 requirements. To go even further (100GbaseLR4), specific RF pads shall be designed which was not the case here.

Due to the fabrication variations (not only during the process but also regarding the III-V epitaxies which are hardly ever alike), it is very hard to predict a laser wavelength with precision, as it could be seen with



the DFB lasers obtained during this work. For this reason, it is very interesting to be able to tune the lasers to obtain the wavelength wanted post-processing. The tuning of the DBR lasers was demonstrated by heating the mirrors: tuning over a 13.8 nm wavelength range was reached but the tuning was not so precise since the only modes that can be selected are those allowed by the Fabry-Pérot cavity between both DBR gratings. To reach continuous tunability on a wider wavelength range, a laser with its cavity based on Vernier effect was designed: a Sample-Grated-DBR laser. It is like a DBR laser except that parts of the gratings are periodically removed thus reaching combs like mirrors responses. A continuous tunability was reached over a 27 nm range with an SMSR higher than 35 dB and a laser output power in the waveguide higher than 7 mW. This wavelength range corresponds to  $\pm 1.03\%$  of the 1.31  $\mu\text{m}$  central wavelength. Since no tunable laser exists yet in the literature at this wavelength, it can be compared with those at 1.55  $\mu\text{m}$ : the best tunability range ever demonstrated was 45 nm which corresponds to  $\pm 1.45\%$  of the 1.55  $\mu\text{m}$  central wavelength. This result is thus very promising since it is the first obtained at this wavelength. It can again be enhanced by using thicker heaters layers to better control the continuity of the tuning and supply less electrical power for the same effect as well as by bonding III-V QWs with wider gain ranges to reach the next higher or lower peaks.

To sum up, III-V/Si lasers at 1.31  $\mu\text{m}$  were demonstrated with high output powers and with good spectral purities. A wide tunability range was also reached with SGDBR lasers. Almost all the requirements needed were fulfilled except for the temperature performances and the number of wavelengths obtained with the DFB lasers (3 instead of 4). To improve those results, some short term prospects shall be:

- To use III-V epitaxies centered on a lower wavelength to reach the fourth wavelength needed for the 'Long Reach 4' requirements (with the DFB lasers).
- Designing pads specifics for RF to increase the RF performances and enable the laser direct modulation at higher speeds.
- Improving the temperature performances (either thanks to quantum dots or quantum dashed instead of QWs or by finding a way to drain away the heat).
- Use III-V QWs with wider gain to reach a higher tunability range.

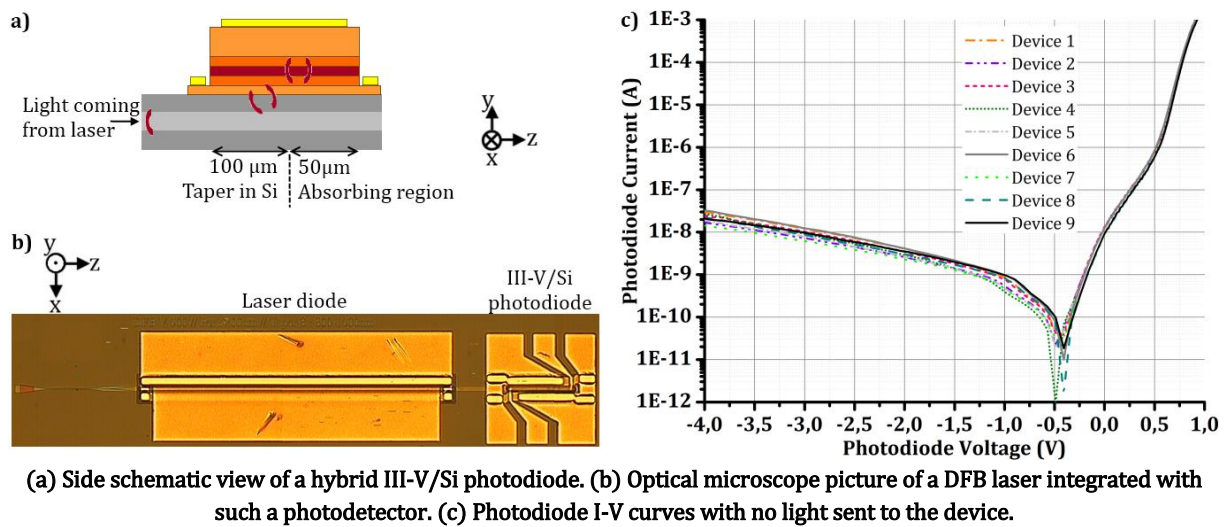
The following sections detail the prospects in the longer term namely the co-integration of the lasers with other devices, the 200-mm process development of the lasers and at last the other applications that could be reached with these lasers.

### ***Co-integration with other devices***

The lasers characterized during this work were demonstrators and were consequently built on wafers dedicated to the laser process only. To be relevant, they shall be integrated on wafers with all the other devices needed in an optical circuit such as photodetectors, modulators and so on. Actually, we took the advantage of the fact that some III-V materials were bonded onto the SOI wafer to co-integrate to the lasers electro-absorption modulators (EAM) and photodetectors with their absorbing region located within the III-V material. Due to a lack of time, neither their design nor their characterization have been optimized which is the reason why they are not much tackled in the body of the text.

As a reminder, a photodetector is a device which absorbs a photon flux and turns it into a current [115]. Its physical principal lies in a PN or a PIN junction (see Figure 1-6) to which a reverse bias is applied thus increasing the junction voltage. If a photon reaches the intrinsic region it is absorbed thus creating an electron-hole pair which is easily separated by the reverse bias (the electron goes toward the *n*-region and the hole toward the *p*-region). As in the case of stimulated emission, absorption is more efficient in a material with a direct bandgap, hence the interest in building hybrid III-V on Si photodetectors. This was first done by Park et al at UCSB [116] and they used the same evanescent structure as for their lasers (see 1.2.2). During my work, in the case when the lasers designed had as much power outgoing from each side

(DFB lasers, symmetric SGDBR lasers), a III-V/Si photodiode had been designed at one of the output to compare the power at both lasers outputs as represented on the figure below. This figure also includes a scheme of the photodiode: the same III-V stack as for the laser is bonded onto the Si waveguide and the PIN junction is processed at the same time as that of the laser. The device consists of a taper (the same adiabatic taper as the one detailed for the laser) which transfers light into the III-V waveguide, and which is followed by a 50- $\mu\text{m}$ -long absorbing region: this is where the photons are turned into a current. The I-V curves obtained are displayed when no light was sent to the photodetector: this gives the dark current response of the device. At low driving voltages ( $< -3$  V), the dark current shall be below the nano-ampere while here, it is above  $1\text{E}-8$  A. Although the laser output power measured from the photodiodes current followed the same trend as that collected from the fiber couplers, the photodiodes current values were biased due to this high leakage current and could not be linked to the power inside the waveguide. However, in spite of these results, this track is very interesting to pursue because it would leverage the fact that III-V is bonded onto the SOI wafer. A design proper to the photodetector shall be implemented using for instance a different III-V waveguide width, a different taper, or a longer absorbing region. This would really be an easy way to co-integrate the photodetectors with the lasers. At CEA/Leti, very good SiGe avalanche photodetectors were demonstrated [33] and it would also be worth adapting the process to co-integrate those photodetectors with the hybrid lasers since they prove to be more efficient than the III-V/Si photodiodes demonstrated until now.

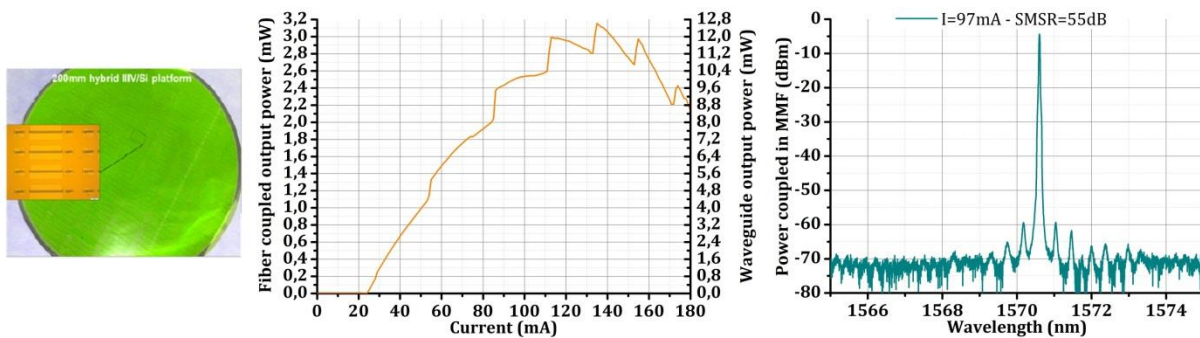


It was seen in this work that there is still room for improvement when it comes to laser direct modulation. Another solution is to modulate the laser signal at its output using what is called an optical modulator [117] whose response is faster than a laser. It is a device which either absorbs light or let it go through depending on its electrical signal: the signal to modulate can thus be sent to the modulator which will then transfer it to the laser optical signal it receives. The emitter-receiver system detailed in Figure 1-16 shows that the co-integration of lasers with modulators is a must-have. Again, hybrid III-V/Si modulators are worth looking into: they are called electro-absorption modulators[118]. Some were built on the wafers processed during this thesis: they are alike the photodiodes described above except that another taper is formed at the other side of the 'absorbing region' so that, when not absorbed, light goes back into the silicon waveguide. Unfortunately, no proper measurements were implemented on these devices. It would really be worthwhile to address the subject more seriously. Besides electro-absorption modulators, other kinds of modulators can be very efficient as well, such as Mach-Zender modulators (MZM). It was quickly mentioned when talking about the DBR lasers characterization, but at the same time as my thesis took place, another PhD student has been working on the co-integration of the DBR lasers I designed, with a MZM to

create an efficient transmitter. The results obtained with MZM he designed were very promising [119] and the whole transmitter measurements are expected very soon. It would be a major step forward for CEA/Leti to obtain those devices thus co-integrated and the results are eagerly awaited.

### 200 mm process development

When detailing the laser fabrication process flow in 2.3, it was specified that the 200-mm wafer had to be downsized after the III-V to silicon wafer bonding. Nonetheless, to comply with the high-volume needed so that silicon photonics becomes attractive in term of costs, the whole fabrication shall be implemented at a 200-mm level. This development is already ongoing at CEA/Leti, but for delay reasons, it was not applied to the lasers demonstrated here. Actually, at the same time as this work occurred, lasers processed on a 200-mm platform were demonstrated and I had the chance to characterize them. They were hybrid III-V/Si DBR lasers at 1.55  $\mu\text{m}$  designed before my arrival [99], [104]. A 2-inch III-V wafers was bonded in the middle of a 200-mm SOI wafer and the whole process detailed in 2.3.4 was transferred to the 200-mm platform which required a lot of developments. The performances obtained for one of the devices are presented on the figure below: an output power in the waveguide higher than 12 mW and a SMSR as high as 55 dB were reached. This result is a real advance since it is the first hybrid III-V/Si laser ever demonstrated on a 200-mm platform.



**Performances of a laser processed on a 200mm hybrid III-V/Si platform.**

This process was not yet developed at the beginning of this thesis and most of all, the aim of this work was rather to focus on new designs (new wavelength, laterally coupled DFB lasers, SGDBR lasers...) with thus new fabrication issues to deal with (small grating period, grating resolution, different III-V dimensions...). Consequently, to limit the risks taken during the fabrication, it was chosen to work with 3" inches bonded wafers. Now that the 200-mm process has been developed, the fabrication of the best III-V/Si lasers operating at 1.31  $\mu\text{m}$  and demonstrated during this thesis shall be implemented on this platform as well.

Moreover, to go further into this development, two mains things need to be enhanced:

- Die to wafer bonding. For now the best performances reached for the lasers used wafer to wafer bonding processes. However, the possibility to implement die-to-wafer bonding was mentioned in 2.3 as a way to minimize the amount of III-V used. This technological process is being developed at CEA/Leti.
- Etching uniformity. As long as the laser fabrication process was led on 2 or 3 inches wafers, the etching un-uniformity did not have so many consequences on the laser performances (yet perceptible). On the 200-mm scale, the impact is much higher: when etching the III-V QWs for instance, the etching is faster on the edges than on the center of the wafer and this can lead to a huge performance un-uniformity. This issue is to be tackled seriously to improve the 200-mm fabrication.

***To go further...***

To reach dense wavelength division multiplexing (DWDM), other solutions could be further developed such as mode locked lasers and arrayed waveguide (AWG) lasers. Both have already been demonstrated using the hybrid III-V/Si technology in [55], [120], [121] for the former kind of lasers and [122] for the latter. Mode-locked lasers are lasers which generate short optical pulses. Their optical bandwidth is large enough so as to select a different mode at each pulse thus enabling wavelength mode-comb and avoiding the need for the integration of several lasers sources. In an AWG laser, several semiconductor optical amplifier (SOA) regions provide the gain for the different wavelengths wanted which are gathered thanks to an AWG. The laser cavity is formed between the input of each SOA and the output of the AWG. Both types of laser are advantageous for they have a lower footprint (which gives less chance for process dispersion). Using the knowledge acquired in this work with the development of grating based lasers, it might be interesting for CEA/Leti to study and fabricate those lasers and why not improve their performances including DBR or SGDBR inside?

The interest raised in silicon photonics for telecommunication developments might also benefit to other fields. Actually, many labs focus on silicon photonics for bio-sensing thus leveraging the possibility to make low costs and high volume sensors. For example, in IMS in Canada [123] as well as in Ghent University in Belgium [124]–[126], ring resonators were formed on SOI wafers to monitor the presence and interaction of targeted bio-molecules. On the devices demonstrated, light is injected to the waveguide thanks to an optical fiber and collected from another one. If lasers were designed specifically for this purpose, it would avoid all the issues linked to fiber injection alignments and also render the diagnostic less cumbersome. The care in this field keeps growing and a need for new kinds of lasers may appear.



# Appendix A. Transfer matrix theory for gratings

This paragraph details the transfer matrix theory and its specific use with gratings.

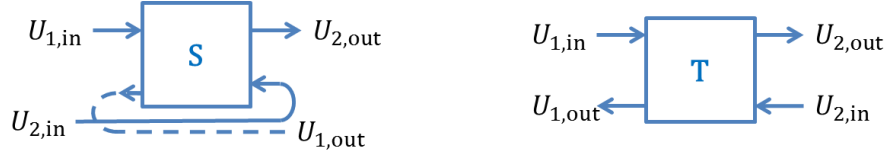


Figure A-1: Representation of an optical system with a scattering (left) or a transfer (right) matrix.

It is possible to regard an optical component (waveguide, grating, cavity...) as a system arbitrarily delimited by an input plane and an output plane from which a forward and backward amplitudes are respectively incoming and outgoing. From this, two formalisms, represented on Figure A-1, can be defined: the scattering matrix and the transmission, or transfer matrix theories. In the former formalism the outputs are reckoned as a linear combination of the inputs which gives:

$$\begin{pmatrix} U_{1,out} \\ U_{2,out} \end{pmatrix} = \begin{pmatrix} S_{11} & S_{12} \\ S_{21} & S_{22} \end{pmatrix} \begin{pmatrix} U_{1,in} \\ U_{2,in} \end{pmatrix} = \begin{pmatrix} r_{12} & t_{21} \\ t_{12} & r_{21} \end{pmatrix} \begin{pmatrix} U_{1,in} \\ U_{2,in} \end{pmatrix} \quad [A.1]$$

The scattering formalism is very convenient in the sense that the physical significance is direct as proved by the second part of equation [A.1] where it is clear that each component of the system either stands for the transmission or the reflection from one plane to the other. In the transfer matrix system, it is the components from plane 2 which are a linear combination of those from plane 1 thus leading to:

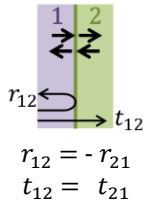
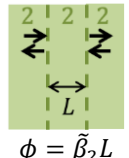
$$\begin{pmatrix} U_{2,in} \\ U_{2,out} \end{pmatrix} = \begin{pmatrix} T_{11} & T_{12} \\ T_{21} & T_{22} \end{pmatrix} \begin{pmatrix} U_{1,in} \\ U_{1,out} \end{pmatrix} \quad [A.2]$$

Although this representation does not allow a direct deduction of physical parameters, it is very useful because when several components follow one another, the transfer matrices of each component can be cascaded to obtain the overall transfer matrix of the system. It is then easy to get the scattering matrix associated using the subsequent relation:

$$\begin{pmatrix} T_{11} & T_{12} \\ T_{21} & T_{22} \end{pmatrix} = \frac{1}{S_{21}} \begin{pmatrix} 1 & -S_{22} \\ S_{11} & -\det(\mathbf{S}) \end{pmatrix} \quad [A.3]$$

The explanations above show that the transfer matrix formalism is very appropriate for the performances' calculation of a grating. The grating can be separated into its elemental constituent: the period. To get to the transfer matrix, the period itself needs to be separated into its different elements namely an interface between two layers and propagation within a single layer. The scattering and transfer matrices associated to these components are represented on Table A-1.

Table A-1: Scattering and transfer matrix of the basic components in a grating.

Structure name	Schematic view	Scattering matrix	Transfer matrix
Interface between layers 1 and 2	 $r_{12} = -r_{21}$ $t_{12} = t_{21}$	$\begin{pmatrix} r_{12} & t_{21} \\ t_{12} & -r_{12} \end{pmatrix}$	$\frac{1}{t_{12}} \begin{pmatrix} 1 & r_{12} \\ r_{12} & 1 \end{pmatrix}$
Propagation along L	 $\phi = \beta_2 L$	$\begin{pmatrix} 0 & e^{-j\phi} \\ e^{-j\phi} & 0 \end{pmatrix}$	$\begin{pmatrix} e^{j\phi} & 0 \\ 0 & e^{-j\phi} \end{pmatrix}$

Using these basic matrices, the transfer matrix of a period can be calculated multiplying the successive matrices encountered when going through the period. This is displayed on Figure A-2 (a): going from right to left, light first propagates through layer 1 ( $T_{pr,1}$ ), then it crosses the interface from layer 1 to layer 2 ( $T_{i,21}$ ), then it propagates again through layer 2 ( $T_{pr,2}$ ) and it eventually go through the interface from layer 2 to layer 1 ( $T_{i,12}$ ):

$$T_p = T_{pr,1} T_{i,21} T_{pr,2} T_{i,12} \quad [A.4]$$

Using the elemental matrices from Table A-1,  $T_p$  can be calculated as in[2]. What we are looking for is the reflectivity of the system, which is issued from the inputs of the matrix, hence the need to go from right to left. With the same reasoning as for a single period, one can deduce  $T_g$ , the transfer matrix of a grating with N periods as illustrated on Figure A-2 (b).

$$T_g = (T_p)^N \quad [A.5]$$

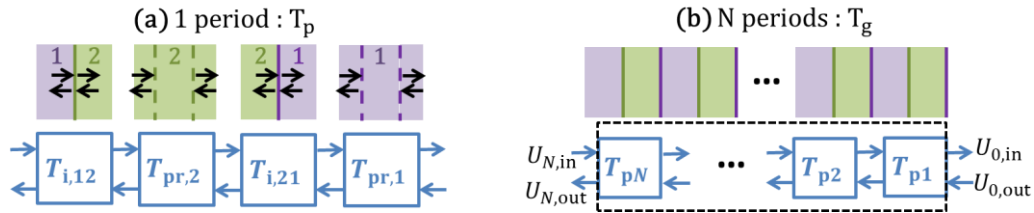


Figure A-2: Transfer matrix cascade for (a) 1 period, (b) a grating of N periods.

Using equations [A.4] and [A.5] it is possible to compute the reflection of the grating ( $r_g$ ) depending on the wavelength as long as the effective indexes of the layers are known. This reflection is given by:

$$r_g = S_{g11} = \frac{T_{g21}}{T_{g11}} \quad [A.6]$$



---

## Appendix B. Author list of publications

---

### *First author*

Article: H. Duprez, A. Descos, T. Ferrotti, C. Sciancalepore, C. Jany, K. Hassan, C. Seassal, S. Menezo, and B. Ben Bakir, "1310 nm hybrid InP/InGaAsP on silicon distributed feedback laser with high side-mode suppression ratio," *Opt. Express*, vol. 23, no. 7, p. 8489, Apr. 2015

Proceeding (Photonics West 2015 – San Francisco): H. Duprez, A. Descos, T. Ferrotti, C. Jany, J. Harduin, A. Myko, C. Sciancalepore, C. Seassal, and B. Ben Bakir, "Heterointegrated III-V/Si distributed feedback lasers," 2015, vol. 9365, pp. 936506–936506–8.

Proceeding (OFC 2015 – Los Angeles): H. Duprez, A. Descos, T. Ferrotti, J. Harduin, C. Jany, T. Card, A. Myko, C. Sciancalepore, S. Menezo, and B. Ben Bakir, "Heterogeneously Integrated III-V on Silicon Distributed Feedback Lasers at 1310 nm," 2015, p. Tu3I.6.

Article: H. Duprez, A. Descos, C. Jany, C. Seassal, and B. Ben Bakir, "Hybrid III-V on silicon laterally-coupled distributed feedback laser operating in the O-band", submitted to *IEEE Photonics Technol. Lett.*

Article: H. Duprez, C. Jany, C. Seassal, and B. Ben Bakir, "Highly Tunable Heterogeneously Integrated III-V on Silicon Sampled-Grating Distributed Bragg Reflector Lasers operating in the O-band", submitted to *Opt. Express*

### *2<sup>nd</sup> author or more*

Proceeding (ECOC 2013 – London): A. Descos, C. Jany, D. Bordel, H. Duprez, G. B. de Farias, P. Brianceau, S. Menezo, and B. Ben Bakir, "Heterogeneously integrated III-V/Si distributed Bragg reflector laser with adiabatic coupling," in *39th European Conference and Exhibition on Optical Communication (ECOC 2013)*, 2013, pp. 1–3.

Proceeding (ECS 2014 – Cancun): B. B. Bakir, C. Sciancalepore, A. Descos, H. Duprez, D. Bordel, L. Sanchez, C. Jany, K. Hassan, P. Brianceau, V. Carron, and S. Menezo, "(Invited) Heterogeneously Integrated III-V on Silicon Lasers," *ECS Trans.*, vol. 64, no. 5, pp. 211–223, Aug. 2014.

Proceeding (Photonics West 2015 – San Francisco): T. Ferrotti, A. Chantre, B. Blampey, H. Duprez, F. Milesi, A. Myko, C. Sciancalepore, K. Hassan, J. Harduin, C. Baudot, S. Menezo, F. Boeuf, and B. Ben Bakir, "Power-efficient carrier-depletion SOI Mach-Zehnder modulators for 4x25Gbit/s operation in the O-band," 2015, vol. 9367, p. 93670D–93670D–11.

Article: C. Sciancalepore, R. J. Lycett, J. A. Dallery, S. Pauliac, K. Hassan, J. Harduin, H. Duprez, U. Weidenmueller, D. F. G. Gallagher, S. Menezo, and B. Ben Bakir, "Low-Crosstalk Fabrication-Insensitive Echelle Grating Demultiplexers on Silicon-on-Insulator," *IEEE Photonics Technol. Lett.*, vol. 27, no. 5, pp. 494–497, Mar. 2015.

Book chapter (chapter 8): P. Bettotti "Nanodevices for Photonics and Electronics: Advances and Applications," *CRC Press*. Available: <https://www.crcpress.com/Nanodevices-for-Photonics-and-Electronics-Advances-and-Applications-Advances/Bettotti/9789814613743>. Chapter 8: B. Ben Bakir, C. Sciancalepore, A. Descos, H. Duprez, D. Bordel, S. Menezo 'Group III-V on Silicon: a Brand-New Optoelectronic'.

Patent: 'Hybrid III-V Si laser architecture' (T. Ferrotti, B. Ben Bakir, A. Chantre, H. Duprez, S. Cremer) – Brevet ST/CEA - ICG30193 / DD15039 / 13-GR4-0661

Patent: 'Substrat pré-structuré pour la réalisation de composants photoniques, circuit photonique et procédé de fabrication associé' (K. Hassan, B. Ben Bakir, C. Sciancalepore, H. Duprez) – Brevet CEA

Patent: 'Source laser multi-longueurs d'onde auto-alignée et émetteur-récepteur intégrant une telle source' (C. Sciancalepore, B. Ben Bakir, K. Hassan, H. Duprez, S. Menezo) – Brevet CEA

---

## Appendix C. French summary

---

### Introduction et objectifs

Avec la mondialisation et l'augmentation quotidienne du débit d'informations échangées dans le monde, il devient indispensable de développer des technologies plus efficaces pour être capable de s'adapter au besoin grandissant dans les années à venir. Non seulement les interconnexions en cuivre développées en micro-électronique ne conviennent pas pour la propagation sur des très longues distances, mais en plus la réduction des dimensions des circuits électroniques induit une surchauffe ainsi que des effets quantiques parasites. C'est pourquoi la recherche en télécommunication s'est tournée vers l'optique pour profiter de la légèreté des fibres optiques, de leur insensibilité au bruit électromagnétique ainsi que de la possibilité d'effectuer du multiplexage en longueur d'onde ce qui augmente la bande passante. Le besoin se tourne maintenant vers l'optique pour des transferts sur de plus courtes distances : d'un circuit à l'autre ou même sur une même puce. L'inconvénient majeur de l'optique reste le prix des composants qui sont fabriqués par faibles volumes et ne peuvent donc être compétitifs face aux composants microélectroniques. Face à ce défi, la photonique sur silicium (Si) paraît être la solution optimale : elle permet de créer des composants optiques (guides, réflecteurs...) à grande échelle, sur des plaques (wafers) de silicium en utilisant la technologie CMOS ('Complementary Metal Oxide Semi-conductor'). Cette possibilité vient du fait que le Si est un matériau transparent aux longueurs d'ondes télécom (1.31  $\mu\text{m}$  and 1.55  $\mu\text{m}$ ) et que sa différence d'indice avec la silice, son oxyde natif, est assez élevée pour permettre de créer des fonctions optiques compactes.

Le seul frein à l'essor de la photonique sur silicium pour les télécommunications vient du fait que c'est un mauvais émetteur de lumière à cause de son gap indirect. Les recherches dans ce domaine se concentrent donc principalement sur l'intégration d'une source laser efficace à un circuit photonique sur silicium. Une des approches possibles, choisie par le CEA/Leti, est d'utiliser un matériau III-V collé au-dessus du Si qui fournirait le gain du laser et de construire le reste de la cavité laser dans le guide Si en-dessous. De tels lasers ont été développés à 1.55  $\mu\text{m}$  au laboratoire depuis 2005 et notamment avec la thèse d'A. Descos qui précédait ces travaux. La thèse ci-contre présente la conception, la fabrication et la caractérisation de lasers hybrides III-V sur Si à 1.31  $\mu\text{m}$ . Je me suis concentrée non seulement sur le couplage entre le III-V et le Si mais aussi sur des cavités à base de réseaux conçues de manière à obtenir une émission monomode avec la possibilité d'accorder la longueur d'onde. Pour ce qui est de la fabrication, toute la structuration des wafers Si, dont je contrôlais l'avancement, a eu lieu sur la plateforme CEA/Leti. Une fois l'épitaxie III-V collée au-dessus du silicium, c'est C. Jany qui s'est chargé de la majeure partie de la fabrication. J'ai ensuite pu procéder à la caractérisation des différents dispositifs obtenus.

Cette annexe est simplement un résumé en français des travaux réalisés (et rédigés en anglais dans le corps de ce manuscrit). Ni la théorie, ni l'aspect fabrication ne sont détaillés ici et le lecteur pourra se référer au manuscrit anglais. Cette introduction aborde le cahier des charges des lasers fabriqués dans cette thèse. Un premier paragraphe détaille ensuite l'architecture des différents lasers fabriqués ainsi que le couplage entre le III-V et le silicium. Les trois lasers réalisés sont ensuite décrits avec leurs résultats dans trois paragraphes distincts : d'abord les lasers à rétroaction distribuée (lasers DFB pour 'Distributed FeedBack'), puis les lasers de Bragg (lasers DBR pour 'Distributed Bragg Reflector') et enfin les lasers de Bragg échantillonnés (lasers SGDBR pour 'Sampled-grating DBR').

### Caractéristiques d'un laser

Les caractéristiques laser peuvent être séparées en deux catégories : statiques et dynamiques. Dans le cas de la réponse statique du laser, on s'intéresse notamment à la puissance optique délivrée ( $P$ ) en fonction soit du courant fourni au dispositif ( $I$ ) soit de la longueur d'onde d'émission ( $\lambda$ ) ; les deux graphes sont données pour exemples sur la Figure C-1. Dans le premier cas, il peut être montré qu'à partir d'un seuil ( $I_{th}$ ), la puissance dépend de manière linéaire du courant jusqu'à une valeur maximale ( $P_{max}$ ) à partir de laquelle elle diminue. Dans le second cas, on étudie la mono-modicité du laser en calculant la différence entre le pic le plus haut et le second pic le plus haut en puissance : on mesure alors le taux de suppression des modes secondaires (SMSR pour 'Side Mode Suppression Ratio'). La largeur à mi-hauteur (FWHM pour 'Full Width at Half Maximum') du pic principal est aussi une caractéristique importante du laser.

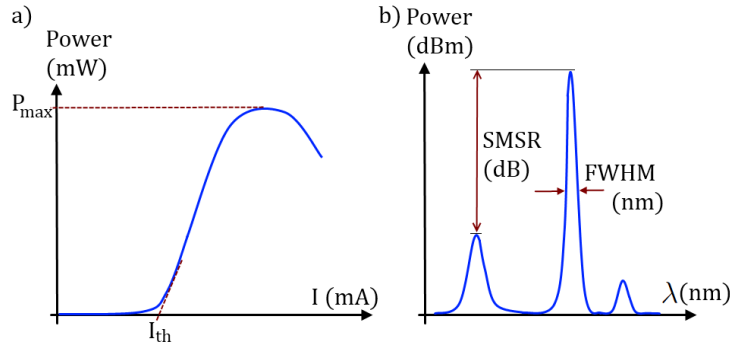


Figure C-1 : Laser characteristics: output power as a function of a) the injected current b) the wavelength

Il peut s'avérer intéressant de moduler le laser directement en fréquence et donc de connaître ses propriétés dynamiques. Pour cela, le laser est modulé suivant le schéma représenté sur la Figure C-2 : un courant DC,  $I_0$ , est appliqué au laser auquel est superposé un courant de modulation AC,  $I_1$  à une fréquence  $f = \omega/2\pi$ . La réponse du dispositif montre qu'il y a une fréquence de résonance à partir de laquelle la puissance du laser diminue (c'est-à-dire que le laser ne répond pas assez vite au courant envoyé). Le paramètre le plus intéressant dans cette courbe est la bande passante à -3dB ( $f_{-3dB}$ ) qui correspond à la fréquence à partir de laquelle la puissance DC du laser est divisée par deux. Plus cette valeur est élevée, plus le laser est rapide.

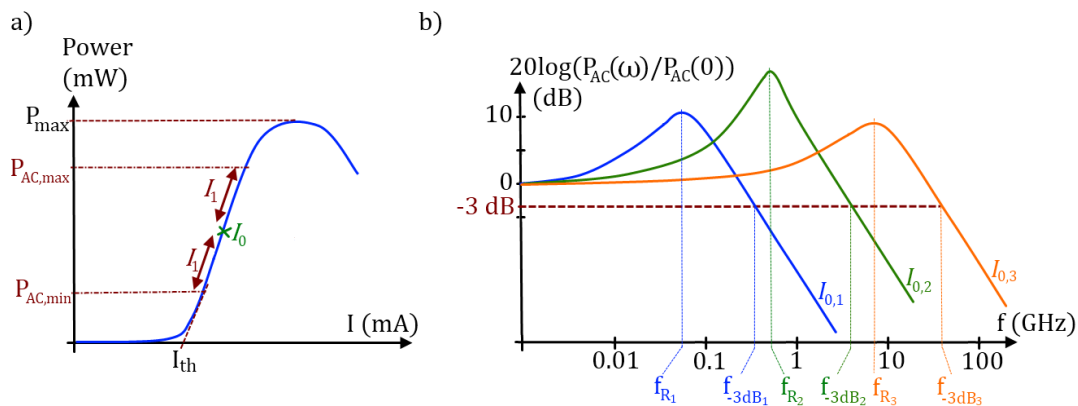


Figure C-2: a) Modulation scheme b) Frequency response of an idealized laser diode for different DC currents ( $I_{0,1}$ ,  $I_{0,2}$  and  $I_{0,3}$ ).

Enfin, pour terminer l'étude dynamique, un diagramme de l'œil du laser est tracé pour différentes fréquences fournies au laser (cf. Figure C-3). Plus l'œil est ouvert à des fréquences élevées, plus le dispositif est capable de répondre rapidement.

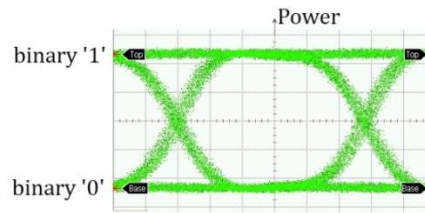


Figure C-3: Eye diagram representation

### *Cahier des charges des lasers et approche proposée*

Bien que les lasers conçus Durant cette thèse puissent être utilisés pour d'autres applications, leur objectif principal est de se plier au cahier des charges à remplir pour les télécommunications et notamment pour les liens optiques de l'ordre du kilomètre 'Long Reach 4' : 100GbaseLR4 ou 40GbaseLR4. L'objectif de ces standards est de fournir de l'information grâce à 4 longueurs d'ondes autour de 1310 nm (1295 nm, 1300 nm, 1305 nm, 1310 nm) sur plus de 10 km grâce à du multiplexage. Les termes '100Gbase' et '40Gbase' font référence à la vitesse du signal : chaque longueur d'onde doit être modulée à 25 Gbit/s ou 10 Gbit/s. Pour que la propagation soit possible sur la distance souhaitée, le laser doit non seulement être assez puissant (i.e. quelques milliwatts dans le guide) mais aussi atteindre un SMSR supérieur à 30 dB pour assurer la différenciation des modes à l'arrivée. De plus, pour que les circuits optiques soient compatibles avec les fluctuations de températures liées aux alimentations, le laser doit être opérationnel de 10 à 80 °C. Enfin, pour assurer une consommation énergétique minimale, le seuil du laser doit être le plus bas possible (<50 mA) et l'efficacité du laser aussi élevée que possible (>10 %). Ces lasers visant une utilisation pour du multiplexage, leur FWHM doit être aussi fine que possible (<1 nm) pour que les différentes longueurs d'onde n'interfèrent pas entre elles. La possibilité d'accorder le laser en longueur d'onde est également un avantage. Même s'il est possible de moduler le signal délivré par le laser à sa sortie grâce à un modulateur électro-optique, la possibilité de moduler directement le laser a été étudiée. Pour répondre aux normes LR4, les dispositifs conçus doivent être modulés jusqu'à des fréquences de 10 ou 25 Gbit/s ce qui correspondrait à des bandes-passantes à -3 dB supérieures à 6.5 GHz et 16.5 GHz respectivement.

Comme expliqué au début de cette introduction, les lasers conçus lors de ces travaux sont hybrides, c'est-à-dire que le gain est fourni par un guide III-V dans lequel la lumière est confinée lors du passage dans la zone active et que le reste de la cavité est construite dans le guide silicium en dessous de la zone III-V. Pour obtenir les propriétés voulues, différentes zones du laser doivent être étudiées. D'abord la zone de gain, mais aussi le couplage entre les deux matériaux (III-V et Si). Celui-ci se base sur la construction de tapers adiabatiques conçus de manière à rester aussi robustes que possible vis-à-vis des variations liées à la fabrication. Enfin, la cavité doit être construite de manière à obtenir un confinement élevé avec malgré tout assez de puissance en sortie. Ces travaux sont concentrés sur les cavités à base de réseaux de Bragg inscrits dans le Si. La longueur d'onde souhaitée (1.31  $\mu\text{m}$ ) rend les choses plus difficiles qu'à 1.55  $\mu\text{m}$  étant donné que la période de ces réseaux est alors plus petite.

## 1. Architecture du laser et couplage adiabatique

Cette partie détaille ce qui est commun aux différents lasers fabriqués au long de cette thèse c'est-à-dire leur architecture globale, mais aussi la méthode de couplage entre le guide III-V et le guide silicium. La méthode de fabrication est vue en détail dans le manuscrit anglais.

### 1.1. Vue d'ensemble d'un laser

Une coupe longitudinale et transversale d'un des lasers étudiés ici est représenté sur la Figure C-4 dans le cas d'un laser DFB. Les guides III-V et Si sont séparés d'une couche de silice d'environ 100 nm. La zone active mesure soit 500  $\mu\text{m}$ , 600  $\mu\text{m}$  ou 700  $\mu\text{m}$  de long ( $L_{\text{gain}}$ ). Le guide III-V est constitué de multiples puits quantiques (MPQ) d'InGaAsP avec un maximum de gain centré (dans le cas idéal) sur 1310 nm. Ceux-ci sont encadrés par des couches d'InP dopées  $n$  ou  $p$  formant ainsi une jonction PIN dans laquelle la zone intrinsèque n'est autre que les MPQ. Puisqu'on est dans une configuration DFB, le réseau est gravé le long du guide Si en-dessous de la zone III-V. Dans le cas d'un DBR, ce réseau aurait également été gravé dans le guide Si mais encadrerait la zone active. Le guide silicium se divise en deux parties : une fine arrête (rib) de 200 nm d'épaisseur posée sur un guide plus large de 300 nm d'épaisseur. Selon le guide où la lumière doit être confinée (Si ou III-V) l'arrête rib est plus ou moins large ( $W_{\text{Si}}$ ).

Il a été choisi ici de confiner la lumière dans le III-V lors de son passage dans la zone active pour maximiser le gain puis de la transférer dans le guide silicium. L'arrête rib doit donc être assez fine sous le guide III-V et s'élargir en sortie de la zone active. Cet élargissement se fait de manière adiabatique sur 100  $\mu\text{m}$  de long comme on le verra dans la suite de cette partie. Le couplage entre le III-V et le Si se fait avec plus de 90 % d'efficacité. La lumière laser est collectée en sortie grâce à une fibre placée au-dessus d'un réseau de couplage conçu spécifiquement.

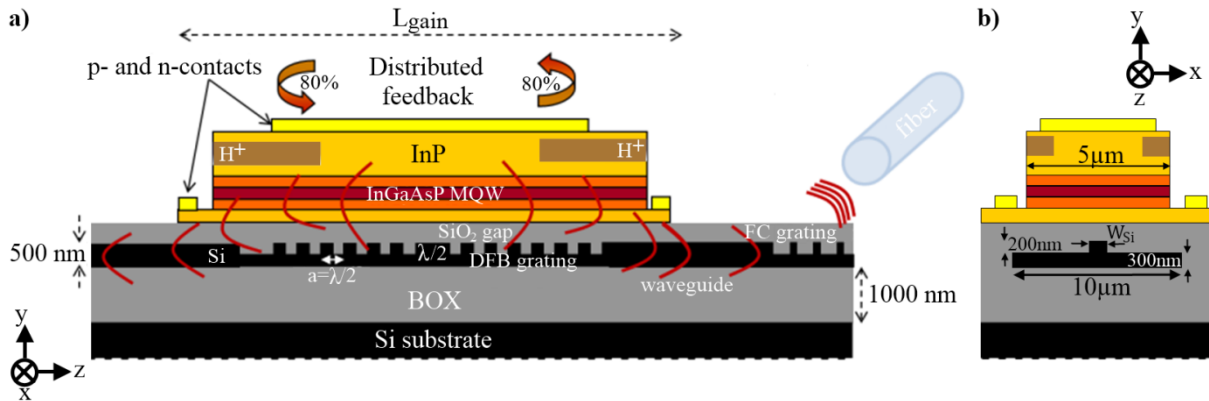


Figure C-4: Longitudinal (a) and transversal (b) schematics views of the laser.

Comme en témoigne la Figure C-4 (b), les bords du guide InP sont implantés avec des ions  $\text{H}^+$  sur environ 3  $\mu\text{m}$ . Cette implantation permet de créer intentionnellement des défauts sur les bords du guide augmentant ainsi leur résistivité. Lors de l'injection de porteurs, ceux-ci vont donc se déplacer préférentiellement au centre du guide III-V. L'efficacité d'injection est ainsi améliorée car les recombinaisons non-radiatives liés à des défauts sur les bords de guide sont limitées. De plus, ça permet également d'augmenter le recouvrement ( $\Gamma$ ) entre le mode optique, situé au centre du guide, et les porteurs et donc de diminuer le seuil du laser.

## 1.2. Couplage entre guide III-V et guide silicium

Le coupleur entre le III-V et le silicium est un élément essentiel du composant. Le transfert de lumière entre deux guides parallèles (comme c'est le cas ici) peut s'effectuer de deux manières : soit par couplage directionnel, soit par un transformateur de mode. Dans le premier cas, aussi appelé couplage résonant, les guides sont conçus de manière à ce qu'à la longueur d'onde d'intérêt, la lumière oscille d'un guide à l'autre lors de sa propagation. La longueur de couplage est très courte dans ce cas mais la technique est peu robuste vis-à-vis des variations dimensionnelles. Dans le second cas, utilisée ici, le guide Si change de forme (s'élargit) afin d'assurer le transfert de l'onde optique. Les longueurs de couplages sont plus longues (plusieurs dizaines de micromètres) mais des variations liées à la fabrication ont beaucoup moins d'impact. Comme le montre ce qui suit, la forme du coupleur est régie par la théorie des supermodes.

### *Théorie des supermodes et critère d'adiabaticité*

Selon la théorie des supermodes, décrite en détail dans le corps du manuscrit, les modes en présence dans la structure couplée ne sont autres que les modes propres de la structure. En faisant l'hypothèse d'un faible couplage, la théorie des modes couplés décrit ces modes comme une combinaison linéaire des modes de chaque guide isolé. Pour un mode dans un guide seul, il faut donc considérer deux modes pour une architecture avec deux guides couplés ; ceux-ci sont appelés modes pair ( $E_e$  pour even) et impair ( $E_o$  pour odd).

Soit  $\beta_1$  et  $\beta_2$  les constantes de propagation dans les guides isolés III-V et Si respectivement ( $\beta_i = \frac{2\pi}{\lambda} n_{\text{eff},i}$ ). Trois cas limites sont à considérer et sont représentés sur la Figure C-5. Lorsque l'indice effectif du guide 1 (2) est plus grand que celui du guide 2 (1), i.e.  $\beta_2 < \beta_1$ ,  $|\delta| \gg |\kappa|$  ( $\beta_1 < \beta_2$ ,  $|\delta| \gg |\kappa|$ ), les calculs montrent que le mode pair est surtout confiné dans le guide III-V (Si) alors que le mode impair est plus confiné dans le guide Si (III-V). Lorsque les deux guides ont le même indice effectif, i.e. ( $\beta_2 = \beta_1$ ) l'intensité de chaque mode est répartie de la même manière dans les deux guides, c'est la coïncidence de phase.

Il apparaît clairement qu'en utilisant ce phénomène, il est possible de transférer un mode optique d'un guide à l'autre en changeant son indice effectif. Pour ce faire, il faut modifier la largeur d'un ou des deux guides assez progressivement pour minimiser les pertes et obtenir un transfert dit adiabatique. La manière la plus facile d'obtenir un transfert adiabatique est d'augmenter la largeur du guide Si de manière linéaire, sur une très longue distance (i.e. plusieurs centaines de  $\mu\text{m}$ ). Le problème c'est que la cavité laser est alors très grande et autorise un trop grand nombre de modes lasers. Pour limiter la longueur du taper à 100  $\mu\text{m}$ , il faut donc trouver une forme d'élargissement plus 'efficace' d'où l'intérêt de l'étude des supermodes. L'objectif étant de transférer un seul deux supermodes pair et impair, des calculs sont faits pour ne garder qu'une fraction ( $\epsilon$ ) très faible ( $< 5\%$ ) du mode impair. On obtient alors la variation optimale de l'indice effectif du guide Si en fonction de la position en  $z$ . Comme des calculs numériques (par éléments finis) nous permettent de connaître la valeur d'indice effectif des modes en fonction de la largeur des guides (cf. Figure C-6), on peut ensuite en déduire la largeur des guides en fonction de la position  $z$  (cf. Figure C-7 (b)).

$$W_{\text{Si}}(z) = W_{\text{in}} + (W_{\text{out}} - W_{\text{in}})f(z) \quad [\text{C.1}]$$

Dans l'équation [C.1],  $W_{\text{in}}$  et  $W_{\text{out}}$  sont respectivement les largeurs d'entrée et de sortie du coupleur Si ; ce sont des paramètres à optimiser une fois qu'on connaît la forme du taper ( $f(z)$ ).



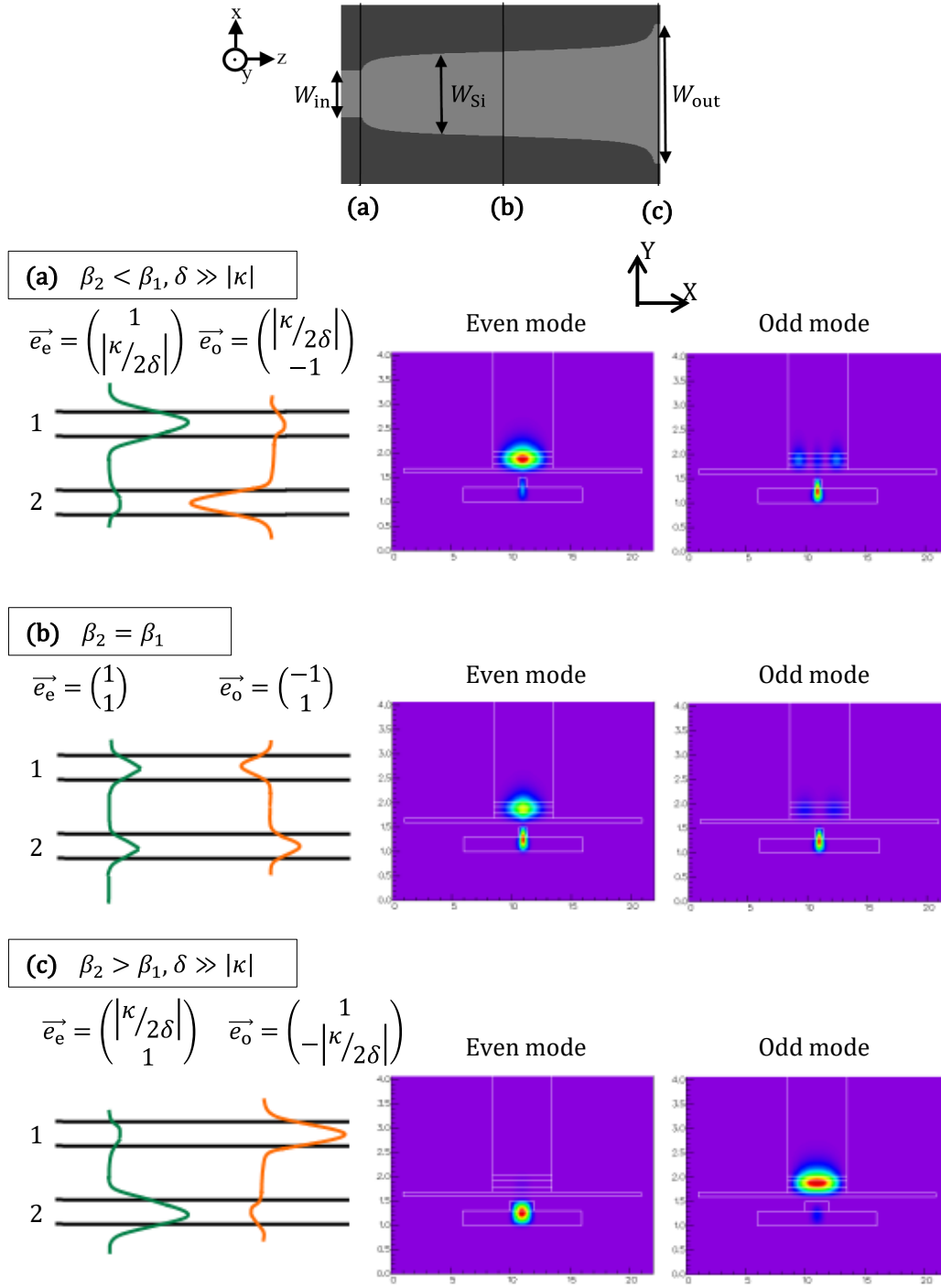


**Figure C-5: Even and Odd mode representation and their transverse intensity for different configurations of the coupled structure with  $W_{III-V}=5\mu\text{m}$ ,  $\text{SiO}_2$  gap=100 nm, and (a)  $W_{Si} = 0.62 \mu\text{m}$ , (b)  $W_{Si} = 0.70 \mu\text{m}$ , (c)  $W_{Si} = 2.00 \mu\text{m}$ . The intensity repartition was calculated with a FEM mode solver. The top figure stands for a top view of the Si waveguide.**

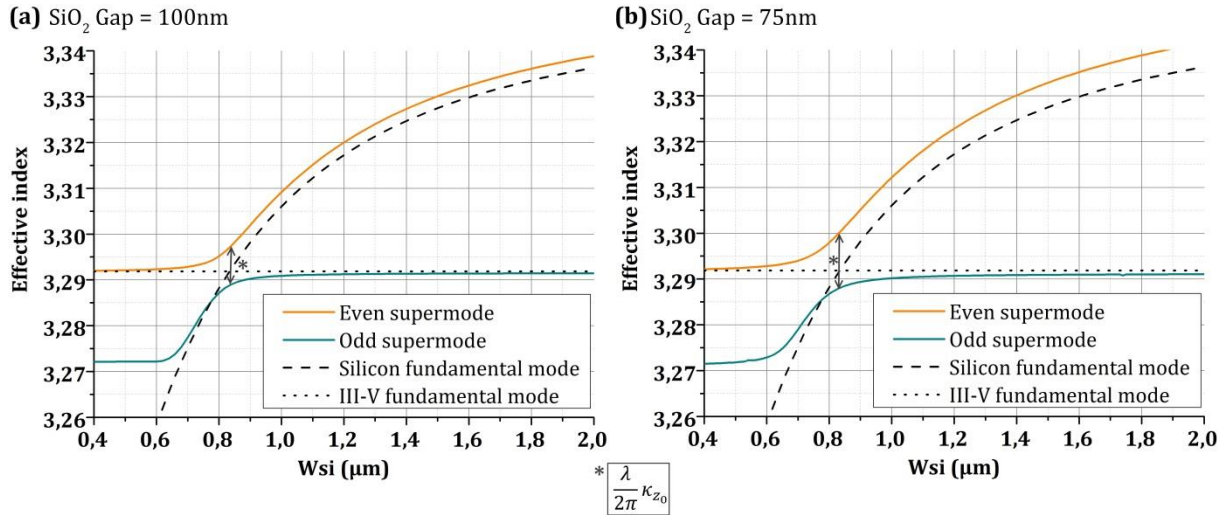


Figure C-6: Supermodes evolution with  $W_{Si}$  for two different oxide thicknesses between III-V and Si:  
(a)  $g=100$  nm, (b)  $g=75$  nm. Calculations were made using a FEM mode solver.

Sur la Figure C-7 (b), il y a aussi les courbes de tapers ‘tronqués’ c’est-à-dire que la forme du taper est calculée en considérant les variations d’indice effectif seulement à partir de  $W_{Si}=0.6 \mu m$  au lieu de  $W_{Si}=0.4 \mu m$ . On verra dans la suite que ces tapers sont nécessaires pour des lasers DFB.

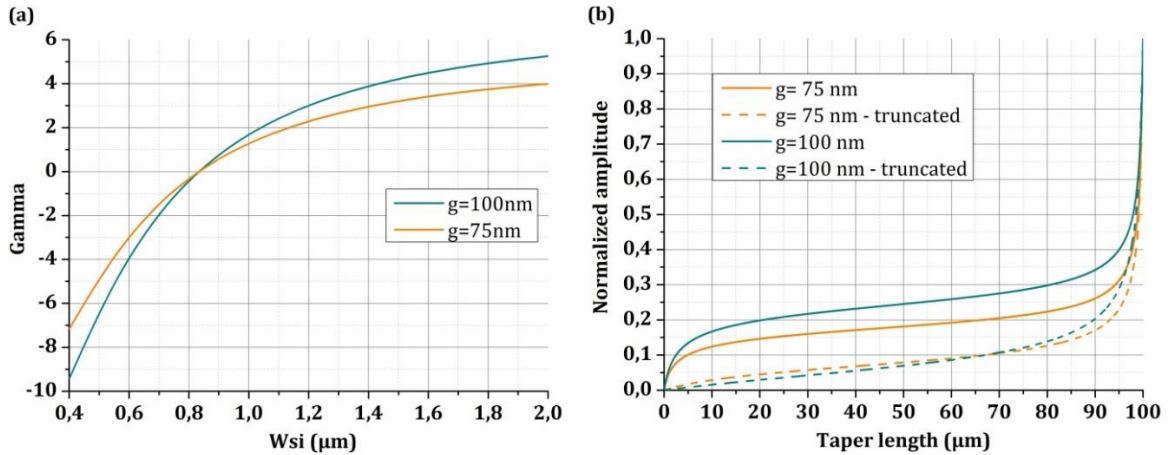


Figure C-7: (a)  $\gamma$  values versus the silicon waveguide width. (b) Normalized amplitude for different taper shapes

### Propriétés des tapers et robustesse

Une fois la forme des différents transformateurs de mode obtenue, il faut étudier leur robustesse en fonction des variations des différents paramètres (largeur d’entrée/sortie, épaisseur entre III-V et Si, alignement des guides...). Pour cela, l’efficacité des tapers est calculée grâce à un solveur de modes qui utilise la BPM (beam propagation method) en fonction de la largeur d’entrée et de sortie. Dans tous les cas, la longueur des tapers est fixée arbitrairement à  $100 \mu m$ . Les résultats sont tracés sur la Figure C-8 pour 4 tapers différents : ils sont conçus pour une épaisseur ( $g$ ) entre le III-V et le Si soit de  $75$  nm soit de  $100$  nm et peuvent être tronqués. Dans chaque cas, il s’agit de sélectionner le couple ( $W_{in}$ ;  $W_{out}$ ) de manière à ce que l’efficacité du coupleur reste supérieure à  $90\%$  dans la fenêtre de variation de la fabrication, comme c’est le cas ici.

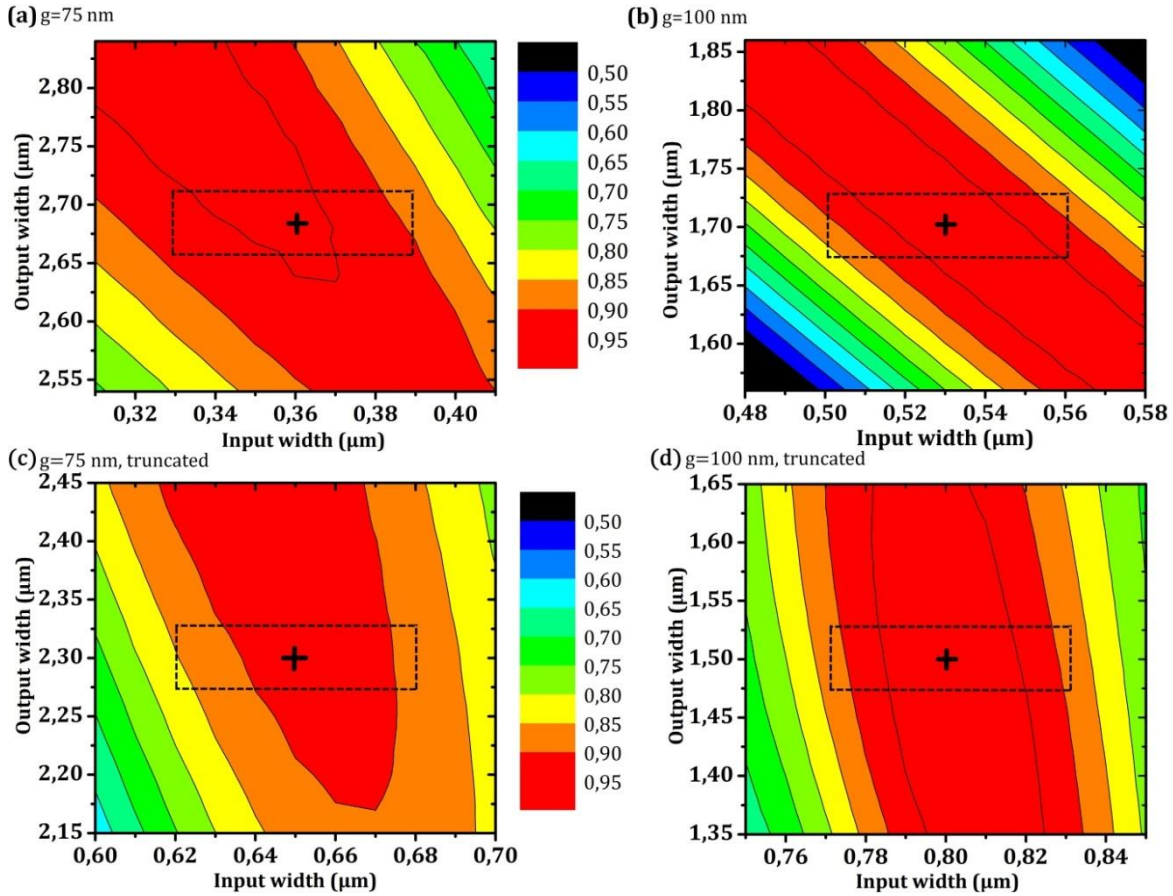


Figure C-8: 2D-map of the 100-μm-long taper's coupling efficiency depending on the input and output widths. The four cases seen above are represented: (a)  $g=75$  nm, (b)  $g=100$  nm, (c) truncated version of  $g=75$  nm, (d) truncated version of  $g=100$  nm. The efficiency was calculated using a BPM mode solver. The cross stands for the highest coupling value and the dashed square for the process window ( $\pm 30$  nm).

Les autres incertitudes liées à la fabrication sont l'épaisseur de  $\text{SiO}_2$  entre le III-V et le Si et le désalignement entre les guides ( $dX$ ). L'efficacité des tapers est tracée pour chacun de ces paramètres sur la Figure C-9. Le désalignement a peu d'impact puisque l'efficacité reste supérieure à 90 % jusqu'à  $dX=0.5$  μm alors que la précision de ce paramètre est de l'ordre de  $\pm 125$  nm. Au contraire, le gap de silice est un paramètre beaucoup plus critique comme le montre la Figure C-9 (b), sachant qu'au centre du wafer (là où sera collée l'épithaxie III-V), la précision sur  $g$  est de  $\pm 15$  nm. C'est la raison pour laquelle, des lasers avec des tapers conçus pour différentes valeurs de  $g$  sont prévus sur chaque plaque. Le graphe montre que pour que les deux types de tapers aient une efficacité acceptable, il faut viser une épaisseur de 90 nm entre les guides.

Pour terminer l'étude des transformateurs de mode, la dernière étape consiste à vérifier s'ils sont bien adiabatiques. Pour ce faire, il faut tracer leur efficacité en fonction de la longueur du taper (qui avait été fixée à 100 μm au départ) comme sur la Figure C-10. Les tapers sont bien adiabatiques car une fois que le maximum d'efficacité est atteint, celui-ci change très peu quelle que soit la longueur du taper. Si le couplage n'avait pas été adiabatique, de fortes oscillations auraient été observées qui correspondraient à un couplage directionnel d'un guide à l'autre. On remarque malgré tout de très faibles oscillations. Celles-ci sont dues au couplage vers le mode impair qui n'est pas nul puisque lors des calculs de la forme du taper, on est obligé de considérer une fraction  $\epsilon$  de ce mode sans quoi le taper serait infiniment long.

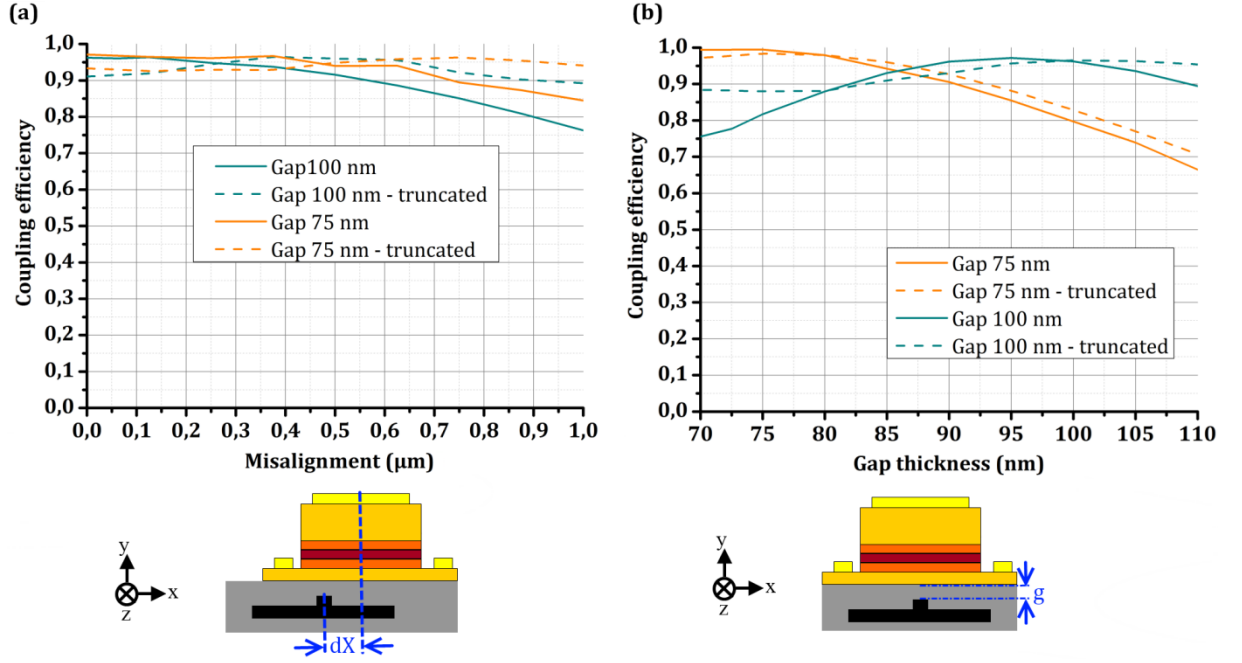


Figure C-9: Tapers' coupling efficiency dependence on the process variations : (a) misalignment between the III-V and the silicon, (b) silicon gap thickness between the waveguides.

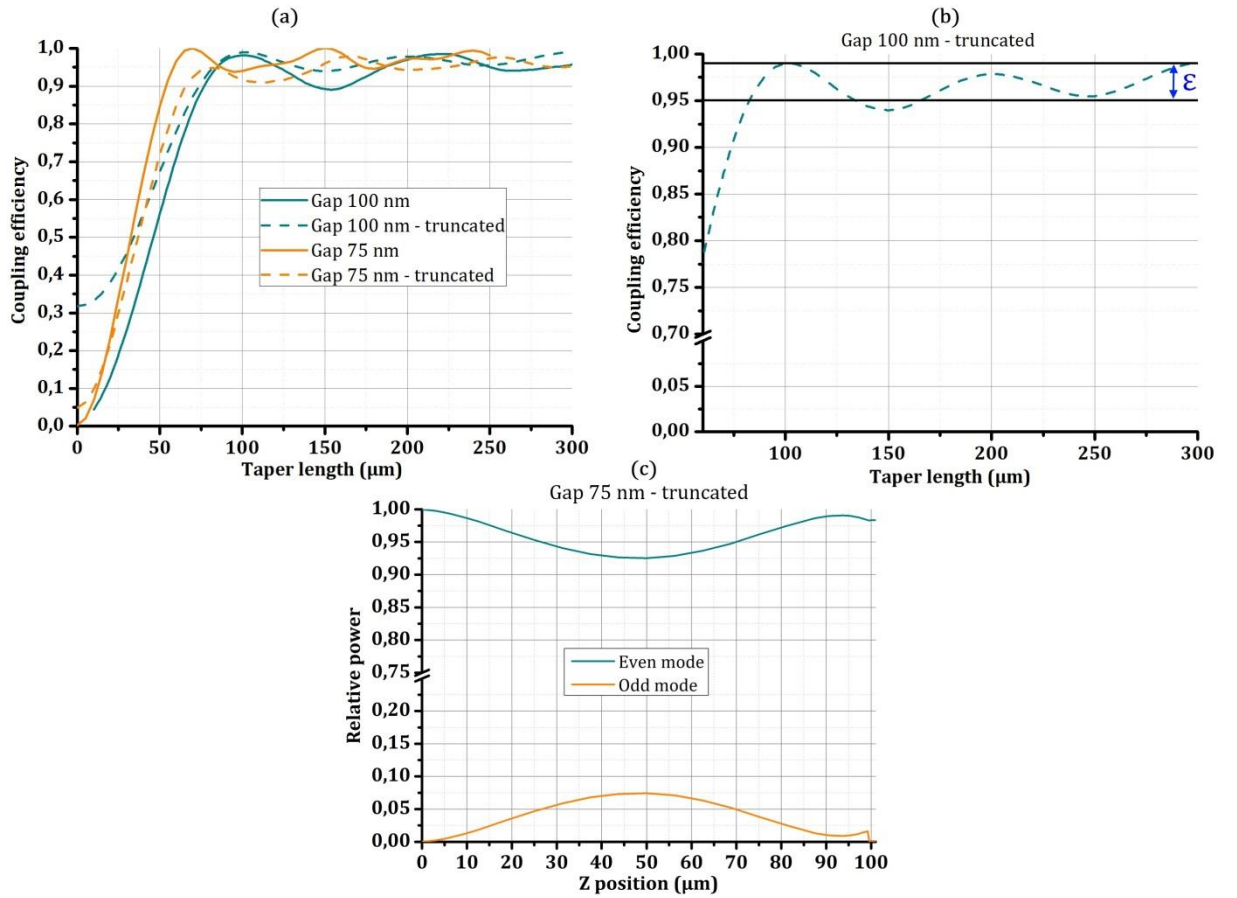


Figure C-10: (a) Coupling efficiency of the mode transformers as a function of their length. (b) Focus on the truncated taper with a 100 nm oxide thickness where the losses toward the odd mode are schematized. (c) Relative power in the even and odd modes along the taper.

## 2. Laser DFB

Comme évoqué lors de la description générale des lasers conçu lors de cette thèse, dans un laser DFB il n'y a qu'un seul réseau inscrit dans le Si sous le III-V (cf. Figure C-11). Deux types de DFB ont été étudiés : soit un réseau couplé verticalement soit couplé latéralement. Dans le premier cas, plus classique, le réseau est gravé sur le dessus du guide alors que dans le second, jamais réalisé sur un laser hybride avant cette thèse, le réseau est gravé sur les flancs du guide. L'avantage d'une telle solution est non seulement d'éviter un niveau de gravure spécifiquement lié au réseau puisqu'il est gravé en même temps que le guide, mais aussi d'ajouter plus de flexibilité au design des tapers (plus de possibilité pour la largeur d'entrée). Les paramètres et résultats des deux types de lasers sont détaillés ci-dessous.

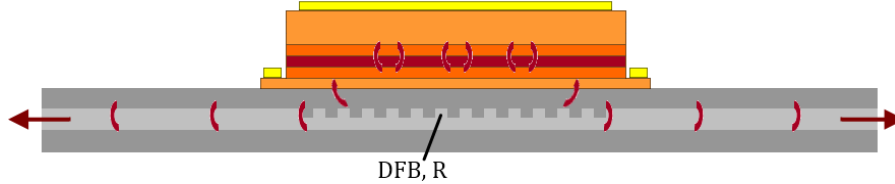


Figure C-11: Schematic representation of a hybrid III-V on Si DFB laser.

### DFB lasers couplés verticalement

Une vue de côté et du dessus de la zone active du DFB couplé verticalement sont représentées sur la Figure C-12. La distribution modale est représentée sur la vue de côté selon que le guide est gravé ou non : dans le second cas, l'indice effectif du mode dans le guide Si isolé est plus grand d'où une plus grande concentration du mode dans le Si. Pour avoir un laser DFB monomode, un défaut doit être inscrit dans le réseau (de préférence au centre) sans quoi il y aurait deux longueurs d'onde amplifiées : ce défaut est appelé 'lame quart-d'onde' car il doit mesurer  $\lambda/4n_{\text{eff}}$ . Les paramètres associés à ce type d'architecture sont :

- La longueur du réseau ( $L_{g,\text{DFB}}$ ) fixée à 500  $\mu\text{m}$  ou 1000  $\mu\text{m}$ ,
- La période du réseau ( $a$ ), où  $a \in [194; 196; 198; 199; 200; 202]$  nm,
- La profondeur de gravure ( $e$ ) fixée à 80 nm ou 100 nm,
- La largeur du guide silicium ( $W_{\text{Si}}$ ) qui est aussi la largeur d'entrée du taper et vaut soit 650 nm soit 800 nm pour cette architecture.

Les simulations et explications qui ont permis de fixer ces différentes valeurs sont données dans le corps du manuscrit. Il est cependant important de noter que pour avoir une réflectivité du réseau convenable,  $W_{\text{Si}}$  doit ici être supérieure à 600 nm d'où l'obligation de tronquer les tapers (car  $W_{\text{Si}} = W_{\text{In}}$ ) ce qui limite le nombre de designs possible pour ces coupleurs.

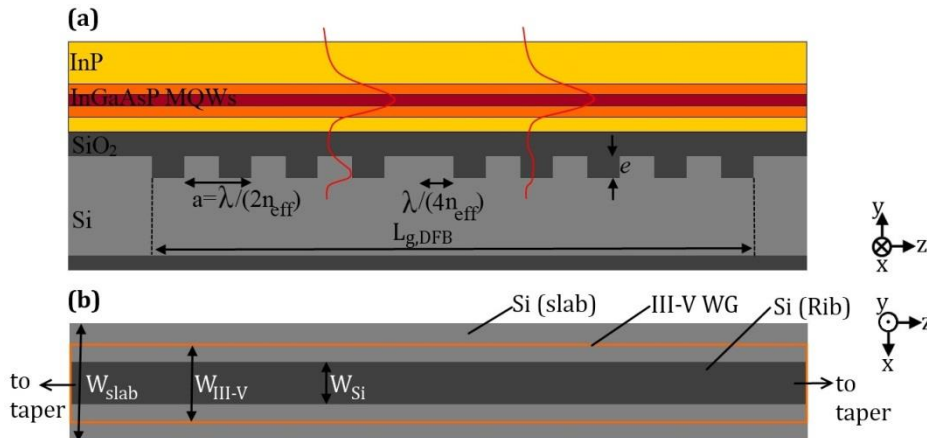


Figure C-12: Side (a) and top (b) schematic views of the DFB laser with a grating etched on the top of the Si waveguide. The Si slab width is  $W_{\text{slab}}=10 \mu\text{m}$  and the III-V WG width is  $W_{\text{III-V}}=5 \mu\text{m}$ .  $W_{\text{Si}}$  needs to be defined.



Les caractérisations de ces lasers ont été effectuées sur trois différentes plaques 2 pouces et un rendement moyen de 89 % a pu être déduit. Cependant, à cause des variations dimensionnelles liées à la fabrication d'une plaque à l'autre, tous les dispositifs ne sont pas aussi bons. Trois des meilleurs composants sont présentés ici ; leurs propriétés sont synthétisées dans le Tableau 1.  $\Delta n_{\text{eff,calc-real}}$  représente l'écart d'indice effectif entre ce qui avait été calculé et ce qui a été obtenu et qu'on a déduit grâce à la longueur d'onde du laser ( $\lambda_{\text{peak}}$ ). Cet écart peut être expliqué par le fait que, pour ce lot, les épitaxies commandées n'étaient pas aussi épaisses que ce qui avait été souhaité. Les mesures des pertes entre le guide et la fibre ont été menées grâce à des motifs de test spécifiques.

**Tableau 1: Propriétés des lasers DFB couplés verticalement sélectionnés.**

Laser	Taper	Gap SiO <sub>2</sub> réel	a (nm)	$\lambda_{\text{peak}}$ (nm)	$\Delta n_{\text{eff,calc-real}}$	Pertes coupleur-fibre
1	Gap 75 nm tronqué	~70 nm	202	1305	-0.07	6 dB
2	Gap 100 nm tronqué	~100 nm	202	1305	-0.06	
3	Gap 75 nm tronqué	~100 nm	200	1292		

La tension ainsi que la puissance de sortie du laser sont représentées en fonction du courant d'injection laser sur la Figure C-13. On en déduit des résistances de 7.0  $\Omega$ , 5.4  $\Omega$  et 5.6  $\Omega$  pour les lasers 1, 2 et 3 respectivement. L'écart entre le premier composant par rapport aux deux autres vient du fait qu'il n'était pas sur la même plaque. En s'affranchissant des pertes liées au couplage vers la fibre, la puissance dans le guide déduite est de 22.3 mW, 11.4 mW et 8.5 mW pour les laser 1, 2 et 3 et l'efficacité différentielle de 25%, 12% et 10%. Le fait que la puissance est supérieure pour le laser 1 peut être expliqué par le fait que la valeur du gap de silice correspond au taper conçu et aussi que dans le cas du taper conçu pour 75 nm de gap et tronqué, la largeur du guide Si est plus fine que pour le cas 100 nm de gap tronqué (650 nm au lieu de 800 nm). Le mode optique est donc plus confiné dans le III-V et par conséquent plus amplifié.

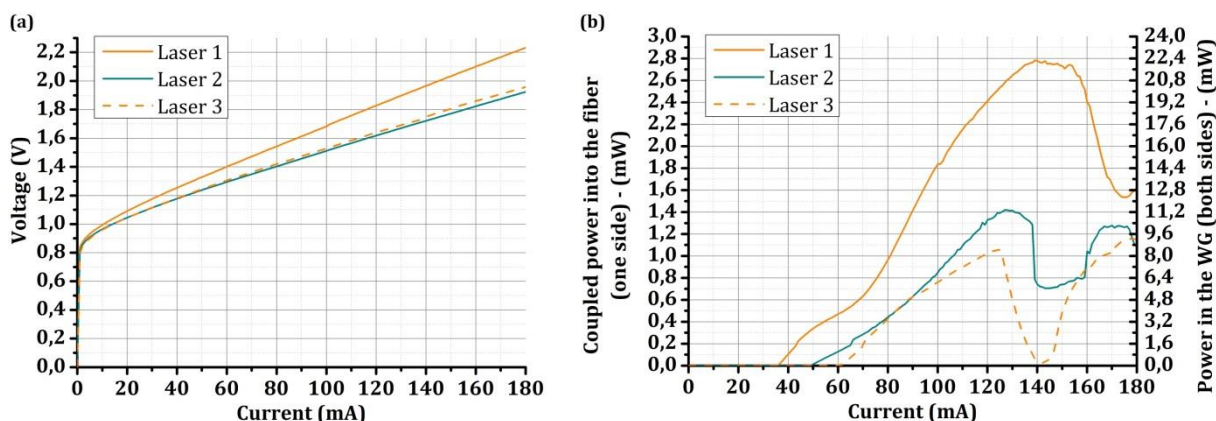


**Figure C-13: Lasers' voltage (a) and output power (b) as a function of the injected current for vertically coupled DFB lasers 1, 2 and 3.**

Les spectres des trois lasers sont tracés en fonction du courant d'injection sur la Figure 3-23. Le SMSR maximum est représenté sur la Figure C-14 (d) et vaut respectivement 56.6 dB, 52.3 dB et 39.9 dB. Le premier laser témoigne d'une très grande pureté spectrale tout au long de l'augmentation du courant. Pour les deux autres lasers, cette pureté n'est pas aussi nette ce qui peut être expliqué par une compétition modale aux courants élevés. Pour le laser 2, on peut voir sur la Figure C-15 (b) qu'il y a une compétition entre le mode DFB et les modes d'air et diélectriques qui sont liés à un réseau DFB qui n'aurait pas de lame quart-d'onde. Ceci prouve que le défaut du réseau est peut-être mal défini dans ce cas et aussi car le mode principal est moins amplifié que pour le laser 1. Pour le laser 3, l'explication est différente : la période est plus faible pour ce dispositif et le mode laser n'est donc pas centré sur le maximum de gain des puits quantiques. Des modes Fabry-Pérot (eux centrés sur ce maximum)

apparaissent donc à partir d'une certaine valeur de courant (cf. Figure C-15 (c)). Les valeurs de SMSR restent cependant bonnes sur une large gamme de courant pour les lasers 1 et 2.

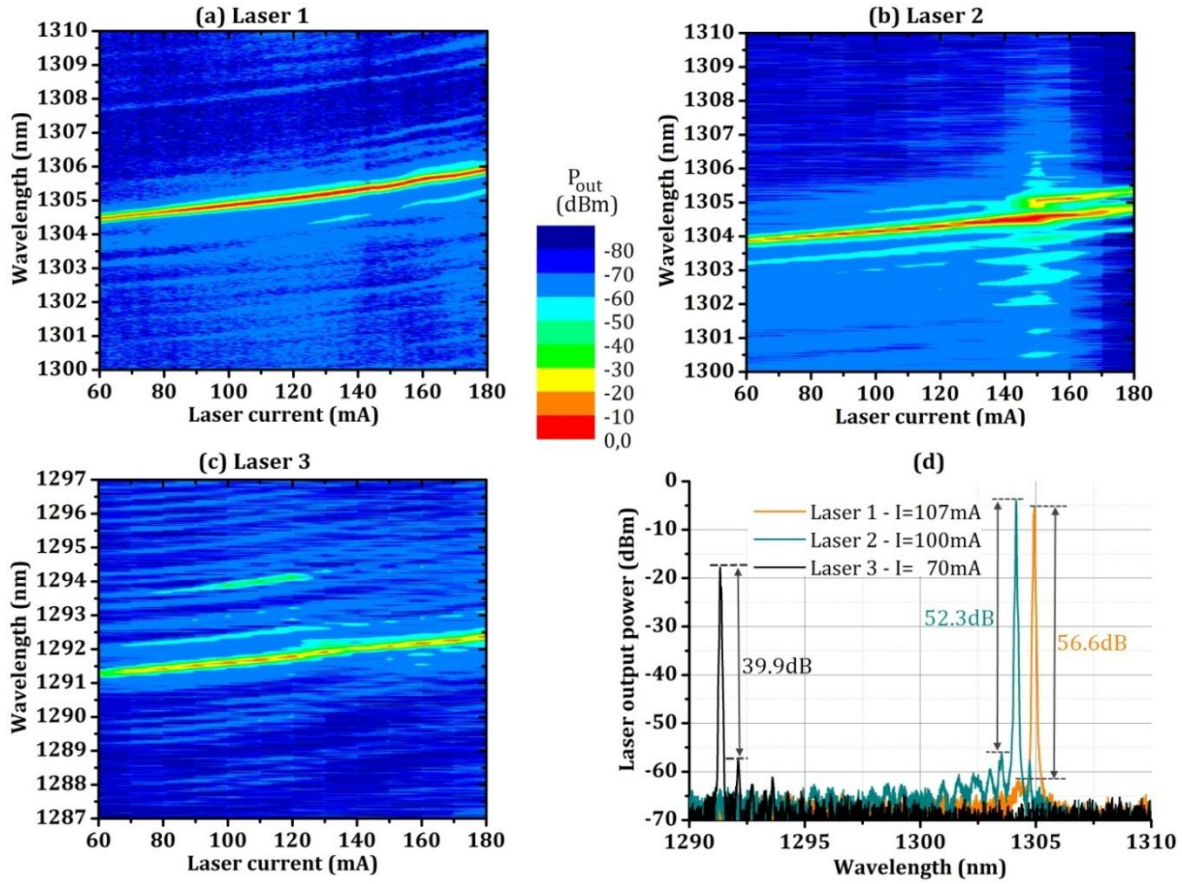


Figure C-14: Lasers spectra with varying injected current for lasers 1 (a), 2 (b) and 3 (c). (d) displays the spectrum of each laser at the current for which the best SMSR is obtained.

Les performances RF et en température ont également été mesurées et sont détaillées dans le manuscrit anglais. La température maximale d'opération de ces lasers est de 55 °C. Une bande passante à -3 dB de 6.7 GHz a été trouvée et le diagramme de l'œil de ce laser est resté ouvert jusqu'à 12 Gbit/s.

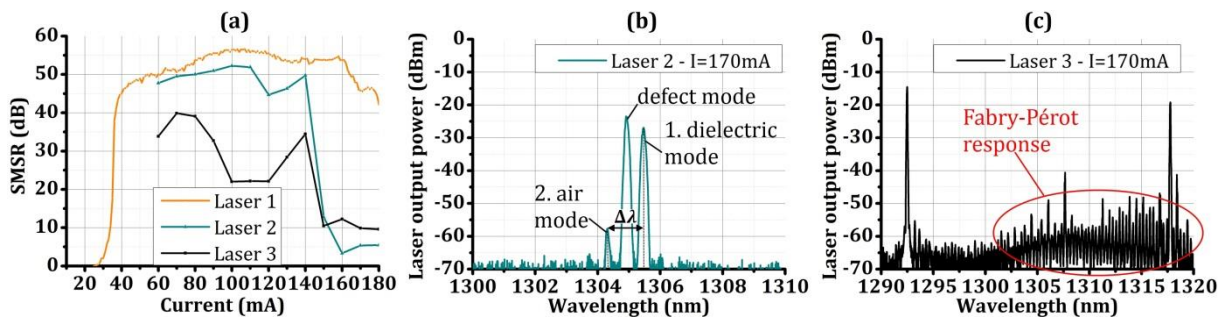


Figure C-15: (a) Lasers SMSR as a function of the injected current. (b) and (c) show spectra of lasers 2 and 3 respectively when the SMSR is low.

Les différentes mesures effectuées sur les trois lasers sont rassemblées dans le Tableau 2.



**Tableau 2: Caractéristiques mesurées de trois lasers DFB couplés verticalement.**

Laser	R ( $\Omega$ )	$\lambda_{\text{peak}}$ (nm)	$\kappa_{\text{g,calc}}$ ( $\text{cm}^{-1}$ )	$\kappa_{\text{g,meas}}$ ( $\text{cm}^{-1}$ )	$I_{\text{th}}$ (mA)	$I_{\text{th}}$ ( $\text{kA}/\text{cm}^2$ )	$P_{\text{max}}$ (mW)	$\eta_{\text{diff}}$ (%)	$\Delta\lambda/\Delta P_{\text{el}}$ (nm/W)	$\text{SMSR}_{\text{max}}$ (dB)
1	7.0	1305	38	43.0	36	1.03	22.3	25.3	3.7	56.6
2	5.4	1305	32	36.5	50	1.43	11.4	12.7	3.5	52.3
3	5.6	1292	9	15.4	61	1.74	8.5	10.5	4.2	39.9

Pour conclure quant aux résultats obtenus pour ces lasers, la puissance des lasers est supérieure à quelques milliwatts ce qui convient par rapport aux requis décrits dans la 1ère partie. De plus, des SMSR largement supérieurs aux 30 dB souhaités ont été montrés. Les propriétés RF mesurées sont compatibles avec la norme 40GbaseLR4 puisque chaque laser doit être modulé à 10 Gbit/s. La seule propriété à améliorer est donc la température puisqu'on n'a eu un fonctionnement qu'à 55 °C au lieu de 80 °C.

### DFB lasers couplés horizontalement

Cette fois encore des schémas de la région active du laser vue de côté ou du dessus sont représentés sur la Figure C-16. La distribution modale montre bien que le mode est plus confiné dans le III-V lorsque la largeur du guide est plus fine. Cette fois, les paramètres à définir sont :

- La longueur du réseau ( $L_{\text{g,DFB}}$ ) fixée à 500  $\mu\text{m}$  ou 1000  $\mu\text{m}$ ,
- La période du réseau ( $a$ ), où  $a \in [194; 196; 198; 199; 200; 202]$  nm,
- La dent la plus étroite ( $W_{\text{narrow}}$ ) dont la valeur est imposée par la largeur d'entrée du taper ; ici 0.36  $\mu\text{m}$  ou 0.53  $\mu\text{m}$ ,
- La dent la plus large ( $W_{\text{large}}$ ) ; pour chaque valeur de  $W_{\text{narrow}}$ , deux valeurs de  $W_{\text{large}}$  ont été sélectionnées afin d'obtenir des réflectivités différentes (et comprises entre 0.4 et 1) dans chaque cas.

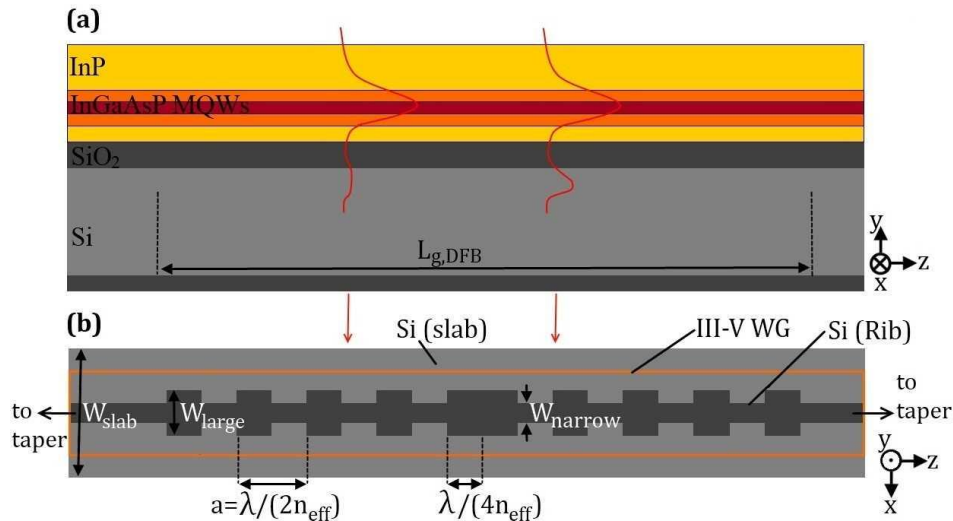


**Figure C-16: Side (a) and top (b) schematic views of the DFB laser with a grating etched on the edges of the Si WG. The Si slab width is  $W_{\text{slab}}=10 \mu\text{m}$  and the III-V WG width is  $W_{\text{III-V}}=5 \mu\text{m}$ .  $W_{\text{large}}$  and  $W_{\text{narrow}}$  need to be defined.**

Dans cette configuration, il n'était pas nécessaire de limiter  $W_{\text{narrow}}$  à des valeurs supérieures à 600 nm et on a pu utiliser des transformateurs de mode non tronqués, c'est-à-dire avec des largeurs d'entrée plus fines. Ces réseaux ont cependant demandé un développement supplémentaire lors de la fabrication car ils étaient mal résolus en photolithographie DUV 193 nm comme en témoigne l'image MEB du réseau sur la Figure C-17 (b). Les lasers testés avec ces réseaux étaient bi-modes ou alors fonctionnaient en mode Fabry-Pérot donc comme si le mode ne voyait pas le réseau. Il a fallu le définir en utilisant de la

lithographie e-beam, et plusieurs essais ont été requis avant d'obtenir le réseau représenté sur la Figure C-17 (c). Il faut cependant noter que certains réseaux définis en e-beam ont subi des erreurs de 'stitching' c'est-à-dire que lorsque le faisceau d'électrons se décale pour écrire plus loin, il ne se replace pas directement à la suite de ce qui est déjà lithographié ce qui induit un défaut non contrôlé dans le réseau. Les composants présentant ces problèmes montraient donc une compétition de mode.

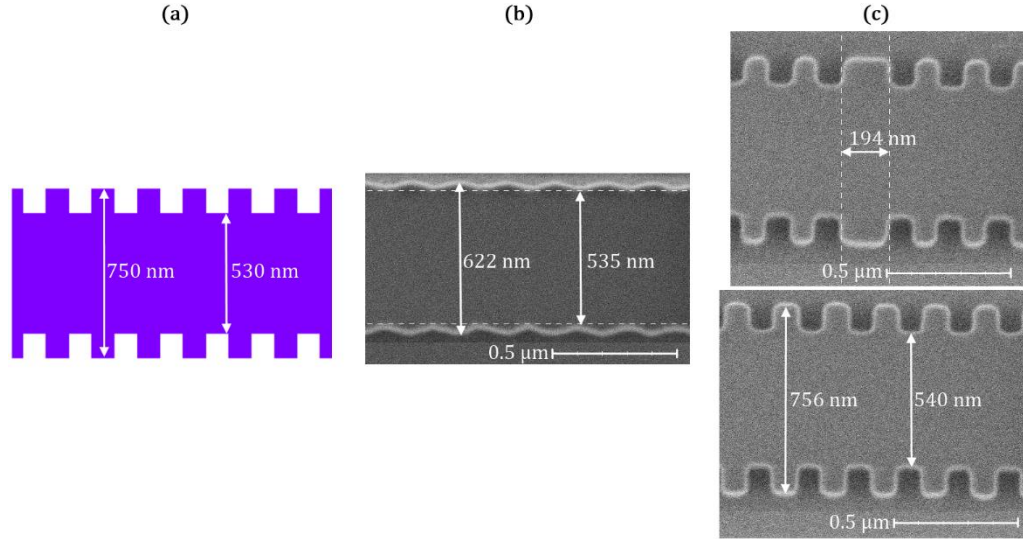


Figure C-17: (a) Grating design (b) SEM pictures after the DUV photolithography (b) or e-beam lithography (c) and the 200-nm-deep etching.

Cette fois encore, les résultats de trois des meilleurs lasers obtenus (en lithographie e-beam) sont présentés. Ils sont issus d'une même plaque pour laquelle l'épaisseur moyenne de silice entre les matériaux III-V et Si est de 120 nm environ. Leurs paramètres respectifs sont résumés dans le Tableau 3.

Tableau 3: Paramètres des lasers DFB couplés horizontalement sélectionnés.

Laser	Taper	$W_{\text{Large}}$ (μm)	$W_{\text{Narrow}}$ (μm)	Real SiO <sub>2</sub> gap	a (nm)	$\lambda_{\text{peak}}$ (nm)	$\Delta n_{\text{eff,calc-real}}$	WG to fiber coupler losses
1	Gap 100 nm	0.950	0.600	~120 nm	199	1299	-0.03	-6 dB
2	Gap 100 nm	0.950	0.600		200	1305		-5.5 dB
3	Gap 75 nm truncated	0.850	0.370		200	1299		-6.5 dB

Comme les graphes de la Figure C-18 le montrent, la résistance des trois lasers est comprise entre 4.1 et 5.0 Ω. L'observation de la puissance de sortie des lasers en fonction du courant d'injection montre que les lasers 1 et 2 ont des réponses classiques et atteignent une puissance dans le guide de 10.3 et 8.5 mW dans le guide avec des seuils de 56 et 50 mA. Pour ce qui est du laser 3, la puissance est deux fois plus élevée (20.2 mW) et  $I_{\text{th}}=48$  mA mais la courbe présente une bosse anormale autour de 150 mA. La meilleure puissance obtenue pour le troisième composant vient probablement du fait que les largeurs de guides Si sous le III-V ( $W_{\text{large}}$  et  $W_{\text{narrow}}$ ) sont plus fine et donc que l'onde optique est plus confinée dans le III-V lui permettant ainsi plus d'amplification.

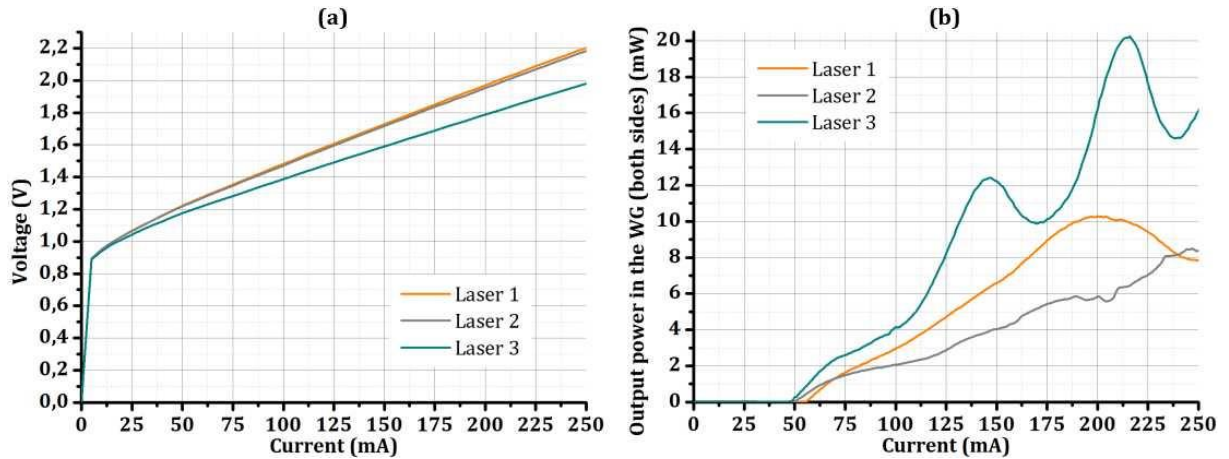


Figure C-18: Voltage (a) and power delivered by the laser in the WG (b) as a function of the laser current for the laterally coupled DFB lasers.

Les performances des lasers en termes de mode sont détaillées sur les Figure C-19 et Figure C-20. Les spectres des lasers 1 et 2 sont purs sur quasiment toute la gamme de courant avec des SMSR supérieurs à 40 dB sauf à certains endroits où une compétition modale avec les modes d'air et diélectrique du réseau est visible. D'une manière assez surprenante, le spectre du laser 3 est pur sur toute la gamme de courant avec un SMSR supérieur à 40 dB également. La bosse observée sur la courbe de puissance en fonction du courant laissait croire à une compétition de mode ce qui n'est pourtant pas le cas. L'origine de cette bosse n'a pu être déterminées avec certitude mais pourrait être expliquée par la présence d'un défaut dans la région III-V qui induirait de l'absorption pour des courants d'injection de 150 à 175 mA. Pour en avoir la certitude, il faudrait faire des observations du guide III-V et donc détruire le composant ce qui n'a pas été fait ici par manque de temps.

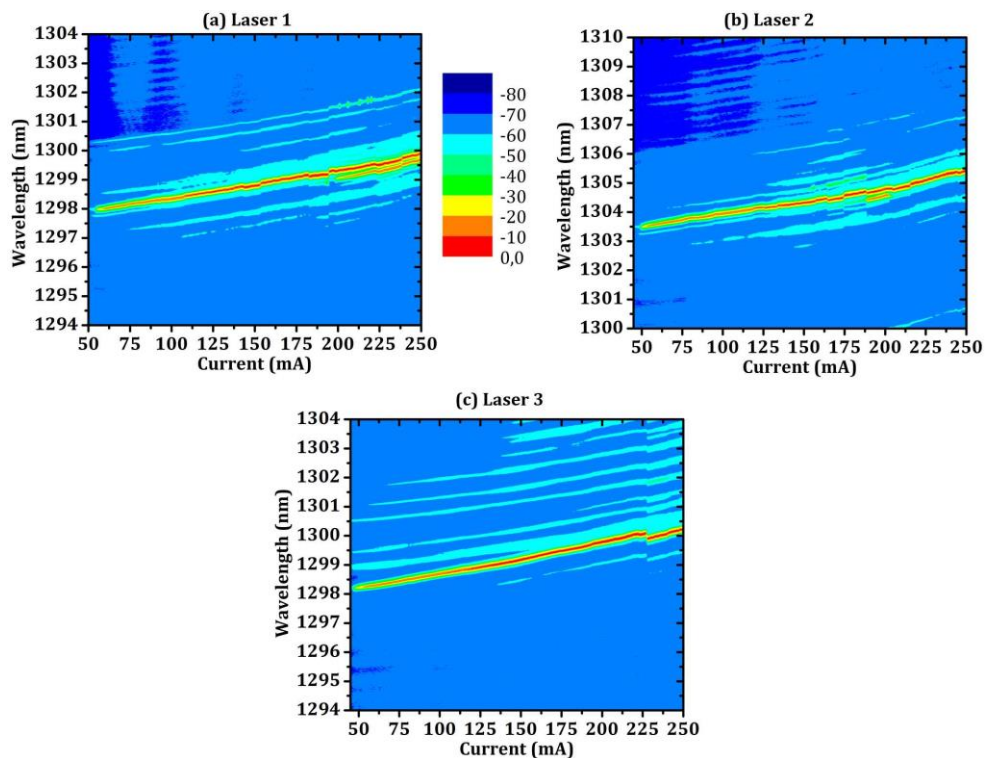


Figure C-19: Lasers spectra with varying injected current for laterally coupled DFB lasers 1 (a), 2 (b) and 3 (c).

La compétition de modes observée pour les deux premiers lasers a pu être expliquée par les analyses de leurs spectres (cf. Figure C-20 (b)). Comme expliqué dans le manuscrit, il est possible en étudiant ces spectres de déduire la force du réseau (et donc leur réflectivité déduite à partir de la constante de couplage du réseau  $\kappa_g$ ). Pour le laser 3, la réflectivité obtenue correspond à celle visée alors que pour les deux autres, elle est bien plus faible. Des calculs ont montré que les réflectivités obtenues correspondraient à des largeurs de guide  $W_{\text{Large}}$  inférieures à 900 nm au lieu des 950 nm attendus et un gap de quasiment 140 nm. Ceci n'a pu être vérifié (car cela aurait détruit les composants) mais l'éventualité d'un gap plus grand pour les dispositifs 1 et 2 est probable étant donné qu'ils sont loin du laser 3 sur la plaque. Les calculs de réflectivité pour le laser 3 montrent également que  $W_{\text{Large}}$  serait plutôt de 800 nm au lieu de 850 nm. On voit donc que même en utilisant la lithographie e-beam, la résolution des réseaux est encore à améliorer. Les études spectrales ont donc montré non seulement que la force du réseau est bien inférieure à celle prévue dans le cas des lasers 1 et 2 mais aussi que pour des constantes de couplage réelles équivalente pour les trois lasers, le laser 3 reste malgré tout plus pur. Cela est attribué au fait que le mode principal est plus confiné dans le III-V pour ce composant donc plus amplifié et moins sujet à une compétition modale.

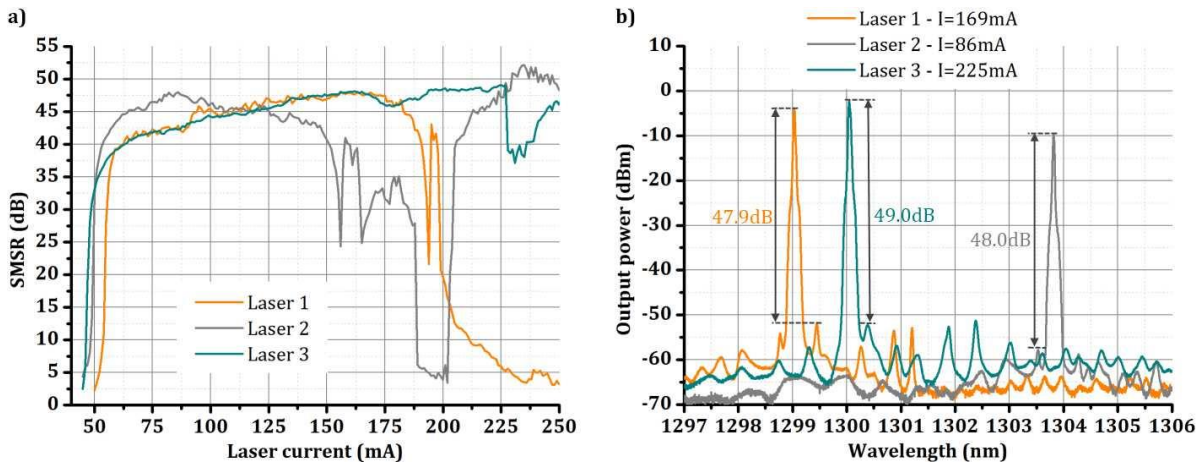


Figure C-20: SMSR with increasing lasers currents (a) and best spectra (b) for laterally coupled DFB laser 1, 2 and 3.

Malgré le fait que les réseaux sont un peu moins bien résolus que prévu, les résultats obtenus pour ces lasers sont très bons étant donné qu'il s'agit des premiers lasers DFB hybrides couplés latéralement fonctionnant à cette longueur d'onde. Leurs caractéristiques sont rassemblées dans le Tableau 4. De plus, les mesures des performances de ces lasers en température ont été menées et un fonctionnement laser jusqu'à 65 °C a été obtenu. Ce résultat, meilleur que dans le cas des lasers DFB couplés verticalement, est attribué au fait que l'épithaxie III-V n'est pas la même et qu'elle est probablement de meilleure qualité.

Tableau 4: Caractéristiques des lasers DFB couplés latéralement.

Laser	R ( $\Omega$ )	$\lambda_{\text{peak}}$ (nm)	$\kappa_{g,\text{calc}}$ ( $\text{cm}^{-1}$ )	$\kappa_{g,\text{meas}}$ ( $\text{cm}^{-1}$ )	$I_{\text{th}}$ (mA)	$J_{\text{th}}$ ( $\text{kA}/\text{cm}^2$ )	$P_{\text{max}}$ (mW)	$\eta_{\text{diff}}$ (%)	$\Delta\lambda/\Delta P_{\text{el}}$ (nm/W)	$\text{SMSR}_{\text{max}}$ (dB)
1	5.0	1299	208	21	56	1.60	10.3	7.7	3.1	47.9
2	4.9	1305	198	23	50	1.43	8.5	4.1	3.1	48.0
3	4.1	1299	46	20	48	1.37	20.2	12.7	3.4	49.0

Pour conclure quant aux résultats obtenus pour ces lasers, leur puissance est supérieure à quelques milliwatts ce qui convient par rapport aux requis décrits dans la 1ère partie et les SMSR sont largement supérieurs aux 30 dB souhaités. La température maximale se rapproche également des 80 °C espérés.

### 3. Lasers DBR

Contrairement aux lasers DFB, la cavité d'un laser DBR est formée par deux miroirs de Bragg encadrant la zone de gain. L'avantage de cette architecture est donc d'avoir plus de degrés de libertés concernant la conception des miroirs mais aussi la possibilité d'accorder la longueur d'onde du laser, comme discuté dans ce qui suit. Ce paragraphe décrit brièvement les différents paramètres des miroirs (dont le design précis se trouve dans le corps du manuscrit) ainsi que les résultats expérimentaux obtenus en terminant par l'accordabilité.

Le schéma d'un DBR est représenté sur la Figure C-21 : les miroirs de Bragg sont inscrits dans le guide silicium. Il a été choisi de n'avoir de la lumière laser que d'un côté des lasers conçus : l'un des miroirs est donc totalement réfléchissant, il s'agit du miroir arrière (BM pour 'Back Mirror') alors que l'autre 'fuit' ; c'est le miroir avant (FM pour 'Front Mirror').

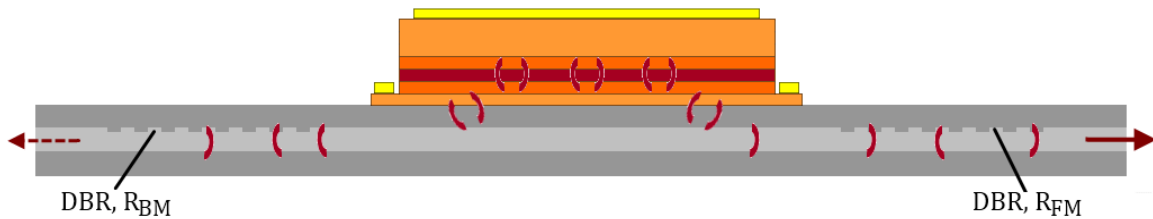


Figure C-21: Schematic representation of a III-V on silicon DBR laser.

#### Mirrors design

La Figure C-22 représente un miroir de Bragg selon deux coupes différentes avec les différents paramètres à fixer c'est-à-dire :

- La largeur du guide silicium ( $W_{Si}$ ), qui vaut ici  $3 \mu m$ ,
- La profondeur de gravure du réseau ( $e$ ), de  $10 \text{ nm}$  pour assurer une réponse des miroirs avec une FWHM assez fine,
- La période du réseau ( $a$ ) ; cette fois encore, plusieurs valeurs ont été choisies pour atteindre plusieurs longueurs d'onde :  $a \in [193; 195; 196; 197; 199] \text{ nm}$ ,
- Le facteur de remplissage du réseau (DC pour Duty Cycle), avec  $DC=0.5$  ce qui assure un miroir plus robuste,
- La longueur du réseau ( $L_g$ ), fixée à  $700 \mu m$  pour le miroir arrière et à  $75 \text{ nm}$ ,  $150 \text{ nm}$  ou  $200 \text{ nm}$  pour le miroir avant.

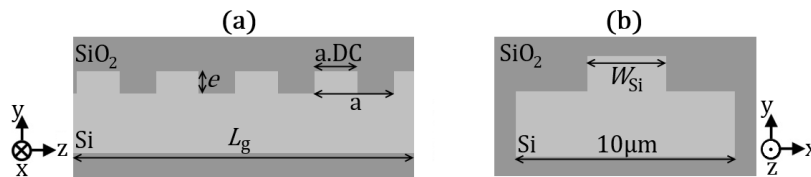


Figure C-22: Schematic view of the DBR in the  $SiO_2$ -Si matrix with the different parameters chosen.

Une campagne de caractérisation des miroirs seuls a pu être menée grâce à des motifs de tests designés spécifiquement sur la plaque. La réponse des miroirs selon leur longueur a pu être comparée aux simulations faites avec la théorie des matrices de transfert, comme en témoigne la Figure C-23. Les courbes expérimentales sont très proches des courbes théoriques ce qui signifie que les dimensions réelles des miroirs respectent ce à quoi on s'attendait.



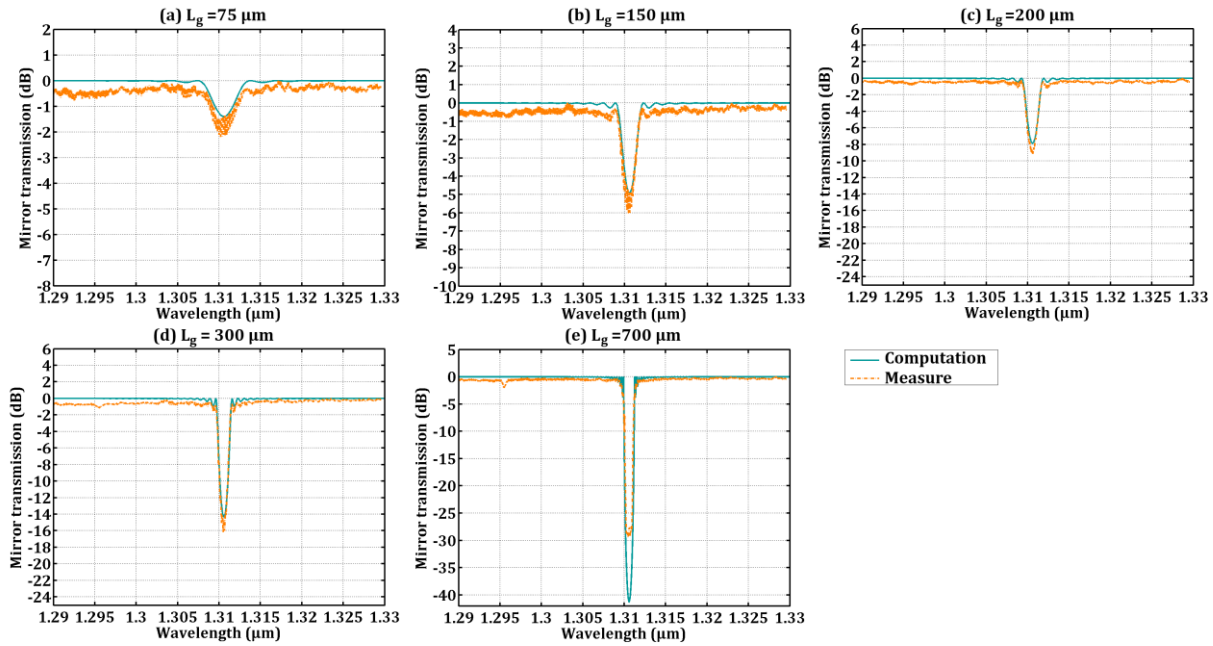


Figure C-23: Comparison between computations and measures of the different DBR mirrors designed with  $a=196$  nm.

### Caractérisation des lasers DBR

La Figure C-24 représente la photo d'un des dispositifs DBR à la fin de la fabrication. Les Pads au-dessus des miroirs servent à alimenter les chauffeuses pour accorder le laser, comme expliqué un peu plus bas.

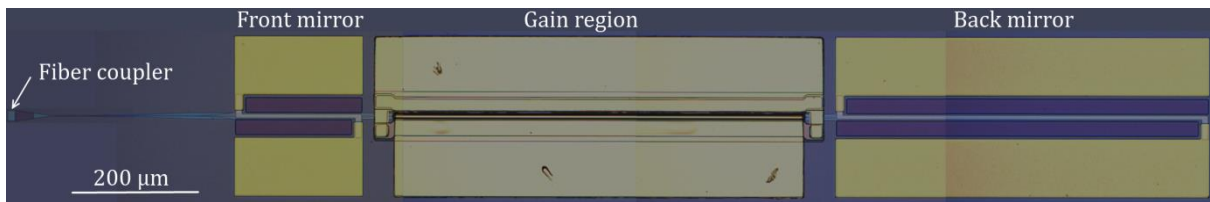


Figure C-24: Optical microscope picture of one of the DBR lasers.

Les lasers présentés ci-contre sont issus d'une plaque pour laquelle l'épaisseur de silice entre les guides n'était que de 60 nm au lieu des 90 nm visés, induisant une efficacité de couplage des tapers inférieure à 70 %. Les performances des dispositifs en ont été très diminuées. Les paramètres des trois lasers choisis sont rassemblés dans le Tableau 5.

Tableau 5: Paramètres des meilleurs lasers DBR mesurés.

Laser	Taper	$a$ (nm)	$\lambda_{\text{peak}}$ (nm)	Real SiO <sub>2</sub> gap	$L_{\text{FM}}$ (μm)	$R_{\text{FM}}$	WG to fiber coupler losses
DBR 1	Gap 100 nm truncated	197	1315	~60 nm	200	0.85	> 6 dB
DBR 2	Gap 100 nm truncated	195	1304				
DBR 3	Gap 100 nm truncated	195	1303				

La tension des lasers ainsi que leur puissance de sortie en fonction du courant d'injection sont tracées sur la Figure C-25. Le premier graphe montre que selon les lasers, la résistance va de  $6.2 \Omega$  à  $14.1 \Omega$  en fonction de la position du laser sur la plaque (preuve d'une mauvaise homogénéité lors de la gravure des puits quantiques). Les puissances maximales atteintes par les DBR 1, 2 et 3 sont 1.60 mW, 0.42 mW et 0.83 mW. Ces faibles valeurs sont expliquées par les pertes liées au couplage du III-V vers le Si ainsi que



par d'éventuelles pertes dans les guides Si. Le DBR 1 est cependant meilleur que les deux autres car sa période permet d'avoir une longueur d'onde laser plus proche du maximum de gain des puits quantiques et donc d'amplifier la lumière de manière plus efficace. Le seuil de ce laser est plus bas, pour la même raison (48 mA à comparer à 73 et 52 mA pour les DBR 2 et 3).

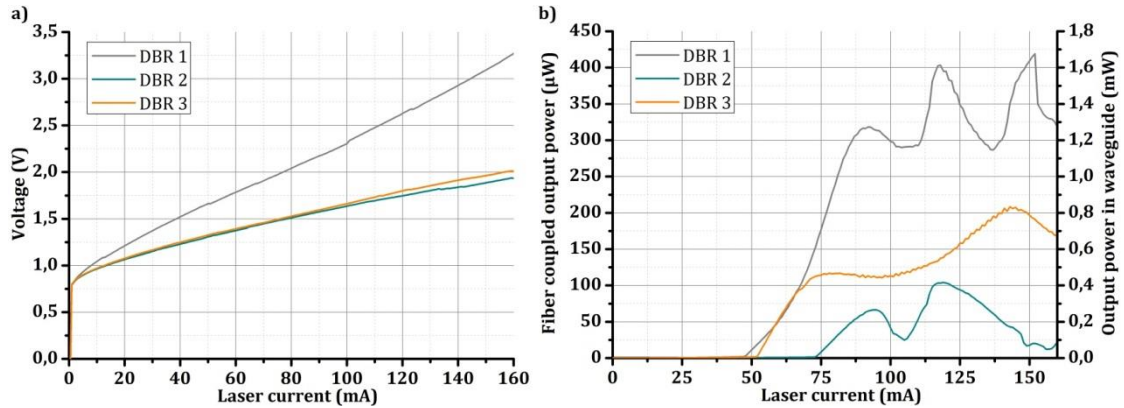


Figure C-25: Voltage (a) and output power (b) depending of the laser current for the three DBR lasers selected.

Les spectres des lasers ainsi que leur SMSR en fonction du courant d'injection dans le laser sont visibles sur la Figure C-26. Etant donné qu'un DBR est un laser de type Fabry-Pérot (FP), on devine sur les spectres les modes Fabry-Pérot de la cavité et on voit qu'à mesure que le courant d'injection augmente, le pic laser saute d'un mode FP au suivant. Dans les trois cas, le SMSR des lasers reste supérieur à 35 dB sur toute la gamme de courant sauf lors d'un saut de mode. Il y a donc bien une signature DBR sur ces réponses lasers.

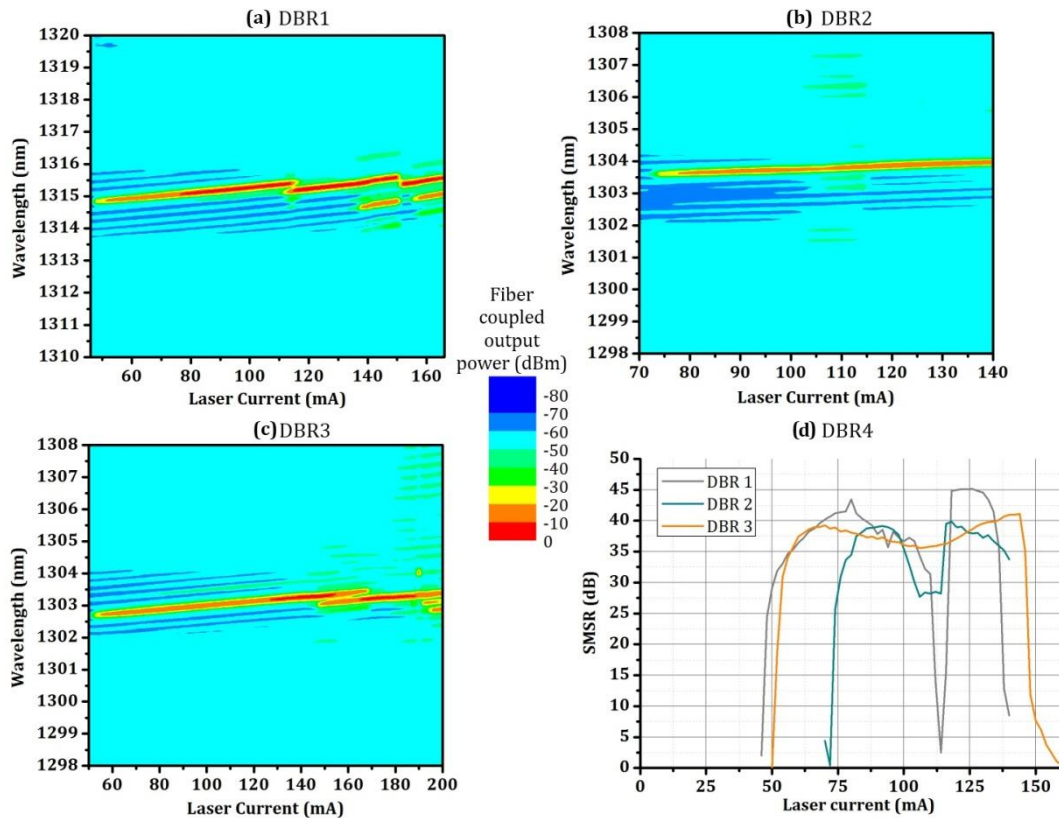


Figure C-26: Spectra as a function of the laser current for DBR 1 (a), 2 (b) and 3 (c). The SMSR of the three lasers are displayed on (d).

Les propriétés statiques obtenues pour ces lasers sont synthétisées dans le Tableau 6. Mêmes si celles-ci ne sont pas aussi bonnes que ce qu'on aurait pu avoir, le design des composants, et notamment des miroirs, est bien validé. Des plaques avec la bonne épaisseur de silice devrait bientôt être terminées et assurer plus de puissance de sortie. Dans ce qui suit, les lasers ont été accordés.

**Tableau 6: Propriétés obtenues pour les meilleurs lasers DBR mesurés.**

DBR laser	R ( $\Omega$ )	$\lambda_{\text{peak}}$ (nm)	$R_{\text{FM,calc}}$	$I_{\text{th}}$ (mA)	$J_{\text{th}}$ (kA/cm <sup>2</sup> )	$P_{\text{max}}$ (mW)	$\eta_{\text{diff}}$ (%)	$\text{SMSR}_{\text{max}}$ (dB)
1	14.1	1315	0.85	48	1.37	1.61	3.6	45.1
2	6.2	1304		73	2.09	0.42	1.6	39.8
3	6.7	1303		52	1.49	0.83	2.4	41.1

### Accordabilité

Pour accorder la longueur d'onde, il faut changer le pic de réponse de chaque miroir. Pour ce faire, le choix a été fait ici de changer l'indice effectif du miroir en modifiant sa température : c'est l'effet thermo-optique. Dans cette thèse, l'augmentation de la température des miroirs est induite par effet Joule grâce à un courant passant dans un matériaux résistif déposé au-dessus du guide et appelé chaufferette (HT pour heater) comme le montre la Figure C-27. La puissance dissipée par la chaufferette ( $P_{\text{dissipated}}$ ) dépend de sa résistance ( $R_{\text{HT}}$ ) comme le montre l'équation suivante :

$$P_{\text{dissipated}} = R_{\text{HT}} I_{\text{HT}}^2 = U_{\text{HT}}^2 / R_{\text{HT}} \quad [\text{C.2}]$$

Cette résistance doit être très supérieure à celle des contacts du HT ( $R_{\text{CT1}}$  et  $R_{\text{CT2}}$ ) pour que la puissance ne soit dissipée qu'au-dessus du miroir.

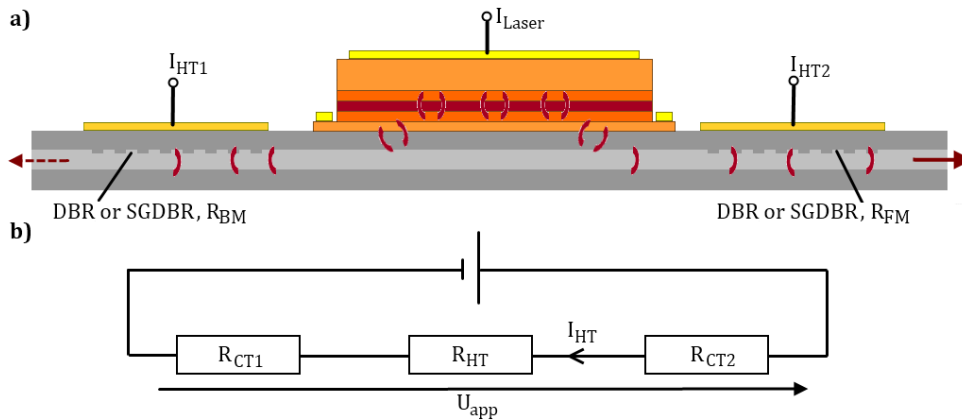


**Figure C-27: a) Schematic view of a SGDBR or DBR laser with a heater on top of each mirror. b) Electrical representation of one heater:  $R_{\text{CT1}}$  and  $R_{\text{CT2}}$  stand for the resistances of each contact and  $U_{\text{app}}$  is the applied voltage.**

La Figure C-28 permet de comprendre clairement l'effet des chauffelettes : pour un courant de miroir avant fixé à 69 mA, le courant du miroir arrière augmente, décalant ainsi la réponse du BM vers les longueurs d'ondes plus élevées et donc la longueur d'onde laser elle-même est sélectionnée à des longueurs d'onde plus grandes. On remarque aussi grâce à cette figure que pour accorder un laser DBR, les réponses des deux miroirs doivent être à peu près alignées et qu'il faut donc chauffer les deux miroirs en même temps.

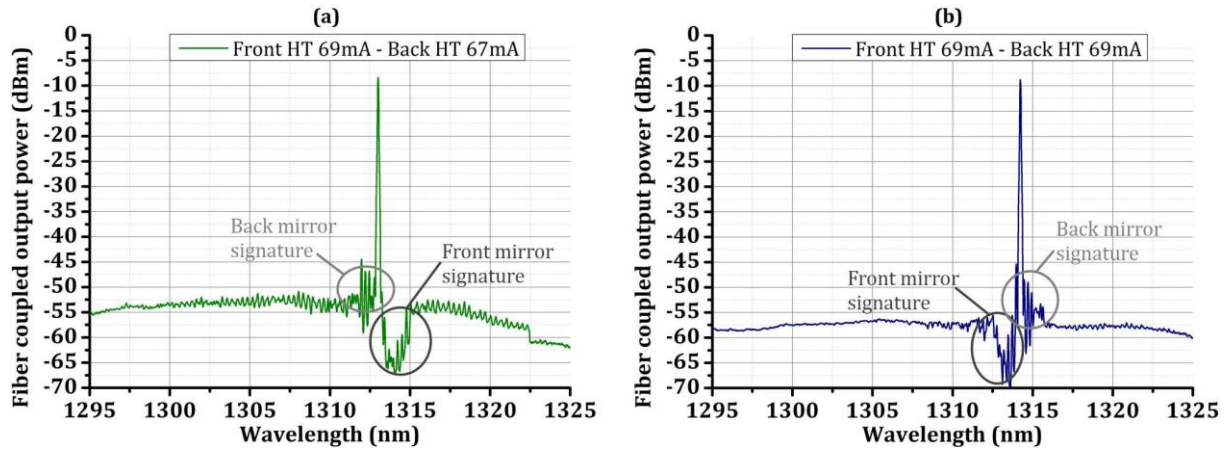


Figure C-28: Spectra for two different injection current for the back mirror heater with a 69 mA current for the front mirror heater of DBR 3.

Le DBR 3 du paragraphe précédent a été accordé selon la méthode que l'on vient d'expliquer. Les spectres obtenus sur la Figure C-29 montrent qu'une accordabilité sur 13.8 nm a été atteinte pour des puissances dans les miroirs avant et arrières de 0.45 W et 1.60 W respectivement. Cette gamme d'accordabilité pourrait être augmenté en épaississant le matériau de la chaufferette pour y faire passer plus de courant (tout en restant attentif à garder une résistance de contact plus faible que celle de la chaufferette), ce qui n'a pas pu être fait par manque de temps. La seule chose qui limiterait alors l'accordabilité serait donc le gain des puits quantiques. Cette expérience ayant été faite à la toute fin de la thèse, nous n'avons pas eu le temps de modifier le courant dans les chaufferettes de manière plus précise que le mA ce qui aurait pu permettre plus de régularité sur l'espace entre les pics obtenus. Cependant, de par son architecture, l'accordabilité dans un DBR ne peut pas être continue et c'est pourquoi des lasers DBR échantillonnés ont été construits et sont détaillés dans ce qui suit.

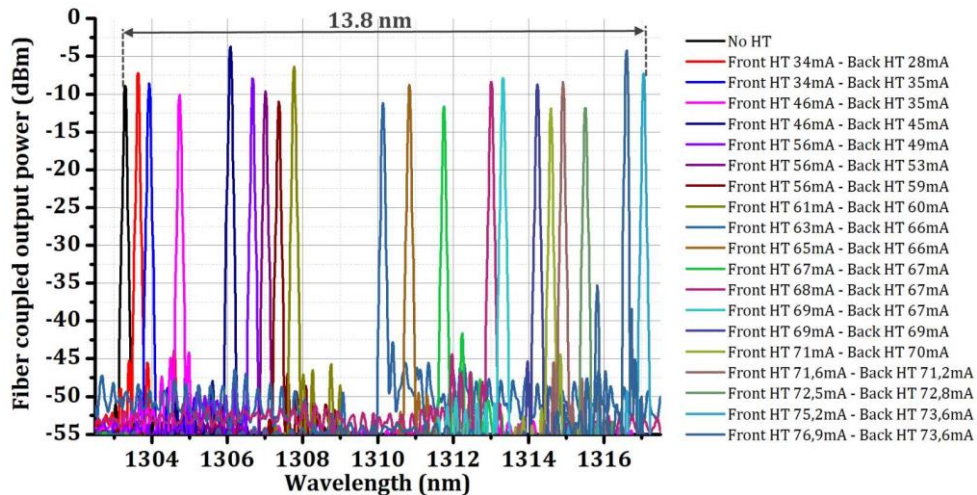


Figure C-29: Example of the tunability range of one of the DBR lasers presented in 3.1.3 (DBR 3).

Pour conclure avec les résultats obtenus concernant les lasers DBR, ceux-ci sont relativement bons notamment en termes de pureté spectrale et d'accordabilité mais les soucis liés à la fabrication n'ont pas permis d'atteindre la puissance espérée. Pour cela, il faudra attendre les plaques avec la bonne épaisseur de silice entre le III-V et le Si.

#### 4. Lasers SGDBR

Comme on a pu le voir dans la partie précédente, si les lasers DBR ont l'avantage d'être accordables par rapport aux laser hybrides DFB, ils ne le sont pas de manière continue et seulement sur une plage de longueur d'onde limitée. C'est pour ces raisons qu'une partie majeure de ces travaux a été de développer des lasers DBR échantillonnés. Le schéma d'un tel laser est représenté sur la Figure C-30. Comme dans le cas d'un laser DBR classique, deux miroirs de Bragg encadrent la zone de gain. Cependant, ces miroirs sont échantillonnés, c'est-à-dire que des parties du miroirs sont retirées de manière périodique.

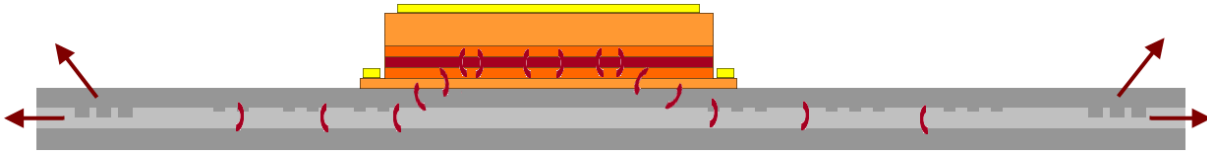


Figure C-30: Schematic view of a III-V on Si SGDBR laser.

##### Principe théorique du miroir SGDBR

La Figure C-31 (a) détaille de manière précise les différents paramètres d'un miroir de Bragg échantillonné : à la période du miroir ( $a$ ), se superpose la période d'échantillonnage ( $a_{sp}$ ). Si on observe un tel système dans l'espace de Fourier (cf. Figure C-31 (b)), on peut voir que la réponse fréquentielle du miroir sera un peigne de pics centré en  $1/a$  et où l'espacement entre les pics vaut  $1/a_{sp}$ . La réponse en longueur d'onde d'un tel miroir est représentée sur la Figure C-32.

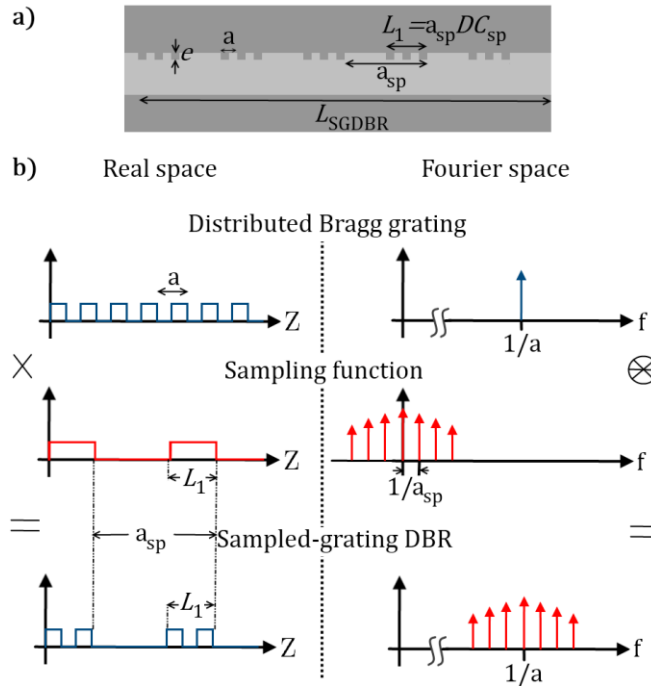


Figure C-31: (a) Side schematic view of a SGDBR. (b) Real and Fourier space representations of such a grating.

Les pics d'un tel miroir sont beaucoup plus fins que dans le cas d'un DBR. En fixant  $n_{g,avg}$ , l'indice de groupe moyen dans le miroir et  $\lambda$  la longueur d'onde, l'espacement entre les pics est donné par :

$$\Delta\lambda_{SGDBR} = \frac{\lambda^2}{2n_{g,avg}a_{sp}} \quad [C.3]$$

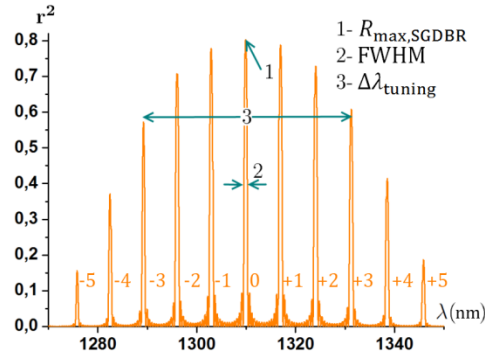


Figure C-32: Example of the response of a SGDBR mirror.

Lorsque la zone de gain est encadrée par deux miroirs de ce type qui diffèrent seulement par leur période d'échantillonnage, la réponse de chacun des miroirs est quasiment la même sauf l'espacement entre les pics : il n'y a donc coïncidence des deux miroirs qu'à une longueur d'onde. C'est l'effet Vernier ; la longueur d'onde est ainsi sélectionnée très précisément et le facteur de qualité d'une telle cavité est très élevé. Deux exemples sont tracés sur la Figure C-33 avec les réponses des deux miroirs et le produit de leur réponse. Il faut cependant remarquer que sur le graphe de droite, il y a coïncidence sur plusieurs longueurs d'onde. En effet, les coïncidences se répètent tous les :

$$\Delta\lambda_{\text{align}} = \frac{\Delta\lambda_{\text{SGDBR},1} \Delta\lambda_{\text{SGDBR},2}}{|\Delta\lambda_{\text{SGDBR},1} - \Delta\lambda_{\text{SGDBR},2}|} \quad [\text{C.4}]$$

Il faut donc choisir la période d'échantillonnage de chaque miroir judicieusement lors du design de manière à n'avoir qu'une seule coïncidence sur la zone de réponse des miroirs.

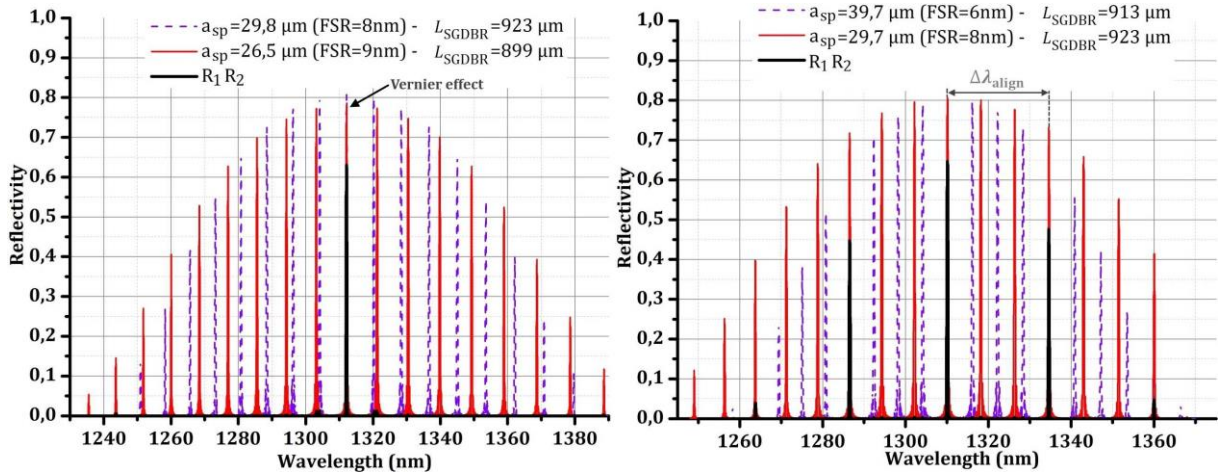


Figure C-33: Spectral response of two SGDBR mirrors with different sampling periods. For all the mirrors,  $a=196$  nm,  $e=20$  nm,  $DC_{sp} = 0.1$  and  $R_{\text{max,SGDBR}} = 0.8$ .

Quant à l'accordabilité d'une telle cavité, la Figure C-33 permet de comprendre que si le miroir 'pointillé-violet' est chauffé, sa réponse va se décaler vers les plus grandes longueurs d'onde et le pic à droite du pic central sera sélectionné pour un effort énergétique très faible. De la même façon, en chauffant le miroir 'rouge', sa réponse se décalera vers les plus grandes longueurs d'onde mais c'est cette fois le pic à gauche du pic central qui sera en coïncidence. Il est donc clair qu'une accordabilité par sauts sur une très grande



plage de longueur d'onde est possible vers les longueurs d'onde plus grandes comme plus faibles (chose impossible avec des lasers DBR classiques). Pour accorder de manière continue, il suffit simplement de chauffer les deux miroirs en même temps.

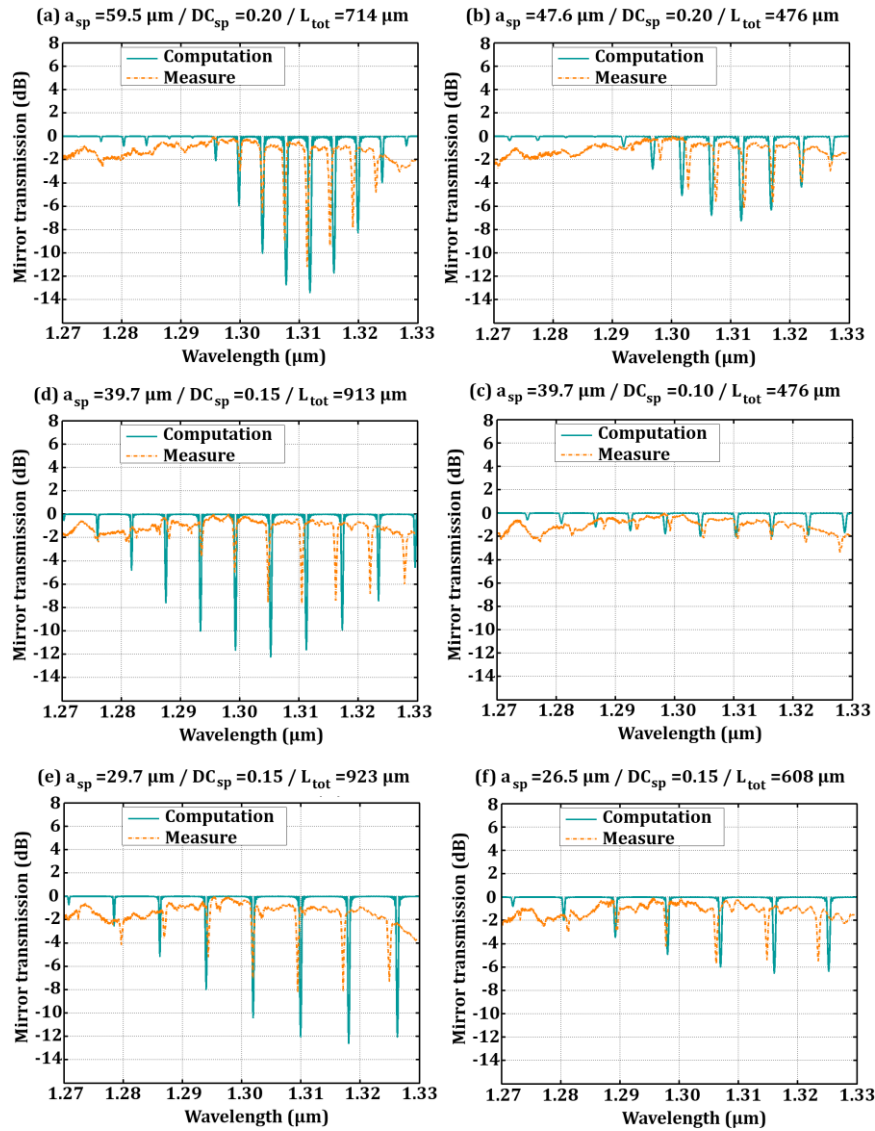


Figure C-34: Comparison between computations and measure of some of the different SGDBR mirrors designed with  $a=196$  nm.

### Paramètres des miroirs SGDBR

En se concentrant sur le schéma Figure C-31 (a), les paramètres des miroirs à définir lors du design sont :

- La longueur des SGDBR ( $L_{SGDBR}$ ), choisie de manière à avoir une réflectivité de chaque côté de 0.4 ou 0.8,
- La période du miroir ( $a$ ) fixée à 196 nm et le facteur de remplissage ( $DC=0.5$ ),
- La profondeur de gravure ( $e$ ) qui vaut 20 nm pour obtenir des pics assez fins mais éviter cependant d'avoir des longueurs de miroir trop grandes,
- La période d'échantillonnage ( $a_{sp}$ ) choisie de façon à avoir des espacements entre les pics allant de 4 à 9 nm,
- Le facteur de remplissage d'échantillonnage ( $DC_{sp}$ ) compris entre 0.1 et 0.2.



Comme dans le cas des lasers DBR, des motifs de test dédiés ont permis de caractériser les miroirs seuls et de comparer leur réponse avec la réponse théorique, calculée avec la théorie des matrices de transfert. La Figure C-34 montre que la simulation et la mesure concordent bien et que la structuration des miroirs correspond au design visé.

### Caractérisation des lasers SGDBR

La photo d'un des lasers obtenus à la fin de la fabrication est représentée sur la Figure C-35 : l'image est très semblable à celle d'un laser DBR, l'unique différence visible étant la longueur des miroirs considérablement supérieure. Comme pour les miroirs DBR, l'accordabilité se fait grâce à des chaufferettes placées au-dessus des miroirs dans lesquelles un courant est transmis.

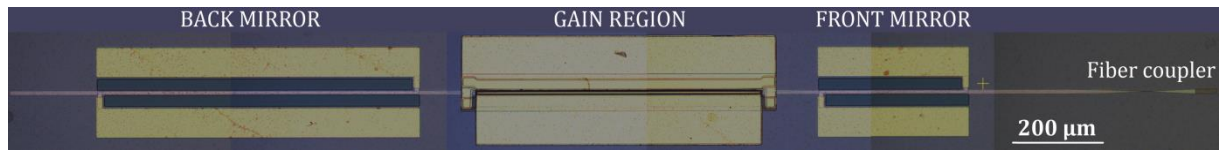


Figure C-35: Optical microscope picture of one of the SGDBR lasers.

Sur les deux plaques terminées, les puits quantiques ont été un peu trop gravés induisant une résistance un peu élevée, comme on le verra dans ce qui suit. Seuls les lasers avec un facteur de qualité très élevé peuvent fonctionner dans de telles conditions c'est pourquoi les lasers dont les miroirs avaient une réflectivité de 0.4 ne permettaient pas d'obtenir d'effet laser ici. Trois lasers mesurés sont présentés dans la suite et leurs paramètres sont rassemblés dans le Tableau 7.

Tableau 7: Paramètres des lasers SGDBR mesurés.

SGDBR laser	Taper	$a$ (nm)	$R$	$DC_{sp}$	Real SiO <sub>2</sub> gap	Fiber coupler losses	
1	Gap	196	0.80	0.10	~85 nm	> 6 dB	
2	100 nm			0.15	~95 nm		
3	truncated			0.10	~95 nm		
SGDBR laser	$FSR_{M1}$ (nm)	$a_{sp,M1}$ (μm)	$L_{tot,M1}$ (μm)	$FSR_{M2}$ (nm)	$a_{sp,M1}$ (μm)	$L_{tot,M1}$ (μm)	$L_{HT}$ (μm)
1	6	39.7	913	6.5	36.6	915	957
2	6	39.7	635	7.5	31.6	602	668
3	4	59.5	953	5.5	43.3	909	957

La puissance de sortie des lasers 1 et 2 ainsi que la tension à leurs bornes est représentée sur la Figure C-36. Ces graphes montrent une résistance de 51 et 22 Ω respectivement ce qui est énorme et prouve qu'il y a eu un problème lors de la gravure des puits quantiques. Malgré cela, des puissances de 7.5 mW dans le guide ont pu être atteintes ce qui est largement satisfaisant. Lors de l'augmentation de courant, la puissance fait des sauts très prononcés qui sont inévitables dans une telle architecture : de petites modifications de la cavité conduisent à la sélection (par effet Vernier) d'un pic plutôt qu'un autre d'où les sauts de mode.

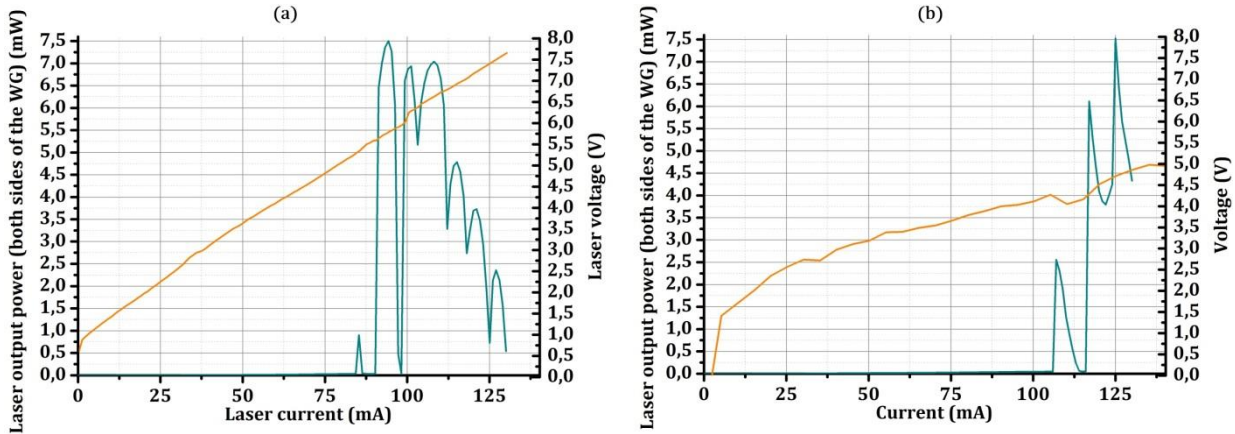


**Figure C-36: Laser output power (taking into account both laser outputs) and voltage as a function of the laser injection current for two different SGDBR lasers (laser 1 and 2 from Tableau 7).**

Les spectres des lasers SGDBR 2 et 3 sont tracés sur la Figure C-37 pour différents courants appliqués aux chauffettes. Sur chacun des spectres, il est facile de distinguer les pics correspondant à l'un ou l'autre des deux miroirs. En observant, lors de la mesure, l'effet de l'augmentation du courant dans chaque chauffette, on a pu déduire que les pics du dessus correspondent à la réponse du miroir de gauche alors que ceux du dessous à celle du miroir de droite.

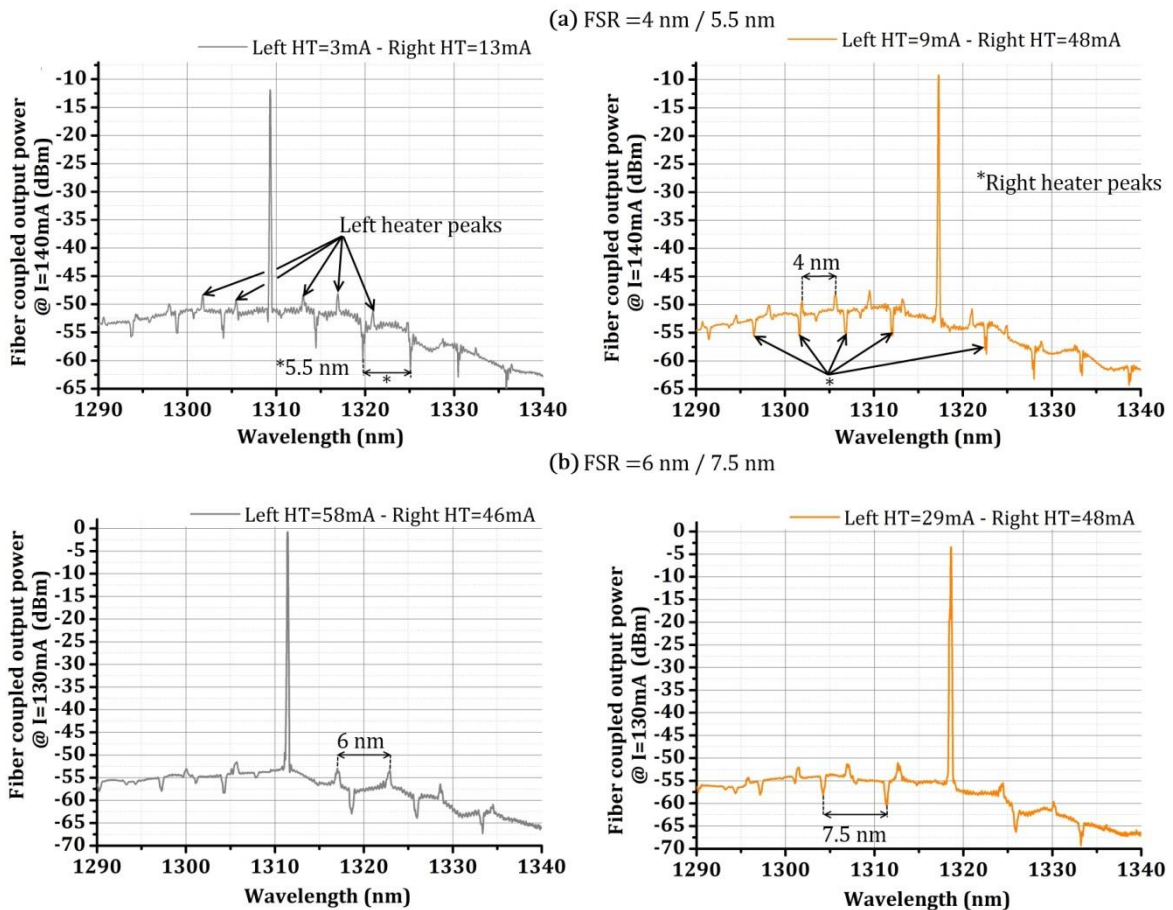


**Figure C-37: Spectra for two SGDBR lasers with their mirrors having different FSR: (a)  $FSR_{\text{left}}=4 \text{ nm} / FSR_{\text{right}}=5.5 \text{ nm}$ , (b)  $FSR_{\text{left}}=6 \text{ nm} / FSR_{\text{right}}=7.5 \text{ nm}$ .**

La Figure C-38 (a) témoigne d'une accordabilité continue du laser SGDBR 2 sur une plage de longueur d'onde de plus de 27 nm pour un SMSR toujours supérieur à 35 dB. Pour mieux comprendre l'effet du chauffage des miroirs, la Figure C-38 (b) représente la longueur d'onde laser en fonction du courant dans

les miroirs de gauche et de droite. Pour une courant sur la chaufferette de gauche fixe, augmenter la température sur le miroir de droite décale la longueur d'onde vers des valeurs plus faibles et vice versa. Pour ce laser, seulement 4 pics sont sélectionnés car le gain des puits pour des valeurs de  $\lambda$  plus éloignées est trop faible. A la fin de cette thèse, une accordabilité continue du laser SGDBR 1 a pu être montrée sur plus de 35 nm avec 6 pics sélectionnés car l'espacement entre les pics principaux est de 6.5 nm au lieu des 7.5 nm du laser SGDBR 2.

Pour atteindre la continuité entre les pics principaux, il faut cependant remarquer que la puissance dans chaque chaufferette atteint le watt et que pour dépenser moins d'énergie, il faudrait optimiser le chauffage (en changeant le matériau, ou modifiant les dimensions par exemple).

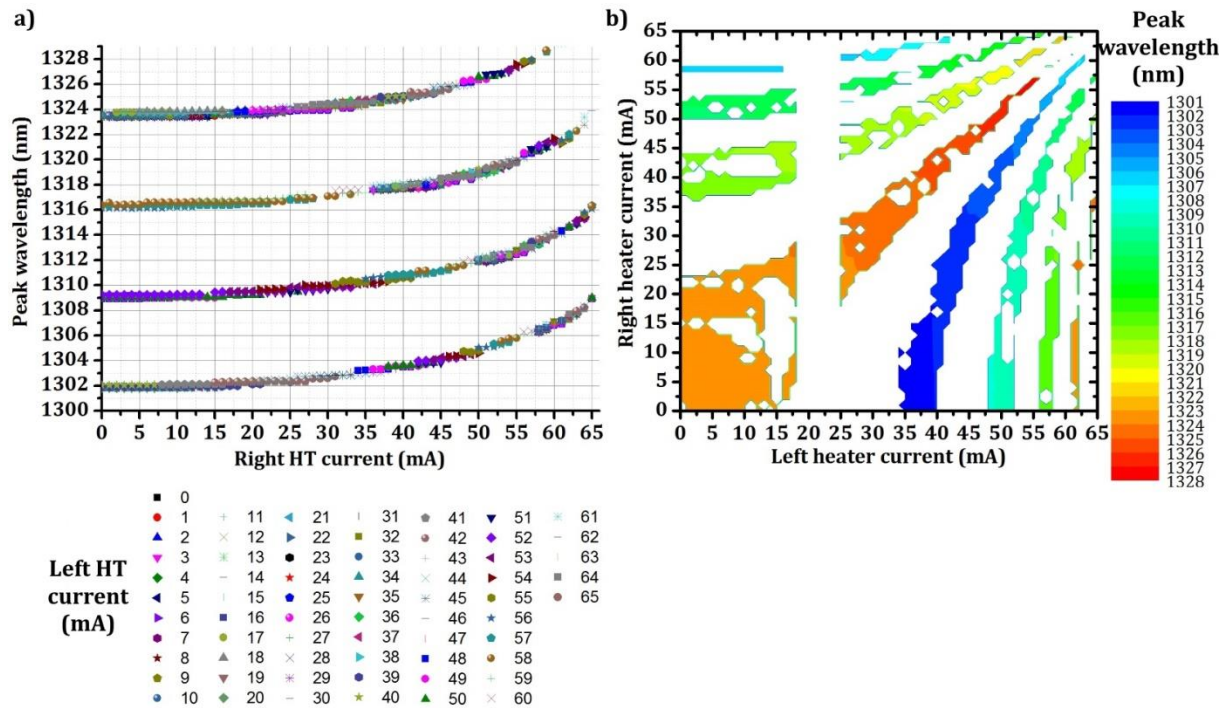
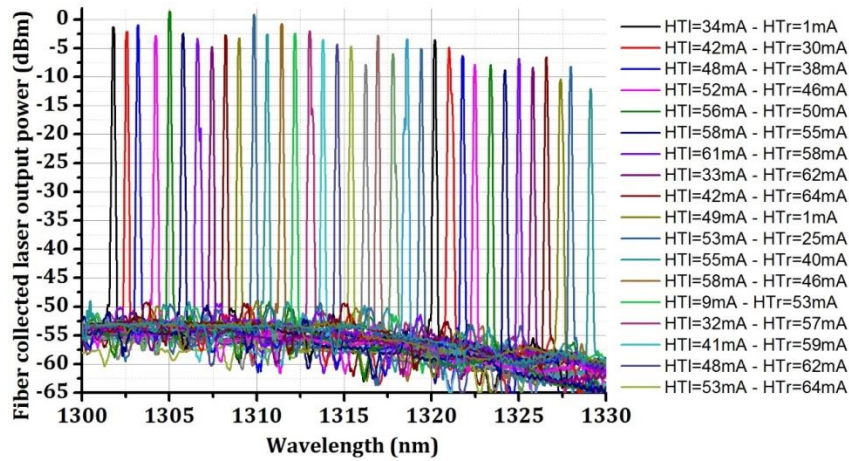


Figure C-38: a) and b) display two different representations of the peak wavelength depending on both heaters injection currents for a fixed laser current of 130 mA applied to laser SGDBR 2. In (b), some data are missing in the [19; 23] range of the left heater current, hence the white column.

Les lasers conçus pendant ce travail pouvant être destinés à du multiplexage en longueur d'onde 'dense' (dense wavelength division multiplexing – DWDM), il faut pouvoir obtenir des sources séparées de 0.8 nm sur une gamme de longueur d'onde aussi grande que possible. La possibilité d'accorder en continu les SGDBR et de contrôler précisément leur longueur d'onde permet d'atteindre cet objectif comme le montre la Figure C-39 où des spectres du laser SGDBR 2 ont été sélectionnés ayant tous un espacement de 0.8 nm. Pour plus de précision sur la puissance de sortie des lasers (la différence entre chaque pic ne devrait pas dépasser 3 dB), il faut ensuite jouer sur le courant d'injection du laser qui était fixé ici à 130 mA.



**Figure C-39: Laser spectra with a 0.8 nm spacing on a 27 nm range reached for a 130 mA laser injection current on laser SGDBR 2. HTI and HTr stand respectively for the left heater and the right heater.**

En conclusion des résultats présentés pour les lasers de Bragg échantillonnés, la puissance ainsi que le SMSR obtenus pour ces composants respectent le cahier des charges. A cause des problèmes de gravures, le seuil des lasers est un peu élevé (car leur résistance l'est aussi) mais on sait qu'on est capable de mieux contrôler cette gravure et donc d'avoir des seuils raisonnables (cf. lasers DFB). Le résultat majeur de cette partie est d'avoir démontré l'opérabilité de lasers accordables de manière continue sur 27 nm pour l'un et 35 nm pour l'autre. Il s'agit d'une première à 1.31  $\mu\text{m}$ .

## Conclusion et perspectives

L'objectif de ces trois ans de thèse était de développer des lasers hybrides III-V/Si à 1.31  $\mu\text{m}$  pour des applications compatibles avec les data communications. Mon travail s'est concentré autant sur la conception, la fabrication et la caractérisation de ces sources. Trois types de lasers ont été démontrés :

- Des lasers DFB avec une gravure du guide silicium soit sur le dessus, soit sur les bords. Dans les deux cas, une puissance et un SMSR supérieurs à 20 mW et 40 dB ont été atteints.
- Des lasers DBR. A cause d'une trop faible épaisseur de silice entre les guides III-V et Si n'a pas permis de dépasser 2 mW dans le guide mais le design est bien validé et d'autres plaques vont être caractérisées bientôt, sans ce problème d'épaisseur. Une accordabilité par sauts de 13.8 nm a été mesurée.
- Des lasers SGDBR. Malgré leur résistance élevée à cause d'une surgravure des puits quantiques, la puissance mesurée atteint 7.5 mW dans le guide. Le résultat majeur obtenu pour les lasers SGDBR est l'accordabilité des dispositifs sur une gamme de 27 nm pour l'un et 35 nm pour l'autre en continu, résultat jamais encore démontré auparavant à cette longueur d'onde.

Comme tout travail est perfectible, les perspectives suivantes sont à envisager pour améliorer encore les performances des dispositifs :

- Concevoir des formes de contacts spécifiques pour la RF pour permettre une modulation directe des lasers à des vitesses plus élevées,
- Augmenter la température d'opération laser (soit en utilisant des boîtes quantiques au lieu de puits quantiques soit en évacuant mieux la chaleur générée),
- Développer toute la chaîne de fabrication en 200 mm au lieu de détourner les plaques une fois l'épitaxie III-V collées,
- Développer le collage de dies plutôt que de wafer pour ne coller le matériau que là où c'est nécessaire,
- Co-intégrer le laser avec d'autres composants (modulateurs, photodiodes...).





---

# Bibliography

---

- [1] B. E. A. Saleh and M. C. Teich, *Fundamentals of Photonics*. Wiley, 2009.
- [2] L. A. Coldren and S. W. Corzine, *Diode lasers and photonic integrated circuits*. Wiley, 1995.
- [3] A. Javan, W. R. Bennett, and D. R. Herriott, "Population inversion and continuous optical oscillation in a gas discharge containing a He-Ne mixture," *Phys. Rev. Lett.*, 1961.
- [4] D. Liang and J. E. Bowers, "Recent progress in lasers on silicon," *Nat. Photonics*, vol. 4, no. 8, pp. 511–517, Aug. 2010.
- [5] C. C. Shen, J. J. Hsieh, and T. A. Lind, "1500h continuous CW operation of double heterostructure GaInAsP/InP Lasers," *Appl. Phys. Lett.*, 1977.
- [6] M. Kondow, S. Natatsuka, T. Titatani, and al, "Room temperature continuous wave operation of GaInNAs-GaAs Laser diode," *IEEE Phys. Tech. Lett.*, 1996.
- [7] Y. Qian, Z. H. Zhu, Y. H. Lo, H. Q. Hou, and al, "1.3um vertical cavity surface emitting laser with double bonded GaAs-AlAs Bragg mirrors," *IEEE Photonics Technol. Lett.*, 1997.
- [8] T. Matsuoka, H. Nagai, Y. Itaya, and al, "CW operation of a DFB-BH GaInAsP-InP lasers in 1.5um wavelength region," *IEEE Vol18*, 1982.
- [9] M. Razeghi, F. Brillouet, and J. C. C. Fan, "First CW operate of a GaInAsP-InP laser on a silicon substrate," *Appl. Phys. Lett.*, 1988.
- [10] K. Iga, "Surface emitting laser - Its birth and generation of new optoelectronics fields," *IEEE J. Sel. Top. Quantum Electron.*, 2000.
- [11] Y. Zhong, X. Zhu, G. Zong, Y. Huang, and L. Chen, "Two dimensional simulation of high order laterally coupled GaAs/AlGaAs DFB laser diodes," *IOP Sci.*, 2004.
- [12] O. Painter, R. K. Lee, A. Scherer, A. Yariv, J. D. OBrien, P. D. Dapkus, and I. Kim, "Two dimensional photonic bandgap defect mode laser," *Science*, 1999.
- [13] M. Lončar, T. Yoshie, A. Scherer, P. Gogna, and Y. Qiu, "Low-threshold photonic crystal laser," *Appl. Phys. Lett.*, vol. 81, no. 15, pp. 2680–2682, Oct. 2002.
- [14] H.-G. Park, S.-H. Kim, S.-H. Kwon, Y.-G. Ju, J.-K. Yang, J.-H. Baek, S.-B. Kim, and Y.-H. Lee, "Electrically Driven Single-Cell Photonic Crystal Laser," *Science*, vol. 305, no. 5689, pp. 1444–1447, Sep. 2004.
- [15] O. Gauthier-Lafaye, D. Mulin, S. Bonnefont, X. Checoury, J.-M. Lourtioz, A. Talneau, and F. Lozes-Dupuy, "Highly monomode W1 waveguide square lattice photonic crystal lasers," *IEEE Photonics Technol. Lett.*, vol. 17, no. 8, pp. 1587–1589, Aug. 2005.
- [16] B. B. Bakir, C. Seassal, X. Letartre, P. Viktorovitch, M. Zussy, L. D. Cioccio, and J. M. Fedeli, "Surface-emitting microlaser combining two-dimensional photonic crystal membrane and vertical Bragg mirror," *Appl. Phys. Lett.*, vol. 88, no. 8, p. 081113, Feb. 2006.
- [17] G. Vecchi, F. Raineri, I. Sagnes, K.-H. Lee, S. Guilet, L. Le Gratiet, F. Van Laere, G. Roelkens, D. Van Thourhout, R. Baets, A. Levenson, and R. Raj, "Photonic-crystal surface-emitting laser near 1.55 [micro sign]m on gold-coated silicon wafer," *Electron. Lett.*, vol. 43, no. 6, p. 343, 2007.
- [18] G. Vecchi, F. Raineri, I. Sagnes, A. Yacomotti, P. Monnier, T. J. Karle, K.-H. Lee, R. Braive, L. Le Gratiet, S. Guilet, G. Beaudoin, A. Taneau, S. Bouchoule, A. Levenson, and R. Raj, "Continuous-wave operation of photonic band-edge laser near 1.55  $\mu\text{m}$  on silicon wafer," *Opt. Express*, vol. 15, no. 12, p. 7551, 2007.
- [19] Bouchard, O., Larrue, A., Gauthier-Lafaye, O., Bonnefont, S., Arguel, P., Lozes-Dupuy, F., ... & Drisse, O., "CW electrical operation of single-mode all photonic crystal DFB-like laser," *Proceedings of 14th European conference on integrated optics (ECIO)*, pp. 301–304, 2008.
- [20] M. Fujita, A. Sakai, and T. Baba, "Ultrasmall and ultralow threshold GaInAsP-InP microdisk injection lasers: design, fabrication, lasing characteristics, and spontaneous emission factor," *IEEE J. Sel. Top. Quantum Electron.*, vol. 5, no. 3, pp. 673–681, May 1999.
- [21] R. Ushigome, M. Fujita, A. Sakai, T. Baba, and Y. Kokubun, "GaInAsP Microdisk Injection Laser with Benzocyclobutene Polymer Cladding and Its Athermal Effect," *Jpn. J. Appl. Phys.*, vol. 41, no. 11R, p. 6364, Nov. 2002.
- [22] L. Zhang and E. Hu, "Lasing from InGaAs quantum dots in an injection microdisk," *Appl. Phys. Lett.*, vol. 82, no. 3, pp. 319–321, Jan. 2003.

- 
- [23] T. Matsuoka, H. Nagai, Y. Itaya, Y. Noguchi, Y. Suzuki, and T. Ikegami, "CW operation of DFB-BH GaInAsP/InP lasers in 1.5  $\mu\text{m}$  wavelength region," *Electron. Lett.*, vol. 18, no. 1, pp. 27–28, Jan. 1982.
  - [24] M. C. Larcson, M. Kondow, T. Kitatani, and al, "GaInNAs-GaAs long wavelength vertical cavity surface emitting Laser diode," *IEEE Phys. Tech. Lett. Vol10*, 1998.
  - [25] T. L. Koch, U. Koren, and B. I. Miller, "High performance tunable 1.5  $\mu\text{m}$  InGaAs/InGaAsP multiple quantum well distributed Bragg reflector lasers," *Appl. Phys. Lett.*, vol. 53, no. 12, pp. 1036–1038, Sep. 1988.
  - [26] J. W. Goodman, F. J. Leonberger, S.-Y. Kung, and R. A. Athale, "Optical interconnections for VLSI systems," *Proc. IEEE*, vol. 72, no. 7, pp. 850–866, Jul. 1984.
  - [27] M. Heck, J. Bauters, M. Davenport, J. Doylend, S. Jain, G. Kurczveil, S. Srinivasan, Y. Tang, and J. Bowers, "Hybrid Silicon Photonic Integrated Circuit Technology," *IEEE J. Sel. Top. Quantum Electron.*, vol. Early Access Online, 2012.
  - [28] M. S. Dahlem, C. W. Holzwarth, A. Khilo, F. X. Kärtner, H. I. Smith, and E. P. Ippen, "Reconfigurable multi-channel second-order silicon microring-resonator filterbanks for on-chip WDM systems," *Opt. Express*, vol. 19, no. 1, pp. 306–316, Jan. 2011.
  - [29] B. Ben Bakir, A. V. de Gyves, R. Orobtcchouk, P. Lyan, C. Porzier, A. Roman, and J. M. Fedeli, "Low-Loss (1 dB) and Polarization-Insensitive Edge Fiber Couplers Fabricated on 200-mm Silicon-on-Insulator Wafers," *IEEE Photonics Technol. Lett.*, vol. 22, no. 11, pp. 739–741, Jun. 2010.
  - [30] M. Antelius, K. B. Gylfason, and H. Sohlström, "An apodized SOI waveguide-to-fiber surface grating coupler for single lithography silicon photonics," *Opt. Express*, vol. 19, no. 4, pp. 3592–3598, Feb. 2011.
  - [31] L. Liao, D. Samara-Rubio, M. Morse, A. Liu, D. Hodge, D. Rubin, U. Keil, and T. Franck, "High speed silicon Mach-Zehnder modulator," *Opt. Express*, vol. 13, no. 8, pp. 3129–3135, Apr. 2005.
  - [32] J. Van Campenhout, M. Pantouvaki, P. Verheyen, S. Selvaraja, G. Lepage, H. Yu, W. Lee, J. Wouters, D. Goossens, M. Moelants, W. Bogaerts, and P. Absil, "Low-Voltage, Low-Loss, Multi-Gb/s Silicon Micro-Ring Modulator based on a MOS Capacitor," in *Optical Fiber Communication Conference*, 2012, p. OM2E.4.
  - [33] L. Virost, P. Crozat, J.-M. Fédéli, J.-M. Hartmann, D. Marris-Morini, E. Cassan, F. Boeuf, and L. Vivien, "Germanium avalanche receiver for low power interconnects," *Nat. Commun.*, vol. 5, Sep. 2014.
  - [34] C. Sciancalepore, R. J. Lycett, J. A. Dallery, S. Pauliac, K. Hassan, J. Harduin, H. Duprez, U. Weidenmueller, D. F. G. Gallagher, S. Menezo, and B. Ben Bakir, "Low-Crosstalk Fabrication-Insensitive Echelle Grating Demultiplexers on Silicon-on-Insulator," *IEEE Photonics Technol. Lett.*, vol. 27, no. 5, pp. 494–497, Mar. 2015.
  - [35] H. Rong, R. Jones, A. Liu, O. Cohen, D. Hak, A. Fang, and M. Paniccia, "A continuous-wave Raman silicon laser," *Nature*, vol. 433, no. 7027, pp. 725–728, Feb. 2005.
  - [36] R. E. Camacho-Aguilera, Y. Cai, N. Patel, J. T. Bessette, M. Romagnoli, L. C. Kimerling, and J. Michel, "An electrically pumped germanium laser," *Opt. Express*, vol. 20, no. 10, pp. 11316–11320, May 2012.
  - [37] W. C. Ding, D. Hu, J. Zheng, P. Chen, B. W. Cheng, J. Z. Yu, and Q. M. Wang, "Strong visible and infrared photoluminescence from Er-implanted silicon nitride films," *J. Phys. Appl. Phys.*, vol. 41, no. 13, p. 135101, Jul. 2008.
  - [38] S. Yerci, R. Li, S. O. Kucheyev, T. van Buuren, S. N. Basu, and L. D. Negro, "Energy transfer and 1.54  $\mu\text{m}$  emission in amorphous silicon nitride films," *Appl. Phys. Lett.*, vol. 95, no. 3, p. 031107, Jul. 2009.
  - [39] M. E. Groenert, C. W. Leitz, A. J. Pitera, V. Yang, H. Lee, R. J. Ram, and E. A. Fitzgerald, "Monolithic integration of room-temperature cw GaAs/AlGaAs lasers on Si substrates via relaxed graded GeSi buffer layers," *J. Appl. Phys.*, vol. 93, no. 1, pp. 362–367, Jan. 2003.
  - [40] L. Cerutti, J. B. Rodriguez, and E. Tournie, "GaSb-Based Laser, Monolithically Grown on Silicon Substrate, Emitting at 1.55  $\mu\text{m}$  at Room Temperature," *IEEE Photonics Technol. Lett.*, vol. 22, no. 8, pp. 553–555, Apr. 2010.
  - [41] T. Mitze, M. Schnarrenberger, L. Zimmermann, J. Bruns, F. Fidorra, J. Kreissl, K. Janiak, S. Fidorra, H. Heidrich, and K. Petermann, "Hybrid integration of III/V lasers on a silicon-on-insulator (SOI) optical board," in *2nd IEEE International Conference on Group IV Photonics, 2005*, 2005, pp. 210–212.
  - [42] F. E. Doany and B. G. Lee, "Flip-chip packaging for dense hybrid integration of electrical and photonic integrated circuits," US 20120207426 a1, 2012.
  - [43] H. D. Thacker, Y. Luo, J. Shi, I. Shubin, J. Lexau, X. Zheng, G. Li, J. Yao, J. Costa, T. Pinguet, A. Mekis, P. Dong, S. Liao, D. Feng, M. Asghari, R. Ho, K. Raj, J. G. Mitchell, A. V. Krishnamoorthy, and J. E. Cunningham, "Flip-chip integrated silicon photonic bridge chips for sub-picojoule per bit optical

- links," in *Electronic Components and Technology Conference (ECTC), 2010 Proceedings 60th*, 2010, pp. 240–246.
- [44] L. Gunn, T. Pinguet, and M. Rattier, "External cavity laser source," US20040228564 A1, 18-Nov-2004.
  - [45] T. Pinguet, B. Analui, E. Balmater, D. Guckenberger, M. Harrison, R. Koumans, D. Kucharski, Y. Liang, G. Masini, A. Mekis, S. Mirsaidi, A. Narasimha, M. Peterson, D. Rines, V. Sadagopan, S. Sahni, T. J. Sleboda, D. Song, Y. Wang, B. Welch, J. Witzens, J. Yao, S. Abdalla, S. Gloeckner, P. De Dobbelaere, and G. Capellini, "Monolithically integrated high-speed CMOS photonic transceivers," in *2008 5th IEEE International Conference on Group IV Photonics*, 2008, pp. 362–364.
  - [46] A. J. Zilkie, P. Seddighian, B. J. Bijlani, W. Qian, D. C. Lee, S. Fatholouloumi, J. Fong, R. Shafiiha, D. Feng, B. J. Luff, X. Zheng, J. E. Cunningham, A. V. Krishnamoorthy, and M. Asghari, "Power-efficient III-V/Silicon external cavity DBR lasers," *Opt. Express*, vol. 20, no. 21, pp. 23456–23462, Oct. 2012.
  - [47] G. Roelkens, J. Van Campenhout, J. Brouckaert, D. Van Thourhout, R. Baets, P. R. Romeo, P. Regreny, A. Kazmierczak, C. Seassal, X. Letartre, G. Hollinger, J. M. Fedeli, L. Di Cioccio, and C. Lagahe-Blanchard, "III-V/Si photonics by die-to-wafer bonding," *Mater. Today*, vol. 10, no. 7–8, pp. 36–43, juillet 2007.
  - [48] K. Tanabe, K. Watanabe, and Y. Arakawa, "III-V/Si hybrid photonic devices by direct fusion bonding," *Sci. Rep.*, vol. 2, avril 2012.
  - [49] T. Hong, Y. Wang, H.-Y. Yu, S. Yue, W.-X. Chen, S. Liang, Z. Li, J.-Q. Pan, and G.-Z. Ran, "A selective area metal bonding method for Si photonics light sources," in *2010 7th IEEE International Conference on Group IV Photonics (GFP)*, 2010, pp. 13–15.
  - [50] S. Stankovic, R. Jones, M. N. Sysak, J. M. Heck, G. Roelkens, and D. Van Thourhout, "Hybrid III-V/Si Distributed-Feedback Laser Based on Adhesive Bonding," *IEEE Photonics Technol. Lett.*, vol. 24, no. 23, pp. 2155–2158, Dec. 2012.
  - [51] M. N. Sysak, H. Park, A. W. Fang, J. E. Bowers, R. Jones, O. Cohen, O. Raday, and M. J. Paniccia, "Experimental and theoretical thermal analysis of a Hybrid Silicon Evanescent Laser," *Opt. Express*, vol. 15, no. 23, pp. 15041–15046, Nov. 2007.
  - [52] B. Ben Bakir, A. Descos, N. Olivier, D. Bordel, P. Grosse, E. Augendre, L. Fulbert, and J. M. Fedeli, "Electrically driven hybrid Si/III-V Fabry-Pérot lasers based on adiabatic mode transformers," *Opt. Express*, vol. 19, no. 11, pp. 10317–10325, May 2011.
  - [53] A. W. Fang, B. R. Koch, R. Jones, E. Lively, D. Liang, Y. Kuo, and J. E. Bowers, "A Distributed Bragg Reflector Silicon Evanescent Laser," *IEEE Photonics Technol. Lett.*, vol. 20, no. 20, pp. 1667–1669, 2008.
  - [54] A. W. Fang, E. Lively, Y.-H. Kuo, D. Liang, and J. E. Bowers, "A distributed feedback silicon evanescent laser," *Opt. Express*, vol. 16, no. 7, pp. 4413–4419, Mar. 2008.
  - [55] B. r. Koch, A. w. Fang, E. Lively, R. Jones, O. Cohen, D. j. Blumenthal, and J. e. Bowers, "Mode locked and distributed feedback silicon evanescent lasers," *Laser Photonics Rev.*, vol. 3, no. 4, pp. 355–369, 2009.
  - [56] D. Liang, M. Fiorentino, T. Okumura, H.-H. Chang, D. T. Spencer, Y.-H. Kuo, A. W. Fang, D. Dai, R. G. Beausoleil, and J. E. Bowers, "Electrically-pumped compact hybrid silicon microring lasers for optical interconnects," *Opt. Express*, vol. 17, no. 22, pp. 20355–20364, Oct. 2009.
  - [57] S. Keyvaninia, G. Roelkens, D. Van Thourhout, C. Jany, M. Lamponi, A. Le Liepvre, F. Lelarge, D. Make, G.-H. Duan, D. Bordel, and J.-M. Fedeli, "Demonstration of a heterogeneously integrated III-V/SOI single wavelength tunable laser," *Opt. Express*, vol. 21, no. 3, pp. 3784–3792, février 2013.
  - [58] B. B. Bakir, C. Sciancalepore, A. Descos, H. Duprez, D. Bordel, L. Sanchez, C. Jany, K. Hassan, P. Briancaeu, V. Carron, and S. Menezo, "(Invited) Heterogeneously Integrated III-V on Silicon Lasers," *ECS Trans.*, vol. 64, no. 5, pp. 211–223, Aug. 2014.
  - [59] A. W. Fang, H. Park, O. Cohen, R. Jones, M. J. Paniccia, and J. E. Bowers, "Electrically pumped hybrid AlGaInAs-silicon evanescent laser," *Opt. Express*, vol. 14, no. 20, pp. 9203–9210, Oct. 2006.
  - [60] A. W. Fang, R. Jones, H. Park, O. Cohen, O. Raday, M. J. Paniccia, and J. E. Bowers, "Integrated AlGaInAs-silicon evanescent race track laser and photodetector," *Opt. Express*, vol. 15, no. 5, p. 2315, 2007.
  - [61] B. Ben Bakir, A. Descos, N. Olivier, D. Bordel, P. Grosse, J.-L. Gentner, F. Lelarge, and J. Fedeli, "Hybrid Si/III-V lasers with adiabatic coupling," in *2011 8th IEEE International Conference on Group IV Photonics (GFP)*, 2011, pp. 169–171.
  - [62] A. Descos, C. Jany, D. Bordel, H. Duprez, G. B. de Farias, P. Briancaeu, S. Menezo, and B. Ben Bakir, "Heterogeneously integrated III-V/Si distributed Bragg reflector laser with adiabatic coupling," in *39th European Conference and Exhibition on Optical Communication (ECOC 2013)*, 2013, pp. 1–3.

- 
- [63] T. Creazzo, E. Marchena, S. B. Krasulick, P. K. L. Yu, D. Van Orden, J. Y. Spann, C. C. Blivin, L. He, H. Cai, J. M. Dallesasse, R. J. Stone, and A. Mizrahi, "Integrated tunable CMOS laser," *Opt. Express*, vol. 21, no. 23, pp. 28048–28053, Nov. 2013.
  - [64] C. Ting, H. Tao, P. Jiao-Qing, C. Wei-Xi, C. Yuan-Bing, W. Yang, M. Xiao-Bo, L. Wei-Li, Z. Ling-Juan, R. Guang-Zhao, W. Wei, and Q. Guo-Gang, "Electrically Pumped Room-Temperature Pulsed InGaAsP-Si Hybrid Lasers Based on Metal Bonding," *Chin. Phys. Lett.*, vol. 26, no. 6, p. 064211, Jun. 2009.
  - [65] G.-H. Duan, C. Jany, A. Le liepvre, A. Accard, M. Lamponi, D. Make, P. Kaspar, G. Levaufre, N. Girard, F. Lelarge, J.-M. Fedeli, A. Descos, B. Ben Bakir, S. Messaoudene, D. Bordel, S. Menezo, G. de Valicourt, S. Keyvaninia, G. Roelkens, D. Van Thourhout, D. J. Thomson, F. Y. Gardes, and G. T. Reed, "Hybrid III-V on Silicon Lasers for Photonic Integrated Circuits on Silicon," *IEEE J. Sel. Top. Quantum Electron.*, vol. 20, no. 4, pp. 158–170, Jul. 2014.
  - [66] P. Rojo Romeo, J. Van Campenhout, P. Regreny, A. Kazmierczak, C. Seassal, X. Letartre, G. Hollinger, D. Van Thourhout, R. Baets, J. M. Fedeli, and L. Di Cioccio, "Heterogeneous integration of electrically driven microdisk based laser sources for optical interconnects and photonic ICs," *Opt. Express*, vol. 14, no. 9, p. 3864, 2006.
  - [67] J. Van Campenhout, P. Rojo Romeo, P. Regreny, C. Seassal, D. Van Thourhout, S. Verstuyft, L. Di Cioccio, J.-M. Fedeli, C. Lagahe, and R. Baets, "Electrically pumped InP-based microdisk lasers integrated with a nanophotonic silicon-on-insulator waveguide circuit," *Opt. Express*, vol. 15, no. 11, p. 6744, 2007.
  - [68] X. Sun, A. Zadok, M. J. Shearn, K. A. Diest, A. Ghaffari, H. A. Atwater, A. Scherer, and A. Yariv, "Electrically pumped hybrid evanescent Si/InGaAsP lasers," *Opt. Lett.*, vol. 34, no. 9, p. 1345, May 2009.
  - [69] H.-H. Chang, A. W. Fang, M. N. Sysak, H. Park, R. Jones, O. Cohen, O. Raday, M. J. Paniccia, and J. E. Bowers, "1310nm silicon evanescent laser," *Opt. Express*, vol. 15, no. 18, pp. 11466–11471, Sep. 2007.
  - [70] S. Stankovic, G. Roelkens, D. Van Thourhout, R. Jones, M. Sysak, and J. Heck, "1310 nm Evanescent Hybrid III-V/Si Laser Based on DVS-BCB Bonding," in *Advanced Photonics*, 2011, p. IWC3.
  - [71] J. D'Ambrosia, "100 gigabit Ethernet and beyond [Commentary]," *IEEE Commun. Mag.*, vol. 48, no. 3, pp. S6–S13, Mar. 2010.
  - [72] H. Boudinov, H. H. Tan, and C. Jagadish, "Electrical isolation of n-type and p-type InP layers by proton bombardment," *J. Appl. Phys.*, vol. 89, no. 10, pp. 5343–5347, May 2001.
  - [73] K. Itoh, K. Asahi, M. Inoue, and I. Teramoto, "Embedded-stripe GaAs-GaAlAs double-heterostructure lasers with polycrystalline GaAsP layers - I: Lasers with cleaved mirrors," *IEEE J. Quantum Electron.*, vol. 13, no. 8, pp. 623–627, Aug. 1977.
  - [74] H. Wada, H. Horikawa, Y. Matsui, Y. Ogawa, and Y. Kawai, "High-power and high-speed 1.3  $\mu\text{m}$  V-grooved inner-stripe lasers with new semi-insulating current confinement structures on p-InP substrates," *Appl. Phys. Lett.*, vol. 55, no. 8, pp. 723–725, Aug. 1989.
  - [75] W. H. Cheng, C. B. Su, K. D. Buehring, S. Y. Huang, J. Pooladdej, D. Wolf, D. Perrachione, D. Renner, K. L. Hess, and S. W. Zehr, "High-speed and high-power 1.3- $\mu\text{m}$  InGaAsP buried crescent injection lasers with semi-insulating current blocking layers," *Appl. Phys. Lett.*, vol. 51, no. 22, pp. 1783–1785, Nov. 1987.
  - [76] K. Tanaka, M. Hoshino, K. Wakao, J. Komeno, H. Ishikawa, S. Yamakoshi, and H. Imai, "Semi-insulator-embedded InGaAsP/InP flat-surface buried heterostructure laser," *Appl. Phys. Lett.*, vol. 47, no. 11, pp. 1127–1129, Dec. 1985.
  - [77] E. Kapon, J. Katz, and A. Yariv, "Supermode analysis of phase-locked arrays of semiconductor lasers," *Opt. Lett.*, vol. 9, no. 4, p. 125, Apr. 1984.
  - [78] A. Yariv and X. Sun, "Supermode Si/III-V hybrid lasers, optical amplifiers and modulators: A proposal and analysis," *Opt. Express*, vol. 15, no. 15, p. 9147, 2007.
  - [79] X. Sun, H.-C. Liu, and A. Yariv, "Adiabaticity criterion and the shortest adiabatic mode transformer in a coupled-waveguide system," *Opt. Lett.*, vol. 34, no. 3, pp. 280–282, février 2009.
  - [80] A. Yariv, "Coupled-mode theory for guided-wave optics," *IEEE J. Quantum Electron.*, vol. 9, no. 9, pp. 919–933, Sep. 1973.
  - [81] D. Liang, S. Srinivasan, J. Peters, A. Fang, and J. E. Bowers, "Demonstration of Enhanced III-V-On-Silicon Hybrid Integration by Using a Strained Superlattice as a Defect Blocking Layer," *ECS Trans.*, vol. 33, no. 4, pp. 421–426, Oct. 2010.
  - [82] D. Liang, A. W. Fang, H. Park, T. E. Reynolds, K. Warner, D. C. Oakley, and J. E. Bowers, "Low-Temperature, Strong SiO<sub>2</sub>-SiO<sub>2</sub> Covalent Wafer Bonding for III-V Compound Semiconductors-to-Silicon Photonic Integrated Circuits," *J. Electron. Mater.*, vol. 37, no. 10, pp. 1552–1559, Jun. 2008.

- 
- [83] D. Pasquariello and K. Hjort, "Plasma-assisted InP-to-Si low temperature wafer bonding," *IEEE J. Sel. Top. Quantum Electron.*, vol. 8, no. 1, pp. 118–131, Jan. 2002.
  - [84] D. Bordel, M. Argoud, E. Augendre, J. Harduin, P. Philippe, N. Olivier, S. Messaoudène, K. Gilbert, P. Grosse, B. B. Bakir, and J.-M. Fedeli, "Direct and Polymer Bonding of III-V to Processed Silicon-On-Insulator for Hybrid Silicon Evanescent Lasers Fabrication," *ECS Trans.*, vol. 33, no. 4, pp. 403–410, Oct. 2010.
  - [85] S. J. Pearton, J. W. Lee, E. S. Lambers, J. R. Mileham, C. R. Abernathy, W. S. Hobson, F. Ren, and R. J. Shul, "High microwave power electron cyclotron resonance etching of III-V semiconductors in CH<sub>4</sub>/H<sub>2</sub>/Ar," *J. Vac. Sci. Technol. B*, vol. 14, no. 1, pp. 118–125, Jan. 1996.
  - [86] T. R. Hayes, U. K. Chakrabarti, F. A. Baiocchi, A. B. Emerson, H. S. Luftman, and W. C. Dautremont-Smith, "Damage to InP and InGaAsP surfaces resulting from CH<sub>4</sub>/H<sub>2</sub> reactive ion etching," *J. Appl. Phys.*, vol. 68, no. 2, pp. 785–792, Jul. 1990.
  - [87] C. Constantine, C. Barratt, S. J. Pearton, F. Ren, and J. R. Lothian, "Smooth, low-bias plasma etching of InP in microwave Cl<sub>2</sub>/CH<sub>4</sub>/H<sub>2</sub> mixtures," *Appl. Phys. Lett.*, vol. 61, no. 24, pp. 2899–2901, Dec. 1992.
  - [88] A. Szerling, P. Karbownik, A. Łaszcz, K. Kosielski, and M. Bugajski, "Low-resistance p-type ohmic contacts for high-power InGaAs/GaAs-980 nm CW semiconductor lasers," *Vacuum*, vol. 82, no. 10, pp. 977–981, Jun. 2008.
  - [89] J. S. Yu, S. H. Kim, and T. I. Kim, "PtTiPtAu and PdTiPtAu ohmic contacts to p-InGaAs," in *1997 IEEE International Symposium on Compound Semiconductors*, 1998, pp. 175–178.
  - [90] A. G. Baca, F. Ren, J. C. Zolper, R. D. Briggs, and S. J. Pearton, "A survey of ohmic contacts to III-V compound semiconductors," *Thin Solid Films*, vol. 308–309, pp. 599–606, Oct. 1997.
  - [91] M. E. Mills, P. Townsend, D. Castillo, S. Martin, and A. Achen, "Benzocyclobutene (DVS-BCB) polymer as an interlayer dielectric (ILD) material," *Microelectron. Eng.*, vol. 33, no. 1–4, pp. 327–334, Jan. 1997.
  - [92] P. Procter and J. Solc, "Improved thermal conductivity in microelectronic encapsulants," in *Electronic Components and Technology Conference, 1991. Proceedings., 41st*, 1991, pp. 835–842.
  - [93] H. Ftouni, C. Blanc, A. Sikora, J. Richard, M. Defoort, K. Lulla, E. Collin, and O. Bourgeois, "Thermal conductivity measurement of suspended Si-N membranes from 10 K to 275 K using the 3 $\omega$ -Völklein method," *J. Phys. Conf. Ser.*, vol. 395, no. 1, p. 012109, Nov. 2012.
  - [94] R. Beigelbeck, F. Kohl, F. Keplinger, J. Kuntner, and B. Jakoby, "A Novel Characterization Method for Thermal Thin-Film Properties Applied to PECVD Silicon Nitride," in *2007 IEEE Sensors*, 2007, pp. 938–941.
  - [95] S. Pinel, A. Marty, J. Tasselli, J.-P. Bailbe, E. Beyne, R. Van Hoof, S. Marco, J. R. Morante, O. Vendier, and M. Huan, "Thermal modeling and management in ultrathin chip stack technology," *IEEE Trans. Compon. Packag. Technol.*, vol. 25, no. 2, pp. 244–253, Jun. 2002.
  - [96] I. Christiaens, G. Roelkens, K. D. Mesel, D. V. Thourhout, and R. Baets, "Thin-Film Devices Fabricated With Benzocyclobutene Adhesive Wafer Bonding," *J. Light. Technol.*, vol. 23, no. 2, p. 517, Feb. 2005.
  - [97] J. D. Joannopoulos, S. G. Johnson, J. N. Winn, and R. D. Meade, *Photonic Crystal - Molding the Flow of Light*. Princeton University Press, 2008.
  - [98] Y.-L. Cao, X.-N. Hu, X.-S. Luo, J.-F. Song, Y. Cheng, C.-M. Li, C.-Y. Liu, H. Wang, L. Tsung-Yang, G.-Q. Lo, and Q. Wang, "Hybrid III-V/silicon laser with laterally coupled Bragg grating," *Opt. Express*, vol. 23, no. 7, p. 8800, Apr. 2015.
  - [99] Descos, Antoine, "Conception, fabrication et réalisation de sources lasers hybrides III-V sur silicium," Institut des Nanotechnologies de Lyon, 2014.
  - [100] C. H. Henry, "Theory of the linewidth of semiconductor lasers," *IEEE J. Quantum Electron.*, vol. 18, no. 2, pp. 259–264, Feb. 1982.
  - [101] H. Ludvigsen, M. Tossavainen, and M. Kaivola, "Laser linewidth measurements using self-homodyne detection with short delay," *Opt. Commun.*, vol. 155, no. 1–3, pp. 180–186, Oct. 1998.
  - [102] K. Hassan, C. Sciancalepore, J. Harduin, T. Ferrotti, S. Menezes, and B. B. Bakir, "Toward athermal silicon-on-insulator (de)multiplexers in the O-band," *Opt. Lett.*, vol. 40, no. 11, p. 2641, Jun. 2015.
  - [103] L. Liu, T. Spuesens, G. Roelkens, D. Van Thourhout, P. Regreny, and P. Rojo-Romeo, "A Thermally Tunable III-V Compound Semiconductor Microdisk Laser Integrated on Silicon-on-Insulator Circuits," *IEEE Photonics Technol. Lett.*, vol. 22, no. 17, pp. 1270–1272, Sep. 2010.
  - [104] "Nanodevices for Photonics and Electronics: Advances and Applications," *CRC Press*. [Online]. Available: <https://www.crcpress.com/Nanodevices-for-Photonics-and-Electronics-Advances-and-Applications-Advances/Bettotti/9789814613743>. [Accessed: 05-Nov-2015].
  - [105] J. C. Hulme, J. K. Doyle, and J. E. Bowers, "Widely tunable Vernier ring laser on hybrid silicon," *Opt. Express*, vol. 21, no. 17, p. 19718, Aug. 2013.

- [106] A. Le Liepvre, C. Jany, A. Accard, M. Lamponi, F. Poingt, D. Make, F. Lelarge, J.-M. Fedeli, S. Messaoudene, D. Bordel, and G.-H. Duan, "Widely wavelength tunable hybrid III-V/silicon laser with 45 nm tuning range fabricated using a wafer bonding technique," in *2012 IEEE 9th International Conference on Group IV Photonics (GFP)*, 2012, pp. 54–56.
- [107] V. Jayaraman, Z.-M. Chuang, and L. A. Coldren, "Theory, design, and performance of extended tuning range semiconductor lasers with sampled gratings," *IEEE J. Quantum Electron.*, vol. 29, no. 6, pp. 1824–1834, 1993.
- [108] V. Jayaraman, A. Mathur, L. A. Coldren, and P. D. Dapkus, "Extended tuning range in sampled grating DBR lasers," *IEEE Photonics Technol. Lett.*, vol. 5, no. 5, pp. 489–491, 1993.
- [109] B. Mason, J. Barton, G. A. Fish, L. A. Coldren, and S. P. DenBaars, "Design of sampled grating DBR lasers with integrated semiconductor optical amplifiers," *IEEE Photonics Technol. Lett.*, vol. 12, no. 7, pp. 762–764, 2000.
- [110] E. J. Skogen, J. S. Barton, S. P. DenBaars, and L. A. Coldren, "Tunable sampled-grating DBR lasers using quantum-well intermixing," *IEEE Photonics Technol. Lett.*, vol. 14, no. 9, pp. 1243–1245, 2002.
- [111] M. N. Sysak, J. O. Anthes, D. Liang, J. E. Bowers, O. Raday, and R. Jones, "A hybrid silicon sampled grating DBR tunable laser," in *2008 5th IEEE International Conference on Group IV Photonics*, 2008, pp. 55–57.
- [112] M. N. Sysak, J. O. Anthes, O. Raday, J. E. Bowers, and R. Jones, "A hybrid silicon sampled grating DBR laser integrated with an electroabsorption modulator using quantum well intermixing," in *34th European Conference on Optical Communication, 2008. ECOC 2008*, 2008, pp. 1–2.
- [113] S. Charbonneau, E. S. Koteles, P. J. Poole, J. J. He, G. C. Aers, J. Haysom, M. Buchanan, Y. Feng, A. Delage, F. Yang, M. Davies, R. D. Goldberg, P. G. Piva, and I. V. Mitchell, "Photonic integrated circuits fabricated using ion implantation," *IEEE J. Sel. Top. Quantum Electron.*, vol. 4, no. 4, pp. 772–793, Jul. 1998.
- [114] V. Veerasubramanian, G. Beaudin, A. Giguere, B. LeDroff, V. Aimez, and A. G. Kirk, "A Vertical SG-DBR Based Tunable Hybrid Silicon Evanescent Laser," in *CLEO:2011 - Laser Applications to Photonic Applications*, 2011, p. JTu10.
- [115] B. Nabet, *Photodetectors: Materials, Devices and Applications*. Woodhead Publishing, 2015.
- [116] H. Park, A. W. Fang, R. Jones, O. Cohen, O. Raday, M. N. Sysak, M. J. Paniccia, and J. E. Bowers, "A hybrid AlGaInAs-silicon evanescent waveguide photodetector," *Opt. Express*, vol. 15, no. 10, p. 6044, 2007.
- [117] L. Vivien and L. Pavesi, *Handbook of Silicon Photonics*. CRC Press, 2013.
- [118] Y. Tang, H.-W. Chen, S. Jain, J. D. Peters, U. Westergren, and J. E. Bowers, "50 Gb/s hybrid silicon traveling-wave electroabsorption modulator," *Opt. Express*, vol. 19, no. 7, pp. 5811–5816, Mar. 2011.
- [119] T. Ferrotti, A. Chantre, B. Blampey, H. Duprez, F. Milesi, A. Myko, C. Sciancalepore, K. Hassan, J. Harduin, C. Baudot, S. Menezo, F. Boeuf, and B. Ben Bakir, "Power-efficient carrier-depletion SOI Mach-Zehnder modulators for 4x25Gbit/s operation in the O-band," 2015, vol. 9367, p. 93670D–93670D–11.
- [120] M. L. Davenport, G. Kurczveil, M. J. R. Heck, and J. E. Bowers, "A hybrid silicon colliding pulse mode-locked laser with integrated passive waveguide section," in *2012 IEEE Photonics Conference (IPC)*, 2012, pp. 816–817.
- [121] A. W. Fang, B. R. Koch, K.-G. Gan, H. Park, R. Jones, O. Cohen, M. J. Paniccia, D. J. Blumenthal, and J. E. Bowers, "A racetrack mode-locked silicon evanescent laser," *Opt. Express*, vol. 16, no. 2, p. 1393, 2008.
- [122] G. Kurczveil, M. J. R. Heck, J. D. Peters, J. M. Garcia, D. Spencer, and J. E. Bowers, "An Integrated Hybrid Silicon Multiwavelength AWG Laser," *IEEE J. Sel. Top. Quantum Electron.*, vol. 17, no. 6, pp. 1521–1527, Nov. 2011.
- [123] D.-X. Xu, M. Vachon, A. Densmore, R. Ma, A. Del  ge, S. Janz, J. Lapointe, Y. Li, G. Lopinski, D. Zhang, Q. Y. Liu, P. Cheben, and J. H. Schmid, "Label-free biosensor array based on silicon-on-insulator ring resonators addressed using a WDM approach," *Opt. Lett.*, vol. 35, no. 16, p. 2771, Aug. 2010.
- [124] K. De Vos, J. Girones, T. Claes, Y. De Koninck, S. Popelka, E. Schacht, R. Baets, and P. Bienstman, "Multiplexed Antibody Detection With an Array of Silicon-on-Insulator Microring Resonators," *IEEE Photonics J.*, vol. 1, no. 4, pp. 225–235, Oct. 2009.
- [125] T. Claes, W. Bogaerts, and P. Bienstman, "Vernier-cascade label-free biosensor with integrated arrayed waveguide grating for wavelength interrogation with low-cost broadband source," *Opt. Lett.*, vol. 36, no. 17, p. 3320, Sep. 2011.
- [126] C. L. Arce, K. D. Vos, T. Claes, K. Komorowska, and P. Bienstman, "SOI Microring Resonator Sensor Integrated on a Fiber Facet," in *Lab-on-Fiber Technology*, A. Cusano, M. Consales, A. Crescitelli, and A. Ricciardi, Eds. Springer International Publishing, 2015, pp. 53–68.





**Title:** From design to characterization of hybrid III-V on silicon lasers for photonic integrated circuit.

**Keywords:** photonic integrated circuits, semiconductor lasers, distributed Bragg grating, adiabatic coupler.

**Abstract:** This 3 years work covers the design, the process and the characterization of III-V on silicon lasers at 1.31  $\mu\text{m}$  for datacommunication applications. In particular, the design part includes the optimization of the coupling between III-V and Si using adiabatic tapers as well as the laser cavity, which is formed within the Si. Three types of lasers were studied, all of them based on cavities which consist of gratings: distributed feedback (DFB) lasers, distributed Bragg reflector (DBR) lasers and finally sampled-grating DBR (SGDBR) lasers. Regarding the DFB lasers, two solutions have been chosen: the grating is either etched on top or on the edges of the Si waveguide to form so called vertically or laterally coupled DFB lasers. The latter type, quite uncommon among hybrid III-V on Si technologies, simplifies the process fabrication and broadens the designs possibilities.

Not only the lasers demonstrated show high output powers ( $\sim 20$  mW in the waveguides) but also very good spectral purities (with a side mode suppression ratio higher than 50 dB), especially for the DFB ones. The SGDBR devices turn out to be continuously tunable over a wavelength range higher than 27 nm with a good spectral purity as well and an output power higher than 7 mW in the waveguide with great opportunities of improvement.

**Titre:** De la conception à la caractérisation de lasers hybrides III-V sur silicium pour des circuits photoniques intégrés.

**Mots clés:** circuits photoniques intégrés, diodes laser, réseau de Bragg distribué, coupleur adiabatique.

**Résumé:** Ces trois années de thèse balayent la conception, la fabrication et la caractérisation de lasers III-V sur silicium à 1.31  $\mu\text{m}$  pour les data-communications. Le design des sources englobe notamment l'optimisation du couplage entre l'empilement III-V et le silicium, effectué grâce à un taper adiabatique, ainsi que l'étude de la cavité laser inscrite, comme le taper, dans le silicium. Trois types de cavités à base de réseaux ont été étudiées: les cavités à contre-réaction distribuée (DFB pour distributed feedback), celles à réseaux de Bragg distribuées (DBR pour distributed Bragg reflector) et enfin celles à réseaux de Bragg échantillonnées (SGDBR pour sampled-grating DBR). Deux solutions ont été abordées concernant les lasers DFB: le réseau, inscrit dans le guide silicium sous la zone de gain, est soit gravé au-dessus du guide Si, soit sur les côtés. La seconde possibilité, appelée 'DFB lasers couplés latéralement', simplifie la fabrication et élargit les possibilités de design.

Les lasers DFB fabriqués sont très prometteurs en terme de puissance (avec jusque 20 mW dans le guide) ainsi que pour leur pureté spectrale (avec une différence de plus de 50 dB entre le mode principal et le mode suivant). Une accordabilité spectrale de plus de 27 nm a été obtenue en continu avec les lasers SGDBR tout en conservant une très bonne pureté spectrale et une puissance de plus de 7 mW dans le guide.